PROGENITOR SCENARIOS OF SUPERNOVAE FROM LOCAL GROUP STELLAR POPULATIONS AND SUPERNOVA REMNANTS

by

Sumit Kumar Sarbadhicary

B. S. in Physics, Louisiana State University, 2012

M. S. in Physics, University of Pittsburgh, 2014

Submitted to the Graduate Faculty of

the Kenneth P. Dietrich School of Arts and Sciences in partial fulfillment

of the requirements for the degree of

Doctor of Philosophy

University of Pittsburgh

2018

UNIVERSITY OF PITTSBURGH

KENNETH P. DIETRICH SCHOOL OF ARTS AND SCIENCES

This dissertation was presented

by

Sumit Kumar Sarbadhicary

It was defended on

June 11, 2018

and approved by

Carles Badenes, Dept. of Physics & Astronomy, University of Pittsburgh

Jeffrey Newman, Dept. of Physics & Astronomy, University of Pittsburgh

Desmond John Hillier, Dept. of Physics & Astronomy, University of Pittsburgh

Ayres Freitas, Dept. of Physics & Astronomy, University of Pittsburgh

Rupert Croft, Dept. of Physics, Carnegie Mellon University

Laura Chomiuk, Dept. of Physics & Astronomy, Michigan State University

Dissertation Director: Carles Badenes, Dept. of Physics & Astronomy, University of Pittsburgh

PROGENITOR SCENARIOS OF SUPERNOVAE FROM LOCAL GROUP STELLAR POPULATIONS AND SUPERNOVA REMNANTS

Sumit Kumar Sarbadhicary, PhD

University of Pittsburgh, 2018

Supernovae (SNe) are the explosive deaths of stars, but the detailed properties of their progenitors are not well understood. For example, while we know Type Ia SNe are explosions of white dwarfs (WDs), it is unclear whether these WDs generally have a stellar companion or another WD companion. For core-collapse SNe, whose progenitors are stars > 8 $M_\odot$, it is unclear whether stars > 18 $M_\odot$ produce a visible SN, or directly collapse to a black hole in a weak transient event. For my dissertation, I have focused on using high-quality surveys of SNRs, stellar populations and interstellar medium in our Local Group galaxies to understand the possible progenitor scenarios of SNe. The goal is to make an accurate measurement of the SN delay-time distribution (DTD), which is the rate of SNe versus stellar evolutionary timescale, assuming these stars were all formed in a burst. The DTD can constrain which set of progenitor models are consistent with the population of Type Ia and core-collapse SNe in a survey. To achieve this goal, I have constructed a model of a SNR survey in the Local Group that can estimate the visibility times of a SNRs as a function of their environment. This can be combined with existing high-quality stellar age distribution maps, constructed from resolved stellar populations, to measure the most accurate DTD. I also calculated DTDs of pulsating variables like RR Lyrae and Cepheids, and found a distribution of evolutionary timescales which are not predicted by canonical models. This helped understand possible systematics in the DTD method, and also reassess the progenitor scenarios of astrophysically significant objects like RR Lyrae and Cepheids in the era of big data surveys. Finally, I used direct observations and modeling of radio emission of old SNe/young SNRs such as SN

1885A and G1.9+0.3 as an alternative, but promising avenue for determining the possible progenitor scenarios of Type Ia SNe.

TABLE OF CONTENTS

LIST OF TABLES

LIST OF FIGURES

PREFACE

The completion of this thesis would not have been possible without the persistent guidance and encouragement from my advisor, Carles Badenes, and my collaborator, Laura Chomiuk. The breadth of research experience between Laura and Carles allowed me to pursue a wide range of exciting research topics, as laid out in this thesis. Besides learning the art of research, working with Carlos taught me the crucial skill of how to convey information based on the setting, such as a research paper, a proposal or a presentation. Working with Laura helped me learn essential tools in radio astronomy, both on the observational and theory front, and I am excited to carry on this collaboration with her for my postdoctoral research.

The diverse areas of astrophysics that had to be covered in this thesis presented a steep and intimidating learning curve for me, which I could not have climbed without the many experts that I had the good fortune of collaborating with. I am particularly grateful to Damiano Caprioli for helping me learn the complex topics in shock astrophysics which led to the modeling of supernova remnants, Cecilia Mateu for guidance with the fairly new territory (for me) of variable stars, Jeffrey Newman for his insights and guidance with various statistical tests, Lilia Tremou for staying up during Christmas and New Years Eve of 2016 to walk me through the rigors of radio data reduction, and Enrico Ramirez-Ruiz for the many thought-provoking discussions on the applicability of my research to supernova feedback. In addition, I have had the pleasure to interact with Ryan Foley, Dennis Zaritsky, Katie Auchettl, Knut Olsen, Dan Maoz, Thomas Matheson, Benjamin Williams, Julianne Dalcanton, Todd Thompson, Christopher Kochanek, and many other leading experts in the field, whose different perspectives and insights helped further enrich my thesis. I am also fortunate to have worked with very bright and passionate junior collaborators − Mairead Heger, an undergraduate at University of Pittsburgh who has done a lot of work on the

theoretical interpretations of the DTDs with MESA, and Jessica Maldonado (current) and Daniel Huizenga (former), graduate students at MSU and collaborators on the supernova remnant projects.

Most of my thesis work was done while I was at University of Pittsburgh, and the amount of help and inspiration I received at the Department of Physics and Astronomy was equally pivotal. A significant part of my intuition for research was built by presenting and discussing papers during Astrocoffee with my graduate student peers and professors in Astronomy. I am thankful to my committee members − Jeffrey Newman, John Hillier, Ayres Freitas and Rupert Croft − for their constructive criticisms and continued encouragements for my work. I have particularly benefited from my colleagues Yao-Yuan Mao (postdoctoral researcher) and Brett Andrews (research professor), who provided crucial guidance with Python programming, proposal writing and general career decisions. I have also benefitted from many impromptu and informal, yet stimulating, discussions with my graduate student peers in the department − Kara Ponder, Kevin Wilk, Hector Martinez Rodriguez, Daniel Perrefort, Brian Flores, Christine Mazzola, Fernando Zago and Rongpu Zhao.

A special thanks goes out to a close friend of mine outside of academia − Dipika Bhandari − for patiently and painstakingly proof-reading my papers and proposals, smoothing out my often clunky scientific prose, and providing the crucial support and motivation towards the end of my PhD.

Last but not least, I am eternally grateful to my parents who have provided the bedrock upon which I have built my career. My mother's curiosity about the stars fed my desire to be an astrophysicist as a child, and her unwavering support and blessings continue to push me along this path today.

I. INTRODUCTION

The deaths of stars are marked by a powerful explosive event, called supernova (SN). Each SN typically produces 10^{51} ergs of energy, which is equivalent to the total light energy produced by the sun in over 10 billion years. Most galaxies typically undergo a few SN every century/millennium, with some starbursts undergoing several SNe per year (e.g. Arp 220, Thrall, 2008). The cumulative energy and momentum generated in these explosions are crucial for providing pressure support in the galaxy and formation of the different phases of the interstellar medium (McKee & Ostriker, 1977; Elmegreen & Scalo, 2004; Joung & Mac Low, 2006), regulating the formation of stars (e.g. Leroy et al., 2008; Faucher-Giguère et al., 2013), launching of galactic winds and fountains (Heckman & Thompson, 2017), chemical enrichment of the interstellar medium (ISM) (Nomoto et al., 2013) and intergalactic medium (Chen, 2017), and accelerating cosmic rays, the highest energy particles pervading the universe (e.g. Baade & Zwicky, 1934; Ackermann et al., 2013; Caprioli, 2015; Amato & Blasi, 2017). In addition, these events can be seen in very distant galaxies, which makes them useful measures of cosmological distances and have provided many unprecedented constraints on our theories of cosmology, most importantly the detection of accelerated expansion in the universe (Perlmutter et al., 1999; Riess et al., 1998). Thus, SNe are at the heart of understanding some of the most important astrophysical processes in the universe, and especially important in the fields of stellar and galactic evolution.

However, our understanding of SNe is far from complete. Specifically, the possible scenarios that lead to the explosion of a star, i.e. the SN progenitor is an active area of research. This gets particularly complicated because we rarely get a direct observation of the progenitor before it explodes, and in general, we have to rely on the characteristics of the SN explosion itself, such as the light curve, spectrum and the SN environment, in order to deduce the

progenitor scenario. This is particularly complicated because of our poor understanding of essential physical processes that affect the evolution of progenitors, such as convection and mass-loss in interacting binaries (Gallart et al., 2005; Conroy, 2013).

In the following subsections, I will elaborate on the lack of understanding about the progenitors of the two major classes of SNe, thermonuclear and core-collapse, and introduce my general strategy of tackling these problems for my thesis.

A. PROGENITOR ISSUES OF TYPE IA SUPERNOVAE

Type Ia is the spectroscopic classification for SNe characterized by lack of hydrogen (H) and helium (He) lines, and presence of a strong, blue-shifted absorption line of Silicon (Si) at rest-frame wavelength of 6355 Å near maximum brightness. The spectrum near maximum light is also characterized by lines from intermediate mass elements like Ca, Mg and S, and by Co and Fe after a few weeks (Filippenko, 1997). The most remarkable property of Type Ia SNe is the uniformity of their light curves and spectra, with peak magnitudes ~ -19.3 mag in the B and V bands, and a dispersion of only ~ 0.3 mag (Phillips, 1993). This enabled the use of Type Ia as 'standardizable candles' (up to 0.15 mag scatter in peak brightness after light-curve corrections Frieman et al., 2008) to measure the distances and recessional velocities of faraway galaxies, which produced the first empirical evidence of the presence of dark energy in the universe (Perlmutter et al., 1999; Riess et al., 1998; Wood-Vasey et al., 2007; Betoule et al., 2014). In contrast with the explosions of massive stars (known as core-collapse, discussed in the next section), Type Ia SNe have been seen in both star-forming, and elliptical galaxies that do not show any active star formation (Filippenko, 1989; Totani et al., 2008).

These characteristics of Type Ia SNe strongly suggest that their progenitors are carbon-oxygen (CO) white dwarfs (WDs). These objects are usually the leftover cores of stars $\lesssim 7$ $M_\odot$ stars, composed primarily of C and O, and are supported by the strong degenerate pressure of electrons (Farmer et al., 2015). At a critical mass of 1.4 $M_\odot$, known as the Chandrasekhar mass, the carbon-oxygen core contracts due to its own weight, under degenerate conditions (Chandrasekhar, 1931). This leads to a rapid temperature increase

and subsequently, a runaway thermonuclear ignition of carbon and the ultimate destruction of the WD (Hillebrandt & Niemeyer, 2000).

The conditions under which WDs undergo thermonuclear explosion is still a topic of debate. The homogeneity of Type Ia light curves have historically motivated a single scenario involving the explosion of a Chandrasekhar mass WD (Branch et al., 1993). However, the diversity of Type Ia explosions ranging from subluminous 1991bg (Turatto et al., 1996; Mazzali et al., 1997) to the unusually luminous 1991T (Filippenko et al., 1992) and the correlation between the properties of the SN population and their host galaxies (Li et al., 2011; Rigault et al., 2013) indicated that there may be a diversity of WD masses exploding. For the comprehensive review of these channels explored in the literature, I will refer the reader to the major review articles that discuss these in detail (e.g. Hillebrandt & Niemeyer, 2000; Wang & Han, 2012; Hillebrandt et al., 2013; Maoz et al., 2014; Livio & Mazzali, 2018). Here I will provide brief descriptions, strengths and drawbacks of the broad class of progenitor models considered relevant to Type Ia and this thesis :-

I. SINGLE-DEGENERATE: In this scenario, the primary WD is accreting hydrogen from a non-degenerate companion, which can be a main-sequence star, a sub-giant, or a red-giant. The accreted material burns on the surface of the WD, which leads to the eventual growth of the WD towards Chandrasekhar mass (e.g. van den Heuvel et al., 1992; Han & Podsiadlowski, 2004). The model has been historically favored as it provides a natural scenario for a Chandrasekhar mass explosion. It is generally assumed that this explosion begins as a subsonic deflagration flame near the core, and transitions to a supersonic detonation front that ultimately disrupts the WD (Khokhlov, 1991). Such an explosion scenario has been largely consistent with the light curves, colors and relative abundances of Fe-group and intermediate mass elements observed in Type Ia spectra (for details, see Blondin et al., 2013; Hillebrandt et al., 2013; Maoz et al., 2014). The high abundances of neutron-rich elements seen in the X-ray spectra of Type Ia SNRs (Martínez-Rodríguez et al., 2017a), and in the galaxy (Seitenzahl et al., 2013) can only be explained by the high densities reached inside a Chandrasekhar mass WD core (Piro & Bildsten, 2008; Martínez-Rodríguez et al., 2016). However, a major issue with the single degenerate scenario has been the requirement of a narrow accretion rate of 1-5$\times10^{-7}$ $M_{\odot}$/yr for

stable hydrogen burning on the surface of the WD (Nomoto, 1982a). Accretion rates below this value will cause nova eruptions that can slowly erode the WDs (Yaron et al., 2005), while rates above this value will lead to engulfment of the binary system in a common envelope, effectively stopping the mass growth of the WD (Iben & Tutukov, 1984). High accretion rates can be theoretically sustained by an increased amount of mass-loss (Hachisu et al., 1996, 1999), but such mass loss is expected to manifest as a circumstellar medium around the progenitor system, which can become visible in X-rays and radio once it interacts with the SN shock (Badenes et al., 2007). However, apart from a few rare detections of CSM in optical emission (Silverman et al., 2013), most Type Ia SN or SNRs have not shown significant signs of circumstellar interaction (Badenes et al., 2007; Panagia et al., 2006; Chomiuk et al., 2016). The single-degenerate scenario was also considered highly unlikely (although not entirely ruled out) for SN 2011fe and SN 2014J – the two nearest Type Ia SNe observed in the modern telescope era, and consequently with the deepest multi-wavelength constraints of any Type Ia (Nugent et al., 2011; Chomiuk et al., 2012; Margutti et al., 2012; Pérez-Torres et al., 2014; Margutti et al., 2014).

II. DOUBLE-DEGENERATE: This scenario involves two WDs in a close binary orbit that gradually spiral-in as they lose orbital energy via gravitational wave emission. Ultimately, the WDs will merge via tidal disruption and accretion of the secondary WD (e.g. Lorén-Aguilar et al., 2009; Moll et al., 2014), or collide head on, if they are in a dense stellar environment, or if a tertiary body is present (Kushnir et al., 2013). The double-degenerate scenario appears consistent with the lack of hydrogen in Type Ia SNe, the lack of X-ray and radio emission in Type Ia events (Chomiuk et al., 2012; Margutti et al., 2014), the long-delay times measured in Type Ia SN surveys(Maoz & Mannucci, 2012; Maoz et al., 2014), the predicted merger rates of galactic WD binaries (Badenes & Maoz, 2012; Maoz et al., 2018) and the absence of surviving companions in some Type Ia SNRs (e.g. Schaefer & Pagnotta, 2012; Kerzendorf et al., 2012). A major uncertainty with this channel is how the merging WDs would ultimately lead to an explosion. In fact, models suggest that the accretion of the secondary will convert the WD into oxygen and neon as a result of an off-center carbon ignition, and ultimately produce a neutron star

as a result of an accretion-induced collapse (Nomoto & Iben, 1985; Shen et al., 2012). In addition, some asymmetry is expected in double-degenerate explosions (e.g. Kromer et al., 2010; Porter et al., 2016), whereas of spectropolarimetry Type Ia SNe (e.g. Maund et al., 2013; Porter et al., 2016) and morphologies of Type Ia SNRs (Lopez & Fesen, 2018) show that Type Ia generally lack asymmetry.

III. SUB-CHANDRASEKHAR: Several authors had proposed that a thermonuclear explosion could be triggered inside a WD before it reaches Chandrasekhar mass, through the double detonation scenario (e.g. Taam, 1980; Nomoto, 1980; Woosley & Weaver, 1994; Woosley & Kasen, 2011). In this scenario, a layer of He accreted from some type of He donor (e.g. He WD) detonates on the surface of the primary WD under certain specific conditions, leading to shocking and a second detonation of carbon in the WD core. In the past, the model had issues because it predicted too much He and high-velocity Ni and Fe in the outer ejecta (see discussion in Hillebrandt & Niemeyer, 2000). Recently however, the model has been revived in light of favorable results, such as the long tail in the Type Ia ejecta mass distribution below 1.4 $M_{\odot}$ (Scalzo et al., 2014), the discovery of an increasingly diverse population of Type Ia events not entirely explained by M_{ch} explosions (Taubenberger, 2017), and the successful double detonations reproduced in recent multi-dimensional simulations (Bildsten et al., 2007; Fink et al., 2010; Sim et al., 2010). Signatures of sub-Mch explosion in the light curves and spectra of Type Ia SNe is currently an active area of research (see discussions in Blondin et al., 2017; Shen et al., 2018).

Making the connection between progenitor models and Type Ia observations is a challenging task. Unlike core-collapse SNe, where certain progenitor channels were validated by direct observations of the progenitors in pre-explosion images (see Section I.B), no such direct observations of the progenitor system of a Type Ia SN have been obtained (although upper limits on SN 2011fe and SN 2014J did put the strongest constraints till date on the companion properties Li et al., 2011; Kelly et al., 2014). Also, the complexity of the essential physical processes involved in Type Ia progenitor models, such as accretion and mass-loss in close binaries, flame propagation and turbulence inside WDs, and the formation of spectral lines in the inhomogeneous, expanding ejecta, has made it difficult to predict unique,

observable signatures for each model (Hillebrandt & Niemeyer, 2000).

Resolving the Type Ia progenitor problem remains one of the most important goals of stellar astrophysics. Constraining the outcomes of these different WD binaries will be very useful in furthering our understanding of binary stellar evolution. Ignoring the possibility of multiple progenitors could contribute to systematic errors in studies of dark energy and ΛCDM cosmology (Howell, 2011; Ponder et al., 2016). For example, the presence of a redshift or host-galaxy dependent progenitors could lead to biases in light curve fitting of Type Ia SNe, and this could affect measurements of the dark energy equation of state parameters. Considering multiple progenitor channels for Type Ia SNe may also be important for chemical evolution because they contribute most of the Fe-group elements in galaxies (Nomoto et al., 2013; Matteucci et al., 2009; Andrews et al., 2017).

B. PROGENITOR ISSUES OF CORE-COLLAPSE SUPERNOVAE

The progenitors of core collapse SNe are typically stars more massive than 8 $M_{\odot}$. Unlike Type Ia, these SNe vary widely in their observational characteristics, and had to be classified accordingly (Filippenko, 1997). Type I refer to hydrogen-poor class of SNe, with Ib referring to SNe having He features in the optical spectra, and Ic where He is absent. Type II refer to SNe showing prominent hydrogen lines. In this category, SNe fall into the IIP category if they show a long plateau phase post-maximum, IIL if such a plateau phase is absent, IIn if they show narrow emission lines aside from the broad hydrogen lines, and IIb if their spectrum gradually transitions from a Type II to a Type Ib.

Despite their observational diversity, core collapse SNe share a common physical mechanism − the collapse of a dense Fe core that was formed in the advanced stages of nuclear burning in these massive stars. As the core collapses, the central region reaches nuclear densities (and ultimately form a neutron star or a black hole), while the collapse is reversed into a 'bounce' shock that travels outwards (Burrows, 2013; Foglizzo, 2017). It is believed that this shock is energized by some combination of neutrino heating, turbulence and/or convection, which ultimately unbinds the star (although simulating this self-consistently with

multi-dimensional simulations is still an active area of research. See discussions in Müller, 2016; Janka, 2017).

Compared to Type Ia, the progenitors of some nearby core-collapse SNe have been directly observed. The two nearest and best-studied events were SN 1987A in the LMC and SN 1993J in M81. Pre-explosion images identified a blue supergiant progenitor for 1987A with an initial mass in the range of 14-20 $M_\odot$ (Smartt et al., 2009; McCray & Fransson, 2016), although 1987A-like events are now considered rare (McCray & Fransson, 2016). SN 1987A was also associated with the first detection of extragalactic neutrinos, which confirmed that a collapse of the Fe core is involved preceding the explosion (Hirata et al., 1987). Observational followups for SN 1993J, a Type IIb SN, revealed for the first time, a binary progenitor system with the exploding star possibly being a stripped supergiant (Maund et al., 2004). Today, many more nearby core-collapse SNe with direct detections (or strong upper limits) on progenitors have been obtained from HST and large ground-based telescopes(e.g. Smartt, 2015; Bersten et al., 2018; Van Dyk et al., 2018). Type II SNe have had the most progenitor detections, with Type IIP being the most abundant subclass, and having red supergiant progenitors. While these observations did not constrain all core-collapse progenitor mechanisms, it provided direct evidence that massive progenitors such as red-supergiant, and binary mechanisms are indeed at play.

An interesting pattern, however, emerged from these progenitor observations − the lack of Type II progenitors with masses above 17-18 $M_\odot$ (Kochanek et al., 2008; Smartt et al., 2009; Smartt, 2015). If the mass distribution of stars above 17 $M_\odot$ follows the Salpeter initial mass function (IMF, or the mass distribution of stars entering the main-sequence, $dN/dM \propto M^{-2.35}$ Salpeter, 1955), then the current Type II sample is missing about 30 % progenitors above this limit. This has been dubbed the red supergiant problem, since the progenitors of Type IIp are normally red-supergiants. There is some debate that the progenitor mass measurements were biased by systematics in stellar evolution and atmospheric models (Davies & Beasor, 2018), dust extinction around massive stars (Kochanek et al., 2012) and/or variations in the IMF (Offner et al., 2014), but on the other hand, the measured masses are consistent with observations of nebular spectral lines (Jerkstrand et al., 2015), and mass-loss and circumstellar constraints from radio and X-ray observations

of these SNe (Chevalier et al., 2006; Dwarkadas, 2014). A physical explanation for this observed dearth of high-mass progenitors is that these stars directly collapse to a black hole, and fail to produce a luminous transient. Simulations of the 'explodability' of stellar cores in massive stars showed that successful explosions occurred in 8-18 $M_\odot$ stars, but above this mass range, successful explosions only occurred for certain sporadic 'islands' of stellar masses (O'Connor & Ott, 2011; Sukhbold & Woosley, 2014; Pejcha & Thompson, 2015). The explodability of the core in these simulations is determined by its compactness – the more massive the star, the more compact the core, and the more difficult it is for the bounce shock to overcome the gravitational potential of the proto-neutron star, and the pressure of the infalling material. Observational efforts have been underway to look for disappearing red supergiants in the nearby universe as candidates for failed SN (Kochanek et al., 2008; Gerke et al., 2015; Adams et al., 2017a). N6946-BH1 emerged as a strongest candidate for such a scenario (Adams et al., 2017b). Monitored for 16 years, the star brightened by a factor of 10, and then dimmed by almost 5 orders of magnitude, indicating that it had disappeared. Alternative scenarios such as dust obscured R-Cor B stars, Mira variables, SN imposters and stellar mergers seem to be inconsistent with the current set of observations available for this object (see discussion in Adams et al., 2017b). Future observations with JWST is expected to shed more light on the failed SN scenario.

A similarly open issue is the progenitor scenarios of Type Ib/c SNe. These SNe are characterized by lack of H and Si lines (and He lines for Ic SNe), indicating that the outer envelopes of H and He were stripped off in the pre-SN stage (Filippenko, 1997). Historically, the progenitors of Type Ib/c were considered to be single Wolf-Rayet (WR) stars (Begelman & Sarazin, 1986; Gaskell et al., 1986; Filippenko & Sargent, 1986; Fransson & Chevalier, 1989; Woosley et al., 1995). WRs are the penultimate stages of main-sequence stars $\gtrsim 25$ $M_\odot$, and are characterized by strong winds (10^{-4}-10^{-5} $M_\odot$ yr^{-1}, 1300-2500 km/s), and strong emission lines of He, C, N, and/or O (Crowther, 2007). The strong winds were considered a plausible mechanism for stripping off the outer layers, leading to the main observational features of Ib/c SNe.

Gradually it became clear that the single WR channel cannot account for all Type Ib/c SNe, and binary evolution of massive stars became an increasingly favored channel (Podsiad-

lowski et al., 1992) based on several lines of observations, such as the high binary fraction in massive stars (Sana et al., 2012), low ejecta-masses of Ib/c SNe (Drout et al., 2011; Taddia et al., 2015; Lyman et al., 2016), detection of Ib and IIb SNe with binary progenitors, and non-detections of Ic SN progenitors (Smartt et al., 2009; Smartt, 2015; Van Dyk, 2017), the fraction of such stripped-envelope SNe in core-collapse surveys (Smith et al., 2011), and their correlation with host-galaxy properties (Graur et al., 2017a,b). However, it is still debated what fraction of Ib/c come from the single WR channel, and the binary evolution channel. For example, mass-transfer in binaries may not efficiently remove the inner He-layers, and some metallicity-driven winds (such as in WRs) may be necessary for Ic SNe (Yoon, 2017; Galbany et al., 2018). Single red-supergiants have been confirmed to produce Type IIp SNe (Smartt et al., 2009), and it may not be surprising if single stellar evolution can also account for some fraction of Type Ib/c SNe. Furthermore, the plethora of uncertainties in massive stellar evolution, such as mass-transfer in binaries, eruptive mass-loss and preSN variabilities (Smith, 2014), and the environmental dependence of the stellar IMF (see e.g. Geha et al., 2013; Weidner et al., 2013) makes it difficult to make any conclusive statements about massive progenitors.

A complete understanding of the terminal stages of massive stars is important in astrophysics for several reasons. Knowing whether red supergiants above 17-18 $M_{\odot}$ result in weak or non explosions is an important missing puzzle in the pre-SN evolution of massive stars. If Type IIp SNe indeed fail to occur above this mass range, it can serve as a physical explanation for the apparent mismatch between the core collapse rate and the star formation rate (Horiuchi et al., 2011; Horiuchi et al., 2014), the observed mass distribution of neutron stars and black holes (Kochanek, 2014), and the unusually high masses of the merging black holes detected by LIGO (Abbott et al., 2016; Woosley, 2016). In addition, knowing the mass-loss rates and contribution to the SN rate from these massive stars maybe important for our current prescriptions of feedback (Naab & Ostriker, 2017) and chemical evolution models (Nomoto et al., 2013).

C. DISSERTATION STRATEGY

For my thesis, I have mainly focused on answering the above questions about SN progenitors using two methods: delay time distribution and direct modeling of radio emission from evolved SNe/SNRs. These methods, along with their effectiveness, is introduced below.

1. The Delay-Time Distribution Method

a. General Technique: One way to address the progenitor questions above is to measure the contribution of different progenitor channels to the SN rate measured in surveys. This is the principle behind the *delay-time distribution (DTD)*, which is formally defined as the hypothetical SN rate versus time elapsed since a brief burst of star formation (Maoz & Mannucci, 2012). In signal processing terminology, the DTD acts like a 'transfer function' or 'impulse-response function' that embodies the 'response' of the system, i.e. by producing SNe, to the burst of the star-formation, i.e. the 'impulse'. Physically, the delay-times correspond to the stellar evolution timescales of the progenitor, and since each progenitor model is associated with a certain timescale, the DTD can directly validate specific progenitor scenarios. The DTD can be measured from a SN survey and the age distributions of the stellar populations targeted in the survey, derived from integrated spectra (or resolved populations if the galaxies are nearby). Mathematically, these quantities are related by the equation (Maoz & Mannucci, 2012; Badenes et al., 2015),

$$\lambda(t) = \int_0^t \dot{M}\,(t-\tau)\,\Psi\,(\tau)\,T_{vis}\mathrm{d}\tau \tag{I.1}$$

where $\lambda(t)$ is the expected number of SNe in a galaxy at a cosmic time t, $\dot{M}$ is the stellar age distribution (SAD, also referred to as the star-formation history) in units $\mathrm{M}_\odot\ \mathrm{yr}^{-1}$, Ψ is the DTD in units of objects $\mathrm{yr}^{-1}\ \mathrm{M}_\odot^{-1}$, and T_{vis} is the visibility time or the control time of the survey, i.e. the average duration of visibility of SNe during all observations of the host galaxy in the survey. The DTD is the unknown parameter in this equation, and has been estimated from SN surveys in galaxy clusters (Maoz & Sharon, 2010), field ellipticals (Totani et al., 2008), volumetric surveys (Gal-Yam & Maoz, 2004), and large extragalactic

surveys like LOSS-SDSS (Maoz et al., 2011), SDSS-II (Maoz et al., 2012) and CLASH (Graur et al., 2014). The solution depends on the type of survey used, but if the complex SADs of individual galaxies in the survey, or sub-regions of the galaxy are known, then Ψ can be estimated by discretizing Eq (III.1) as

$$\lambda_i = \sum_j M_{ij} \Psi_j T_{vis,i} \tag{I.2}$$

and inverting the set of linear equations. Here λ_i is the expected number of SNe per galaxy/sub-region i, M_{ij} is the discretized SAD, or the stellar mass formed in galaxy/sub-region i in the age-bin j, and $\mathrm{T}_{vis,i}$ is the visibility time in galaxy/sub-region i. We can constrain Ψ by statistically comparing with the observed number of SNe per galaxy N_i. Since the SN rate in galaxies is generally small, one would expect $N_i = 0$ for most galaxies, $N_i = 1$ for some, and so on. The likelihood of observing N_i SNe in a survey where the expectation is λ_i is therefore assumed to be a Poisson distribution,

$$p(N_i|\lambda_i) = \prod_{i=1}^{K} \frac{\mathrm{e}^{-\lambda_i} \lambda_i^{N_i}}{N_i!} \tag{I.3}$$

Where K is the total number of galaxies/sub-regions in the survey. The known quantities include M_{ij}, which can be obtained from modeling the spectra or broadband photometry of the galaxy using stellar population synthesis models (e.g. Tojeiro et al., 2009), and $\mathrm{T}_{vis,i}$, which can be estimated by accounting for the on-target observation time, flux sensitivity of the telescope, detection efficiency and distance to the galaxy (e.g. Leaman et al., 2011). Deriving M_{ij} for sub-regions of nearby galaxies is discussed in Section III.A.4, and deriving $\mathrm{T}_{vis,i}$ for sub-regions is the subject of Chapter II.

b. Expectations from Theory: The measured DTD can be compared with predicted DTDs from population synthesis models to infer the rates and efficiencies of different SN progenitor models (see Nelemans et al., 2013; Maoz et al., 2014, for a review of Ia DTD models). In the single degenerate channel, the DTDs depend sensitively on the binary evolution physics adopted in the simulation, but usually have a common feature: a cutoff at a delay-time of roughly a few Gyrs. This is because longer delay-times correspond to

smaller companion masses, and companions < 2 $M_\odot$ are not able to transfer mass at the required rates for stable growth of the primary WD (Section I.A). DTDs of double degenerate channels, on the other hand, typically follow a t^{-1} form (where t =delay-time), and can extend all the way upto a Hubble time, because of the long in-spiral timescales as a result of gravitational wave emission. Comparison of the observed and model DTDs showed that the single degenerate channel cannot account for all Type Ia because of the statistically significant signal present in the Type Ia SN DTD for delay times $> 7 - 8$ Gyrs. However, many sources of systematic uncertainties affected these measurements (described in more detail in Chapter II), which prevented any detailed inference about progenitor scenarios.

The DTD method can be similarly applied to core collapse SN surveys, although no detailed DTD measurement has been attempted (Maoz et al., 2012, measured the DTD in a single delay-bin between 0-40 Myrs). Theoretical DTDs have been calculated with binary population synthesis codes by Zapartas et al. (2017) and Eldridge et al. (2017). In both studies, core collapse SNe were produced on delay-times of 3-50 Myrs, or 100-8 $M_\odot$ for solar metallicity and single stellar evolution. These delay-times can extend to 200 Myrs if one includes binary stellar evolution, which overlaps with the prompt channel $\sim 40 - 100$ Myrs of the Type Ia DTD. Measurement of a core-collapse DTD in the age range of 6-12 Myrs correspond to the red-supergiant mass-range, and the presence of a signal in this range can verify whether red-supergiants contribute to the supernovae sample, i.e. whether they successfully explode as SNe.

In Chapter II, I lay down the path to measuring a DTD with SNRs in the Local Group galaxies, which is expected to be the most accurate version of a SN DTD.

However, the applicability of the DTD does not end with SNe. Because the DTD is a 'transfer function' representing evolutionary timescales, it can be applied to *any* stellar object in the Local Group to understand its evolutionary properties, as long as information on the stellar age distribution in that survey exists. Our current stellar evolution models are mainly one-dimensional, and a major downside is that essential physical physical processes like convection, mixing and mass-loss occur in three-dimensions. The physics behind these processes are either not well understood, or computationally intractable in one-dimensional models. As a result, systematic uncertainties still exist in our models of different stellar

objects. Following up on Badenes et al. (2015) which calculated the DTD for planetary nebulae, the first category of objects other than SNe for which a DTD was calculated, I have started calculating the DTDs of RR Lyrae and Cepheid variables, which is described in Chapter III. The goal of this project is twofold: 1) To shed some light on their model uncertainties (e.g. the Cepheid mass-discrepancy problem, the second parameter problem) using the unique perspective provided by the DTD method. 2) To test the robustness of the DTD method by applying it to different objects with better understood stellar evolution properties than SNe. While there are uncertainties in the models of RR Lyrae and Cepheids, their progenitors are much more observationally constrained than SNe. This is because of their abundant populations in the Milky Way and the Magellanic Clouds (e.g. more than 140,000 RR Lyrae have been discovered in the *Gaia* Data Release 2 for the galaxy, Clementini et al., 2018), the high completeness of their surveys as a result of their brightness and variabilities, constraints on their structural physics from pulsation models, and constraints on ages and chemical compositions from host stellar clusters (see Section III.A.1). Applying the DTD method to different problems will help improve our understanding of how reliably the method performs, and make the most accurate interpretation the SN DTD we expect to measure with SNRs.

2. Progenitor clues from late-time radio observations

Radio emission from SNe probes the mass-loss history of the progenitor, thereby providing another way of identifying the associated progenitor channel (Patnaude & Badenes, 2017). While optical observations of SNe mainly trace properties of the slow-moving bulk ejecta, radio emission directly probes the circum-stellar medium (CSM) around the progenitor. When the SN shock collides with the CSM, electrons are accelerated to relativistic speeds, and they give rise to optically-thin synchrotron radio emission observable at frequencies of 1-10 GHz (Chevalier, 1982, 1998). Modeling radio emission is therefore relatively simple, and also less affected by extinction effects that are more pronounced in optical observations. Combining radio observations with wavelengths like optical and X-ray can therefore provide stronger constraints on progenitor scenarios of specific SNe, particularly in the era of pow-

erful, upcoming radio interferometers that can reach unprecedented spatial resolution and sensitivities (Lien et al., 2011).

The CSM around the progenitor that will be probed by radio emission will depend on mass-loss and evolutionary history of the progenitor. For example, for Type Ia SNe, it is believed that the accretion-driven mass-loss in single-degenerate progenitors will produce a denser CSM around the white-dwarf than in double-degenerate channels (Badenes et al., 2007, although there are nuances to this picture, which is further discussed in Chapter IV). However, till date no radio emission has been detected in Type Ia SNe, which has nevertheless provided useful constraints on the progenitor rates (Panagia et al., 2006; Weiler et al., 2002; Chomiuk et al., 2016). Core-collapse SNe on the other hand have produced visible radio emission as they are more likely to be associated with denser CSM due to strong winds and eruptive events (Owocki, 2014; Smith, 2014). Extensive radio observations of Type Ib/c SNe (e.g. Soderberg et al., 2006; Wellons et al., 2012; Corsi et al., 2016) and Type II SNe (Stockdale et al., 2006, 2007) have provided independent constraints on the mass-loss rates, the diverse circumstellar environments carved out by the progenitors, and possible associations with gamma-ray burst jets (for the case of Ib/c).

While young SNe generally trace mass-loss episodes immediately prior to the explosion, late-time observations of SNe and/or SNRs can probe mass-loss histories on much longer timescales (e.g. $10^3 - 10^5$ years before explosion) (Patnaude & Badenes, 2017; Patnaude et al., 2017). These mass-loss histories are intimately linked to the long-term stellar evolution of the progenitor, and thereby provides additional constraints on the progenitor channels of SNe that may be missed in early-time observations (Margutti et al., 2017; Milisavljevic & Fesen, 2017). In Chapter IV, I modeled VLA observations of SN 1885A and G1.9+0.3: the two youngest Type Ia SNe in the Local Group with ages $\gtrsim 100$ years. The radio emission at these ages will probe progenitor-driven mass-loss on the aforementioned timescales of $10^3 - 10^5$ years prior to explosion, and therefore provides a unique way to determine which of the Type Ia progenitor channels discussed in Section I.A apply.

For an introduction to the radio emission process in supernova remnants, please refer to Section II.B.1.d, and the Appendix of the thesis for detailed calculations.

D. LIST OF ACRONYMS USED IN THIS THESIS

SN (SNe) - Supernova (pl: Supernovae)

SNR - Supernova Remnant

HB - Horizontal Branch

ZAMS - Zero-Age Main Sequence

RGB - Red Giant Branch

OGLE - Optical Gravitational Lensing Experiment

MESA - Modules for Experiments in Stellar Astrophysics

MIST - MESA Isochrones and Stellar Tracks

VLA - Very Large Array

ATCA - Australian Telescope Compact Array

HST - Hubble Space Telescope

IR - Infra-red

DTD - Delay Time Distribution

SAD - Stellar Age Distribution

LGGS - Local Group Galaxy Survey

ACS - Advanced Camera for Surveys

ISM - Interstellar Medium

LF - Luminosity Function

MCs - Magellanic Clouds

LMC - Large Magellanic Cloud

s SMC - Small Magellanic Cloud

PHAT - Panchromatic Hubble Andromeda Treasury

CMD - Color Magnitude Diagram

CSM - Circum-stellar Medium

WD - White Dwarf

CC - Core Collapse

RMS - Root Mean Square

II. TOWARDS A LOCAL GROUP DELAY-TIME DISTRIBUTION WITH SUPERNOVA REMNANT SURVEYS

Most of the content in this chapter was published in the Monthly Notices to the Royal Astronomical Society journal as Sarbadhicary et al. (2017a), titled *"Supernova Remnants in the Local Group - I. A model for the radio luminosity function and visibility times of supernova semnants"*. Collaborators: Carles Badenes (University of Pittsburgh), Laura Chomiuk (Michigan State University), Damiano Caprioli (University of Chicago) & Daniel Huizenga (Michigan State University).

A. INTRODUCTION

1. Why a Local Group DTD?

The challenge of calculating DTDs accurately using SN surveys (Section I.C.1) is the limited information on the stellar populations of distant galaxies. Because the stellar populations are unresolved in these galaxies, the SADs are determined from the luminosity-averaged, integrated spectra of these galaxies. Younger, more luminous stars will primarily dominate the spectra, even though they form only a fraction of the total stellar mass, and this can introduce systematic errors in the derived stellar ages and masses that are difficult to account for (Wuyts et al., 2011; Conroy, 2013). The stellar age information from these galaxies also gets averaged over large spatial scales because of the limited resolution of the telescope, and

it might not be representative of the local age distribution of the SN. Local Group galaxies, on the other hand, can provide more accurate SADs (Harris & Zaritsky, 2004, 2009; Lewis et al., 2015). These galaxies are near enough for ground and space-based telescopes to detect and resolve older and fainter stars, providing a more reliable census of the total stellar mass in the galaxies (for more details on SADs maps in the Local Group, refer to Section III.A.4). Unfortunately, the small SN rate in the Local Volume ($\sim$ 1 SN per 50-100 years) makes it impossible to get a sizable SN survey. On the other hand, the Local Group has an abundant reservoir of SNRs (SNRs) left from the SN explosion that can serve as the SN survey.

2. Supernova Remnants (SNRs)

Once a SN shock travels through and interacts with the interstellar medium, the swept-up gas and expelled debris is illuminated across the electromagnetic spectrum, and this structure is visible as a 'SNR'. SNRs generally have lifetimes of several 10^4 years, depending on the strength of the explosion and external conditions. The evolution of the SNR can be divided in the following phases,

I. *Free-Expansion* (also called the ejecta-dominated phase), which lasts upto about a 1000 years. In this phase, the ejected mass is much higher than the swept-up ISM mass, and the ejecta travels ballistically ($R \sim t$) outward at several 10^4 km/s. The outward moving shock accelerates ions and electrons to relativistic energies, which makes the SNR visible in X-ray and radio wavelength (see Section for details). Gradually, the SNR decelerates as it pushes against the ISM, and deviates from the asymptotic $R \sim t$ solution (Truelove & McKee, 1999). This deceleration drives a *reverse shock* into the ejecta inwards (in the rest frame of the shock), and contributes to the thermal and line emission from the ejecta observed in X-rays and optical wavelengths.

II. *Sedov-Taylor* lasts upto a few 10^4 years, and initiated when the swept-up ISM mass is roughly equal to the ejecta mass. At this point, the expansion of the SNR can be approximated as a point explosion that drove an adiabatically-expanding shock into the surrounding medium. The evolution is described by the self-similar solution of Taylor (1950) and Sedov (1959), i.e. the properties of the remnant at any time can be described

in terms of a 'characteristic' length and time, and depends only the initial explosion energy and ISM density.

III. *Snowplow* (beyond few 10^4 years): The SNR is now old enough that significant radiative losses occur from the shock front. The gas immediately behind the shock cools, and forms a thin dense shell. Further interior however, the gas is still hot, and the pressure of this hot gas mainly drives the expansion. Gradually, the hot interior would have radiated most of its thermal energy and the pressure will equalize with the ISM. From this point, the gas shell expands with a constant momentum (Cioffi et al., 1988; Kim & Ostriker, 2015). Note that for radio emission, the radiative phase is considered unimportant as the shock does not have enough energy to accelerate electrons.

IV. Once the shock decelerates to the turbulent velocity of the ISM, the shock front disintegrates and merges with the ISM.

SNRs, particularly the young objects (< 1000 years), have been very useful for studying SN progenitors as they still bear imprints of the original explosion and nucleosynthesis. The presence of neutron-rich isotopes inferred from the X-ray spectra of Type Ia SNRs can distinguish between progenitor scenarios because the isotopic abundances depend sensitively on the central conditions of the progenitor WD (e.g. Park et al., 2013; Yamaguchi et al., 2015; Martínez-Rodríguez et al., 2017b). Emission lines of He, O in the Balmer-dominated spectra of Type Ia SNRs can reveal whether the progenitor was a hot, accreting WD (Woods et al., 2017, 2018). Proper motion studies of the stars inside nearby Type Ia SNRs have been used to constrain the presence of surviving companions of WD progenitors (Kerzendorf et al., 2009; Schaefer & Pagnotta, 2012; Edwards et al., 2012; Kerzendorf et al., 2012; Pagnotta & Schaefer, 2015; Boubert et al., 2017; Kerzendorf et al., 2018). Useful inferences about the theory of core-collapse SNe have also been obtained from well-studied SNRs like Cas A, SN 1987A, Crab, W49B etc. In particular, detailed observations of the non-uniform spatial and velocity distribution of synthesized elements in the SNR ejecta - something not available in observations of distant SNe - provided the opportunity to study the asymmetric nature of core-collapse explosions, the role of large-scale fluid instabilities and mixing, and the possibility of jet-like mechanisms driving core-collapse SNe (Grefenstette et al., 2014, 2017; Wongwathanarat et al., 2017; Fesen & Milisavljevic, 2016; Milisavljevic & Fesen, 2017;

Lopez & Fesen, 2018). SNRs can also help explain the origin of neutron-star kicks and further constrain the asymmetric nature of core-collapse explosions (Holland-Ashford et al., 2017; Katsuda et al., 2018). Additionally, the effects of pre-SN mass-loss and its effects on the subsequent evolution can be understood from the SNR spectra (see references in Patnaude & Badenes, 2017; Patnaude et al., 2017).

However these techniques are limited to the handful of young and nearby SNRs that can be reliably classified as Type Ia or Core-collapse subtypes. Most SNRs on the other hand are old, and dominated by emission from swept-up ISM.

The DTD technique allows one to study progenitor scenarios by taking advantage of the full SNR survey in any Local Group galaxy. Several 100s of SNRs have been surveyed in the Local Group in optical, X-ray and radio, e.g. see Badenes et al. (2010) for LMC and SMC, Long et al. (2010); Lee & Lee (2014); Garofali et al. (2017) for M33, Lee & Lee (2014) for M31 and Chomiuk & Wilcots (2009) for radio SNR catalogs of nearby galaxies, including dwarf galaxies. Larger ground-based telescopes and *HST* have also made SNR surveys possible outside the Local Group, e.g. M83 (Blair et al., 2012). These SNR surveys serve as an effective SN survey that is hypothetically conducted over 10^4 years, i.e. the average visibility time of SNRs. While Milky Way also has one of the largest and well-studied SNR catalog (Green, 2014a), these are not as useful for our statistical calculations because of distance uncertainties, large range of angular sizes, and interstellar extinction in the galactic plane.

3. Goal of this Study

Badenes et al. (2010) and Maoz & Badenes (2010) pioneered the technique of using SNR surveys as 'effective' SN surveys to calculate the SN DTD. A catalog of 77 SNRs in the LMC and SMC, along with the SAD maps of Harris & Zaritsky (2004, 2009), yielded a SN DTD with 3 age-bins (3-40 Myrs, 40-100 Myrs, and 100 Myrs-10 Gyrs). The DTD was consistent with measurements from SN surveys, although the small SNR sample restricted the number of age-bins to 3. Additionally, the sample was heterogeneously compiled from different surveys, making the completeness of the sample hard to interpret. An accurate DTD with higher age-resolution would require a large survey of SNRs with well-understood

completeness limits. This is further discussed in Section II.I.

Measuring the DTD from SNRs also requires an estimate of their *visibility time*, the duration for which SNRs in the survey would remain detectable, which is related to the environment-sensitive evolution of SNRs. The visibility time allows us to predict the number distribution of SNRs in the galaxy for a given DTD, which can be compared with the observed distribution from the SNR survey to constrain the DTD. Badenes et al. (2010) approximated the visibility times of the Magellanic SNR population as the cooling timescale of the SNR plasma transitioning from the Sedov to the radiative stage (Blondin et al., 1998; Bandiera & Petruk, 2010). This approximation does not take into account the details of the synchrotron radio light curves of SNRs produced by particle acceleration at the shock-ISM interface. Radio SNR surveys are also sensitivity-limited, and possibly missing many faint SNRs (Gordon et al., 1999; Chomiuk & Wilcots, 2009), which needs to be accounted for.

In this study, we model the radio visibility times of a catalog of SNRs statistically, by simulating their radio light curves and accounting for completeness of the SNR catalog. Our work is a proof-of-concept, with the goal of extracting physical information relevant to SN studies, such as the SN rate and DTD, from radio continuum-selected SNR surveys and knowledge of the ISM in Local Group galaxies. We model the radio light curves of SNRs using current theories of electron acceleration and magnetic field amplification in SNR shocks (Caprioli & Spitkovsky, 2014a,b, and references therein). The population of model SNRs is then constrained using multi-wavelength maps of the host galaxy, which trace the ambient ISM and stellar population, and the observed luminosity function (LF) of a radio-continuum selected SNR survey. We focus on the radio properties of SNRs over other wavelengths because: (1) SNRs have been traditionally easier to model in the radio (Chevalier, 1982; Berkhuijsen, 1984; Chevalier, 1998; Berezhko & Völk, 2004a; Chevalier & Fransson, 2006) compared to X-ray or optical wavelengths. X-ray spectra of SNRs is produced by a mix of thermal and non-thermal processes that require complex hydrodynamical modeling (Badenes, 2010; Vink, 2012), while the [SII]/Hα ratio, commonly used in optical surveys to identify SNRs (Mathewson & Clarke, 1973; Gordon et al., 1998; Blair et al., 2012; Lee & Lee, 2014), is sensitive to the properties of the interstellar clouds interacting with the shock (McKee & Cowie, 1975; Dopita, 1979; Dopita et al., 1984; White & Long, 1991)

and the ionization state of the ambient medium (Morlino et al., 2012), making it difficult to model. (2) SNR catalogs based on radio synchrotron emission will be largely unaffected by extinction compared to X-ray or optical. Similar statistical studies of Local Group SNR populations have also been done to explain their size distribution of SNRs (Asvarov, 2014) and constrain the microphysics of interstellar shocks (Barniol Duran et al., 2016).

For this paper, we apply our model to the M33 SNR population since M33 currently has the largest single-survey radio SNR catalog in the Local Group (Gordon et al., 1999), and is free of distance uncertainties, unlike Galactic SNRs (Green, 2014a). In the future, our model will be extended to M31 and the Magellanic Clouds. In Section II.B.1, we describe the generation of model SNR populations using a Monte-Carlo method, with emphasis on our radio light curve model, the strategy for placing SNRs in the ISM, and comparison with the radio SNR catalog in M33. In Section II.C, we show the constraints on the model parameter space from the radio LF of the M33 SNR catalog. Section II.D uses these constraints to predict the visibility times of M33 SNRs as a function of the HI column density. Section II.E investigates the correlation between the radio luminosity of the brightest SNR and the SN rate, and Section II.F discusses the implications of these findings, as well as the effects of changing key assumptions in the model.

B. MODELING SUPERNOVA REMNANT SURVEY

1. Generating SNR populations

We create synthetic SNR populations by generating multiple SNRs following a Poisson process, where the probability of an SNR exploding in a given year is given by the SN Rate, R. We fix the ratio of Type Ia to CC SNe at 1/3 (Li, 2011, combining Type Ib/c and Type II SNe into the CC rate, for simplicity. We checked and found that our results has little sensitivity to changes in Ia/CC ratio within the range of values measured in galaxy surveys). We wait until the SNR population reaches a 'steady state', i.e the rate of SNRs forming and fading roughly balance each other, and then compare the LF of this steady state with

observations. Since the steady state is reached within a few 10^4 years, much smaller than galactic timescales, we keep R and the Ia/CC fraction constant. For each SNR, we select a spatial location in M33, an ambient density at that location, and the kinetic energy and ejecta mass that serve as initial conditions for the SNR radio light curve.

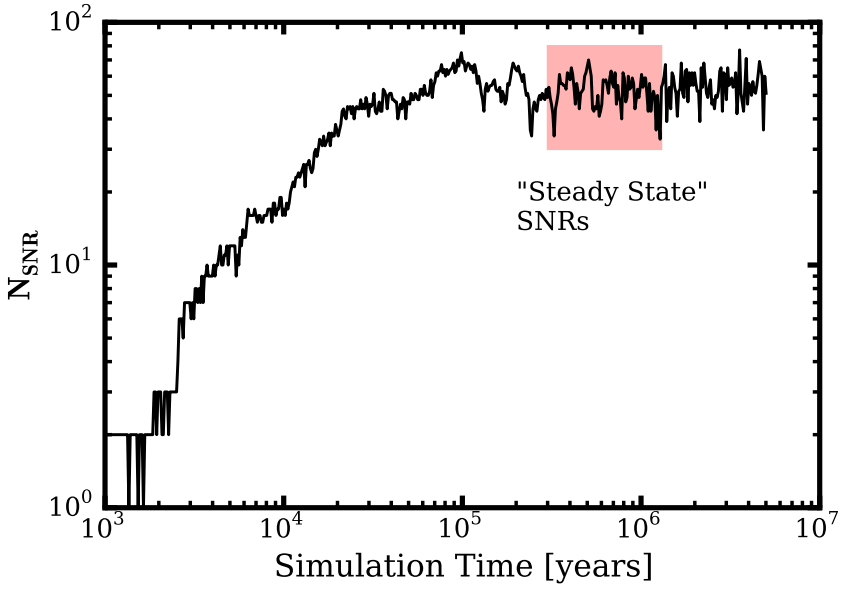

Figure 1: Generation of a synthetic SNR population using our model. SNRs are created at a rate R, with a Ia/CC ratio = 1/3, and radio light curve properties drawn by the method described in the text. The number of SNRs in the population reaches an equilibrium on a timescale of roughly the visibility time of SNRs. We use the radio luminosity function of this 'steady-state' population (for the given set of free parameters) to compare with observations.

a. Spatial Location The spatial location of each SNR, depending on whether it is a Type Ia or CC, is selected from a set of multi-wavelength maps of M33 (Figure 2, with details of the observations summarized in Table II.B.1). We assign locations of CC SNRs in M33 using FUV (Gil de Paz et al., 2007) and 24 μm (Dale et al., 2009) images, which trace recent star formation (Kennicutt & Evans, 2012). Since FUV is prone to extinction, it is supplemented with the 24 μm image, which traces dust-enshrouded young stellar populations.

Table 1: Summary of multi-wavelength data for M33 used in the SNR model.

Waveband [a]	Facility	θ [b] (arcsec)	d_{sp} [c] (pc)	Utility	Reference
Radio (21 cm)	VLA + GBT	20.0	77.0	ISM (HI)	1
Radio (6, 20 cm)	VLA + WSRT	7.0	29.0	Radio SNR survey	2
R (658 nm)	4 m Mayall/Mosaic	1.0	4.0	Type Ia tracer SNRs	3
FUV (1539 Å)	GALEX	4.2	17.1	Core-collapse tracer	4,5
IR (24 μm)	Spitzer/MIPS	6.0	24.4	Dust-obscured regions	6

[a] Median wavelength quoted in parentheses

[b] Angular resolution in arcseconds

[c] Spatial resolution, assuming a distance to M33 = 840 kpc (Kennicutt, Jr. et al., 2008)

References: (1) Braun (2012) (2) Gordon et al. (1999) (3) Massey et al. (2006) (4) Gil de Paz et al. (2007) (5) Morrissey et al. (2007) (6) Dale et al. (2009)

We apply the correction in Hao et al. (2011),

$$\mathrm{L_{FUV}} = \mathrm{L_{FUV}^{obs}} + 3.89\ \mathrm{L_{24\mu m}} \tag{II.1}$$

to produce the combined FUV and 24μm map for placing CC SNRs in our model. The probability of a CC SNR exploding in a given image pixel scales with the combined FUV and 24μm luminosity in that pixel. We chose FUV over the widely used Hαf line tracer of star formation, since Hα reflects young stellar populations with ages up to 30 Myrs, whereas FUV emission mainly arises from young stellar populations with ages up to 100 Myrs, which accounts for the abundant, lower ZAMS mass progenitors of CC SNRs (Hao et al., 2011).

Type Ia SNRs are positioned by the distribution of stellar mass traced by an r-band image of M33 (Massey et al., 2006). This is motivated by an observed correlation between the Type Ia rate with the r-band luminosity of the host galaxy (Yasuda & Fukugita, 2010). Note that we only place SNRs in the survey area of Gordon et al. (1999) shown by the dashed box in Figure 2. This is to ensure comparison of our model within the same area

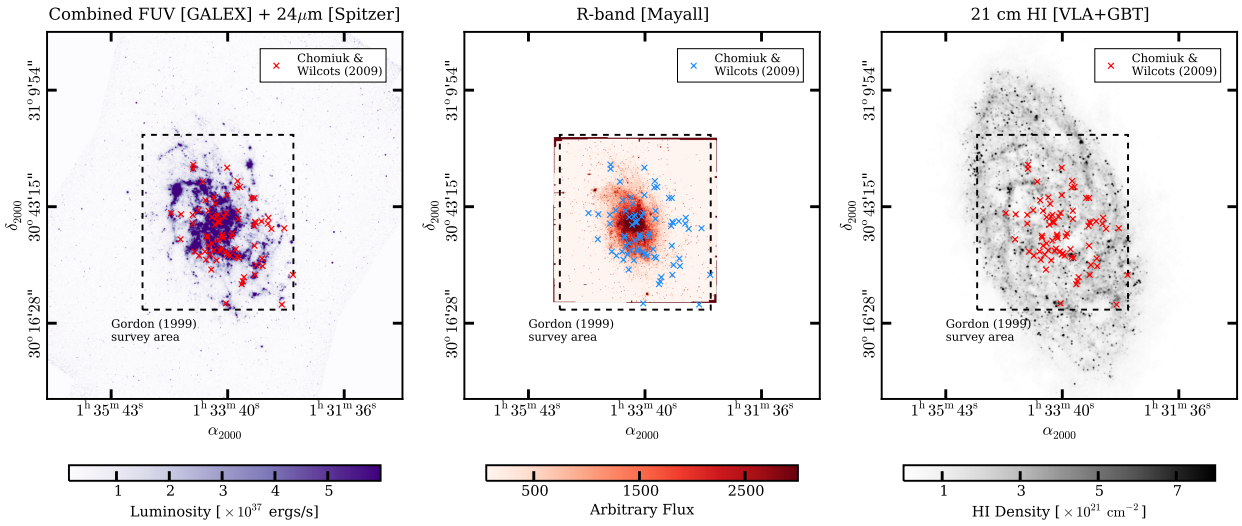

Figure 2: Multi-wavelength maps of M33, with their properties and usage described in the text and summarized in Table II.B.1. Each plot shows the 77 radio selected SNRs (Chomiuk & Wilcots, 2009) as colored 'x'. The dashed square region marks the 40 sq. arc-minutes area surveyed for radio SNRs by Gordon et al. (1999). All images were scaled to the resolution of 21 cm HI image.

that contains the observed SNRs. Although the actual survey area may be close to circular, a square survey area is not a bad approximation since very few model SNRs will be going off near the corners because of the low UV, IR and optical luminosities in these regions.

The vertical height z at which the SNR goes off, for a given spatial location in M33, is drawn from an exponential distribution (Yoachim & Dalcanton, 2006; Jurić et al., 2008),

$$p(z) \propto \exp\left(-\frac{|z|}{z_*}\right) \tag{II.2}$$

where z_* is the SN scale height. We set $z_* = 90$ pc for CC SNRs and 320 pc for Type Ia, assuming that CC SNe follow the distribution of bright stars near the Galactic plane and Type Ia SNe follow the bulk stellar disk population (Miller & Scalo, 1979; Heiles, 1987). These values are commonly assumed in simulations of SN-driven ISM (see Joung & Mac Low, 2006; Hill et al., 2012; Girichidis et al., 2016, and references therein). We comment on the effects of changing these assumptions in Section II.F.3.

Our method of placing SNRs does not explicitly assume any particular form of DTD. We are simply stating that there are two kinds of SN progenitors - one associated with young, dense star forming environments, and one that is not correlated with recent star formation, according to observations. This simple approach is sufficient for our proof-of-concept study. More sophisticated placement strategies are certainly possible, and in the future we will explore them and the influence they can have on the derived DTD.

b. Ambient Densities We assume a disk-like distribution of the M33 ISM and infer a volumetric density at the vertical position z of the SNR,

$$n_0(z) = \frac{N_H}{\sqrt{\pi z_0^2}} \exp\left(-\frac{z^2}{z_0^2}\right) \tag{II.3}$$

where N_H is the HI column density. We select N_H at the spatial location of each SNR (selected in Section II.B.1.a) from an HI column map corrected for self-absorption (shown in Figure 2, Braun, 2012). The scale height of the HI column, z_0 is treated as a free parameter in our model. More precisely, z_0 is the apparent scale height of M33, owing to its inclination. The Gaussian form of our ISM disk follows from observations of the vertical HI distribution near the Galactic mid-plane (Dickey & Lockman, 1990).

The motivation for our relatively simple ISM model is to explore the parameter space of SNR evolution. Disk galaxies have a complex, multi-phase and inhomogeneous ISM (McKee & Ostriker, 1977; Hopkins et al., 2012; Hill et al., 2012; Gent et al., 2013) that may modify the evolution of SNRs (Martizzi et al., 2015; Li et al., 2015). But the assumption of a uniform ISM traced by HI serves as a good first approximation since HI has the highest ISM volume filling factor (Ferrière, 2001) and has been previously used to constrain the properties of various SNe and SNRs (e.g. Badenes et al., 2006; Chomiuk et al., 2012, 2016). In a future paper, we will make use of the analytical fits for radius and velocity of an SNR shock in an inhomogeneous, turbulent medium by Martizzi et al. (2015) to understand the extent of modification imposed by an inhomogeneous ISM.

c. Kinetic Energy and Ejecta Mass We draw kinetic energies, E for Type Ia and CC SNe from a log-normal distribution centered on 10^{51} ergs,

$$p(\mathrm{logE}) = \frac{1}{\sqrt{2\pi\sigma^2_{\mathrm{logE}}}} \exp\left(-\frac{(\mathrm{logE} - \mu_{\mathrm{logE}})^2}{2\sigma^2_{\mathrm{logE}}}\right) \tag{II.4}$$

with $\mu_{\mathrm{logE}} = 51$ chosen for both Type Ia and CC SNe. The 1σ error of the CC SN kinetic energy distribution, $\sigma_{\mathrm{logE}} = 0.28$, is chosen such that the fraction of normal CC (with 10^{51} ergs) to energetic gamma-ray bursts/hypernovae (with $\gtrsim 10^{52}$ ergs) is $\sim 10^{-3}$, consistent with observations (Podsiadlowski et al., 2004; Smartt et al., 2009). Type Ia's, on the other hand, are a more homogenous class of explosions, and are expected to have a narrower spread in kinetic energies. We chose $\sigma_{\mathrm{logE}} = 0.1$, which is consistent with the observed rates of super-luminous and sub-luminous Type Ia (Meng et al., 2010) as well as the range of energies inferred from the X-ray spectra of well studied Type Ia SNRs (Badenes et al., 2008). We will discuss the effect of changing our assumptions on the kinetic energy distributions of Type Ia and CC SNe in Section II.F.3.

Even though SNe can have different ejecta masses, we fix the ejecta masses ($\mathrm{M_{ej}}$) for CC SNRs and Ia's at 5 $\mathrm{M_\odot}$ and 1.4 $\mathrm{M_\odot}$ respectively. This is justified because SNR surveys are dominated by objects in the Sedov stage of evolution where ejecta mass has a negligible effect on the evolution (See Section II.B.1.d and Figure 4).

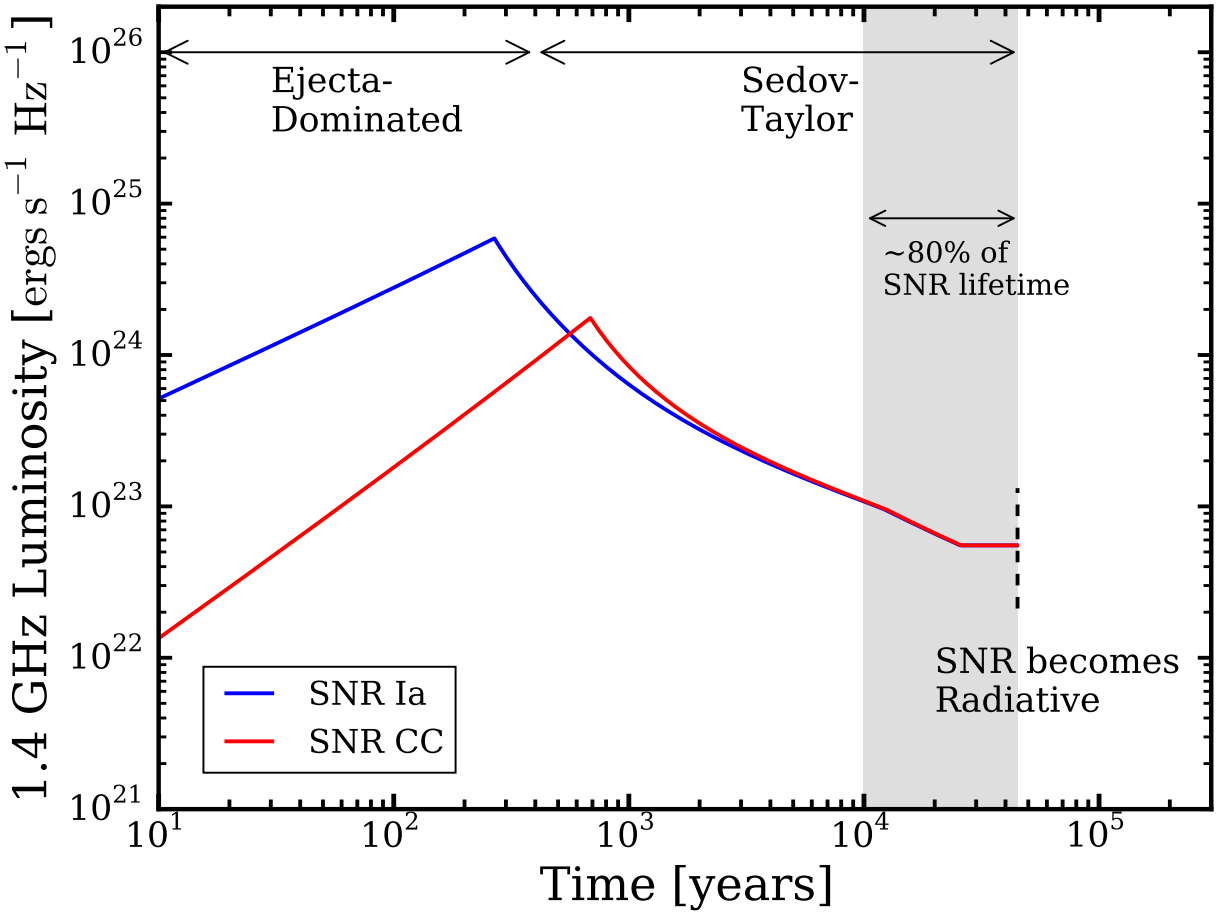

Figure 3: Illustration of a model radio light curve for Type Ia and CC SNR, evolving through the ejecta-dominated and Sedov-Taylor phases. The dashed line marks the transition to the radiative phase, where we assume the synchrotron emission becomes inefficient, as discussed in Section II.D. Both types of SNRs exploded with kinetic energy of 10^{51} ergs in an ISM density, $n_0 = 1$ cm^{-3}. For CC, we chose $M_{\rm ej} = 5$ M$_\odot$, and for Ia, $M_{\rm ej} = 1.4$ M$_\odot$. Most SNRs will be found in the Sedov-Taylor stage, as shown by the shaded region.

d. Radio Light Curve For each SNR, we calculate its radio luminosity at a given age with a synthetic radio light curve model. Radio emission in SNRs comes from synchrotron radiation emitted by electrons that are accelerated to relativistic energies by the shock (Bell, 1978; Chevalier, 1982, 1998; Berezhko & Völk, 2004a; Chevalier & Fransson, 2006). The accelerated particles produce instabilities and turbulence in the magnetic field upstream of the shock, which amplifies the SNR magnetic field and further contributes to the particle acceleration in a non-linear way (recall that a current $\mathbf{j}$ in a magnetic field $\mathbf{B}$ induces a plane-perpendicular force $\propto \mathbf{j} \times \mathbf{B}$. This force mainly contributes to the turbulent amplification of the upstream field in SNRs due to the cosmic-ray current. For details of the acceleration physics, please refer to Bell, 2004; Amato & Blasi, 2009; Caprioli & Spitkovsky, 2014a). The net result of this process is a power-law distribution of accelerated cosmic-rays that produces synchrotron radio emission in SNRs (Thompson et al., 2009; Chomiuk & Wilcots, 2009).

In this section, we will only explain the main features of our SNR light curve model, and refer the reader to the Appendix for the equations governing the 1.4 GHz radio luminosity vs age for SNRs. Quantitatively, the radio emission depends on the shock radius R_s, the shock velocity v_s, the energy in the relativistic electrons and the amplified magnetic field. We assume a small fraction $\epsilon_{\rm e}$, of the shock energy is shared by the relativistic electrons accelerated by the shock (referred to as electron acceleration efficiency in this paper) and is considered a free-parameter in our model. The spectrum of the acceleration electrons is $N(E) = N_0 E^{-p}$ based on the theory of diffusive shock acceleration. We fix $p = 2.2$ from gamma-ray observations of Galactic SNRs (Morlino & Caprioli, 2012; Caprioli, 2012) and in Section II.F.3, we discuss the effects of changing our assumptions on p.

A novel aspect of our light curve model is the treatment of magnetic field amplification, which is induced upstream of the shock (Morlino et al., 2010; Caprioli & Spitkovsky, 2014b) and parameterized by $\epsilon_{\rm b}^{\rm u}$, the fraction of shock energy contained in the amplified upstream magnetic field, B_u. The downstream field, B is then a simple compression of B_u. Instead of leaving $\epsilon_{\rm b}^{\rm u}$ as a free parameter, we use results of simulations of particle acceleration from first principles (Caprioli & Spitkovsky, 2014b) to scale $\epsilon_{\rm b}^{\rm u}$ with the Alfvén Mach number of the shock and the cosmic ray acceleration efficiency (Eq .7). The form of the scaling depends on whether the amplification is induced by resonant (Bell, 1978) or non-resonant (Bell, 2004)

streaming instabilities (see Section A.2 for a detailed discussion). No equipartition between energy densities of the magnetic fields and relativistic electrons is assumed.

The SNR radio light curve (Figure 3) is determined by the competing effects of expansion, which increases the emitting volume ($\sim R_s^3$), and deceleration (decreasing v_s), which reduces the abundance of relativistic electrons and the streaming instabilities that amplify the magnetic field. Expressions for R_s and v_s as the SNR evolves from ejecta-dominated to Sedov-Taylor phase are given in Table 5. During the ejecta-dominated phase (the first $10^2 - 10^3$ years), $L_{1.4}$ increases as the shock expands rapidly through the ISM. The light curve peaks at the beginning of the Sedov-Taylor phase, once the shock has swept-up an ISM mass equivalent to the ejected mass. At this point, a period of enhanced deceleration ($v_s \propto t^{-3/5}$) slows down the expansion and causes $L_{1.4}$ to drop. When B ($\propto v_s$) drops to a simple compression of the ambient magnetic field, B_0 (Eq. .4), we fix $B = 4B_0$, which balances the effects of expansion and deceleration, causing the light curve to flatten out. The general shape of our analytical light curve is consistent with numerical calculations (Berezhko & Völk, 2004a). The slight curvature around 10^3 years represents the increasing contribution from resonant instabilities, and the 'knee' (around 10^4 years) is because of the decreasing particle acceleration efficiency (Section A.2). Note that the SNR spends most of its lifetime in the Sedov-Taylor phase, and therefore *most Local Group SNRs are expected to be found in their Sedov phase.*

The SNR radio light curve also depends on the ambient medium density, kinetic energy and ejecta mass of each SNR (Figure 4). Denser ISM causes SNRs to decelerate faster (hence, smaller diameters), and remain radio visible for a shorter period, assuming they remain above the survey detection limit. SNRs in denser ISM are also brighter due to greater energy available to the downstream magnetic field and relativistic electrons (Eq .2, .3). In the same way, higher kinetic energies also produce brighter SNRs, but these SNRs are larger and radio visible for longer periods because of greater energy in the forward shock. Finally, the ejecta mass mainly affects SNRs in their ejecta-dominated phase, with higher ejecta masses implying smaller energy per unit mass of ejecta (assuming energy is conserved) and thus fainter SNRs. The onset of the Sedov-Taylor phase is also delayed because the SNRs need to sweep up a larger mass of ISM (equal to their ejected mass). However, *the ejecta*

mass does not affect the Sedov-Taylor light curve, since the evolution in this phase is driven by the swept-up ISM, which far exceeds the initial ejecta mass. Because of this, we kept the ejecta masses of our model Type Ia and CC SNRs fixed in Section II.B.1.c.

We also show in Figure 4 that for reasonable ranges of values of ISM densities, kinetic energies and ejecta masses, our model predicts radio luminosities and diameters that are similar to well-known SNRs in the Galaxy (Case & Bhattacharya, 1998). This is a consistency check. The galactic SNRs are not used to constrain the model light curves, since reproducing the individual luminosities and diameters require more detailed modeling of the SNR and its environment.

2. Comparison with SNR catalogs

Within the assumptions discussed in Section II.B.1, our model has three free parameters - SN Rate (R), HI scale height (z_0) and electron acceleration efficiency (ϵ_e). We can constrain these parameters by comparing the radio LF of our steady-state model SNR populations with the observed SNR LF in M33.

Figure 5 shows the radio LF of SNRs in M33 from the catalog of Chomiuk & Wilcots (2009), and whose locations are also shown in Figure 2. The catalog consists of 77 SNRs, a subset of the 186 radio sources in M33 compiled by Gordon et al. (1999) from 6 and 20 cm observations (Duric et al., 1993) having a noise limit of 50μJy per beam, where the beam diameter was 7" or 29 pc at 840 kpc, the adopted distance to M33. The 77 SNRs were classified by their radio images (sources with 3σ detection above noise, with a synchrotron signature $S_\nu \propto \nu^{-\alpha}$, where $\alpha \geq 0.2$ was used to distinguish from HII regions) and by detection of an Hα counterpart to distinguish them from background galaxies, which would be redshifted out of the narrowband filter.

Because of the homogenous selection criteria for our SNR catalog, we are able to define a *completeness limit* above which we consider the sample to be complete. SNRs can be missed if they are below the noise sensitivity of the radio survey, which increases at larger radii from the phase center of the image and in regions of vigorous star-formation. To account for these SNRs missing from the faint end of the LF, Chomiuk & Wilcots (2009) showed that the radio

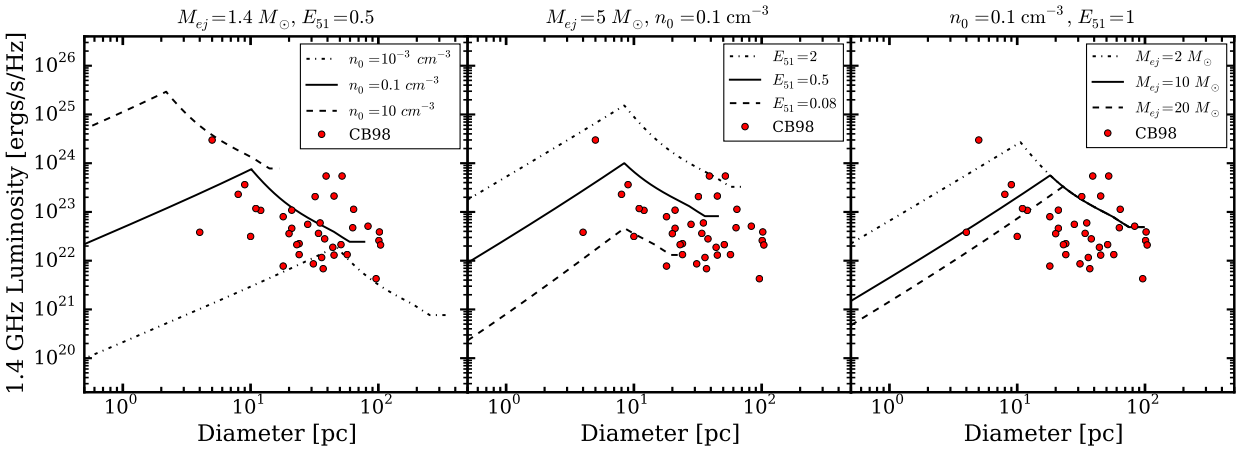

Figure 4: The effects of varying the ISM density (n_0), kinetic energy (E_{51}, in units of 10^{51} ergs) and ejecta mass (M_{ej}, in units of $M_\odot$) on the SNR light curves. For each panel, we fix $\epsilon_e = 5 \times 10^{-3}$, and hold the parameters in the title constant, while changing the parameter in the legend box. E.g. in the left panel, we show radio light curves for varying n_0, at fixed M_{ej} and E_{51}. The red data points are SNRs taken from Case & Bhattacharya (1998), denoted as CB98.

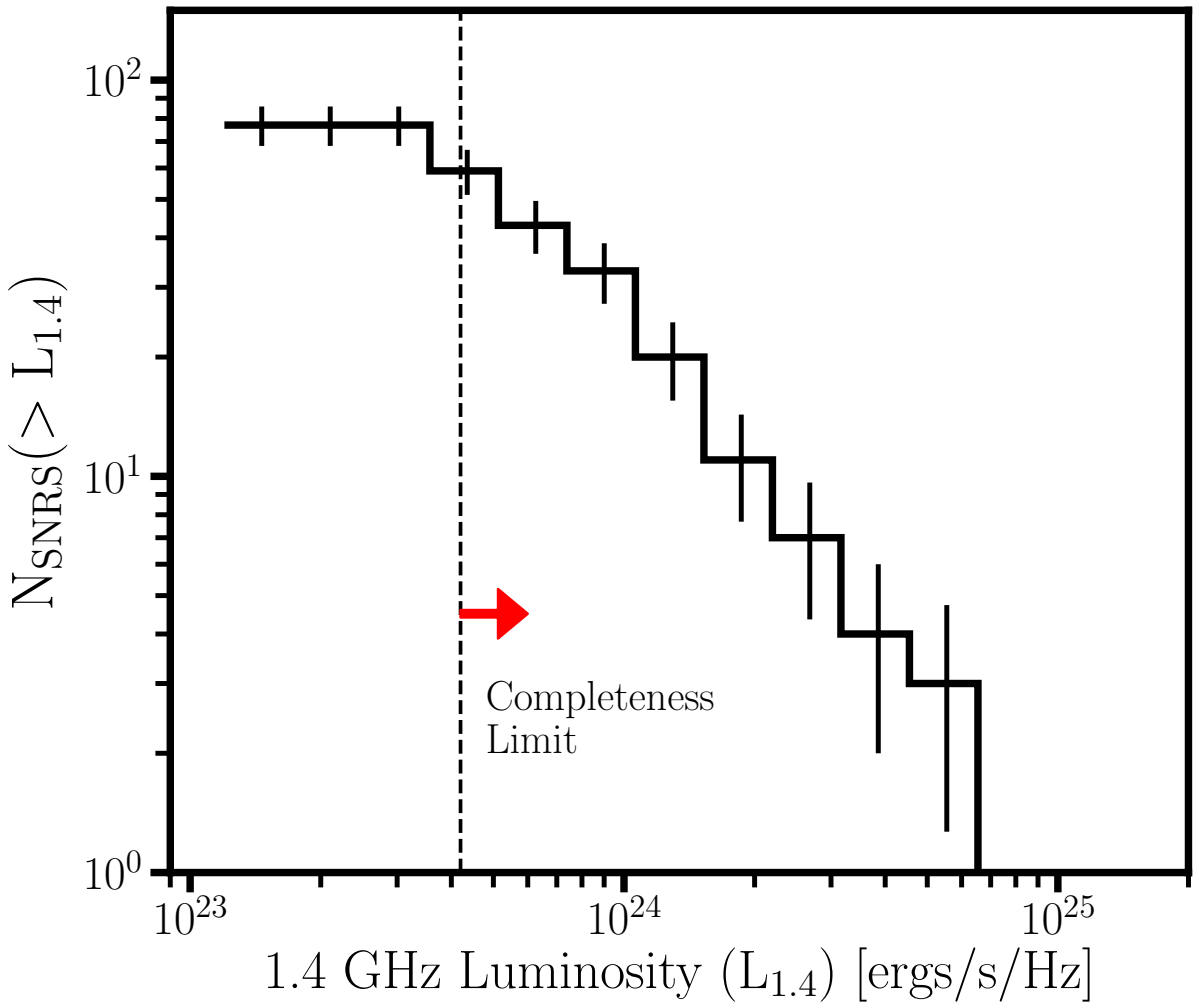

Figure 5: The cumulative LF of 77 SNRs in M33 (Chomiuk & Wilcots, 2009), with Poissonian error bars, used for constraining the model parameters, R, z_0 and ϵ_e. The completeness limit is indicated by the dashed vertical line at 4.2×10^{23} ergs/s/Hz, and 59 SNRs that have luminosities greater than this limit are considered part of the 'complete' SNR survey.

LFs of SNRs can be adequately described as a power-law, and defined the completeness limit of an SNR sample as the flux where the LF 'turns over'. We set the completeness limit of M33 SNRs at 4.2×10^{23} ergs/s/Hz, and 59 of the 77 SNRs have luminosities above this limit.

We assumed flat priors for our model parameters, R, z_0 and ϵ_e. The star-formation rate of M33 is about a factor of 10 lower than that of the Milky Way (Chomiuk & Povich, 2011), so we assumed the M33 SN rate is similarly lower than that of a Milky Way-like spiral (Li, 2011) and set the prior for R within $(1 - 7) \times 10^{-3}$ per year. We set z_0 within 0 - 500 pc, which is the net extent of the neutral phase seen in most SN-driven ISM simulations (Hill et al., 2012; Gent et al., 2013; Walch et al., 2015; Kim & Ostriker, 2015). The electron acceleration efficiency is assigned a wide prior in logarithmic space, $10^{-1} - 10^{-5}$. The upper and lower limits for the prior on ϵ_e are roughly consistent with values derived for radio SNe and young SNRs respectively (see Section II.F.1). The statistical comparison of the model and observed radio LFs is done with a maximum likelihood method described in Appendix section A.5.

C. SNR MODEL PARAMETER SPACE

The model parameter space constrained by the M33 SNR catalog is shown in Figure 6. Darker areas represent parameter values for which our model and observations agree, while the contrary is true for lighter areas. Visual comparisons between the predicted and observed LFs are shown in Figure 7 for parameter values taken from different regions in Figure 6. Values of R, z_0 and ϵ_e taken from the darkest regions predict LFs that agree with the observed LF above the completeness limit, whereas the ones from lighter regions do not. The discrepancy with observations below the completeness limit for the green histogram implies that faint SNRs may be missing from the catalog, and this issue is discussed further in Section II.F.2. The small discrepancy at the bright end ($L_{1.4} > 3 \times 10^{24}$ ergs/s/Hz) is because the statistical comparison between the model and observed LFs is dominated by SNRs near the completeness limit, which are larger in number. Nonetheless, the green LF agrees within the Poisson errors of the bright end of the observed LF.

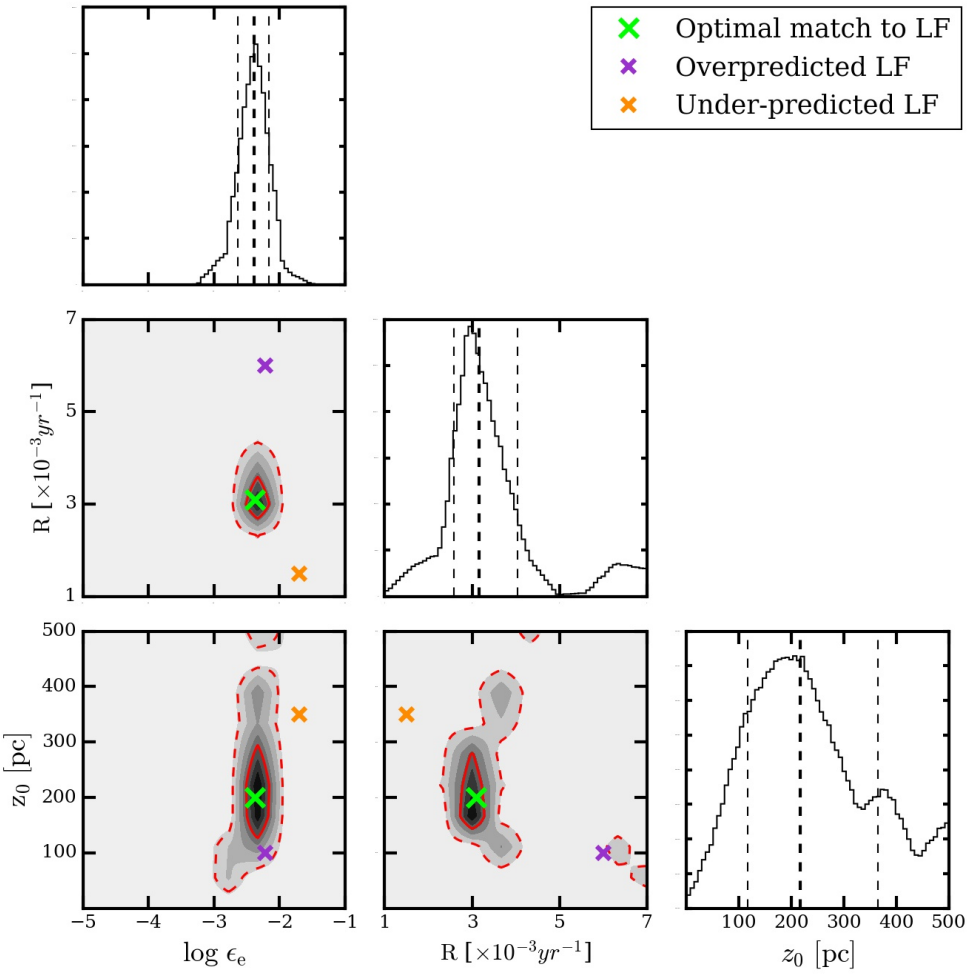

Figure 6: The parameter space of our model constrained by the observed SNR LF in M33 in Figure 5. The dark contours represent favorable regions of parameter space where the model reproduces the observed SNR LF, with solid and dashed red lines showing the 1σ and 2σ contours respectively. The histograms are the marginal probability densities of each parameter, with bold dashed line being the median, and the normal dashed lines showing the 16th and 84th percentiles. As a consistency check, we pick values of R, z_0 and ϵ_e from different areas of parameter space (shown by colored crosses) and compare the predicted LFs in Figure 7.

Figures 6 and 7 highlight the crucial role of SNR catalogs in our model. We can use them to constrain the unknown parameters in our model, and then use their observationally-constrained values to predict accurate radio visibility times (Section II.D). The radio LF of SNRs rules out significant areas of parameter space for parameters of physical interest, such as R and $\epsilon_{\rm e}$. For M33, we measure a median value of $R \sim 3.1 \times 10^{-3}$ SN per year and $\log\ \epsilon_{\rm e} \approx -2.38$, or $\epsilon_{\rm e} \approx 4.2 \times 10^{-3}$. Since the radio LFs are particularly sensitive to $\epsilon_{\rm e}$ ($L_{1.4} \propto \epsilon_{\rm e}$), we obtain tighter constraints on $\epsilon_{\rm e}$ than the other parameters. For higher values of $\epsilon_{\rm e}$, SNRs are more luminous and this shifts the bright end of the cumulative LF right, towards higher luminosities. While R does not affect the radio luminosities of individual SNRs, it directly controls the number of SNRs per luminosity bin. Therefore, increasing R shifts the LF up (towards higher $\rm N_{SNR}$), with all other parameters fixed. The HI scale height z_0 is the least sensitive of the three parameters and has the poorest constraints. This is because we choose the vertical heights of SNRs in the ISM (z) from the stellar distribution (Eq. II.2), which produces SNRs in a wide range of z ($z_* = 90$ pc for CC SNRs and 320 pc for Type Ia SNRs). Thus, changes in the value of z_0 within this range do not affect the radio LFs of the model SNRs as much as R or $\epsilon_{\rm e}$. However, the constrained values of z_0 still fall intermediate to the assumed scale heights for the young and old stellar populations. Although these measurements are based on the partial 40 sq. arc-minute coverage of the M33 disk in Figure 2, they can be scaled to the entire galaxy with a SNR survey that covers the entire disk. We only show the median values of our measurements in Figure 6 because of the asymmetric nature of the probability histograms (particularly z_0), and discuss the effects of changes in the parameter space in Section II.F.3.

The predicted and observed size distribution of SNRs in M33 are also consistent as shown in Figure 8, even though we did not attempt to fit the SNR sizes. However, the model does not reproduce the largest SNRs in M33 (> 80 pc), which we discuss later in Section II.F.2. A conspicuous feature is the correlation between the luminosities and diameters of SNRs over several decades, which is not apparent in the observed SNRs. This is because large SNRs are usually expanding into low ambient densities, and thus experience weaker electron acceleration and field amplification, yielding smaller radio luminosities. For a given size, the scatter in radio luminosities comes from the range of kinetic energies and ambient densities

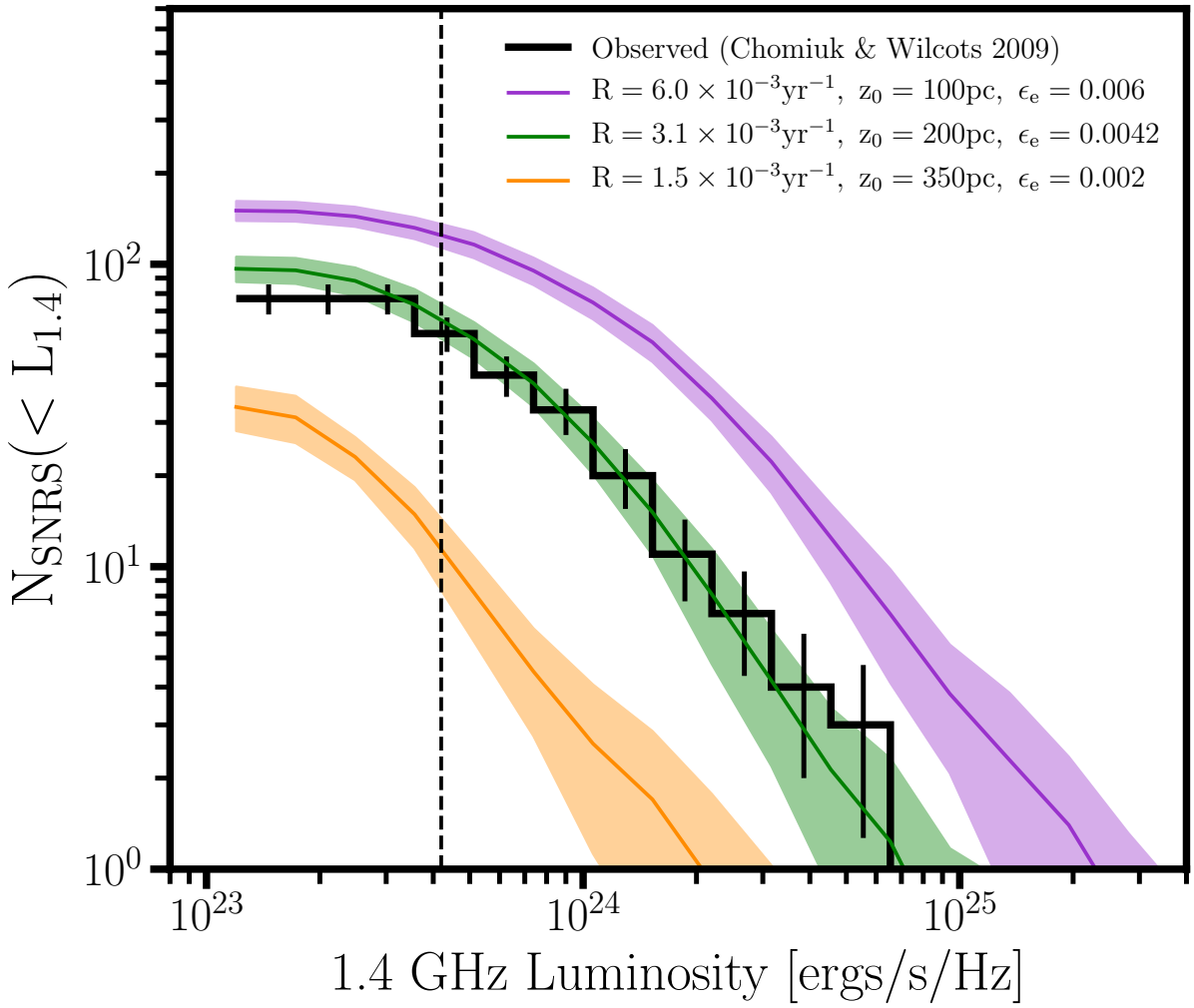

Figure 7: Comparison of the observed M33 SNR LF (black) with different LFs (colored) predicted by the model. Green LF corresponds to the best fits values of R, z_0 and ϵ_e (green crosses in Figure 6) that reproduce the observed LF, while the purple and orange LFs (purple and orange crosses in Figure 6) are inconsistent with observations. The colored solid lines and shaded region represent the median and $\pm 1\sigma$ uncertainties of the LFs respectively. The vertical dashed line is the completeness limit $= 4.2 \times 10^{23}$ ergs/s/Hz.

of SNRs. Type Ia's show a smaller scatter than CC's in the model because Type Ia's are drawn from a narrower range of kinetic energies. We note that SNRs exploding in densities $< 10^{-3}$ cm^{-3} do not appear in our model since these are densities more characteristic of the warm ionized phase of the ISM (Draine, 2011).

Our model also predicts that radio surveys will be dominated by CC SNRs above the 3σ detection limit, with characteristically higher luminosities and smaller diameters than Type Ia, since CC SNe preferentially evolve in higher ambient densities than Type Ia. For the best fit parameters, the fraction of Ia/CC SNRs produced above the 3σ detection limit of the Gordon et al. (1999) survey is 0.1-0.25, less than our input fraction of Type Ia/CC SNe of 1/3. Because of the characteristically different light curves of Type Ia and CC SNRs, the ratio of Ia/CC SNe cannot be estimated from SNR surveys that do not account for completeness limits.

D. SNR VISIBILITY TIME

Deriving the visibility times of SNRs is more challenging than for SNe. Firstly, the ages of SNRs are difficult to estimate. Only SNRs with historical records or light echoes have reliably determined ages, and most of these are young SNRs. Secondly, we do not have observations of SNR light curves on their characteristic timescales ($\sim 10^4$ years). Thirdly, reliable classification of SNRs as Type Ia or CC in origin is not possible except for young SNRs using e.g. X-ray spectra (Badenes, 2010; Yamaguchi et al., 2014), light echoes (Rest et al., 2005) or association with neutron star or pulsars. Older SNRs are much harder to classify as their spectra is dominated by the swept-up ISM, although their origins may be indirectly guessed from morphology (Lopez et al., 2009, 2011; Peters et al., 2013) or association with stellar populations (Badenes et al., 2009; Lee & Lee, 2014; Lee & Lee, 2014; Maggi et al., 2016). Most of these techniques become increasingly difficult for distances beyond the Magellanic Clouds.

As an alternative, Badenes et al. (2010) estimated the visibility time of SNRs in a given subregion of the Magellanic Clouds from the *in-situ* ISM column density. SNRs in regions

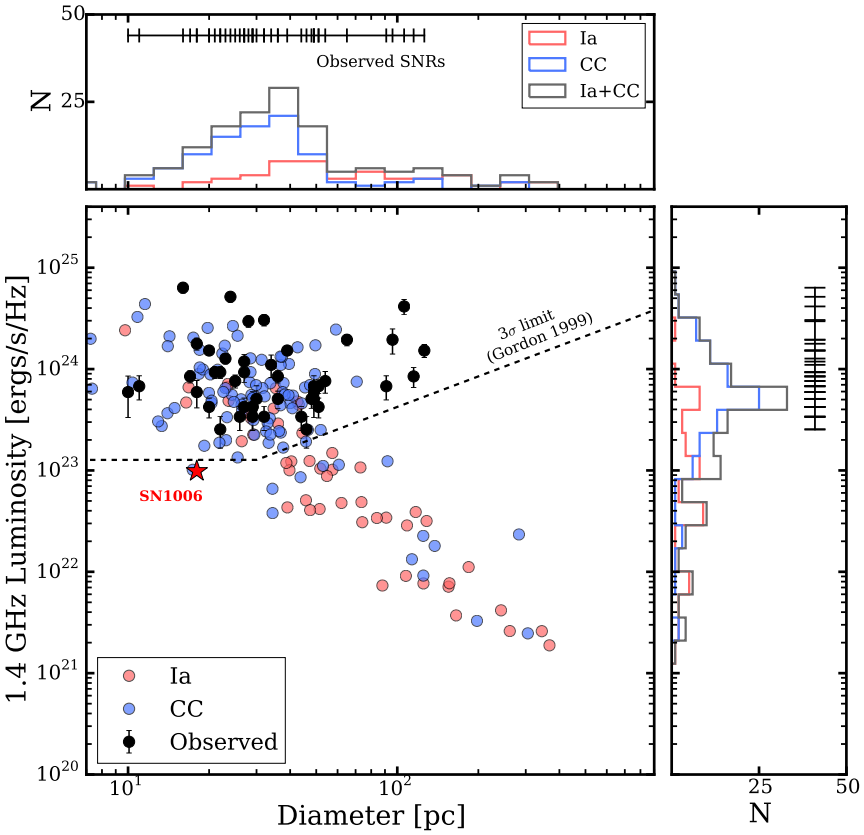

Figure 8: *Central panel* shows a snapshot of a best-fit steady state model population produced for $R = 3.1 \times 10^{-3}$ SN per year, $z_0 = 200$ pc and $\epsilon_e = 4.2 \times 10^{-3}$ in luminosity-diameter space. The red and blue symbols represent model Type Ia and CC SNRs respectively. The solid data points are 44 of the 77 radio-selected SNRs (Chomiuk & Wilcots, 2009) that have diameters available from optical images (Gordon et al., 1998). The 3σ detection limit for the Gordon et al. (1999) survey ($\sigma = 50\mu$Jy/beam with a 7 sq. arc-seconds beam at 840 kpc, the distance to M33) is shown with a dashed black line. *Upper panel* shows the diameter histograms of the model SNRs, compared to the observed 44 SNRs shown with black ticks. *Right panel* shows the same information, but for the 1.4 GHz luminosity.

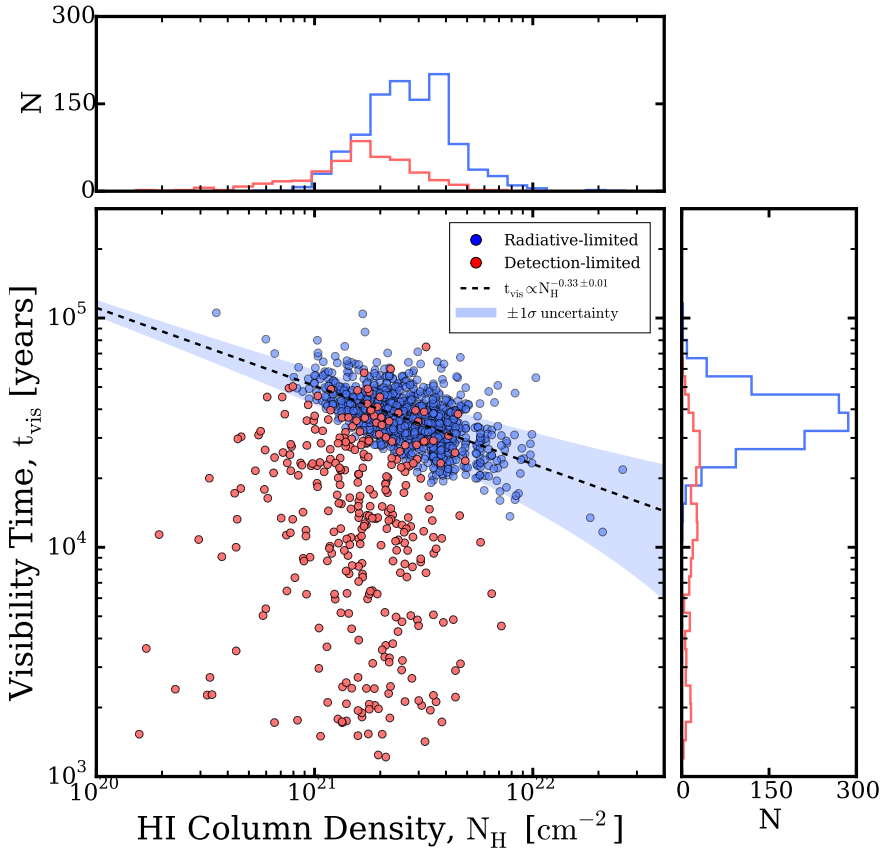

Figure 9: Radio visibility times of SNRs generated for $R = 3.1 \times 10^{-3}$ SN per year, $z_0 = 200$ pc and $\epsilon_e = 4.2 \times 10^{-3}$. Blue circles represent visibility times determined by the transition to the radiative phase, while red points represent visibility times determined by the 3σ detection limit of the Gordon et al. (1999) survey. The same color scheme is followed for the histograms for column density and visibility times in the upper and right panels respectively. The line of regression fit to the radiative-limited population is shown with a dashed line, with the shaded region representing $\pm 1\sigma$ interval

.

of denser ISM will be brighter but remain visible for shorter periods of time than SNRs in tenuous ISM. Assuming all Magellanic SNRs are in their Sedov stages and that the SNR sample was complete, the visibility time was approximated as $t_{\rm vis} \propto N_H^{-1/2}$. This is related to the cooling timescale of a Sedov SNR transitioning to the radiative phase, with a cooling function of the form, $\Lambda(T) \propto T^{\epsilon}$ for 10^6 K shocked gas, with $\epsilon = -1/2$ to -3/2.

In this paper, the visibility time of each SNR can be derived from its radio light curve (Figure 3), which is terminated when either of these two conditions are met: (1) If the SNR falls below the detection limit of the radio survey. For the M33 catalog, the detection limit is 3σ above the root-mean square (RMS) sensitivity of 50μJy per beam for the Gordon et al. (1999) survey. (2) If the SNR shock transitions to the radiative phase (Bandiera & Petruk, 2010). At this point, we assume the synchrotron mechanism becomes inefficient because the magnetic field amplification is too low, and not enough relativistic electrons are produced by the weakened SNR shock (Berezhko & Völk, 2004a; Blasi et al., 2007). To the first order, we assume this radiative transition occurs when $v_s \approx 200$ km/s (Blondin et al., 1998).

Figure 9 shows the relation between the SNR radio visibility times and the ambient HI column density for a population of model SNRs generated using the best-fit parameter values (from Figure 6). Most SNRs have visibility times between 20-80 kyrs, and correlated with the column density as $t_{\rm vis} \propto N_H^{-a}$ with $a = 0.33 \pm 0.01$. SNRs in high column densities evolve in higher ambient densities and so, being brighter, remain above the detection limit. As a result, their radio visibility is decided by their transition to the radiative phase (when $v_s \approx$ 200 km/s). This occurs quicker at higher column densities because of the strong deceleration by the dense ISM. The scatter in the relationship is due to SNR light curves with different ambient densities and kinetic energies. Most CC SNRs will have visibility times decided by the transition to the radiative phase, since they explode in higher densities and have surface brightnesses above the detection limit of the radio survey. About 30% of the SNRs, mostly Type Ia exploding in lower densities, deviate from this relation by exhibiting smaller visibility times. These SNRs have low surface-brightness because of lower ambient densities, causing their light curves to be truncated by the detection limit of the survey. The visibility times predicted by our model are consistent with the ages of SNRs associated with pulsars and magnetars (Martin et al., 2014). These predictions can be further tested by future radio

SNR surveys using images with deeper sensitivity limits (Huizenga et. al, in prep).

We therefore have a unique pathway to calculating the visibility times of an SNR population using a model that is equipped with the physics of SNR evolution and synchrotron emission, and observationally constrained by multi-wavelength surveys of the host galaxy. While our results nicely confirm the conjecture of Badenes et al. (2010) that the visibility time of SNRs in the Local Group is roughly their Sedov-Taylor lifetimes, our model also has the added advantage of being able to characterize the population of detection-limited SNRs, which is significant at distances farther than the Magellanic Clouds. In addition, the model also helps us understand the scatter in visibility times arising from the diversity of ambient densities and kinetic energies of SNRs. Understanding these subtleties is crucial because the model-based visibility times will be the main source of systematic uncertainties in the derivation of a SN DTD in the Local Group.

E. CORRELATION BETWEEN THE BRIGHTEST SNR AND THE SN RATE

We examine the correlation between the brightest model SNR and the SN rate in M33 as a consistency check for our model. Chomiuk & Wilcots (2009) showed that host galaxies with the highest star formation rates (SFRs) produce the brightest SNRs. Such a trend can also be expected with SN rate, since it is proportional to the SFR. Figure 10 shows such a correlation exists for over two decades in radio luminosity, and 3 decades in SN rates in our model, assuming $z_0 = 200$ pc and $\epsilon_e = 4.2 \times 10^{-3}$ as determined in Figure 6. The shaded region represents the spread in luminosities for a given SN rate due to different kinetic energies and ambient densities of the SNRs.

There are several possible reasons for this correlation. For higher SN rates, there's a greater chance of a bright SNR exploding with a higher kinetic energy at explosion, making them more radio bright. The higher SN rate also increases the probability of the brightest SNR going off in a denser region of the M33 ISM, or an SNR being detected near maximum radio luminosity. A caveat with this analysis is that our model ISM remains unchanged with

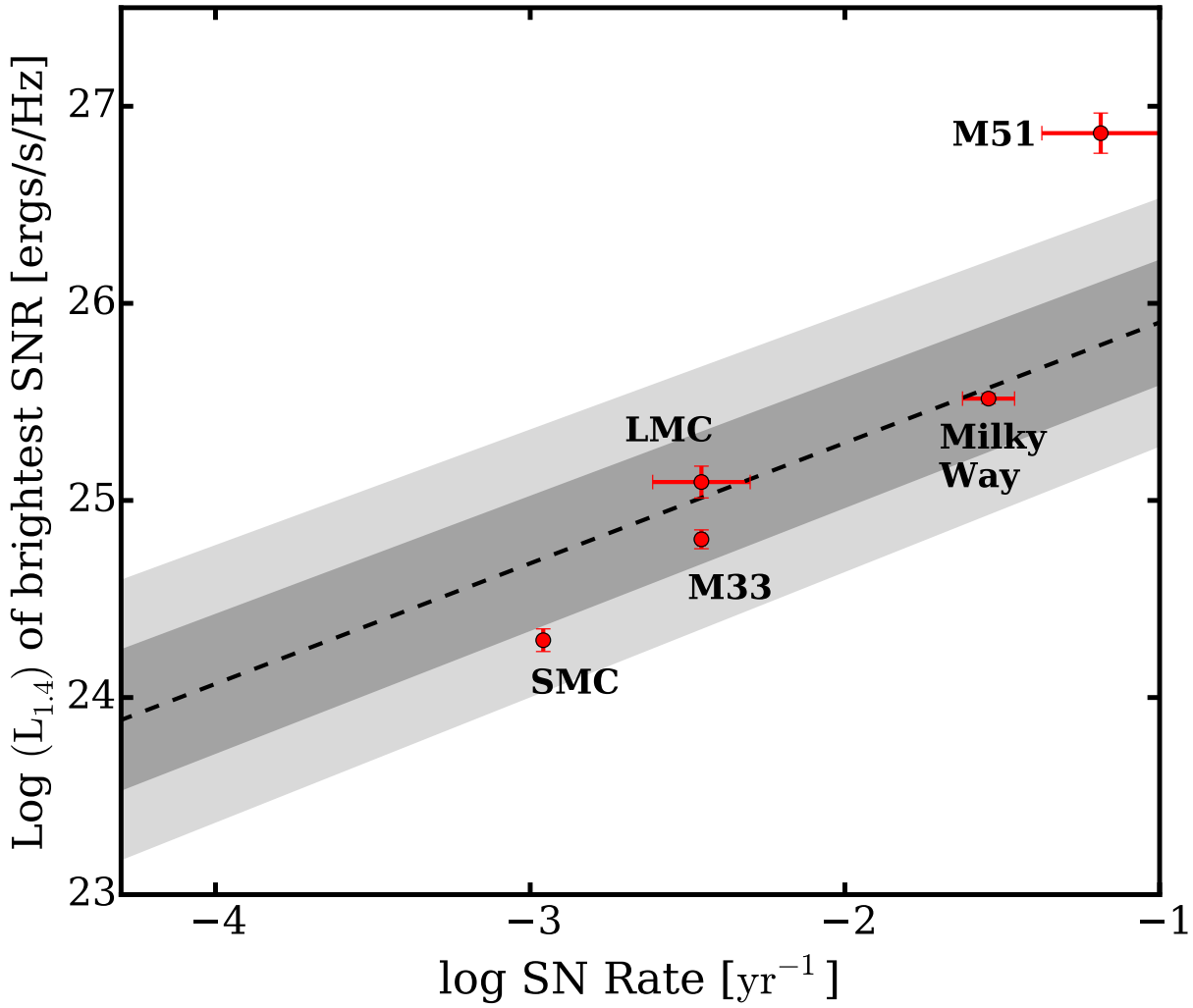

Figure 10: Radio luminosity of the brightest SNR produced by the model as a function of SN rate, assuming $z_0 = 200$ pc and $\epsilon_e = 4.2 \times 10^{-3}$. The two shades of grey represent $\pm 1\sigma$ and $\pm 2\sigma$ regions for our model. The red points represent galaxies with known SN rates (M51: Rampadarath et al. (2015), Milky Way: Li et al. (2011), M33: this work, LMC: Badenes (2010), SMC: Tammann et al. (1994)) and luminosities of the brightest SNRs in these galaxies (Chomiuk & Wilcots, 2009).

SN rate, whereas galaxies with higher SN rates will have a denser ISM (Kennicutt, Jr., 1998) and distinctly different ISM properties due to feedback (Hopkins et al., 2012).

For comparison, we show the SN rates and radio luminosities of the brightest SNRs in nearby galaxies. Galaxies with higher SN rates host brighter SNRs, and with the exception of M51, falls within the 2σ shaded region. The discrepancy could be because the SFR of M51 is nearly twice that of the Milky Way (Chomiuk & Wilcots, 2009) and forms an interacting pair with M51b. Galaxies with such high SFRs or extreme environments may also host objects that mimic spectral signatures of radio SNRs, such as SNe, super-bubbles, remnants of hypernovae or ultra-luminous X-ray sources (ULXs) (Chomiuk & Povich, 2011).

F. DISCUSSION

1. Understanding electron acceleration in interstellar shocks with an SNR catalog

We estimated the electron acceleration efficiency in SNR shocks, $\epsilon_{\rm e}$ from a catalog of SNRs mostly in their Sedov phase. On average, the M33 SNRs have $\epsilon_{\rm e} \sim 4.2 \times 10^{-3}$, which falls in between conventional estimates for radio SNe and young SNRs. Type Ib/c SNe with relativistic shocks commonly require $\epsilon_{\rm e} \sim 0.1$ to explain their radio light curves assuming equipartition between magnetic field and electron energy densities, or $\epsilon_{\rm e}/\epsilon_{\rm b}^{\rm u} = \alpha$ where α is a constant. (e.g. Chevalier, 1998; Li & Chevalier, 1999; Berger et al., 2002; Soderberg et al., 2005; Chevalier & Fransson, 2006). For non-relativistic SNR shocks, $\epsilon_{\rm e} \approx K_{\rm ep}\xi_{\rm cr}$, where $K_{\rm ep}$ is the electron-to-proton ratio and $\xi_{\rm cr}$ is the acceleration efficiency of cosmic rays. Based on multi-wavelength spectra of Tycho, Morlino & Caprioli (2012) deduced $K_{\rm ep} = 1.6 \times 10^{-3}$ and $\xi_{\rm cr} \sim 0.06$, which implies $\epsilon_{\rm e} < 10^{-4}$. Similarly low values of $K_{\rm ep} \sim 10^{-3} - 10^{-4}$ have been deduced for young SNRs (Berezhko & Völk, 2006; Berezhko et al., 2009a,b), while $\xi_{\rm cr} \lesssim 0.2$ for strong shocks characteristic of young SNRs (Caprioli & Spitkovsky, 2014a). Furthermore, particle-in-cell (PIC) simulations of electrons and ions in non-relativistic shocks recover $K_{\rm ep} \approx 10^{-3} - 10^{-2}$ for shock velocities $v_s/c \sim 0.01 - 0.1$ as seen in young SNRs (Park

et al., 2015). Recently, Barniol Duran et al. (2016) deduced that for the Badenes et al. (2010) LMC SNR sample, $\epsilon_e\epsilon_b \sim 10^{-3}$ (the product was calculated because of the degeneracy between these parameters in their model). This is higher than the values we obtain for the M33 sample, $\epsilon_e\epsilon_b \sim 10^{-3} - 10^{-5}$ (based on Figures 6 and 44). This discrepancy could be a result of differences in model assumptions and completeness limits, and will be further explored in a future paper where we apply our model to the LMC SNRs recovered from deeper radio surveys (Huizenga et. al, in prep).

Our result suggests that older SNRs are more efficient at accelerating electrons than younger ones. In fact, our estimate of ϵ_e gives $K_{ep} \sim \epsilon_e/\xi_{cr} \sim 0.04$, which is consistent with the value of $K_{ep} \sim 0.01$ measured in the cosmic rays detected on Earth, which are thought to originate from SNRs with a wide variety of ages (Beringer et al., 2012; Morlino & Caprioli, 2012). In addition, equipartition between electrons and magnetic field energies is neither assumed in our analysis, nor retrieved from it. A caveat in our measurement is that we do not consider the effect of orientation of the ambient magnetic field near the shock vicinity on the electron/proton acceleration (Reynoso et al., 2013; Caprioli & Spitkovsky, 2014a; Caprioli, 2015). The electron spectral index, p can also shift the value of ϵ_e, but as discussed in Section II.F.3, $\epsilon_e \gtrsim 10^{-3}$ for reasonable variations in p, which implies a $K_{ep}(\gtrsim 0.01)$ that is still comparable to cosmic-rays.

2. Missing SNRs and Superbubbles

Our work implies that archival radio surveys of Local Group galaxies have missed a significant fraction of SNRs as shown in Figure 8. For the best-fit parameters and our simple ISM model, nearly $30-40\%$ of the simulated population of SNRs in M33 falls below the 3σ detection limit of Gordon et al. (1999) survey. Most of these SNRs are Type Ia, which explode farther from the mid-plane than CC SNRs and encounter lower densities on average. In fact SN1006, a well-known, young, low surface brightness Galactic Type Ia SNR that evolved in a low ISM density 550 pc from the Galactic mid-plane (Winkler et al., 2003; Berezhko et al., 2012) would have been missed by the survey at M33. Future radio surveys with deeper sensitivity limits will be able to increase the SNR inventory in the Local Group and provide us with a

larger sample of objects for calculating the Local Group DTD.

We suspect that the largest radio-selected SNRs in M33 (ones with diameters > 80 pc in Figure 8) may be superbubbles (Mac Low & McCray, 1988) due to their unusually large luminosities and diameters. Even with the best-fit parameter values and observationally constrained distribution of SNR kinetic energies and ambient densities, SNRs rarely occur in this region of luminosity-diameter space. Long et al. (2010) echoed the same concern that several SNRs in their X-ray catalogs may be superbubbles, as even our Galaxy, there are no known SNRs larger than 90 pc. It is beyond the scope of our current study to prove that the largest SNRs in Figure 8 are indeed, super-bubbles. Gordon et al. (1999) warned that some of the largest SNRs in the catalog may be associated with or embedded in HII regions, causing over-estimated optical diameters. Long et al. (2010) also concede that super-bubbles are mainly powered by ionizing radiation of OB stars, and therefore unlikely to create high [SII/Hα] ratios that would be indicative of shocked gas, as seen in SNRs. For this work, we do not expect superbubbles to affect the statistical results since there are so few of them compared to the total SNR sample of M33. In a future version of our model, we will include a simple treatment of super-bubbles and reinvestigate the observed SNR distribution.

3. Effects of changing key assumptions

Our parameter constraints depend on certain assumptions made in our model. The electron spectral index, p can vary between 2.2 and 2.4 (Caprioli, 2012) with steeper electron spectra yielding lower radio luminosities because fewer GeV electrons contribute to the synchrotron emission. In general, for diffusive shock acceleration (DSA), the electron spectra is expected to steepen with weakening shocks. We found a $\sim 25\%$ increase in $\log \epsilon_{\rm e}$ when varying p from 2.1 to 2.5, but without any significant change in the SN rate. The distribution of kinetic energies, which is uncertain for SNe, also affects the radio LFs. While Type Ia and CC both deposit a similar amount of energy ($\sim 10^{51}$ ergs) in our model, CC SNe are known to be intrinsically fainter than Type Ia in SN surveys (Li et al., 2011). Based on this, if we instead assume CC SNe deposit a mean energy of $10^{50.5}$ ergs, $\log \epsilon_{\rm e}$ increases by 25% since the model tries to compensate for production of fainter SNRs. Increasing $\sigma_{\rm logE}$ for CC SNe from 0.1 to

0.4 causes the radio LFs to be brighter by $\sim 3\sigma$, where σ is the shaded uncertainty regions of the LFs in Figure 7. Despite these variations, the value of $\epsilon_{\rm e}$ remains above 10^{-3}, which is still 10 times higher than conventional estimates for young SNRs.

Our assumption of z_* for Type Ia and CC SNe are based on observations in the Milky Way, but they may be different for M33. For the best fit values of R, z_0 and $\epsilon_{\rm e}$, we found that changing the scale height of Type Ia has little effect on our parameters since only 25% of the SNe produced in our model are Type Ia. But changing the CC scale height, e.g. from 90 to 200 pc, increases the SN rate by $\sim 30\%$, with a negligible increase in $\epsilon_{\rm e}$.

We therefore checked the effects of changing R, z_0 and $\epsilon_{\rm e}$ on the visibility time. Out of the three parameters, z_0 has the strongest effect on the visibility time since it controls the volume densities where SNRs explode for a given value of N_H. For example, changing z_0 from 200 to 400 pc changes the correlation, $t_{\rm vis} \propto N_H^{-a}$ in Figure. 9 from $a = 0.33$ to $a = 0.44$, and the fraction of detection-limited SNRs from 30% to $\approx 42\%$. In comparison, increasing R by a factor of 6 had a negligible effect on a or the fraction of detection-limited visibility times, but increasing $\epsilon_{\rm e}$ by a factor of 2 increased the luminosities of SNRs by a factor of 2, and reduced the fraction of detection-limited visibility times rom 30% to 18%. In subsequent papers, we will explore ways to reduce the errors, both statistical and systematic, in our parameter constraints and incorporate them into our calculation of the Local Group DTD.

G. CONCLUSIONS

We introduced a semi-analytical model capable of reproducing the radio luminosity function of SNRs in Local Group galaxies, taking into account the measured ISM distribution of the galaxy, the physics of SNR evolution and synchrotron emission, the diversity of SN explosions and the detection limits of a radio survey. We also introduced a scaling relation for ϵ_b - the fraction of shock energy shared by the amplified magnetic field - based on the most current first-principle kinetic simulations of non-relativistic shocks. This is an important contrast with previous analytical radio light curve models of SNe that leave ϵ_b as a free parameter.

Using this model, we can obtain observationally constrained estimates of radio visibility times of an SNR catalog in a galaxy - a critical ingredient in calculating SN rates and DTDs using SNRs. We applied our model to the M33 radio SNR catalog of Gordon et al. (1999) and Chomiuk & Wilcots (2009), and derived the following essential results,

I. M33 has an estimated SN rate $\sim 3.1 \times 10^{-3}$ SN per year, or roughly 1 SN every 320 years. The measurement is unique since it combines physical modelling of SNR shocks and constraints from an SNR catalog with a well-defined completeness limit (Chomiuk & Wilcots, 2009), and is therefore relatively robust to observational limitations.

II. We measured the electron acceleration efficiency by SNR shocks, $\epsilon_e \sim 4.2 \times 10^{-3}$ in an SNR sample dominated by SNRs in the Sedov stage, using the current models of field amplification in SNR shocks and taking into account the possibility of missing faint SNRs in the sample. Our estimate of the electron-to-proton ratio, $K_{ep} \sim 0.04$ is consistent with measurements in cosmic rays detected on earth, and much higher than in young, ejecta-dominated SNRs.

III. The model predicts a correlation between the radio luminosity of the brightest SNR and the SN rate, similar to the prediction by Chomiuk & Wilcots (2009) and Chomiuk & Povich (2011) on the correlation between the brightest SNR and the star-formation rate. The correlation roughly agrees with measurements of the brightest SNR and SN rates in nearby galaxies, and therefore serves as a consistency check for our model.

IV. On average, about $30-40\%$ of our simulated SNRs in M33 fall below the detection limit of Gordon et al. (1999), given the assumptions in our model and our best-fit parameters. Most of the SNRs above the detection limit consists of core-collapse SNRs, whereas the missing SNRs are mostly Type Ia, which evolve in lower ambient densities and have lower surface-brightnesses.

V. The radio visibility times (t_{vis}) of $\sim 70\%$ SNRs in M33 are determined by their transition to the radiative phase, with characteristic timescales of 20-80 kyrs and a correlation with the ISM column density (N_H) in which they explode, i.e., $t_{vis} \propto N_H^{-a}$, with $a \sim 0.33$. About 30% of the SNRs will have shorter visibility times, determined by the detection limit of the radio survey.

H. ACKNOWLEDGEMENTS

We are grateful to Anatoly Spitkovsky for his suggestions on the treatment of magnetic field amplification, Jeffrey Newman for his suggestions on the statistical methods, and Robert Braun for sharing the HI data in the Local Group. We also thank Dan Maoz for his comments on the SNR visibility times and acknowledge helpful discussions with Christopher Kochanek and Rodolfo Barniol Duran. Lastly, we thank the anonymous referee for the constructive comments on our manuscript. SKS, LC, and CB acknowledge NSF/AST-1412980 for support of this work. This research has made use of NASA's Astrophysics Data System (ADS) Bibliographic Services, as well as the NASA/IPAC Extragalactic Data base (NED). The National Radio Astronomy Observatory is a facility of the National Science Foundation operated under cooperative agreement by Associated Universities, Inc., and the Westerbork Synthesis Radio Telescope is operated by the ASTRON (Netherlands Institute for Radio Astronomy) with support from the Netherlands Foundation for Scientific Research (NWO)

I. AN OPTIMAL SNR SURVEY WITH RADIO INTERFEROMETRY

A crucial part of the Local Group DTD calculation is the SNR survey with uniform selection criteria and well-understood completeness. This is currently being carried out by our collaborator, Laura Chomiuk at Michigan State University, and will become the thesis of her student, Jessica Maldonado. The SNR survey is being carried out with VLA for the M31 disk covered by the PHAT area (see Figure 11), and with the Australia Compact Telescope Array (ATCA) for the Magellanic Clouds (Chomiuk et al, in prep). As mentioned earlier, we focus our selection efforts in the radio because SNRs are easier characterized and well distinguishable in the radio compared to optical or X-ray, with sensitivity being the main limitation in historical radio surveys. Current radio interferometers like the VLA allows us to reach unprecedented μJy sensitivities and arcsecond resolution, which is excellent for picking up faint and small remnants. The selection of SNRs will be carried out using the same selection criteria defined in Chomiuk & Wilcots (2009) for all galaxies. Resolved ob-

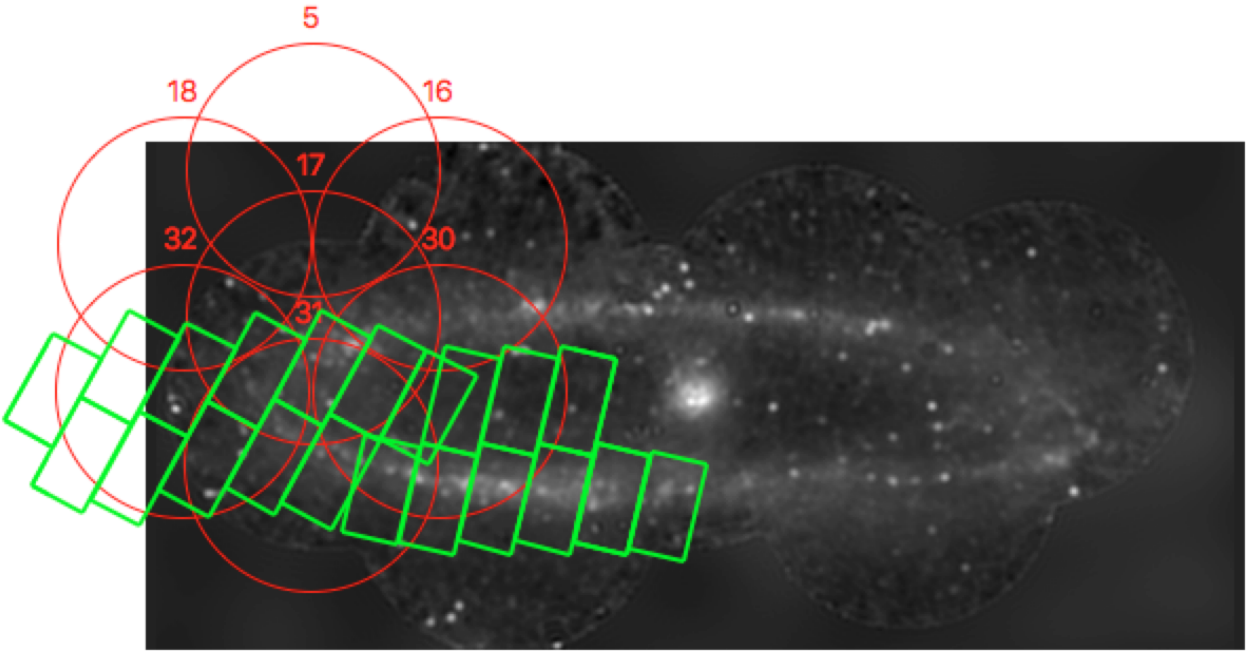

Figure 11: The PHAT survey footprint (green) and B/C configuration pointings of the VLA (red) overlaid on an image of M31. We will request additional pointings to cover the PHAT footprint for our SNR survey. *Figure courtesy: Jessica Maldonado (MSU)*

jects will be identified using image-recognition algorithms, and the possibility of the SNR being confused for an HII region will be statistically factored in. These steps will provide a quantitative understanding of the completeness limit of the survey in different regions of the galaxy, and help accurately calculate our DTD. For M31, we are already working with B & C configuration data under project VLA/15A-175 in the VLA archive. We will be applying for A configuration data (the highest resolution configuration of the VLA) for the current VLA cycle (PI: J. Maldonado). The combination of A, B and C configurations will provide sensitivity on scales of 1-14″, which is needed for identifying SNRs that generally span sizes in the range of 3-100 pc (or $\sim 1 - 26''$ at the distance of M31 Case & Bhattacharya, 1998). The A-configuration data can be potentially useful for identifying small SNRs, or SNRs embedded in vigorous star-forming regions and HII regions, and these SNRs may be crucial for accurately measuring core-collapse signal of our DTD. We are currently testing this idea with recently-awarded 9 hours of exploratory time (PI: Maldonado) with the VLA A-configuration.

III. TESTING THE DELAY-TIME DISTRIBUTION METHOD WITH VARIABLE STARS SURVEYS

This chapter will split into two publications that will be submitted to The Astrophysical Journal: Sarbadhicary et al (2018a) titled *"The Delay-Time Distribution of RR Lyrae: Rates, Progenitors and Lifetimes"*, and Sarbadhicary et al (2018b) titled *"The Delay-Time Distribution of Classical Cepheids: Rates, Progenitors, and Period-Age Relation"*. Collaborators: Carles Badenes (University of Pittsburgh) , Mairead Heger (University of Pittsburgh), Cecilia Mateu (Centro de Investigaciones de Astronomia), Jeffrey Newman (University of Pittsburgh), Robin Ciardullo (Pennsylvania State University), Dan Maoz (Tel-Aviv University) & Laura Chomiuk (Michigan State University).

A. INTRODUCTION

1. Revisiting Stellar Evolution Models with DTDs

Understanding the full diversity of stellar evolution remains one of the ultimate goals in astrophysics. Although the theory of stellar evolution has greatly benefited from advances in computational methods and observations, widely used stellar evolution codes (e.g. MESA, Paxton et al., 2011), are still one-dimensional, and must make approximations to treat processes like convection, mixing, rotation, mass-loss and mass-transfer in close binaries. This contributes to uncertainties in our progenitor models for the products of stellar evolution such as SNe, pulsating variables, and interacting binaries (Gallart et al., 2005; Conroy, 2013). A critical reappraisal of stellar evolution theories is in order, especially if we want to correctly

interpret the vast amounts of photometric and spectroscopic data on stellar populations coming from current and future surveys (e.g. APOGEE, LSST, *Gaia*, TESS etc.).

The DTD method described in this thesis can also be applied to stellar objects other than SNe, and SNRs, giving the opportunity to revisit and test stellar evolution models in the context of big-data surveys. The DTD is a statistical characterization of the relationship between a class of objects and their stellar progenitors, and it is the only such characterization that takes into account all the available information. The SADs of the parts of the galaxy that contain no objects, for example, also contribute to the DTD, which makes the DTD superior to studies that only consider the stellar populations around a limited number of objects (Badenes et al., 2009; Jennings et al., 2014). Its main limitations are in the quality of the object catalog (e.g. completeness and statistical sample size) and the SAD maps (e.g. systematics, extinction and other such uncertainties). Yet the flexibility of the DTD has been shown by studies applied to SNRs (Badenes et al., 2010; Maoz & Badenes, 2010), and planetary nebulae (Badenes et al., 2015). The DTDs for these objects uncovered key features of their progenitors, such as the presence of a 'prompt' SN Ia population in the Magellanic Clouds, and a young (30 - 800 Myr) progenitor channel for the formation of planetary nebulae.

In this chapter, we will calculate DTDs for an important class of well-studied and abundant astrophysical objects: pulsating variables, specifically RR Lyrae and Cepheids. These objects play a crucial role in determining distances in the Local Group, and tracing stellar populations of various ages, which has led to many important results in studies of galaxy formation and cosmology. To calculate the DTD, we will make use of the large catalog of RR Lyrae and Cepheids from the Optical Gravitational Lensing Experiment (OGLE-IV) survey, and the resolved SAD maps of LMC. In the next few sections, I will further describe the properties of these variable stars, and the SAD maps.

2. RR Lyrae

a. Basic Properties RR Lyrae are low-mass stars (< 1 $M_\odot$) that are undergoing pulsations with periods between 0.3-1 day (Preston, 1964; Smith, 2004). They occupy a thin

region in a color-magnitude diagram, called the instability strip, where the stellar envelopes are generally unstable to pulsations. The pulsations are driven by the κ-mechanism, where the opacity (κ) of the second ionization state of He in the envelope plays a central role (Eddington, 1926; Cox, 1963; Marconi, 2009). Basically, a compression of a gas shell in the envelope causes an increase in opacity and trapping of heat. The increase in temperature and density of the shell makes it expand, which allows the excess heat to escape and causes the star to brighten. Once the density and temperature equilibrates, the gas shell sinks, gets recompressed and expands again, setting up a cycle of pulsations.

RR Lyrae are further classified based on their pulsation modes, similar to the vibrational modes on a string (Bono et al., 2016). Fundamental pulsators (also called radial pulsators, or 'RRab') are the most abundant type of RR Lyrae, and are easily identified by the saw-tooth shape of their light curves. First overtone pulsators ('RRc') are the next abundant type, characterized by shorter periods and more sinusoidal light curves. Rarer types of RR Lyrae are characterized by pulsations in both fundamental and first overtone modes (called 'RRd', or 'mixed-mode' pulsators), and by pulsations in the second overtone ('RRe').

RR Lyrae variables have played an important role in understanding galaxy formation and cosmology. RR Lyrae have popularly served as standardizable candles for measuring distances to the Galactic bulge, halo and the Magellanic Clouds owing to their well-defined metallicity-luminosity relation (see reviews in Cacciari & Clementini, 2003; Sandage & Tammann, 2006; Bono et al., 2011), and period-metallicity-luminosity relation in the near-infrared (Longmore et al., 1986, 1990; Marconi et al., 2015). The low masses of RR Lyrae also make them excellent tracers of older stellar populations that are characteristic of the central regions, halos and globular clusters of Local Group galaxies (e.g. Vandenberg et al., 1996; Clementini, 2010; Minniti et al., 2016). They are particularly effective for studying crowded stellar fields (e.g. globular clusters), and characterizing low surface brightness dwarf galaxies (Baker & Willman, 2015, and references therein) because of their variability and brightness ($\sim$ 3-3.5 mag above the main-sequence turnoff, Piersimoni et al., 2002; Ripepi et al., 2007). Additionally, their light curves provide independent constraints on the metallicity distribution (Jurcsik & Kovacs, 1996; Sandage, 2004; Nemec et al., 2013), and extinction/reddening of different stellar fields (Sturch, 1966; Blanco, 1992; Kunder et al., 2010).

b. Evolutionary Scenarios RR Lyrae belong to the evolutionary class of *horizontal branch* (HB) stars - low-mass stars that had ignited their He-core under degenerate conditions (called a 'He-flash'), and are powered by a stable He-burning core and a H-burning shell. The name 'horizontal' is due to the roughly constant luminosity of these stars, which is because He-cores ignite at nearly the same core-mass ($\sim$ 0.45 $M_{\odot}$) under degenerate conditions (Kippenhahn & Weigert, 1990; Salaris & Cassisi, 2005). The HB can span a wide range of temperatures (or colors), depending on the distribution of envelope masses of the stars (Salaris & Cassisi, 2005). In reality, the HB is never completely horizontal, and bluer HB stars can be fainter than redder HB stars because of the dependence of the H-shell burning efficiency on the envelope mass.

It is not completely understood what combination of parameters determine properties of the HB. While metallicity is considered the main parameter (metal-rich clusters will tend to have redder HBs), some pairs of clusters with similar metallicities (e.g. M13 and M3, NGC 288 and NGC 362) have shown differences in HB morphologies (Sandage & Wallerstein, 1960; Sandage & Wildey, 1967; van den Bergh, 1967; Catelan & de Freitas Pacheco, 1995; Buonanno et al., 1999; Catelan et al., 2001; Mackey et al., 2006). This implied that a second parameter, or combination of parameters must play an important role in determining the properties of HBs, and this is known as the *second parameter* effect. A number of parameters have been proposed as potential second parameter candidates, such as age, mass-loss on the red giant branch, He-enrichment, core concentration, CNO abundances, stellar rotation, planetary engulfment, but the issue still remains an open problem (see Fusi Pecci & Bellazzini, 1997; Catelan, 2009; Dotter, 2013, for an extensive review of these parameters). The second parameter effect makes it difficult to characterize HB in stellar evolution models, and can potentially affect models and calibrations of RR Lyrae (van den Bergh, 1995; Pritzl et al., 2001).

Additionally, RR Lyrae are assumed to be low-mass stars older than 10 Gyrs, but there is no measurement of the age distribution of the full RR Lyrae population of a galaxy. Existing age measurements of RR Lyrae have mainly come from globular clusters, whose ages can be reliably estimated because the member stars are born at approximately the same age and with the same metallicity. Olszewski et al. (1996) noted that the minimum age of RR Lyrae

being 10 Gyrs was first established based on the observation that NGC 121, a > 10 Gyr cluster in the SMC hosted 4 RR Lyrae, while L1, a younger cluster, had none. Subsequent observations of globular clusters in the Milky Way (Clement et al., 2001; Soszyński et al., 2014a) and LMC (Soszyński et al., 2016a) have shown that significant RR Lyrae populations are found in clusters older than 10 Gyrs (note that cluster age measurements can have systematic errors on the order of 1-2 Gyrs Sarajedini, 2009). However, several authors have shown that this canonical 'ancient' model may not apply to all RR Lyrae. Olszewski et al. (1996) pointed out that although L1 has no RR Lyrae, it is 7 times fainter than NGC 121, and NGC 121 would host only 1 RR Lyrae if scaled to the luminosity of L1, subject to Poisson uncertainties. 'Metal-rich' field populations of RR Lyrae (which would probably have younger progenitors) are present in the solar neighborhood and in the Galactic disk (Preston, 1959; Taam et al., 1976; Kraft, 1977; Clementini et al., 2018). Metal-rich clusters hosting large RR Lyrae populations have also been discovered in our Galaxy (Layden et al., 1999; Pritzl et al., 2001, 2002). Theoretically, such metal-rich (and therefore younger) RR Lyrae can be produced if significant mass-loss on the red-giant branch occurs, forcing the star to cross the instability strip (Bono et al., 1997a,b). Lastly, a great majority of RR Lyrae are part of the general stellar field, i.e. unassociated with clusters, (Soszyński et al., 2014a, 2016a) and it is difficult to uniquely measure their ages (Olszewski et al., 1996; Soderblom, 2010).

3. Cepheids

a. Basic Properties: Cepheid variables are pulsating variables that are distinguished from RR Lyrae by their longer pulsation periods (1-100 days) and brighter magnitudes (spanning I = 13-18 mag in the LMC, compared to RR Lyrae with I = 18-20 mag Soszyński et al., 2015a). The physics governing the pulsations is the same as in RR Lyrae, although the pulsational periods are longer because Cepheids are more massive than RR Lyrae, and the timescales on which hydrodynamical perturbations propagate inside the star is consequently longer. Cepheids are broadly classified into three major categories: *Classical* (metal-rich, population I species), Type II (metal-poor, population II species) and Anomalous Cepheids.

In this paper, we will focus only on the DTD for classical Cepheids, which are the brightest and commonly used category of Cepheids. Similar to RR Lyrae, Classical Cepheids also show different pulsation modes, with fundamental pulsators (FU) being the most common and characterized by highly asymmetric light curves, following by the first (FO), second and mixed overtone pulsators.

Classical Cepheids are one of the most important types of stars in astrophysics owing to their strong correlation between pulsational period and luminosity (Leavitt, 1908; Soszyński et al., 2017a). Milky Way and LMC Cepheids have been used to anchor the Type Ia distance scale, which was critical for measurements related to dark energy (Perlmutter et al., 1999; Riess et al., 1998). Classical Cepheids are also bright enough to be measured in galaxies beyond the Local Group, and this was used to measure the local Hubble constant (H_0) upto 1-2% precision (Freedman & Madore, 2010; Riess et al., 2016, 2018), which can shed more light on the 3σ tension in H_0 measurements between the local and early universe. In addition, the combination of Cepheids being reliable distance indicators and tracers of young stellar populations have been useful to understand the formation history of the bulge and spiral arms in our galaxy (Kraft & Schmidt, 1963; Majaess et al., 2009; Dékány et al., 2015), as well as the 3D structure of the Magellanic system (Soszyński et al., 2015a).

b. Evolutionary Scenarios and Open Issues: Cepheids are powered by a He-burning core and H-burning shell like RR Lyrae, but the main difference is that the He-cores in Cepheids are ignited under stable, *non-degenerate* conditions, i.e. without a He-flash. Cepheids are believed to be crossing the instability strip during the *blue loop* phase of their evolution (Figure 12). While we refer the reader to Kippenhahn & Weigert (1990) and Maeder (2009) for details, the basic mechanism is as follows: after He-core ignition on the red-giant branch, the star contracts and decreases in luminosity in order to maintain thermal equilibrium. Once the star reaches point A, the stellar envelope has transitioned from being mostly convective to mostly radiative. This results in radiative diffusion of photon outwards, which along with the ongoing contraction of the star, causes an increase in temperature and luminosity (leftward motion). This continues until point B when the core abundance of He has dropped to about 30%, resulting in contraction of the core (now mostly containing C ash

from He-burning) and expansion of the envelope, similar to the post main-sequence evolution of stars. The envelope expansion results in cooling, and therefore a rightward evolution upto point C, after which the star proceeds to the asymptotic giant phase. This marks the end of the blue loop.

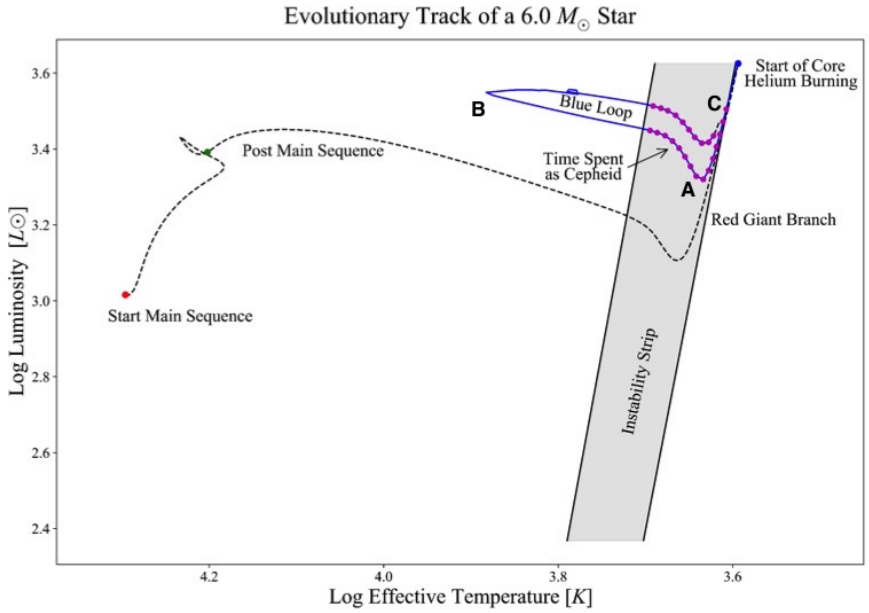

Figure 12: Schematic diagram of the evolution of a 6 $M_\odot$ on a luminosity (log L) - temperature (log T) diagram. The difference stages are labelled, with emphasis on the blue loop phase (colored) that is relevant for Cepheid variables. (*Figure credit*: Mairead Heger)

Uncertainty in Cepheid evolutionary models stems from the sensitivity of the blue loop morphology to model assumptions and input physics. The extent of the loop not only depends on mass and metallicity, but also on the models adopted for core and envelope overshoot (this makes convective zones inside stars larger because the inertia of convective bubbles causes them to overshoot the nominal boundaries of the zones), rotation, and mass-loss (Bertelli et al., 2009; Choi et al., 2016). Because the physics behind these models are not fully established (e.g. we still lack a three-dimensional model of convection), they cannot be implemented self-consistently in state-of-the-art stellar evolution codes, and are instead implemented in parameterized forms that are empirically calibrated from observations (e.g. in MIST, the overshoot parameters are calibrated using the main-sequence turn-off of the

cluster M67, Choi et al., 2016). Different calibrations are adopted by different stellar evolution codes (see e.g. Figure 15 in Choi et al., 2016), leading to model-based uncertainties when interpreting Cepheid data or constructing period-luminosity relations of Cepheids. A well known manifestation of this issue is the Cepheid mass-discrepancy problem – a difference of about 15-20% in Cepheid masses separately derived from evolutionary models and pulsational models (see reviews in Cox, 1980; Bono et al., 2006, 2016). The discrepancy can be removed by adjusting the mass-loss (e.g. Neilson & Lester, 2008, 2009), rotation (Anderson et al., 2017) and overshoot parameters (Keller, 2008; Bertelli et al., 2009), but the question remains whether only one of these parameters, or a specific combination of these parameters need to be adjusted to explain the discrepancy, and whether these calibrations are consistent with other phases of stellar evolution.

The DTD is expected to shed some light on the evolutionary histories of RR Lyrae and Cepheid. The advantage of the DTD method is that it uses full survey of objects, objects that have evolved in a wide variety of environments and star-formation histories, to constrain the stellar evolution scenarios for that class of object. As mentioned before, the two main ingredients in the DTD method is the survey of objects, and a map of the SAD from resolved populations of stars. The latter is described in further details in the next section.

4. Stellar Age Distribution (SAD) Maps in the Local Group

SAD maps are maps of the star formation rate (or stellar mass formed) per age-bin in the surveyed region of the galaxy. Full SAD maps of galaxies were first calculated for the Magellanic Clouds using the Magellanic Cloud Photometric Survey (MCPS) survey (Zaritsky et al., 2004; Harris & Zaritsky, 2004, 2009), and subsequently calculated for M31 by the Panchromatic Hubble Andromeda Treasury team (Dalcanton et al., 2012; Lewis et al., 2015; Williams et al., 2017), and Local Group dwarfs (Weisz et al., 2014). A full SAD map for M33 is currently ongoing, called the M33 Legacy Survey team (PI: J Dalcanton). These maps have provided a high-quality, spatially-resolved perspective on the role of interactions in galaxy evolution (e.g. Besla et al., 2012; Hammer et al., 2018), calibration of star-formation rate indicators (Lewis et al., 2017), connection between molecular cloud and star formation

properties (Reina-Campos & Kruijssen, 2017; Johnson et al., 2017) and evolutionary mechanisms of of supernova remnants (Badenes et al., 2009; Jennings et al., 2014; Auchettl et al., 2018), X-ray binaries (Antoniou & Zezas, 2016; Lazzarini et al., 2018; Garofali et al., 2018) and other stellar objects of interest (e.g. emission-line stars, Prichard et al., 2017).

a. General Properties of the Maps: The SAD maps are constructed by modeling the color-magnitude diagrams (CMDs) of stars from a detailed photometric survey of each region of the galaxy. The map is divided into cells, and the size of each cell is selected large enough so that enough stars are available for precise statistical measurements, but also small enough so that fine spatial variations in stellar properties and extinction values do not get averaged over. The model CMDs are constructed from a linear combination of isochrones (the locus of stars of a single age and metallicity on a CMD) of different ages and metallicities, and the combination that best reproduces the observed CMD gives the SAD of that region of the galaxy. These isochrones are generally pre-constructed and made publicly available using numerical stellar evolution codes (e.g. Padova, MIST).

The two major factors affecting the accuracy of these measurements are extinction and photometric errors. Extinction is the amount of starlight absorbed and scattered by dust along the line of sight. This can shift the position of stars on a CMD, and therefore must be corrected. Modeling extinction is challenging because the dust distribution in the galaxy can be highly non-uniform, and also vary with the age distribution of stars. For the LMC and SMC, Zaritsky (1999) derived extinction maps by modeling the color distribution of stars, while for M31, Dalcanton et al. (2015) derived extinction maps by modeling the near-infrared photometry of red-giant stars. Photometric errors are the uncertainties in the measured brightnesses of the stars. They depend on a number of factors such as atmospheric transmission, seeing conditions, point spread function, but the major factor is stellar crowding, which can particularly affect the detectability of faint stars in dense stellar regions. Photometric errors and the completeness of the survey is estimated with 'artificial star tests, i.e. injecting artificial stars in selected regions of the galaxy, and testing their recovery using the same data-reduction pipeline. This is generally computationally expensive, as stellar crowding varies with position in the galaxy, and many (10^4) stars per region need to be inserted

to accurately and representatively measure the photometric errors in each region (Harris & Zaritsky, 2009; Lewis et al., 2015).

Uncertainties in the SAD maps consist of both statistical uncertainties, and uncertainties from model assumptions. Statistical uncertainties were estimated by varying the parameter space (generally the number of age-bins $\times$ number of metallicity bins) and tracking the deviation of the fitting statistic (e.g. χ^2) from the best-fit solution. Correlated uncertainties between the age-bins were also accounted for in the calculations, and the total uncertainties were published in the papers. Systematic uncertainties stem from assumptions made about dust extinction, and in the stellar models (e.g. about convection, mass-loss, core-overshoot etc). Lewis et al. (2015) modeled the M31 SAD upto 400 Myrs and found that uncertainties from dust models were the dominant source of systematic uncertainty, while uncertainties from assumptions in stellar models were generally less than half the statistical uncertainties. Williams et al. (2017) modeled the M31 SAD upto a Hubble time, and explored the impact of stellar model assumptions in more detail using isochrones from 4 different evolutionary codes. Model-based uncertainties were at the level of 20% in the 8-12 Gyr age-range, arising primarily due to the uncertainty of modeling red-clump stars (metal-rich, horizontal branch stars).

b. SAD of the LMC: The SAD map of the Large Magellanic Cloud was constructed from the MCPS survey which recovered nearly 4 million stars down to a completeness of V=20-21 mag using the 1m Swope telescope (Zaritsky et al., 2004; Harris & Zaritsky, 2009). Using the general methodology described above, Harris & Zaritsky (2009) divided the LMC into 1376 cells, and evaluated the SAD per region in 16 age-bins from 4 Myr-20 Gyr, and 4 metallicity bins from Z=0.001-0.008. Stars $>$ 4 Gyrs tended to fall below the completeness limit, particularly in the LMC bar, where stellar crowding is the highest. As a result, the authors used archival HST observations in isolated fields across the LMC bar to anchor the age distribution beyond 4 Gyrs, the assumption being that the stars $>$ 4 Gyrs have had enough time to mix and make the SAD across the bar roughly uniform.

The LMC SAD map unveiled the global history of star formation in the galaxy. LMC underwent active star formation 12 Gyrs ago, then a quiescent phase that lasted between

5-12 Gyrs ago, followed by intermittent episodes of star formation that peaked at 2 Gyrs, 500 Myrs, 100 Myrs and 12 Myrs ago. The central bar of the LMC is its longest lived structure, and houses the greatest concentration of stars in the LMC. The bar is invisible in images of gas distribution and shows no recent star formation activity, which makes it unlikely to be dynamical bar found at the centers of spiral galaxies. Zaritsky et al. (2004) proposed that the bar is a concentration of stars obscured by the LMC disk, although the true nature of the bar is still an open question. Both RR Lyrae and Cepheids show a high concentration in the LMC Bar. While most of the oldest stars were formed uniformly throughout the LMC, star formation in the last 100-500 Myrs occurred in the spiral arm features, and recent active star formation (in the last few 10 Myrs) has been occurring in the 30 Doradus and Constellation III regions. The star forming episodes in the LMC coincide with those in the SMC as well, which indicates that these episodes were possibly triggered by repeated interactions with the SMC and the Milky Way.

B. THE RR LYRAE DELAY-TIME DISTRIBUTION

1. Sample selection

The Optical Gravitational Microlensing Experiment (OGLE) was primarily designed to detect *microlensing* events, i.e, distortions, magnifications and/or brightening of a background star due to the gravitational lensing effect of a passing foreground star (Udalski et al., 1992). The experiment was initially designed to detect microlensing signals of Massive Compact Halo Objects (MACHOs) − non-radiating, baryonic objects like neutron stars, black holes and brown dwarfs that could manifest as dark matter (Paczynski, 1986; Griest, 1991), and significant regions of the MACHO parameter space was constrained by the OGLE-II and OGLE-III experiments (Alcock et al., 2000; Wyrzykowski et al., 2011a,b). Regular and large-scale monitoring of stars was necessary for detecting micro-lensing events, and as a result, OGLE ended up becoming one of the largest photometric variability surveys in operation. By the 4th phase of the experiment (OGLEIV - 2009 to present, Udalski et al., 2015),

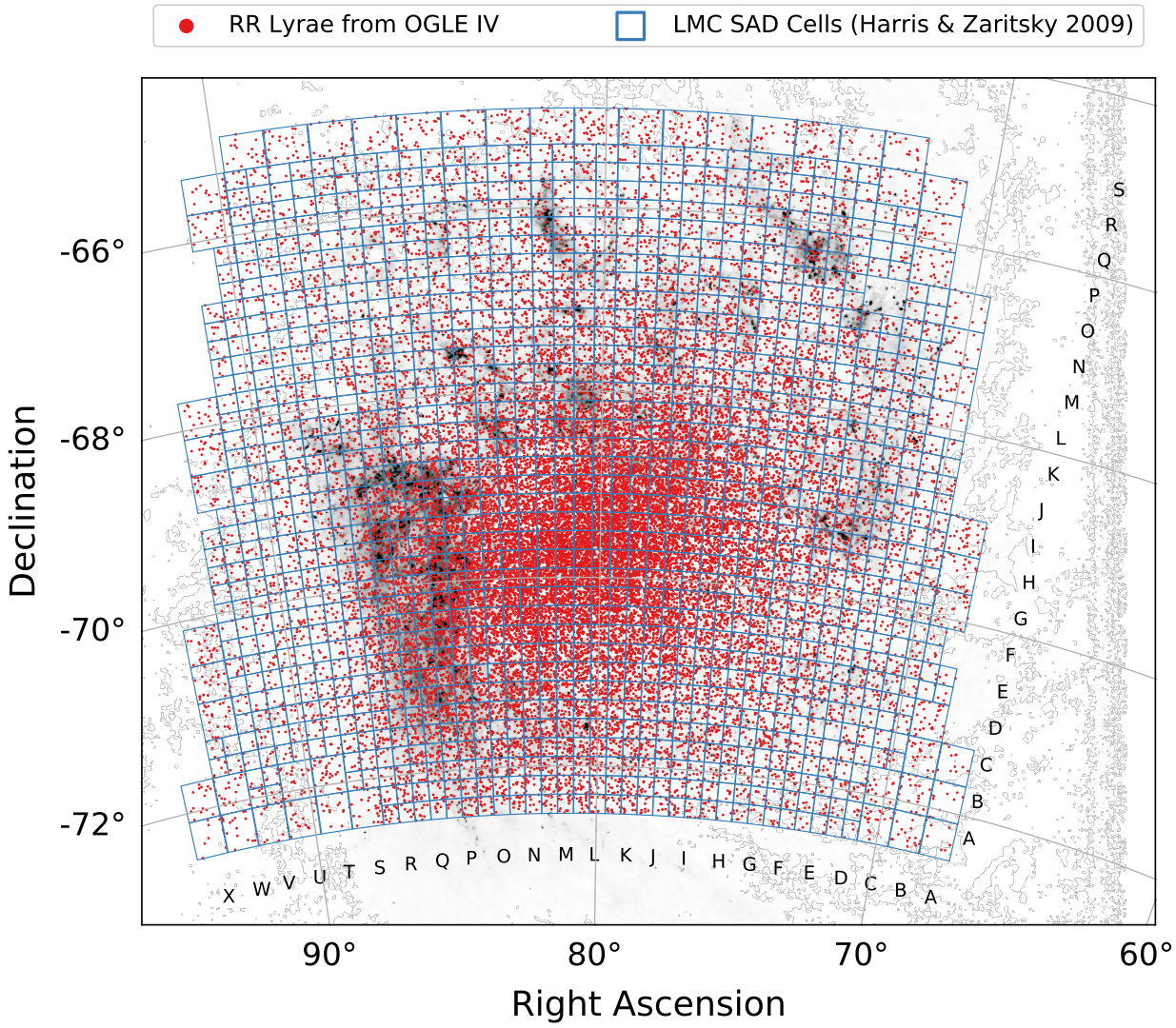

Figure 13: The distribution of RR Lyrae (red dots) in the OGLE IV sample, shown on an HI map of the Large Magellanic Cloud by (Braun, 2012). Overlaid are the spatially-resolved stellar-age distribution cells (blue, labelled with letters) from the (Harris & Zaritsky, 2009) map of the LMC. The cells are $24' \times 24'$ cells, further divided into $12' \times 12'$ cells if the star-count exceeds 25000. Our DTD analysis is carried out only in the OGLE IV survey area common with the SAD map, and this area contains 29,810 RR Lyrae.

OGLE had regularly monitored nearly a billion stars in the Galactic Bulge, Halo and the Magellanic Clouds, and produced one of the largest catalogs of variable stars (e.g. Soszyński et al., 2014b, 2015a, 2016a,b, 2017b), as well as detections of exoplanets (e.g. Udalski et al., 2008; Skowron et al., 2018), SNe and other transients (Kozłowski et al., 2013). The latest version fo the survey was carried out with a 32 chip, 262 Megapixel CCD camera fitted in the 1.3m Warsaw telescope, and obtained observations in the BVI bands with cadences as low as 19-60 mins (in the Galactic bulge) to 1-3 days in the Magellanic Clouds (see Udalski et al., 2015, for details). All observations have been made publicly available [1].

The OGLEIV RR Lyrae sample consists of 39,082 RR objects in the LMC. We excluded objects in the catalog that were flagged as RR Lyrae in the Galaxy, eclipsing variables or objects with uncertain classification, and also excluded objects that fall outside the stellar-age distribution maps, which brought down the total sample to 29,810 RR Lyrae (Figure 13). About 96% of the RR Lyrae in the OGLE III field (98% for fundamental pulsators, RRab) was re-detected by the OGLE IV. Photometrically (as shown in Figure 14), the RR Lyrae I-band luminosity function has a median I = 19.3, and $\sigma_I = 0.5$, which makes the median of the luminosity function about 2.3σ above the completeness of the most crowded fields in the LMC bar (with I $\approx$ 20.5). In addition, about 99% of the sample is above the shallow completeness limit. In the next section, we will describe the calculation of the DTD for the total RR Lyrae sample, and also DTDs for *RRab* and *RRc* subtypes to assess their contribution to the total DTD signal.

2. Method

We use the OGLE IV RR Lyrae sample (Soszyński et al., 2016a) to calculate the DTD using the technique described in Maoz & Badenes (2010) and Badenes et al. (2015). We used the SAD maps of the LMC from Harris & Zaritsky (2009), which contain the stellar-masses formed, with 1σ upper and lower limits, in 16 bins of lookback time from 4.5 Gyrs - 20 Gyrs. The SAD map consists of $24' \times 24'$ spatial cells, which were further subdivided into $12' \times 12'$ cells, if the star-count per SAD cell exceeded 25000 (Figure 13). We can use all 1376 cells

[1] http://ogle.astrouw.edu.pl/

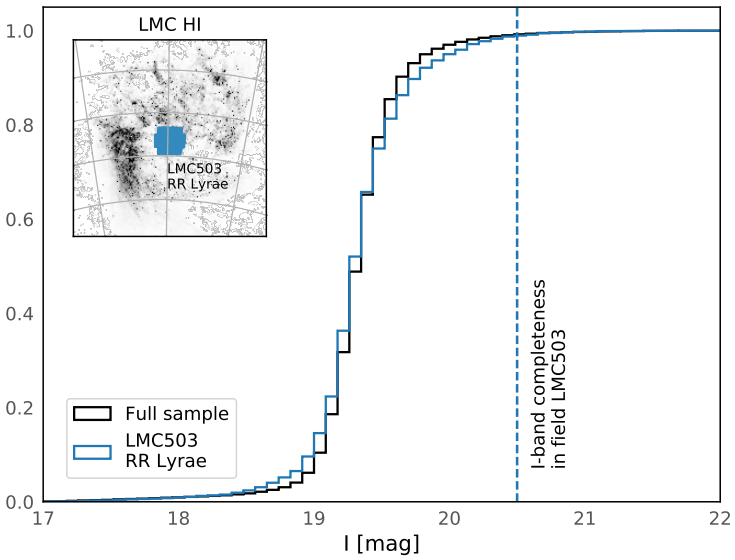

Figure 14: I-band luminosity function of the OGLE IV RR Lyrae. The cumulative histograms show the fraction of RR Lyrae dimmer than a certain I-band brightness. Luminosity function of the full RR Lyrae sample from Figure 13 is shown in black, and that of RR Lyrae in the 'LMC503' field, a region with dense stellar crowding in the Magellanic OGLEIV survey (Udalski et al., 2015), is shown in blue. The inset shows the location of the LMC503 RR Lyrae superimposed on the HI map of the LMC. The I-band completeness limit of the LMC503 region is shown with the dashed line. This shows that the sample is quite complete, with 99% of the full OGLE IV RR Lyrae being brighter than the completeness limit of the some of the most photometrically shallow regions of the survey.

of the SAD map, since they completely fall within the OGLE IV survey area.

The discretized DTD recovery equation is,

$$\lambda_i = \sum_{j=1}^{N} M_{ij} \left(\Psi T_{RR}\right)_j \tag{III.1}$$

where λ_i is the predicted number of RR Lyrae in the ith spatial cell of the SAD map, M_{ij} is the stellar mass in the ith cell and jth lookback time bin, N is the number of lookback-time bins used, Ψ is the rate at which RR Lyrae stars are produced per stellar mass (in units of number yr^{-1} $\mathrm{M}_{\odot}^{-1}$), and T_{RR} is the visibility time or pulsational lifetime of RR Lyrae. Because of the large sample of RR Lyrae, we can use the native age-resolution of the SAD maps ($N = 16$) to calculate the DTD, which was not possible previously with SNRs or planetary nebulae.

The product $\mathbf{\Psi T_{RR}} = \{(\Psi T_{RR})_j\}$, is what we refer to here as the DTD, and is in units of number of RR Lyrae observed per $\mathrm{M}_{\odot}$. We divide $\mathbf{\Psi T_{RR}}(t)$ into 16 age-bins (or delay-time bins), treat the values of these bins as free parameters, and solve for the full vector statistically using the Markov-Chain Monte-Carlo (MCMC) formalism described in (Badenes et al., 2015). We note that our current recovery technique yields a DTD containing the total contribution from the different metallicity bins of the (Harris & Zaritsky, 2009) map. In a future project, we will extend our recovery technique to also constrain the metallicity contribution in each delay-time bin.

A novel aspect of this work is the propagation of uncertainties in the SAD maps into the DTD calculation. We generate 100 random realizations of the SAD map, assuming that the stellar masses in each lookback-time bin is normally distributed, with the best-fit value being the mean, and the upper and lower limits being the 1σ uncertainties. The DTDs were then measured from each of the randomized SAD maps and combined into a single posterior. The mode of this posterior was treated as the best-fit DTD, and the 68% and 95% credible intervals, calculated using the highest posterior density method, were treated as the 1σ and 2σ uncertainties on the DTD. If the best-fit DTD in each delay-time bin exceeds 0 by 2σ, we treat that as a detection. The robustness of these detections are further tested in Section III.B.4.

Once ΨT_{RR} is estimated, we will also try to calculate the mean lifetime of the RR Lyrae, T_{RR}, which can be interpreted as the average time spent by RR Lyrae inside the instability strip (discussed further in Section III.B.5). The lifetimes can be calculated by dividing the measured ΨT_{RR} with a simple estimate of Ψ using Eq. (4) of (Badenes et al., 2015). Since RR the Lyrae phase begins after the He-flash, we can approximate Ψ as the rate at which low-mass stars undergo a He-flash per observed stellar mass, and estimate it from relation between the age at which He-burning begins and zero-age main-sequence mass, i.e. $t_{HeB} \sim M^{\beta}$, weighted by the Salpeter IMF ($\alpha = -2.35$, $\mathrm{M}_{min} = 0.1$ $\mathrm{M}_{\odot}$). We used the MIST (Choi et al., 2016, MESA Isochrone and Stellar Tracks) evolutionary tracks to estimate $\beta = -3.27$ for a typical LMC metallicity, $\mathrm{Z} = 0.25$ $\mathrm{Z}_{\odot}$ (Harris & Zaritsky, 2009) in Figure 15. This leads to,

$$\Psi(t) = \left(0.021 \text{ stars/Gyr/M}_{\odot}\right) \left(\frac{t}{\text{Gyr}}\right)^{-0.59} \tag{III.2}$$

We use the central age of each lookback-time bin to calculate $\Psi(t)$. The uncertainties in the derived T_{RR} is assumed to only come from the uncertainties in ΨT_{RR}.

3. Results

The recovered DTD for RR Lyrae is shown in Figure 16(a) and tabulated in Table 2. The DTD signal is statistically significant in the age range of 0.8-20 Gyrs, although the 0.8-1.3 Gyr bin has a significance of only 2.7σ, whereas the other bins are detected at $> 6\sigma$. We can get the contribution of the DTD to the total RR Lyrae sample by integrating in a given age-bin and multiplying the total stellar mass formed in that bin from the SAD map. Nearly 41.5% of the DTD is contributed from delay-times > 10 Gyr, which is consistent with the notion that RR Lyrae originate from an older stellar population. In addition, we recover a younger signal between 0.8-10 Gyrs, with a contribution of 51.9%. All the age-bins with 2σ detections have nearly the same production efficiency of RR Lyrae of about 1-2 RR objects per 10^5 $\mathrm{M}_{\odot}$.

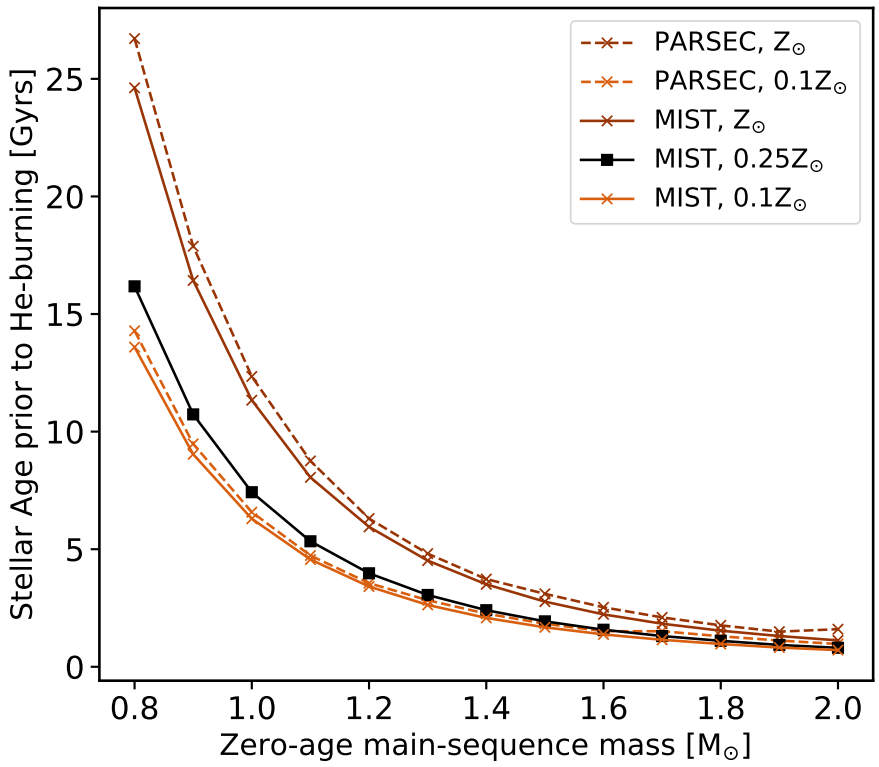

Figure 15: The relation between the zero-age main-sequence mass and the age at which He-flash occurs, based on the MIST tracks (solid) and PARSEC tracks (dashed). MIST is used for calculating the RR Lyrae lifetimes, which is compared with the instability strip crossing timescales from PARSEC, because PARSEC includes separate tracks for the horizontal branch phase. The stellar ages are smaller for lower metallicities. We use the track for Z = 0.25 $Z_{\odot}$, which is typical for the LMC, for calculating the age-mass relation in Section III.B.2. We note that the assumed value for $Z_{\odot}$ = 0.02 by the authors of the PARSEC tracks, and 0.014 for the MIST tracks.

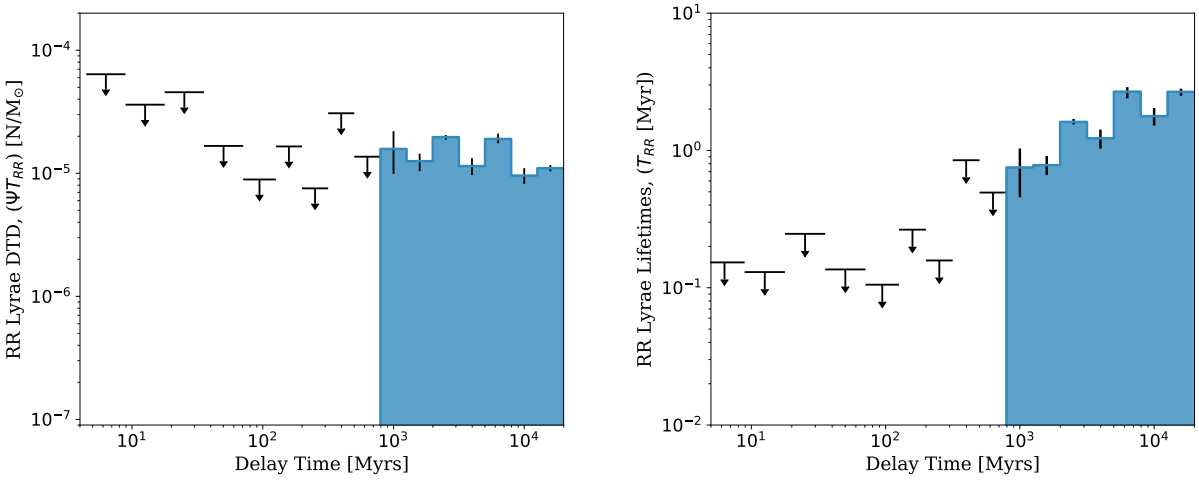

(a) (b)

Figure 16: a) The delay-time distribution, in units of number of RR Lyrae per $M_\odot$, as a function of delay-time in Myrs. The blue histogram represent bins with a statistically significant signal from the MCMC analysis. The error bars are 1σ uncertainties that include uncertainties from the stellar-age distribution maps. The arrows represent 2σ upper limit on the bins, since these did not have a statistically significant signal. b) The lifetimes of RR Lyrae as derived in Section III.B.2. The blue histograms also correspond to the detected DTD bins. The errors represent propagated 1σ uncertainties from the DTDs, and the arrows represent 2σ upper limits.

Table 2: The RR Lyrae DTD calculations, with lifetimes, significance of detection and contribution to the OGLE IV RR Lyrae sample considered in this study.

Delay-Times (Myr)	DTD (ΨT_{RR}) (N/10^5 $M_\odot$)	Lifetime (T_{RR}) (Myr)	Significance ($N\sigma$)	Contribution (%)
4.5 - 8.9	< 6.38	< 0.15	–	< 0.37
8.9 - 17.8	< 3.63	< 0.13	–	< 0.46
17.8 - 35.5	< 4.55	< 0.25	–	< 0.85
35.5 - 70.8	< 1.67	< 0.14	–	< 0.43
70.8 - 125.9	< 0.89	< 0.11	–	< 0.55
125.9 - 199.5	< 1.64	< 0.26	–	< 0.53
199.5 - 316.2	< 0.75	< 0.16	–	< 0.27
316.2 - 501.2	< 3.07	< 0.85	–	< 4.52
501.2 - 794.3	< 1.36	< 0.49	–	< 3.05
794.3 - 1300	$1.58^{+0.57}_{-0.64}$	$0.75^{+0.27}_{-0.30}$	2.73	$1.94^{+0.08}_{-0.05}$
1300 - 2000	$1.23^{+0.19}_{-0.22}$	$0.77^{+0.12}_{-0.14}$	6.28	$7.94^{+0.11}_{-0.08}$
2000 - 3200	$1.97^{+0.10}_{-0.08}$	$1.62^{+0.08}_{-0.07}$	22.76	$20.75^{+0.25}_{-0.14}$
3200 - 5000	$1.16^{+0.19}_{-0.17}$	$1.25^{+0.20}_{-0.18}$	6.88	$5.78^{+0.18}_{-0.08}$
5000 - 7900	$1.92^{+0.17}_{-0.18}$	$2.71^{+0.24}_{-0.27}$	10.56	$12.64^{+0.39}_{-0.17}$
7900 - 12600	$0.94^{+0.12}_{-0.16}$	$1.72^{+0.39}_{-0.30}$	6.16	$6.30^{+0.26}_{-0.10}$
12600 - 20000	$1.10^{+0.06}_{-0.07}$	$2.54^{+0.19}_{-0.18}$	17.60	$38.00^{+0.51}_{-0.26}$

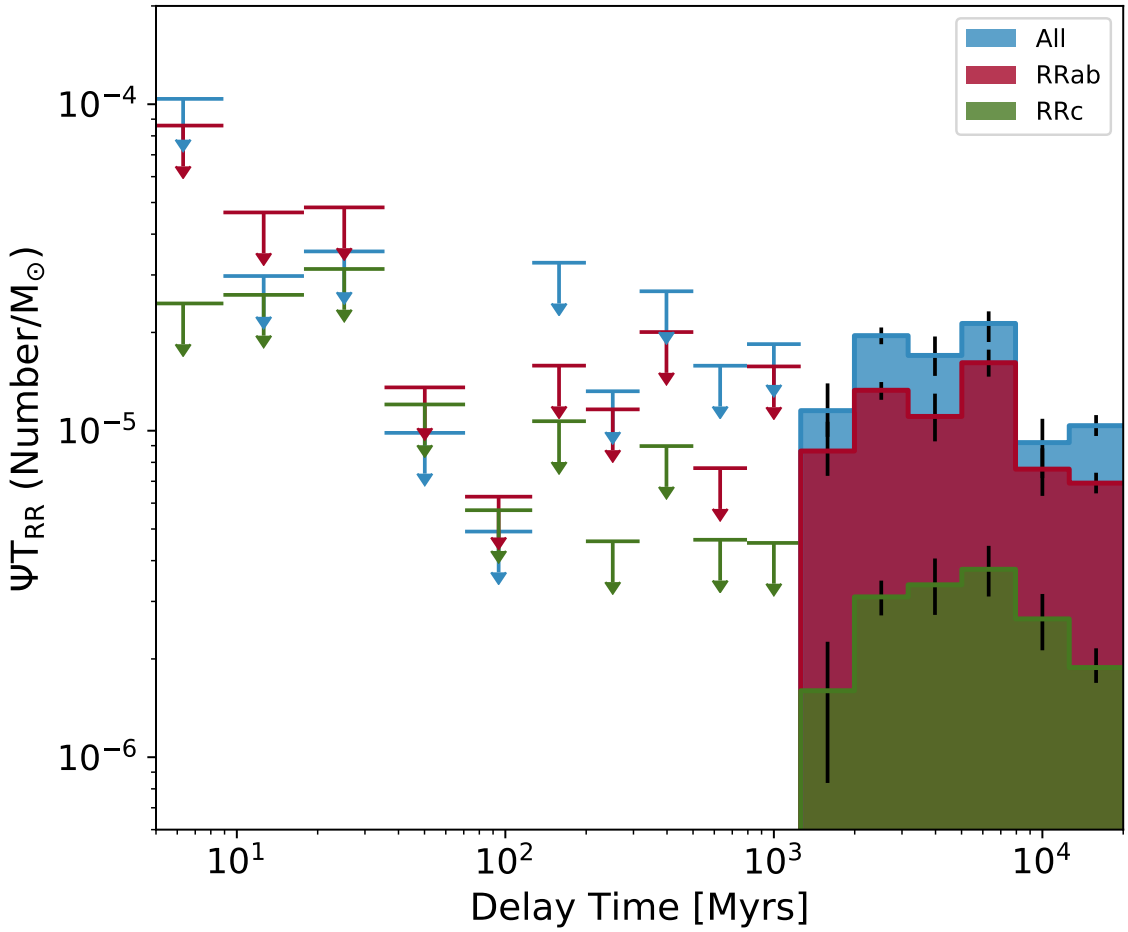

Figure 17: Same as Figure 16(a), but for the different RR Lyrae subtypes: *RRab* and *RRc*, which form the majority of the OGLE IV sample.

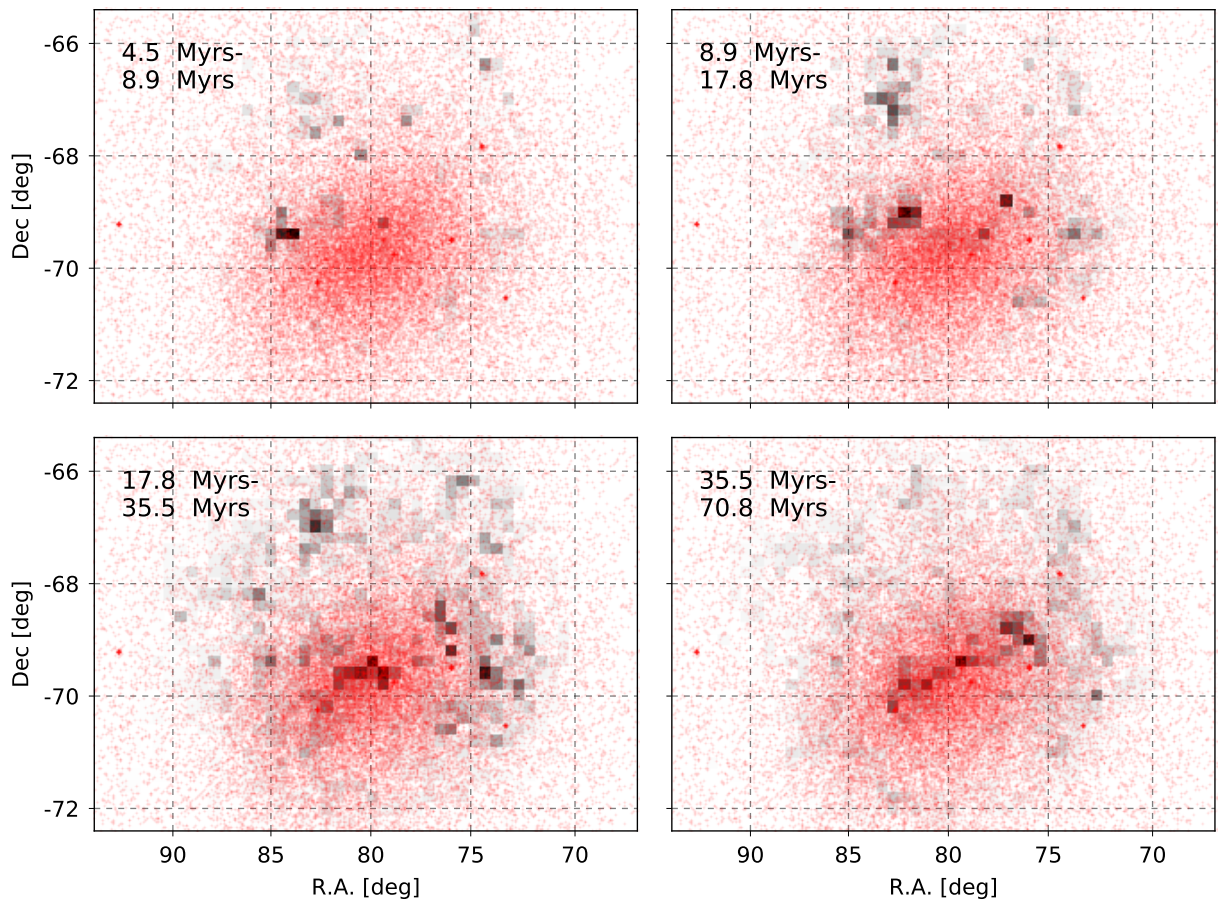

Figure 18: The OGLEIV RR Lyrae (red) shown against the SAD map of (Harris & Zaritsky, 2009) (grey shaded pixels corresponding to cells in Figure 13). Darker the pixel, the more stellar mass formed in that pixel. These panels show the stellar mass formed between 4-70 Myrs.

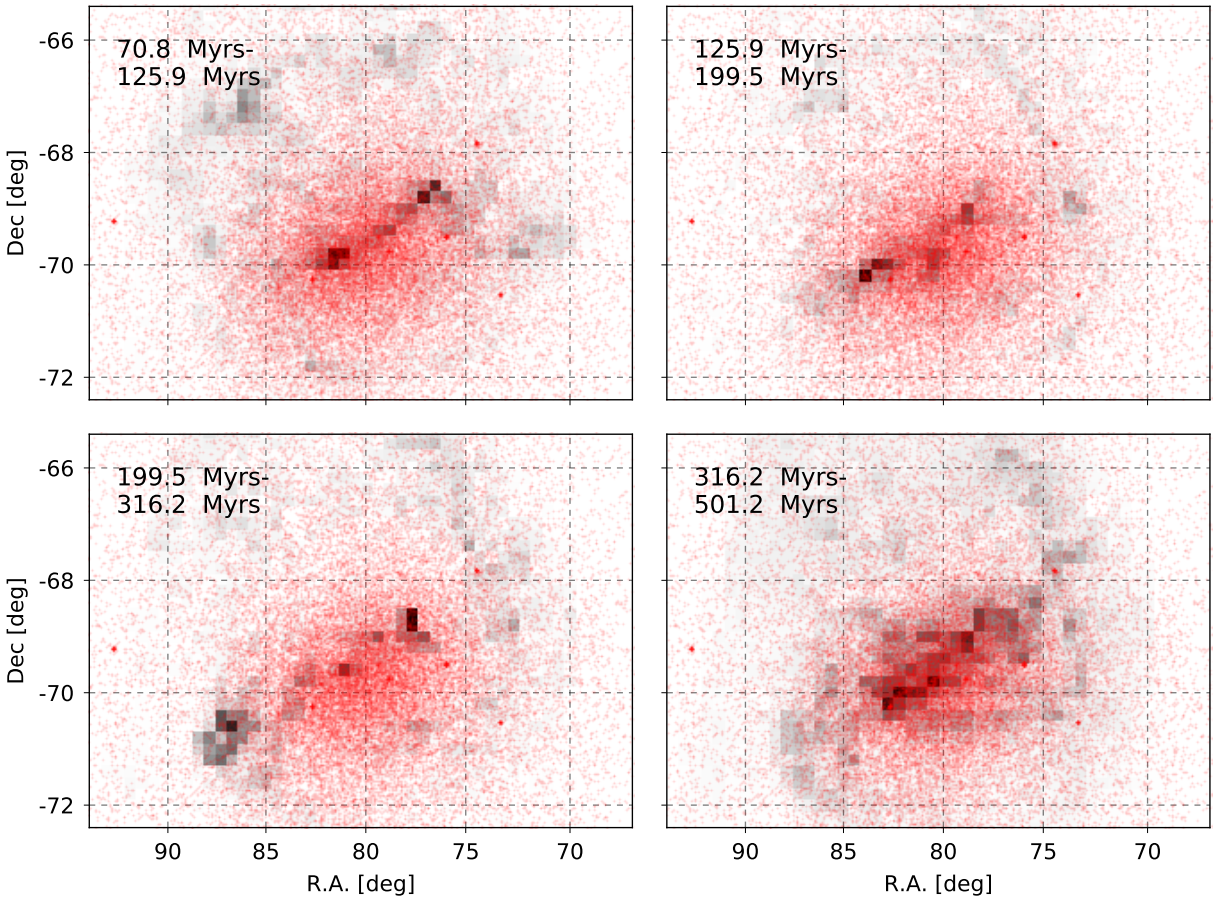

Figure 19: Same as Figure 18, but for 70-500 Myrs

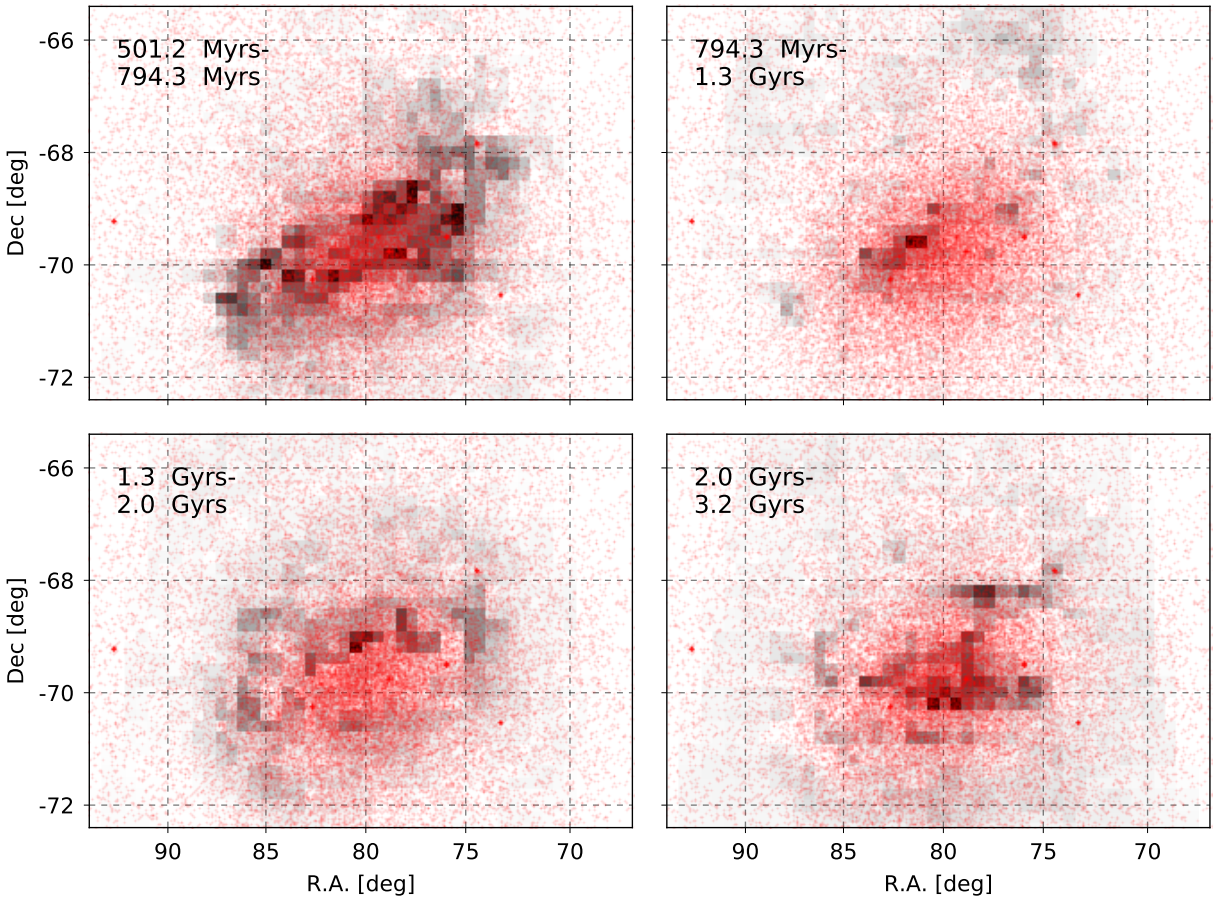

Figure 20: Same as Figure 18, but for 500 Myrs - 3 Gyrs

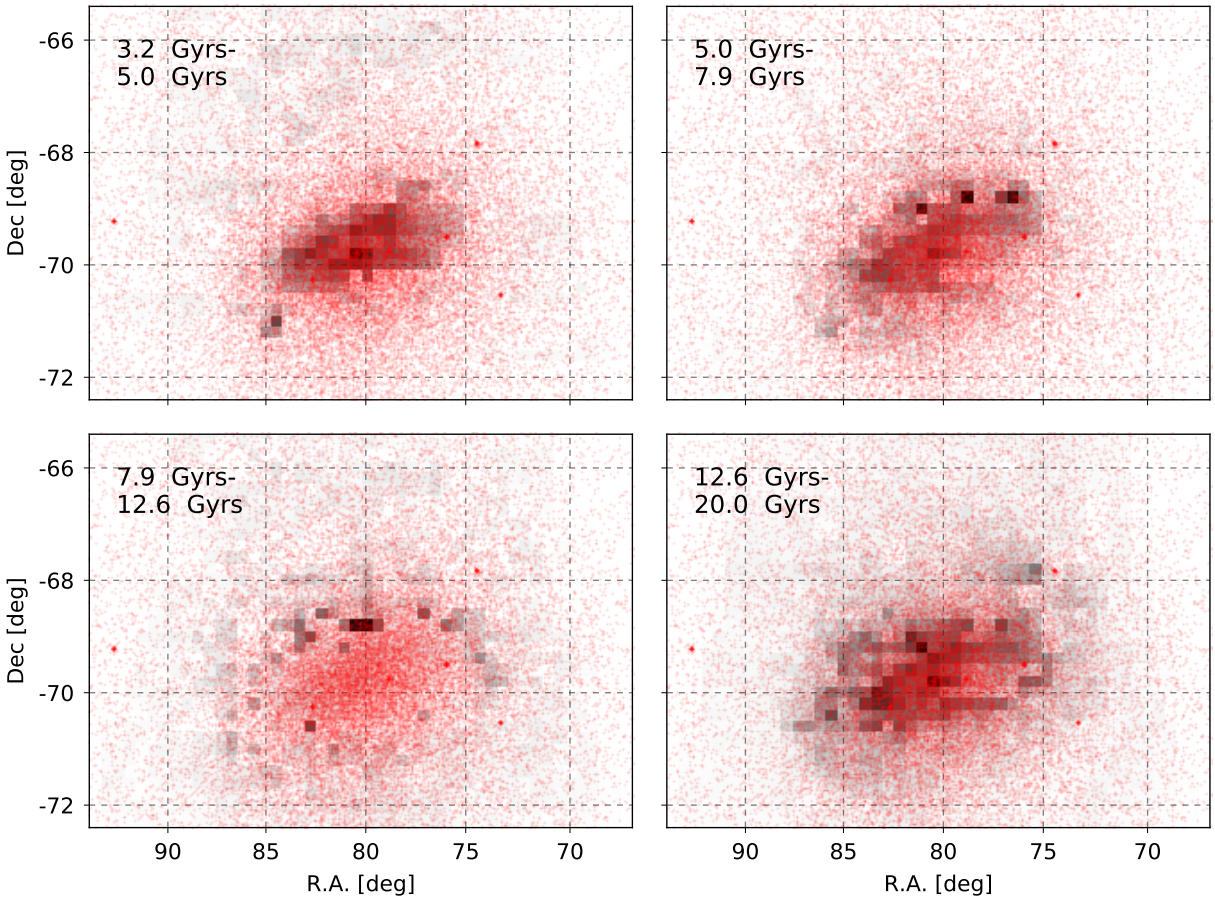

Figure 21: Same as Figure 18, but for 3-20 Gyrs

Among the different RR Lyrae subtypes, *RRc* is the second most abundant subtype in the OGLE IV sample after *RRab*, and is known for being susceptible to period confusion with other variable sources in time-domain surveys, unlike *RRab* (Kinman & Brown, 2010; Mateu et al., 2012; Drake et al., 2014). It is possible therefore that *RRc* could be a potential source of contamination in the total DTD signal, particularly in the younger 1.3-10 Gyr range. However, Figure 17 shows that the *RRab* subtype provides the dominant contribution to the total DTD signal in all the detected bins, which ensures that the effects of contamination are minimal. In addition, both the *RRab* and *RRc* DTDs span the same range of delay-times as the total sample, which shows that both subtypes are associated with the same progenitor ages (or masses).

The mean lifetime of the RR Lyrae based on the DTD is about 0.7-3 Myrs (Figure 16(b), Table 2), which is about 1-3% of the total He-burning lifetime of the MIST tracks. There is a slight positive slope in T_{RR} vs. delay-time because of the IMF in Eq. (III.2) which means that RR Lyrae < 10 Gyrs will have smaller lifetimes compared to the ancient ones. The derived lifetimes depend on the metallicity assumed for the MIST tracks in Eq. III.2, but the effect of this assumption is small. The lifetimes decrease by about 8% if Z = 0.1 $Z_{\odot}$, and increases by about 20% if Z = $Z_{\odot}$. These lifetimes are compared with predictions from theoretical models in Section III.B.5.

A visual inspection of the RR Lyrae DTD is made in Figures 18-21, showing the spatial distribution of RR Lyrae against the stellar mass distribution in each age-bin from the SAD maps. Because of the high spatial density and large number of RR Lyrae, it is difficult to interpret their association with the stellar mass formed in Figures 18-21 with the same clarity as e.g. planetary nebula in Figure 3 in Badenes et al. (2015). Nevertheless, some interesting patterns can be seen from this comparison. The stellar-mass distribution along the LMC bar is well correlated with the high central concentration of RR Lyrae in the 12.6-20 Gyr and 3.2-7.9 Gyr bins. The stellar-mass distribution in the 1.3-2 Gyr and 7.9-12.6 Gyr bins are more correlated with RR Lyrae in the LMC outer bar region than the central region, although these stages appear to have lower star-formation activity than the other age-bins that had $> 2\sigma$ DTD signals. Note however that the DTD signals in these two quiescent bins also have the largest errors and are therefore least significant of the detected bins. For the

age-bins < 0.8 Gyr, the stellar-mass distribution either shows no spatial correlation or does not have the same morphology as the RR Lyrae distribution.

4. Validity of the recovered DTD

The RR Lyrae DTD, while consistent with the expectation that their progenitors are stars > 10 Gyrs, also show a substantial contribution in the 1-10 Gyr range. Before delving into the implications of this finding, we performed a number of statistical checks on the validity of this signal.

a. Changing assumption about DTD Errors: Although we take into account uncertainties in the stellar masses in the HZ09 map when generating randomized SADs, we do make an assumption that the uncertainties are Gaussian. However, the stellar mass errors in the HZ09 map are asymmetric, both in linear and logarithmic mass, and in some cases, the best fit stellar mass is 0 $M_{\odot}$. To check if our assumption about the probability distribution affects our science results, we recalculate the DTD errors based on the technique in (Badenes et al., 2015). In this case, we treat the difference between the DTDs for the best fit SAD map and for the 68% upper/lower limit SAD map as our 1σ systematic error, which is added in quadrature to the statistical error in the DTD. Ideally, this represents an upper limit to the DTD errors. We use this method to look for DTD signals at the level of 2σ, since the DTD errors using the B15 method are much larger than the randomized method. We find that the RR Lyrae DTD still has significant signal below 10 Gyrs, with detections in the age bins of 2-3.2 Gyrs, 3.2-5 Gyrs and 5-7.9 Gyrs at significance levels of 2.1σ, 6.7σ and 16.6σ. The total contribution from these bins is about 42.8%. The oldest age-bin also has a signal detected at 3.4σ, and contributes about 40.4% to the sample. We therefore conclude that the DTD signal below 10 Gyrs is robust to our assumption about the stellar mass error distribution in the SAD map.

b. False positive check with an artificial DTD: We can check whether the DTD signals at ages < 10 Gyrs are false positives by testing our DTD recovery method on an

RR Lyrae population artificially created by an old DTD. Our model 'old' DTD is 2×10^{-5} objects per $M_\odot$ for the two oldest age-bins in the map (8-12.5 Gyrs, and 12.5-20 Gyrs), and 0 for all other bins. The artificial RR Lyrae map is generated by a Poisson process, where the expected number of RR Lyrae per spatial cell is the convolution of our model DTD and the best fit SAD map using Eq. (III.1). The DTD method is then re-ran on this map. We show in Figure 22 that we do indeed recover the model DTD with high accuracy, which implies that the signals in the younger bins of the RR Lyrae are not false detections. However, the RR Lyrae map will have some stochasticity as it is generated from a Poisson distribution. We therefore repeat our DTD measurement on 100 different artificial RR Lyrae maps to estimate a false detection probability, i.e. the probability that a DTD signal $> 2\sigma$ would be recovered in any bin < 8 Gyrs in a given measurement. We find that the false detection probability is $0 - 1\%$ for all bins < 5 Gyrs, and about 16% for the 5-8 Gyr bin. This is a small fraction of false positives, and the detections in these cases are generally marginal ($\sim 2\sigma$) when compared to the oldest bins, which have 100% detection fractions and detection significances of $\gtrsim 20\sigma$ in each trial. One can therefore conclude that the statistical signal in this age-bin is probably not significant enough the produce significant signal below < 10 Gyrs. To further verify, we show the spatial distribution of RR Lyrae in the LMC expected from our model old DTD versus our recovered DTD in Figure 23. Visually at least, it seems that the RR Lyrae distribution from our recovered DTD matches the OGLEIV RR Lyrae distribution better than a purely old DTD. This indicates that our DTD signal is most likely a physically meaningful detection, and not because of any artifacts borne out of the measurement process. In the final paper, we will validate this with a more sophisticated p-value test where we compare the 'old' DTD with our DTD in Figure 16(a).

c. Stellar mixing: A common concern with the DTD method is that the age distribution of the stellar population around the object may not always be representative of the progenitor age because it may have migrated or diffused from another region of the galaxy, and it now appears in projection with the current age distribution of stars. This was countered in Maoz & Badenes (2010) and Badenes et al. (2015) by arguing that the progenitor population is part of the bulk stellar population, and are therefore subjected to the same diffusion/migration

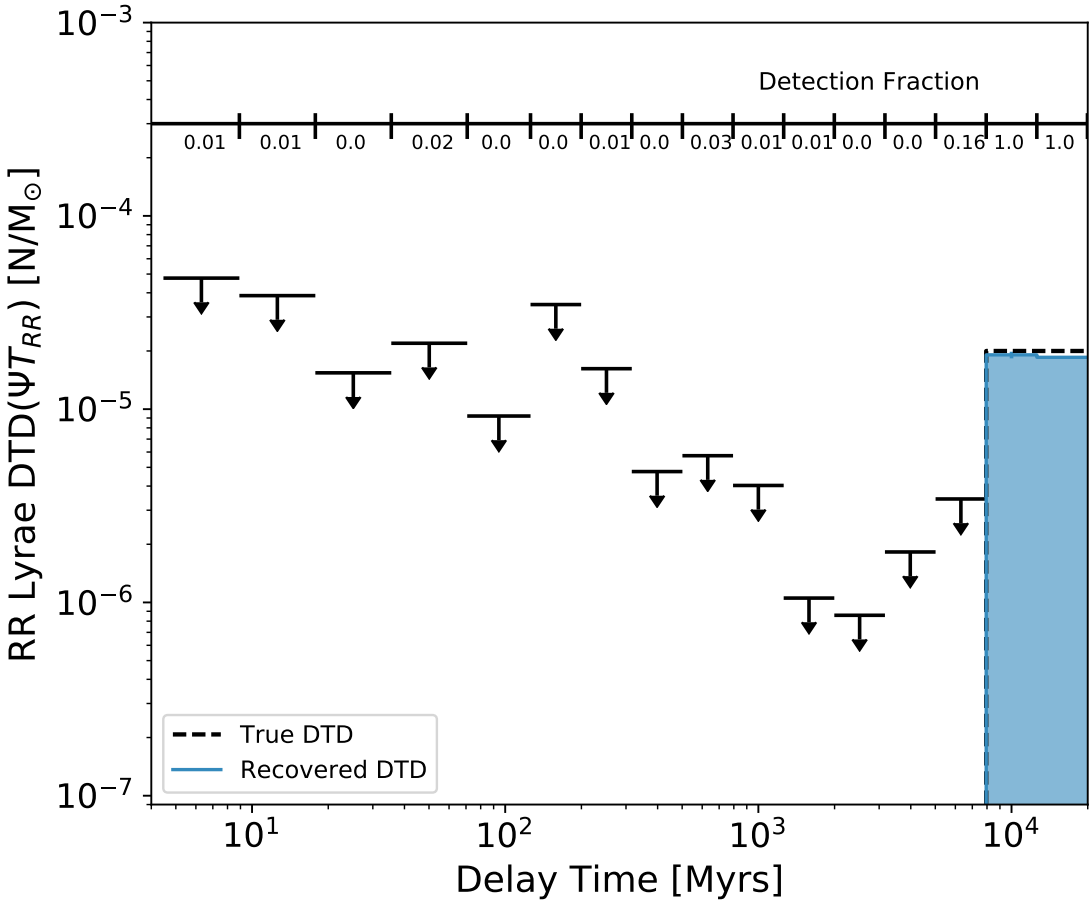

Figure 22: Result of testing our DTD recovery method on an RR Lyrae map generated with artificially 'old' DTD (black dashed line). The recovered DTD from this map is shown in blue, and 2σ upper limits are shown with black arrows. The fraction of detections in each delay bin for different realizations of the RR Lyrae map based on the old DTD is shown with the scale on top.

effects. As a result, the number of RR Lyrae formed per mass of the stellar population in any region of the galaxy (basically, the DTD) should statistically remain the same.

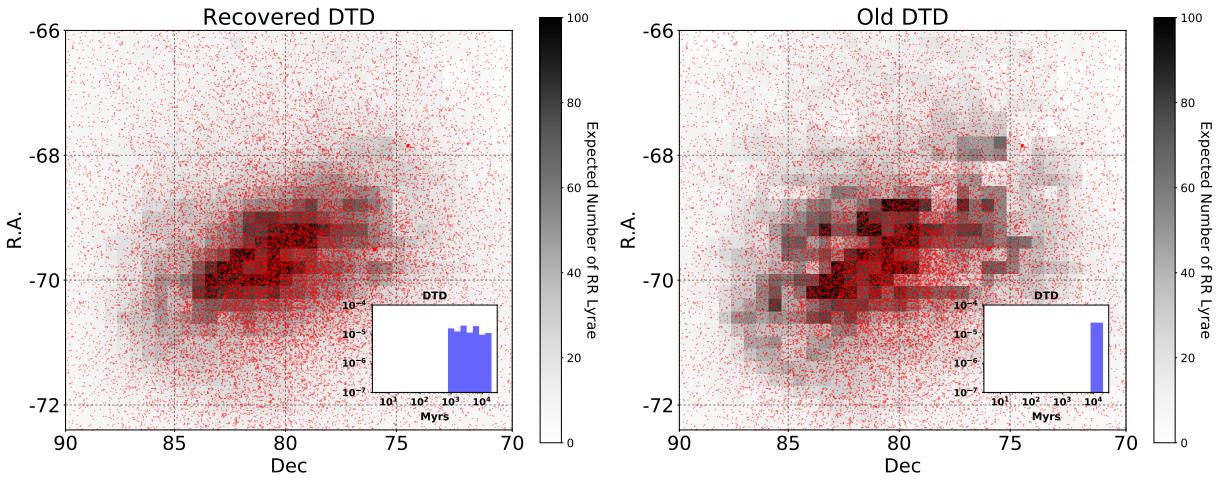

Figure 23: The predicted distribution of RR Lyrae in the LMC with the best-fit SAD map and our recovered DTD (left) and a model DTD that assumes all RR Lyrae are formed from > 10 Gyr progenitors (right). The old DTD was normalized such that it roughly produces the number of RR Lyrae in the OGLEIV survey. The inset in each panel shows the form of the DTD used. The red dots represent the OGLEIV RR Lyrae.

We perform an additional statistical check in this paper to confirm this idea. We redo our DTD measurements with a artificially mixed SAD map, i.e. the stellar mass in each cell i consists of the mass measured in that cell, plus some fraction f of the global stellar mass of the LMC mixed into that cell. This is represented by the following mixture model,

$$M'_{ij} = (1 - f)M_{ij} + f\left(\frac{M_i M_j}{M_{tot}}\right) \tag{III.3}$$

where M'_{ij} is the scaled mass per cell-age bin i, j, M_{ij} is the original mass per cell-age bin i, j, $\mathrm{M}_i = \sum_j M_{ij}$, $\mathrm{M}_j = \sum_i M_{ij}$ and $\mathrm{M}_{tot} = \sum_i \sum_j M_{ij}$. Note that in this form, the total

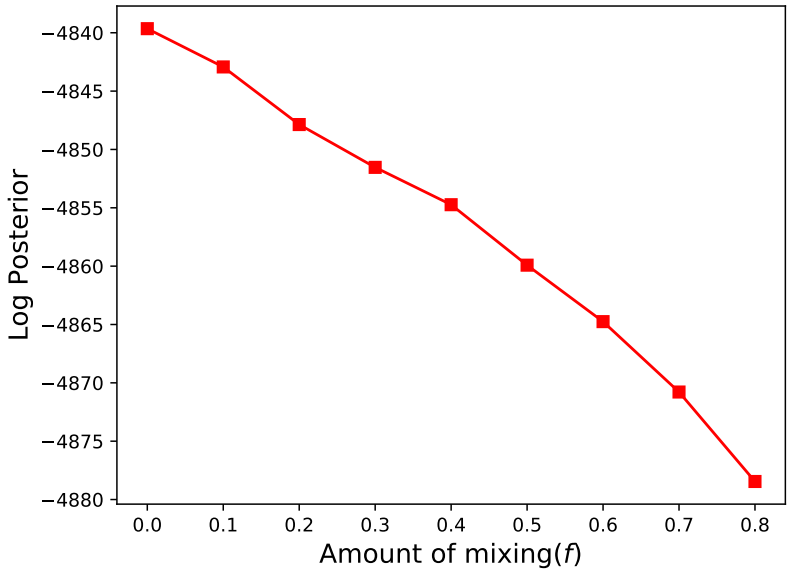

Figure 24: Log probability of the DTD recovered for SAD maps modified by each value of mixing parameter f introduced in Equation (III.3).

mass of the LMC is preserved, i.e. $\sum_i \sum_j M'_{ij} = \sum_i \sum_j M_{ij} = M_{tot}$. We find that for $f = 0$ (no mixing), the MCMC algorithm recovers a DTD solution with the maximum log posterior probability (Figure 24). This indicates that statistically, our DTD solution is probably not biased by some unaccounted-for stellar mixing in the galaxy.

d. Accounting for LMC star clusters A curious discrepancy with our DTD result is the fact that very few RR Lyrae are seen in stellar clusters younger than 10 Gyrs. Soszyński et al. (2016c) identified only 2 globular clusters younger than 10 Gyrs that hosted a significant number of RR Lyrae, NGC 1928, (1.7 Gyrs old) and NGC 1939 (1.6 Gyrs old). However, these clusters only had 7-8 RR Lyrae coincident with their position, whereas the older clusters a significantly larger number of RR Lyrae, with the smallest being NGC 121 with 15 RR Lyrae, and the largest being 1835 with almost 125 RR Lyrae (but note that the older clusters are about 4 times more massive than the 1-10 Gyr clusters, and would therefore hold more stellar mass Baumgardt et al., 2013). It is possible that because of the small size of the

old clusters ($\sim$ 10 pc) compared to the size of the SAD map spatial cells ($\sim$ 200 pc), the information about the RR Lyrae association with the clusters is lost due to spatial averaging. We test this possibility by recalculating the DTD, but this time treating all the star clusters in the LMC as separate spatial cells in the SAD map. This is done with the following steps :-

I. Use the positions, masses and ages of clusters in the LMC from Baumgardt et al. (2013), and their corresponding sizes from Bica et al. (2008).

II. Find the SAD cells in which these clusters are located, and adjust the stellar mass in each cell by subtracting the cluster mass at the age bin corresponding to the cluster age.

III. Adjust the number of RR Lyrae in each cell by subtracting the number of RR Lyrae that are within the area of the cluster. We do this only if the number density of RR Lyrae in the cluster is atleast twice the number density of RR Lyrae in the SAD cell.

IV. Create additional SAD cells corresponding to each LMC cluster. Each cell has mass = cluster mass formed at an age = cluster age.

V. The number of RR Lyrae in these additional cells is the number of RR Lyrae that are statistically associated with each cluster (derived in step 3).

VI. Calculate the DTD using the combination of the adjusted SAD map and cluster SAD map.

However, using this method, the new DTD is effectively unchanged from the original DTD. A significant signal is still present between 1-10 Gyrs, with even smaller error bars because of additional cells contributing to the likelihood equation. It appears that RR Lyrae associated with SADs between 1-10 Gyrs have a significant statistical weight in our recovered DTD signal, and this result is robust even with the careful treatment of the old RRLyrae-hosting cluster. We discuss the implications of this in Section IV.F.

5. Comparison with stellar evolution tracks

We can get a qualitative understanding of the above results by checking with the ages and lifetimes of published low-mass stellar evolution tracks. The delay-times can be compared with the ages at which the He-flash occurs, and the measured lifetimes can be compared with

the instability strip crossing timescales of stars evolving off the horizontal branch. We note that stars can also cross the instability strip after the He-flash and before settling on the horizontal branch, but this phase is short-lived. Evolutionary models usually do not trace this phase, and instead start their models from a suitable point on the horizontal branch (Salaris & Cassisi, 2005). We define the instability strip based on Eq. 3 & 4 of (Marconi et al., 2015), which also includes a metallicity dependence.

Although we used MIST to determine the onset rate of He-burning, the < 2 $M_\odot$ MIST tracks do not cross the instability strip except for very low metallicities. This might be related to the treatment of mass loss in MIST, which will be explored further in future versions of MIST (Choi, J., private communication). Because of this, we also compared our results with the published horizontal branch tracks of the PARSEC [2] (Bressan et al., 2012). The PARSEC tracks, like MIST, include the physics of convective overshoot, atomic diffusion and the latest opacities from the OPAL group, all of which affect the main-sequence lifetime. We checked that PARSEC models yield $\beta = -3.28$ for LMC-like metallicity, which is roughly the same as the MIST calculation in Section III.B.2, and therefore Eq. III.2 remains the same for the PARSEC tracks. The low mass stellar tracks (> 0.45 $M_\odot$) of PARSEC were evolved from the pre-main sequence stage up to the point when the He-burning luminosity exceeded the surface luminosity by a factor of 200. We treat this point as the age when the He-flash occurs. The subsequent horizontal branch track started from the same core-mass and composition as the He-flash, and evolved up to the thermally pulsing AGB phase.

The comparison between our measured DTD and the predicted stellar age at He-burning is shown in Figure 25(a). Higher mass and lower metallicity stars have hotter cores, and therefore reach the He-burning stage quicker. The comparison suggests that stars in the mass range of $0.7 - 2$ $M_\odot$ are likely the main-sequence progenitors of RR Lyrae. The age-mass relation in Figure 25(a) flatten out for masses < 0.8 $M_\odot$ because the tracks for these masses were evolved up to a maximum age of 30 Gyrs.

The comparison between the lifetimes and the instability strip crossing timescales of the PARSEC models are shown in Figure 25(b). Only stars < 0.7 $M_\odot$ cross the instability strip on timescales comparable to the measured lifetimes, with metal-poor stars having a larger

[2] http://people.sissa.it/ sbressan/parsec.html

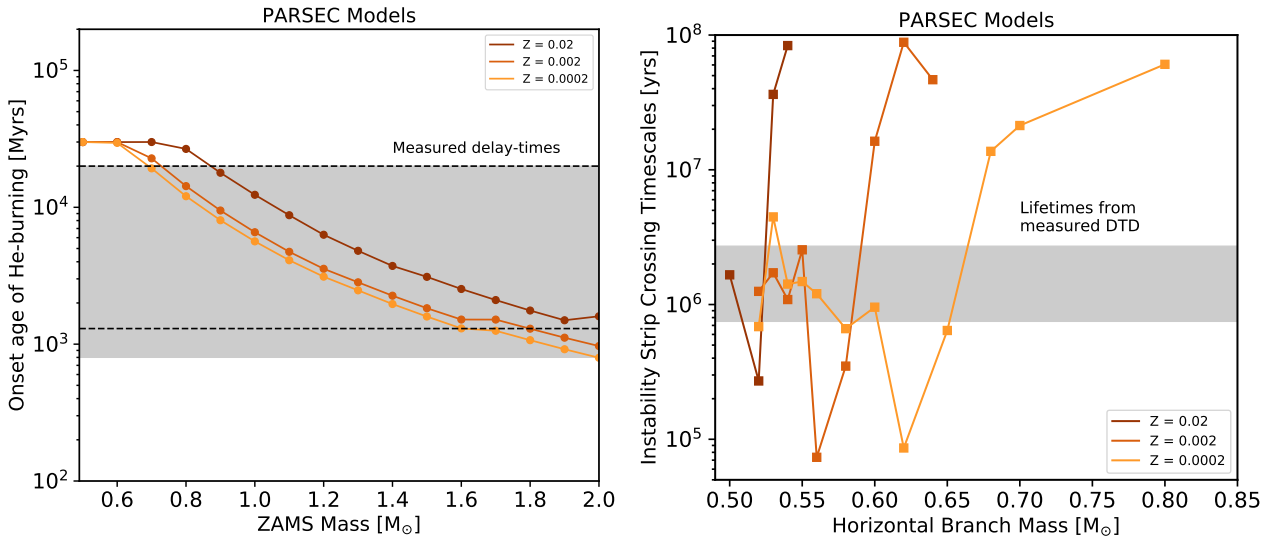

(a) (b)

Figure 25: Comparison of the DTD measurements with the PARSEC stellar evolution tracks. a) The range of delay-times from Figure 16(a) (gray shaded region) with the ages at which He-flash occurs as a function of the initial mass. The color scheme represent initial metallicities from Z = 0.02 to 0.0002. The black dashed lines enclose the region where the DTD measurements were made at a significance $> 6\sigma$. b) The timescales on which stellar tracks cross the instability strip (colored lines), compared with the lifetimes measured in Figure 16(b) (gray shaded region). The tracks are somewhat non-linear because of few interpolating points exist during this relatively fast phase of evolution. The color scheme is the same from the left panel.

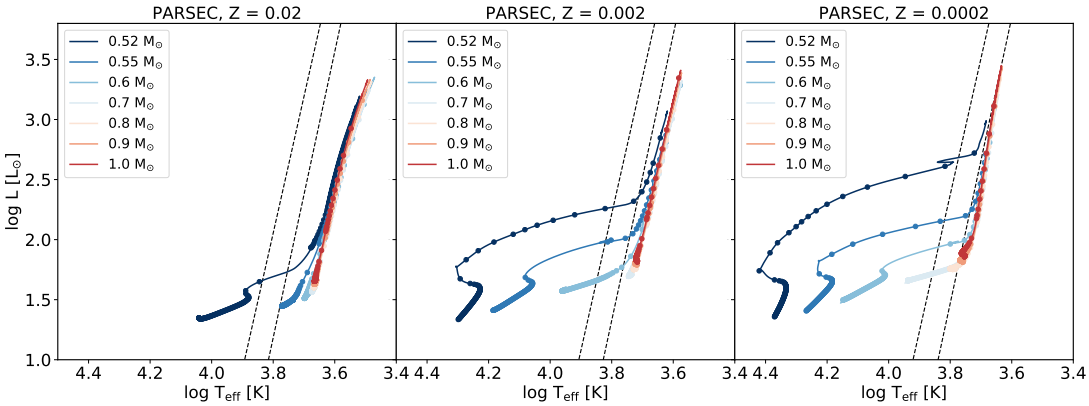

Figure 26: HR Diagams show instability strip crossings for tracks of different horizontal branch masses and metallicities. The dashed line represents the instability strip of RR Lyrae from (Marconi et al., 2015). The markers on each track represent time-steps of 1 Myr, showing that the lower mass tracks evolve faster than the higher mass ones.

range of masses that are consistent with the lifetimes. This can be further understood from Figure 26. Lower-mass stars tend to cross the instability strip from the left as they evolve off the horizontal branch. They have smaller envelopes after mass-loss on the red giant branch, and therefore hotter surface temperatures, and they cross the instability strip quickly since the He-burning core and H-burning shells have exhausted most of the fuel by this time. On the other hand, more massive horizontal branch stars have more massive envelopes, and therefore cooler temperatures, which makes them initially settle in the middle or to the right of the instability strip. As a result, higher mass stars spend longer time inside the instability strip, as seen in Figure 25(b) (Faulkner & Iben, 1966; Iben, 1974; Salaris & Cassisi, 2005). Lower metallicity also makes it more likely for stars to cross the instability strip as their surface temperatures are higher, which allows their horizontal branch evolution to begin farther left of the instability strip. Therefore, the metal-poor stars, for the same mass, have shorter crossing timescales in Figure25(b).

The above comparisons show that the stars with initial masses of 0.7 - 1.8 $M_{\odot}$ that are

consistent with the DTD in Figure 25(a), are not consistent with the measured lifetimes in Figure 25(b), because these stellar tracks either never cross the instability strip or evolve much longer than the measured lifetimes inside the strip, even for the lowest metallicities. The implications of this are discussed in the next section.

6. Discussion

Our measured RR Lyrae DTD shows that the mere presence of RR Lyrae may not be indicative of an ancient ($>$ 10 Gyr) stellar population (Alonso-García et al., 2004; Sarajedini, 2011; Sarajedini et al., 2012), since more than half the RR Lyrae could be coming from younger (1.3-10 Gyr) progenitors. The assumption of an ancient population came from age-measurements of globular clusters in the Magellanic Clouds, where only the older and brighter clusters had detectable RR Lyrae populations (Olszewski et al., 1996; Soszyński et al., 2016c). However, our DTD signal below 10 Gyrs is quite strong, with most signals being detected at a significance level $> 6\sigma$ (with the exception of 800 Myr - 1.3 Gyr signal, which is detected at only 2.7σ). The result appears robust to the various statistical checks we performed in Section III.B.4. Even if we assume that the RR Lyrae DTD should only have signal $>$ 10 Gyr, i.e. RR Lyrae only come from $>$ 10 Gyr populations, it cannot reproduce the OGLE IV RR Lyrae distribution as well as our recovered DTD as shown in Figures 23 and 22. It is also unlikely that there are any particular systematics in the SAD maps that may be biasing the DTD towards younger delay times. The completeness limit in most of the LMC fields in the SAD map is V=21 mag, which is just deep enough to reach the ancient main-sequence turnoff. In the LMC bar, the effect of crowding limits the completeness to V $\approx$ 20, and isolated HST fields were used to anchor the SAD $>$ 4 Gyrs (Holtzman et al., 1999; Olsen, 1999; Smecker-Hane et al., 2002). However, these HST studies, as well as later observations of the bar that reach well below the ancient main-sequence turnoff (Weisz et al., 2013; Monteagudo et al., 2018), have shown that the LMC bar appears to have a well-mixed population of stars, with little variation in the SAD across the bar. Based on our RR Lyrae DTD, we suggest that the spread in ages of RR Lyrae is important to consider when using RR Lyrae for studying the formation and assembly history of dwarf galaxies, and the halos

and bulges of major Local Group galaxies.

The RR Lyrae DTD may be explained by enhanced mass-loss on the red-giant branch (RGB). This is evident from Figures 25(a) and 25(b). The range of main-sequence masses for RR Lyrae allowed by the DTD range is 0.8 - 1.8 $M_{\odot}$. The range of horizontal branch masses allowed by the DTD lifetimes are 0.5-0.7 $M_{\odot}$. As a result, stars would need to lose about 0.3 $M_{\odot}$ - 1.1 $M_{\odot}$ to settle on the horizontal branch and manifest as RR Lyrae while crossing the instability strip (this is assuming that mass-loss rate is proportional to the stellar mass, i.e. 0.8 $M_{\odot}$ will most probably form a 0.5 $M_{\odot}$ RR Lyrae, and 1.8 $M_{\odot}$ will form 0.7 $M_{\odot}$ star).

The mass-loss values appear higher than what is estimated in the literature. There is no well-established theory of mass-loss on the RGB (Espey & Crowley, 2008; Catelan, 2009), in comparison with the theories of line-driven mass-loss from massive stars (Smith, 2014). As a result, mass-loss rates are usually parameterized (e.g. Reimer's law Reimers, 1975; Schröder & Cuntz, 2005) and tuned to match observations. For example, constraints from horizontal branch studies and globular clusters put the required mass-losses on the RGB to about 0.1-0.3 $M_{\odot}$ (see e.g. Salaris et al., 2007; Dotter, 2008; Salaris et al., 2016, and references therein), which is lower than our estimates. On the other hand, enhanced mass-loss rates (0.5-1 $M_{\odot}$) have been proposed as an explanation for some nearby giant stars (see Section III in Taam et al., 1976), as well as metal-rich RR Lyrae discussed in Section III.A.2.b. It may not be surprising if higher mass-loss rates are indeed responsible for the RR Lyrae DTD, because mass-loss has been proposed as a possible second-parameter candidate for horizontal branches (Peterson, 1982; Catelan, 2000; Silva Aguirre et al., 2008). In the case of massive stars, enhanced mass-loss can be episodic and eruptive, and also occur through binary interactions (Smith, 2014), so it may be plausible that one or more of these causes could also be affecting the pre-RR Lyrae evolution of stars (see e.g. Moehler et al., 2000; Origlia et al., 2007). For example, Karczmarek et al. (2017) has shown that close binary mass-transfer episodes can bring stars into the instability strip and make them manifest as RR Lyrae or Cepheids (referred to as binary evolution pulsators in their paper).

A detailed analysis of the mass-loss in RR Lyrae is beyond the scope of this thesis, but we will revisit the issue before publishing the paper. Most of the above studies estimate that a small percentage of the populations will have enhanced mass-loss, so it remains to be

investigated if enhanced mass-loss can explain the entire 0.8-10 Gyr spread of the RR Lyrae DTD. We will take into account the metallicity dependence of the mass-losses from Figures 25(a) and 25(b), make plausible estimates of a plausible Reimers wind parameter based on these values (since it is one of the most widely used mass-loss parameterizations in stellar evolution codes), and also check the effect of changing the instability strip boundaries on our mass-loss estimates.

The apparent discrepancy between the number of RR Lyrae per stellar cluster and the RR Lyrae DTD is probably an effect of metallicity. LMC clusters show a conspicuous age-metallicity relation, with the oldest clusters being generally more metal poor than younger clusters (Harris & Zaritsky, 2009). This means more low-mass stars in the oldest clusters are likely to cross the instability strip on their way to and from the horizontal branch, and therefore manifest as RR Lyrae. On the other hand, our RR Lyrae DTD was calculated by summing over all the metallicity bins in the SAD maps, which makes it less straightforward to compare the DTD with the ages of the RRLyrae-hosting clusters. In a forthcoming paper, we will investigate the effect of metallicity on the DTD by adding metallicity as an extra dimension to the parameter space, and comparing our results with both the spatial and photometric metallicity distribution of the RR Lyrae (Skowron et al., 2016).

C. DELAY-TIME DISTRIBUTION OF CLASSICAL CEPHEIDS

1. Sample Selection

For the DTD, we use the classical Cepheid sample from the OGLEIV survey (Soszyński et al., 2015a). More specifically, we use a subset of this sample created and made publicly available [3] by Jacyszyn-Dobrzeniecka et al. (2016) for studying the three-dimensional structure of the Magellanic system. Cepheids that deviated by more than 3σ from the period luminosity relation, and/or having log periods (days) < -0.3 were excluded since they were likely affected blending and crowding effects (for details of the sample selection, see Section 2 of

[3] http://ogle.astrouw.edu.pl/

the paper). The final sample consists of 4222 Cepheids, with 2292 fundamental pulsators, 1589 first overtone pulsators, and 441 mixed mode pulsators. The sample completeness is almost 99%, based on redetections of OGLEIII Cepheids in the OGLEIV fields. In addition, the OGLEIV Cepheid sample has a median I = 16 and $\sigma_I = 0.7$ mag, which is almost 6.2σ higher than the completeness limit of the most crowded field in the LMC Bar (Figure 28). Similar to RR Lyrae, we only include the Cepheids that fall within the HZ09 survey area, thus bringing the sample to 4021 objects. The distribution of our sample is shown in Figure 27.

2. Results and Discussion

We reapply the method in Section III.B.2 to the Cepheid sample, and recover the DTD as shown in Figure 29 and tabulated in Table 3, using the same 2σ criterion to define a signal detection in each delay-time bin. We find that the Cepheid DTD has most of its signal between 18 and 200 Myrs. These bins contribute almost 57% of the DTD signal measured, with the strongest detections in the 70-200 Myr range at significance levels of 9.7σ and 13σ respectively. These results are, to the first order, consistent with the expectation that Cepheids come from a more massive, younger population of stars. Based on MIST single stellar evolution tracks at solar metallicity, the detected age ranges suggest that most Cepheids have a progenitor mass range of 3.8 - 11 $M_\odot$, which is roughly consistent with the classical Cepheid mass-range generally measured in the literature (Bono et al., 2005; Pietrzyński et al., 2010; Bertelli et al., 2009) The DTD also appears roughly consistent with period-based age distribution of the same sample of Cepheids in Figure 30. The peaks of both distribution are coincident, although our DTD has significant signals buried in the upper limits at other delay-time bins. The period-age relation is based on the period-age and period-age-color relations derived in Bono et al. (2005) using a grid of evolutionary and pulsational models that are consistent with host cluster ages derived from isochrone analysis to about 20%. Our DTD predicts that the majority of OGLEIV Cepheid sample were produced on timescales of 70-200 Myrs, with a production rate of almost 15 Cepheids per 10^5 $M_\odot$ of stars, and contributing about 42.3% of the OGLEIV sample (note that there is

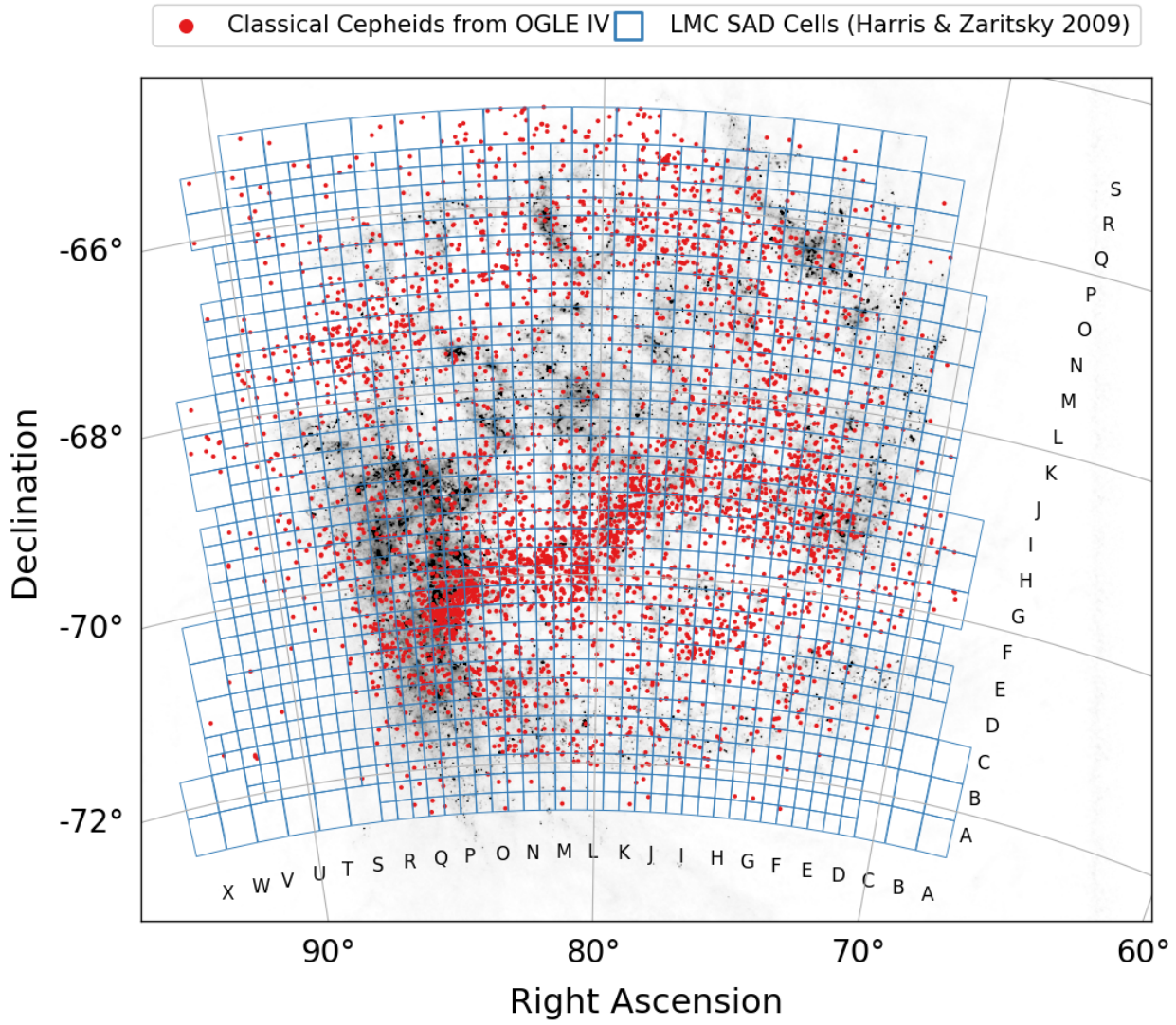

Figure 27: OGLE IV Classical Cepheids (red) in the LMC, overlaid on the Harris & Zaritsky (2009) survey area (blue squares).

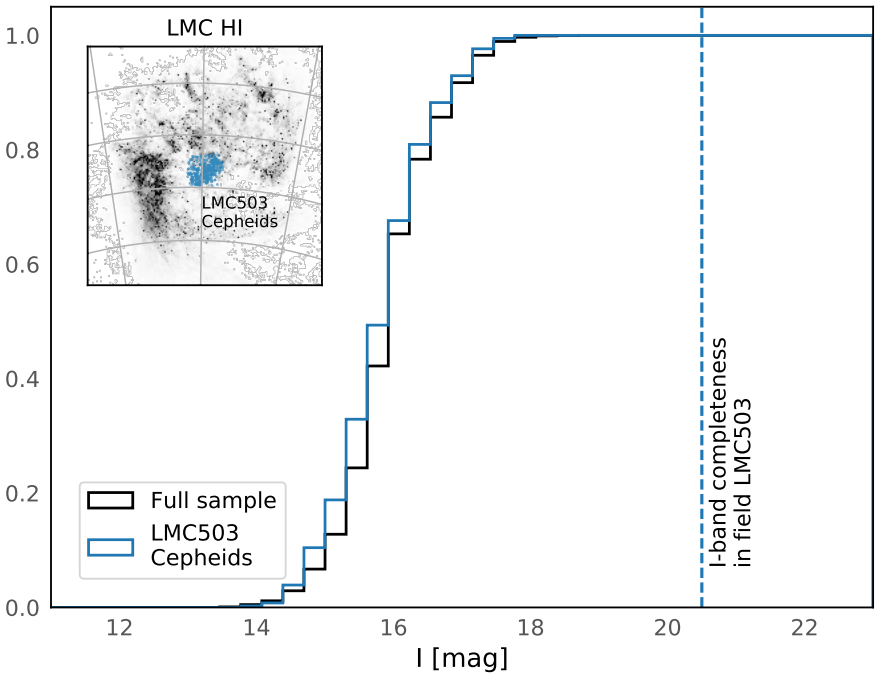

Figure 28: I-band luminosity function of the OGLE IV Classical Cepheids. The cumulative histograms show the fraction of RR Lyrae brighter than a certain I-band brightness. Luminosity function of the full Cepheid sample from Figure 27 is shown in black, and that of Cepheids in the 'LMC503' field, the most crowded and least photometrically complete region of the OGLEIV survey, is shown in blue. The inset shows the location of the LMC503 Cepheids superimposed on the HI map of the LMC. The I-band completeness limit of the LMC503 region is shown with the dashed line. This shows that the sample is quite complete, with the full OGLE IV Cepheids being brighter than the completeness limit of the most photometrically shallow region of the survey.

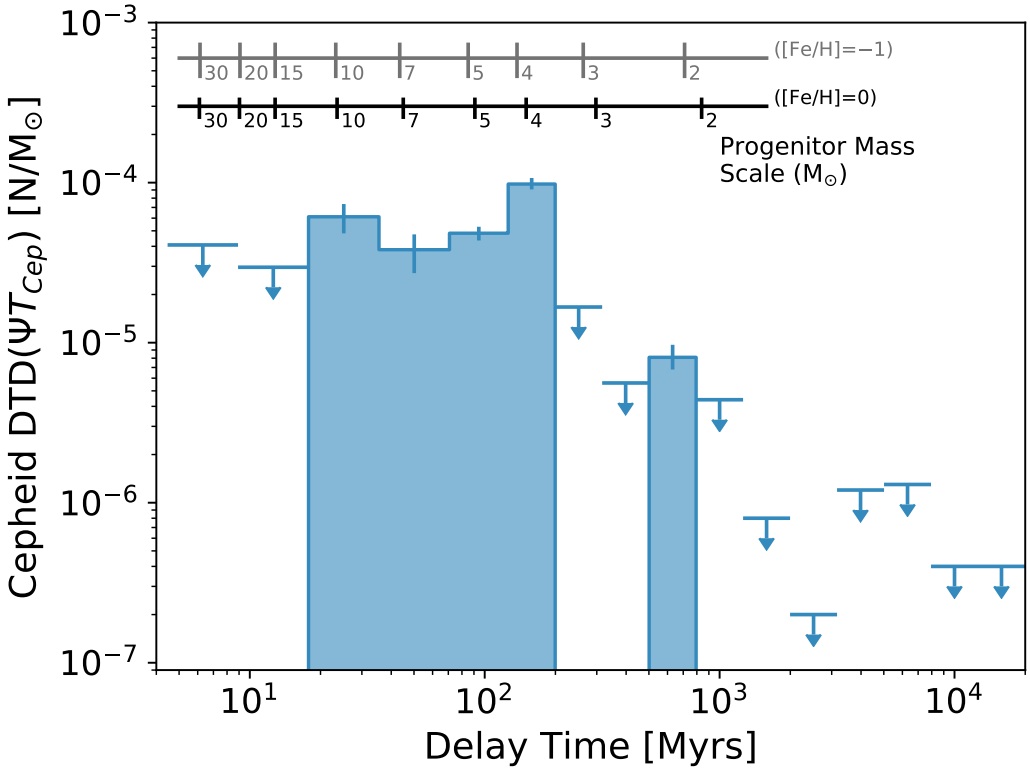

Figure 29: DTD for the OGLE IV sample of Cepheids. Similar to the RR Lyrae plot, the blue filled histogram represents detections at a significance $> 2\sigma$, while 2σ upper limits are shown with blue arrows. For reference, the progenitor mass scale corresponding to the delay-times for different metallicity values are shown on top (calculated with MIST).

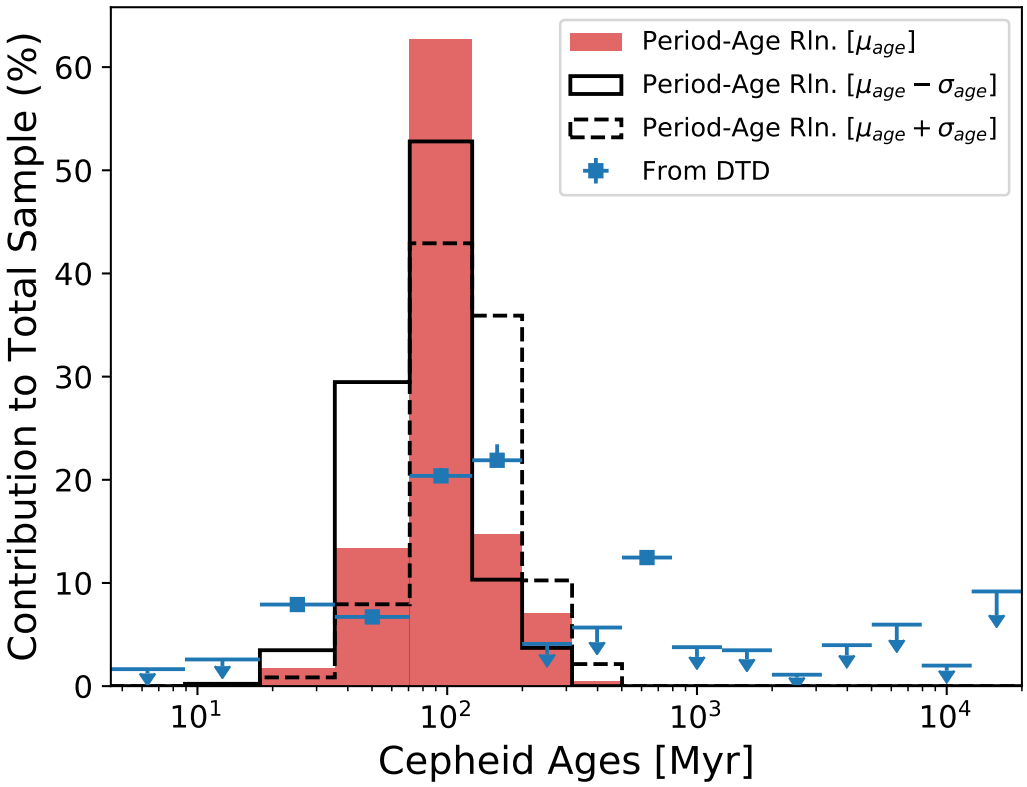

Figure 30: Comparison of the Cepheid DTD with the age distribution measured by the period-age relation of Bono et al. (2005). Not that these ages were already calculated and made publicly available by Jacyszyn-Dobrzeniecka et al. (2016). The solid and dashed histograms were created by shifting the best-fit model ages up or down by their 1σ uncertainties. The blue points are the fractional contribution of the Cepheid DTD to the full sample, as tabulated in Table 3.

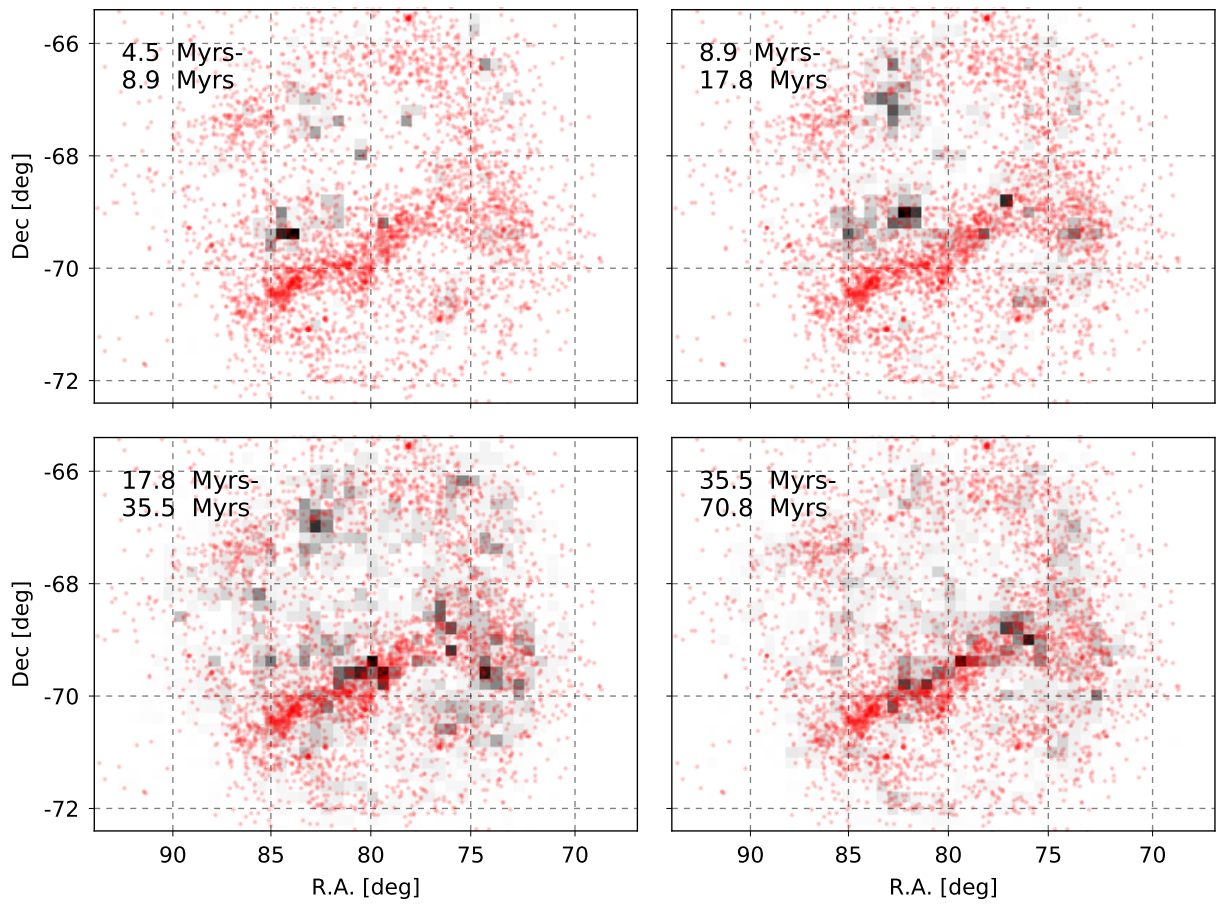

Figure 31: The OGLEIV Classical Cepheids (red) shown against the SAD map of (Harris & Zaritsky, 2009) (grey shaded pixels corresponding to cells in Figure 27). Darker the pixel, the more stellar mass formed in that pixel. These panels show the stellar mass formed between 4-70 Myrs.

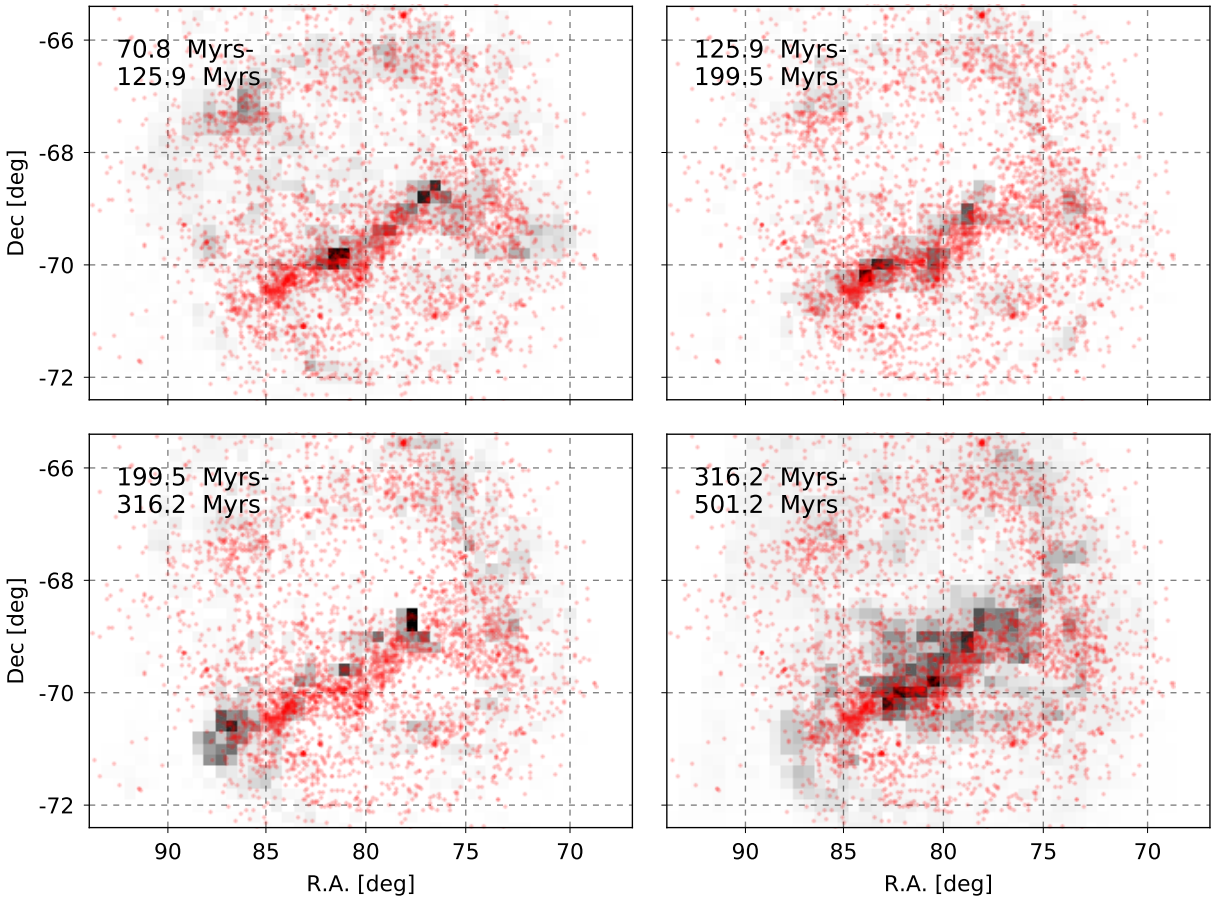

Figure 32: Same as Figure 31, but for 70-500 Myrs

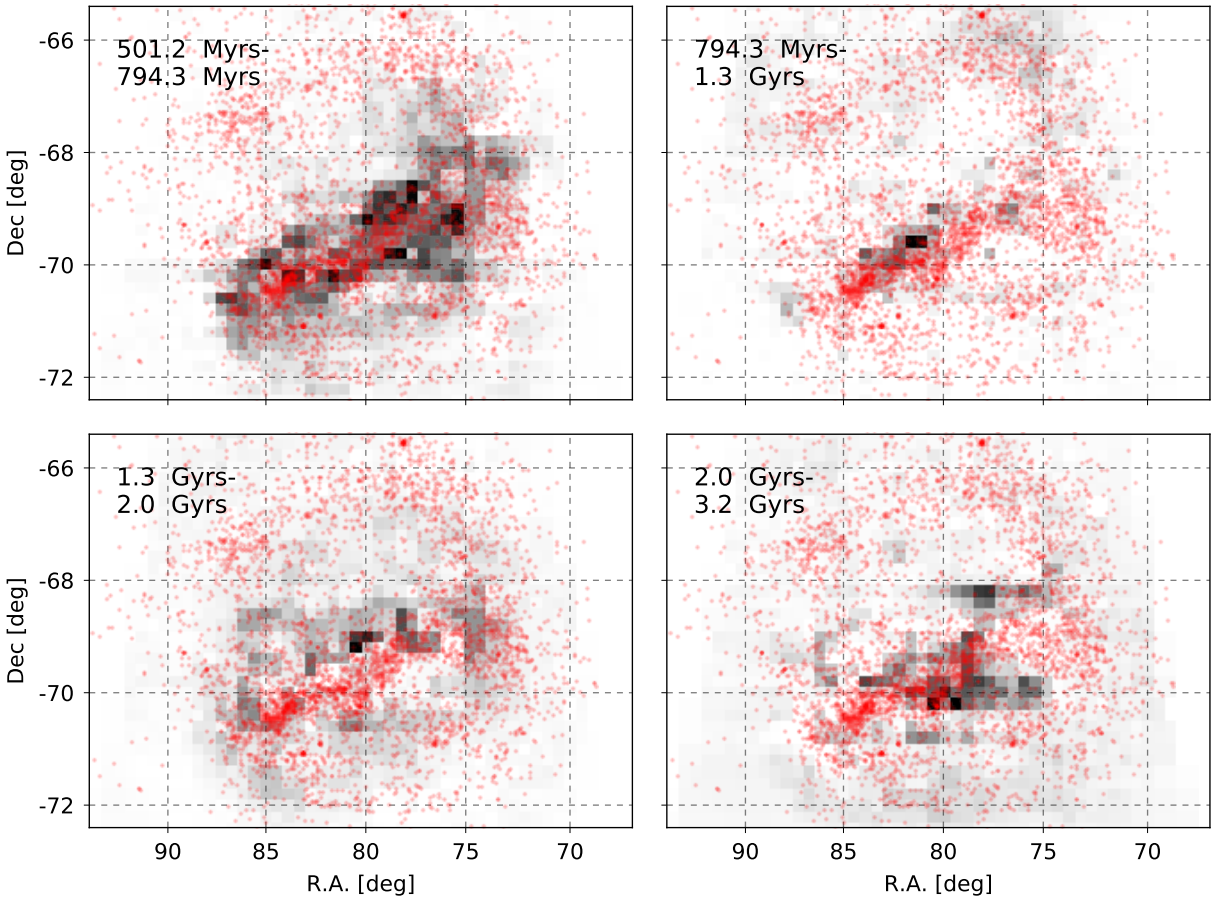

Figure 33: Same as Figure 31, but for 500 Myrs - 3 Gyrs

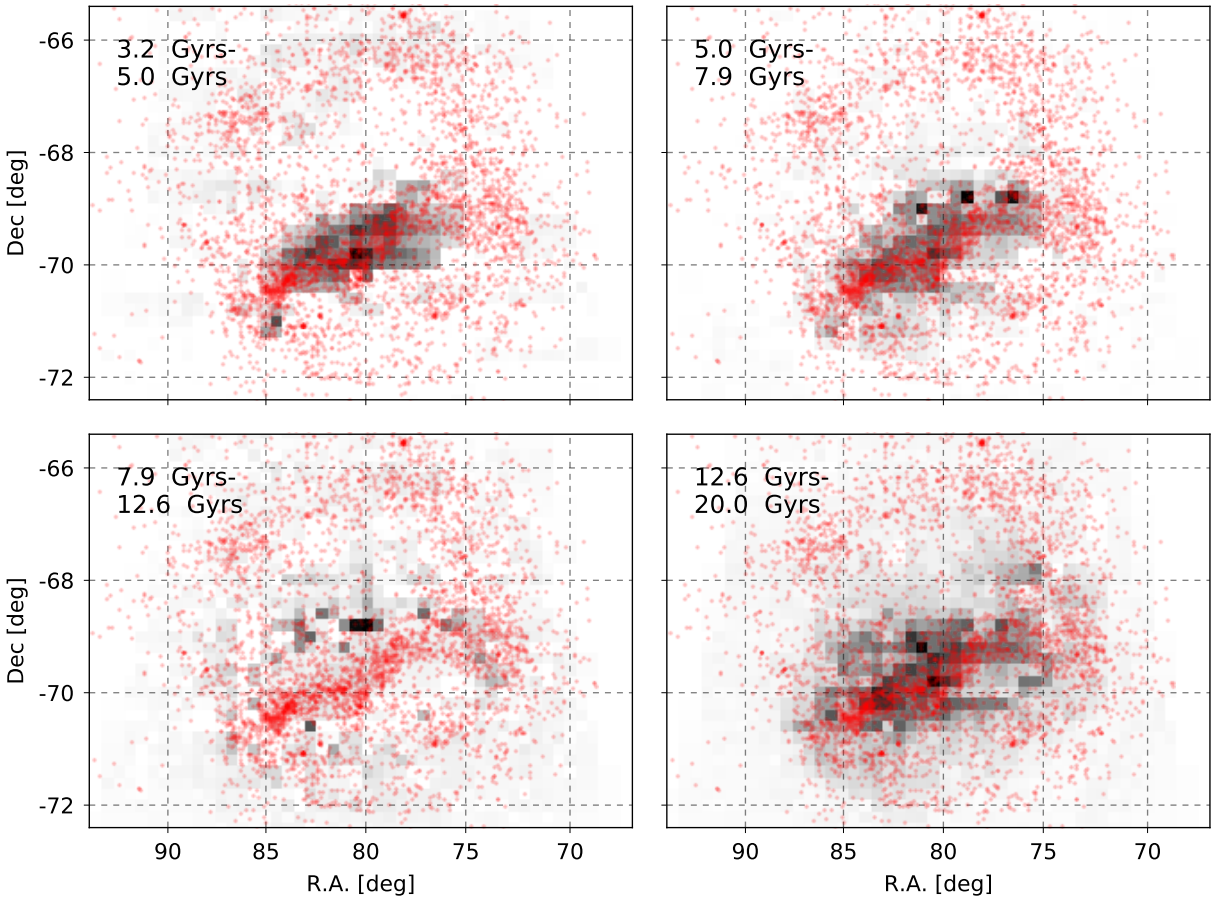

Figure 34: Same as Figure 31, but for 3-20 Gyrs

significant contribution contained in the upper limits derived). We checked the coincidence of the Cepheid sample with the Baumgardt et al. (2013) sample of clusters, and found that two clusters hosted a significant number of Cepheids: NGC 1866 with 56 Cepheids, and NGC 2031 with 19 clusters. The ages of these clusters are $\sim$ 132 and 136 Myrs respectively, which is also consistent with the delay-times measured by our DTD.

However, unlike the DTD, the period-based age distribution do not show any Cepheids at ages 500-800 Myr, corresponding to a mass range of 2.26-2.66 $M_{\odot}$. To verify the DTD signal in this age-range, we repeat the artificial DTD test that we had carried out with RR Lyrae. We test the DTD recovery on an artificial Cepheid map derived from a DTD that excludes any signal in the 500-800 Myr range. As shown in Figure 35, we do recover the original DTD signal, with a false-positive detection rate of only 0.07 in the 500-800 Myr bin. Visually, the difference in the Cepheid distribution for our recovered DTD and artificial DTD is much more subtle compared to the RR Lyrae case (Figure 36, but a close inspection shows that the recovered DTD produces a slightly higher number of Cepheids in the Outer Bar region (as seen from the slightly darker pixels). Based on the artificial DTD test, we believe that the 500-800 Myr signal is real. The underlying origin of the signal is pending further investigation. It is possible that the faint end of the Cepheid luminosity function is most responsible for the signal, based on the mass-luminosity relation. The faint end of the classical Cepheid luminosity function also coincides with the brighter Type II Cepheids, Anomalous Cepheids and RR Lyrae, so there is a possibility of contamination from these objects as well (See Figure 6 of Soszyński et al., 2015b). However, we find that 500-800 Myr goes away only for $I < 14.4$ mag, whereas most of the above objects have $I \geq 16$ mag. It is possible that the Bono et al. (2005) period-age relation, which was only calibrated with fundamental and first overtones, may not correctly apply to mixed-mode pulsators in our sample. However, even if we remove the mixed-mode pulsators and recalculate the DTD, the 500-800 Myr signal remains, although at a lower detection significance of 4σ. Further investigation of the faint end of the classical Cepheid distribution will be needed to establish the origin of this signal.

Comparing the spatial distribution of Cepheids with the SAD maps can provide some clues as to where these Cepheids formed (Figure 31-34). We see evidence that the Cepheids

in the detected DTD range are mainly associated with star formation in the LMC Blue Arm and the Inner Bar. This is also evident in the three-dimensional study of the Cepheid spatial/age distribution in the LMC in Jacyszyn-Dobrzeniecka et al. (2016). It is interesting to note that although there is star formation in the bar and the northern arm regions at longer lookback times (e.g. > 2 Gyrs) that are coincident with the Cepheid distribution, this does not show up in the Cepheid DTD as a statistically significant contribution. This shows the importance of using a DTD, as opposed to only relying on the age distribution of the background stellar population, to interpret the rates and progenitor channels of stellar objects.

3. Future Work

Interpreting the DTD of Cepheids is complicated. Firstly, about 35%-60% of Cepheids are in binaries (Evans et al., 2013; Neilson et al., 2015), just like their B-type main-sequence progenitors (Chini et al., 2012; Moe & Di Stefano, 2017), and therefore single stellar evolution models may not apply to the full sample. Secondly, the morphology of the Cepheid blue loop has a complex dependence on a number of parameters such as metallicity, mass-loss and core-overshooting (Cordier et al., 2003; Matthews et al., 2012; Neilson, 2014), which is also responsible for the mass-discrepancy problem of Cepheids.. A more sophisticated analysis with a population synthesis model that can predict rates and delay-times will help understand the physical underpinning of our DTD. However, we will include some basic analysis in this paper with MIST models, just like we did for RR Lyrae. Specifically, we will see how well the Cepheid DTD can be explained by variations in mass and metallicity. It is possible e.g. that our 2.3-2.6 $M_{\odot}$ signal could be coming from very metal-poor, low-mass stars that are undergoing a small blue loop intersecting the instability strip, as is believed to be the case for the OGLE sample of SMC Cepheids (Cordier et al., 2003; Bertelli et al., 2009). In addition, the MIST models can also help constrain the Cepheid crossing timescales of the instability strip, as in the case of RR Lyrae.

The wide range of parameter space spanned by the OGLE IV Cepheids will allow us to calculate DTDs for various subsamples. An important result we want to get is a period-

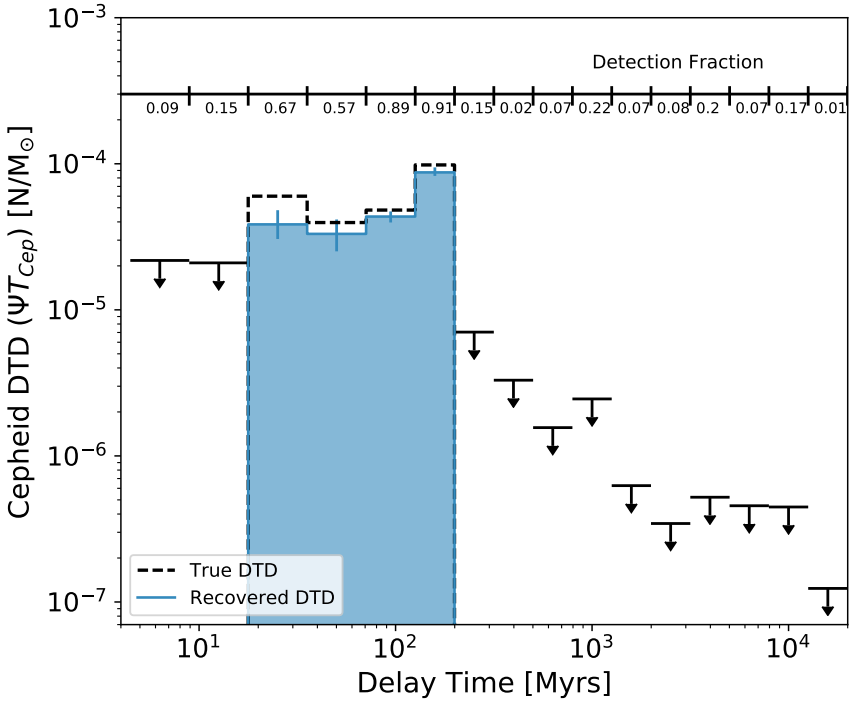

Figure 35: Same as Figure 22, but with the OGLEIV Cepheids

age relation by subdividing our sample into different ranges of pulsational periods, and finding the delay-times constrained by the DTD. This relatively model-independent period-age relation can be compared with existing period-age relations (e.g. Bono et al., 2005) derived from stellar evolution and pulsational models to identify effects of model assumptions, and possible biases in the calibrations of Cepheid period-luminosity relations that are used to measure Hubble constants. Additionally, DTDs for various pulsational types (fundamentals, first overtones, mixed-mode pulsators, Type II) will also be useful to constrain the stellar evolution channels for these objects.

D. CONCLUSION

We have calculated the delay time-distribution of RR Lyrae sample in the Magellanic Clouds from the OGLE IV survey (Soszyński et al., 2016a). Our DTD, shown in Figure 16(a) and

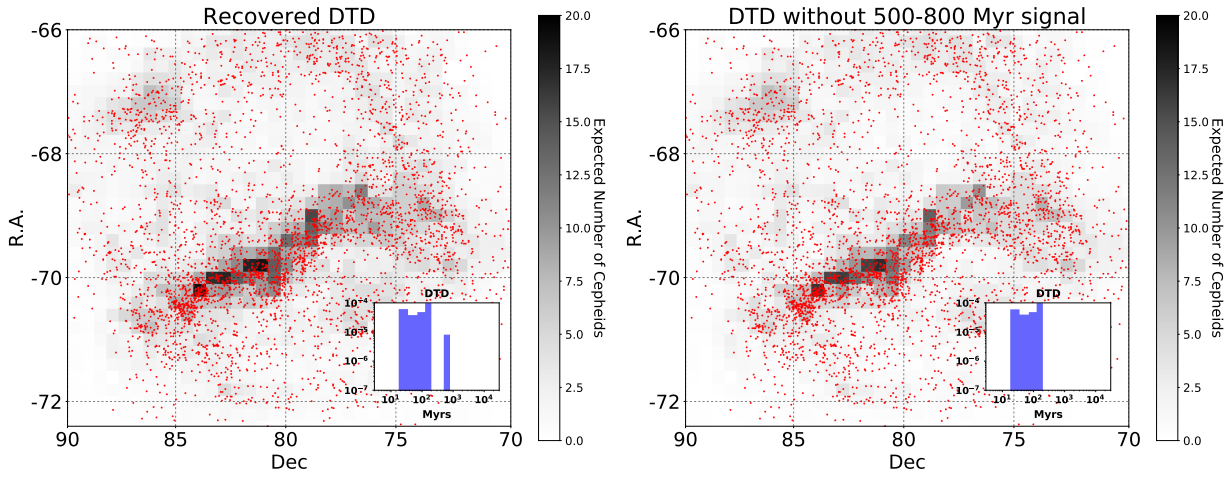

Figure 36: Similar visual DTD analysis with the inset DTDs as in Figure 23, but for the OGLEIV Cepheids.

Table 4 constrains the timescales on which RR Lyrae are produced by their parent stellar populations, as mapped by the SAD analysis in (Harris & Zaritsky, 2009). The OGLE IV sample overlapping with the SAD map of Harris & Zaritsky (2009) contains 29,810 objects, which allowed us to recover a DTD with the native age-resolution of the SAD map (16 bins from 4.5 Myrs to 20 Gyrs). We determine the DTD signal in each bin with an MCMC solver, and form the first time, use a randomization technique to propagate uncertainties in the SAD map into the final DTD.

The DTD for RR Lyrae is statistically significant for delay-times between 1.3 Gyr - 20 Gyrs. Although this is consistent with RR Lyrae originating from an older stellar population ($>$ 10 Gyrs), a significant fraction ($\sim$ 54%) is associated with ages of 1.3-10 Gyrs. This implies that stellar ages older than 10 Gyrs cannot be inferred from the presence of RR Lyrae alone. We also constrain the lifetimes of RR Lyrae to be between 0.7-3 Myrs, using the onset rate of He-burning calculated from the MIST stellar evolution tracks.

We compared our results with the predictions from the stellar evolution tracks of PAR-

SEC, which is the latest stellar evolution code with a set of pre-calculated horizontal branch tracks. We find that the DTD and derived lifetimes cannot be simultaneously explained using mass and metallicity alone. While the constrained delay-times require stars with initial masses $0.7 - 1.8$ $M_{\odot}$, these same stars are inconsistent with the measured lifetimes, since PARSEC models with masses larger than 0.9 $M_{\odot}$ never crossing the instability strip, even for the lowest metallicities. This may be an indication that an additional parameter (such as mass loss or helium enrichment) plays an important role in the evolution of RR Lyrae, a result echoed by studies of the second parameter problem for the horizontal branch (Catelan, 2009; Dotter, 2013). Our results can be used to guide future evolutionary models of low-mass stars relevant for old populations of red giants and horizontal branch stars, and also to better understand the formation and assembly of dwarf galaxies, globular clusters, and the halos and bulges of Local Group galaxies.

We also made preliminary DTD calculations of the OGLEIV Classical Cepheids in the LMC. Our DTD suggests that Cepheids are produced at a rate of 4-10 objects per 10^5 $M_{\odot}$ of stellar populations of ages 20-200 Myrs. This delay-time range is consistent with the age-distribution of Cepheids based on established period-age relations in the literature (Bono et al., 2005). We also measured a signal between the ages 500-800 Myr at almost 5σ, which however does not show up in the period-age based measurements. Statistically, this signal is not consistent with a false positive, although further investigation is needed to understand the physical origin of the signal. The Cepheid DTD is an ongoing project, where we will further compare our DTD measurements with predictions from MIST models, and derive a period-age relation from different sub-samples in the pulsational period space.

E. ACKNOWLEDGEMENTS:

We are grateful to Dennis Zaritsky, Knut Olsen, Thomas Matheson, and Benjamin Williams for insightful discussions and feedback on this work. The work in this chapter made use of the publicly available OGLE IV variable star catalog (http://ogledb.astrouw.edu.pl/ ogle/OCVS/). This research has made use of NASA's Astrophysics Data System, and the VizieR catalogue

access tool, CDS, Strasbourg, France. The original description of the VizieR service was published in A&AS 143, 23. This work made use of the IPython package (Pérez & Granger, 2007), SciPy (Jones et al., 2001–), NumPy (Van Der Walt et al., 2011), matplotlib, a Python library for publication quality graphics (Hunter, 2007), and Astropy, a community-developed core Python package for Astronomy (Astropy Collaboration et al., 2013)

Table 3: The Cepheid DTD calculations, with significance of detection and contribution to the OGLE IV Cepheid sample considered in this study.

Delay-Times (Myr)	**DTD** (ΨT_{Cep}) ($N/10^5$ $M_\odot$)	**Significance** ($N\sigma$)	**Contribution** (%)
4.5 - 8.9	< 4.08	–	< 1.64
8.9 - 17.8	< 2.95	–	< 2.58
17.8 - 35.5	$6.01^{+1.1}_{-1.42}$	4.56	$7.91^{+0.15}_{-0.14}$
35.5 - 70.8	$3.96^{+1.1}_{-0.93}$	4.00	$6.71^{+0.13}_{-0.13}$
70.8 - 125.9	$4.82^{+0.47}_{-0.48}$	9.65	$20.38^{+0.77}_{-0.28}$
125.9 - 199.5	$9.82^{+0.87}_{-0.75}$	12.94	$21.89^{+1.55}_{-0.45}$
199.5 - 316.2	< 1.67	–	< 4.09
316.2 - 501.2	< 0.56	–	< 5.68
501.2 - 794.3	$0.78^{+0.13}_{-0.16}$	4.97	$12.46^{+0.27}_{-0.15}$
794.3 - 1300	< 0.44	–	< 3.78
1300 - 2000	< 0.08	–	< 3.48
2000 - 3200	< 0.02	–	< 1.11
3200 - 5000	< 0.12	–	< 3.97
5000 - 7900	< 0.13	–	< 5.96
7900 - 12600	< 0.04	–	< 1.99
12600 - 20000	< 0.04	–	< 9.18

IV. PROGENITORS OF YOUNG THERMONUCLEAR SUPERNOVAE USING RADIO OBSERVATIONS

This chapter has been submitted for publication to The Astrophysical Journal and pending review as Sarbadhicary et al. (2017b), titled *"The two most recent thermonuclear SNe in the Local Group: radio constraints on their progenitors and evolution"*. Collaborators: Laura Chomiuk (Michigan State University), Carles Badenes (University of Pittsburgh), Evangelia Tremou (Michigan State University), Lorant Sjouwerman (National Radio Astronomy Observatory) and Alicia Soderberg (Harvard University).

A. INTRODUCTION

Young, ejecta-dominated SNRs (SNRs) provide a unique way to constrain the progenitors and evolution of SNe. The forward shock can probe the circum-stellar medium around these SNRs on pc-scales, corresponding to the pre-SN mass-loss history on timescales of $10^3 - 10^5$ years, which provides an independent way of discriminating progenitor scenarios (Badenes et al., 2006, 2007; Yamaguchi et al., 2014; Patnaude et al., 2015; Patnaude & Badenes, 2017). Additionally, these objects can trace how late-stage SNe, i.e. older than a few years, transition to the SNR (SNR) phase (Milisavljevic & Fesen, 2017). Radio emission from late-stage SNe usually declines (Stockdale et al., 2001; Eck et al., 2002; Weiler et al., 2002; Stockdale et al., 2006), but young SNRs usually brighten as the forward shock encounters the bulk interstellar medium (ISM) (Berezhko & Völk, 2004a; Green et al., 2008). However,

this transition phase is very short compared to the lifetime of an SNR (Sarbadhicary et al., 2017a), and therefore relatively unconstrained by observations. The oldest radio-detected SN is SN 1923A (Eck et al., 1998) at an age of 80 years, while the youngest SNR (before the discovery of G1.9+0.3) was Cassiopeia A at 325 years, located in our Galaxy (Fesen et al., 2006). Fortunately, there are two objects in the Local Group that fill this gap, both with thermonuclear origins: SN 1885A in M31 and SNR G1.9+0.3 in our Galaxy.

SN 1885A, or S And, is a unique Local Group SN that exploded in 1885, about 65 pc from the center of M31. It was the first and one of the brightest recorded extragalactic SN, with $M_V = -19.2$ (de Vaucouleurs & Corwin, 1985). The expanding ejecta of SN 1885A was first imaged in optical *absorption* in the Fe I resonance band against the backdrop of the M31 bulge (Fesen et al., 1989). Observations of its historical V-band light curve, color evolution and reconstructed spectrum pointed to a thermonuclear origin (de Vaucouleurs & Corwin, 1985). Subsequent observations by the *HST Space Telescope* (Fesen et al., 1999; Hamilton & Fesen, 2000; Fesen et al., 2007, 2015, 2016) revealed stratified Ca and Fe layers, indicative of a Type Ia origin. The unusually fast light curve of SN 1885A, with a rise-time of 6 days and $\Delta m_{15}(B) \sim 2.2$ (de Vaucouleurs & Corwin, 1985; Perets et al., 2011), makes it part of an emerging class of fast-transients that are being discovered by high-cadence surveys (See e.g. Kasliwal, 2012; Kasliwal et al., 2012; Foley et al., 2013; Drout et al., 2013, 2014; Taubenberger, 2017). These transients extend the explosive endpoints of stellar evolution beyond the classic core-collapse and thermonuclear SNe. In this regard, SN 1885A provides a unique perspective to studying transients because we not only have observations of the historical light curve and spectra, but also of the freely expanding ejecta. However, even a century after the explosion, the ejecta of SN 1885A has not shown any detectable emission in optical (Fesen et al., 1989), X-ray (Williams et al., 2006; Li et al., 2009) or radio (Crane et al., 1992, , this work).

Here we present the deepest radio image at the site of SN 1885A by co-adding archival observations from the Karl G. Jansky Very Large Array (VLA), yielding an upper limit on the radio flux that is almost a factor of 3 deeper than Crane et al. (1992). We use this upper limit to constrain the radio light curve model from Sarbadhicary et al. (2017a) model, exploring the parameter space of ambient density, and progenitor kinetic energy

and ejecta mass for SN 1885A. We also apply this model to SNR G1.9+0.3, extending the constraints on its progenitor mass and kinetic energy from previous studies (Reynolds et al., 2008; Ksenofontov et al., 2010; Carlton et al., 2011; De Horta et al., 2014; Yang et al., 2016; Chakraborti et al., 2016; Pavlović, 2017).

The paper is organized as follows - Section IV.B details the VLA observations and data reduction for the inner arc-minute of M31, Section IV.C describes the final, co-added 6.2 GHz image, with particular focus at the site of SN 1885A, Section IV.D summarizes the radio light curve model of Sarbadhicary et al. (2017a) and how it is applied to the observations from the previous sections, Section IV.E shows the results of our parameter space studies and Section IV.F discusses these results in the context of progenitor scenarios and further evolution of SN 1885A and G1.9+0.3.

B. RADIO OBSERVATIONS OF THE M31 CORE

We co-added 18 archival data sets obtained with the VLA in 2011 and 2012 (listed in Table 4) to produce a deep high-resolution image at 6.2 GHz. These data were observed by programs 11A-178 (PI Z. Li), SD487 (PI M. Garcia), 11A-137 (PI L. Sjouwerman), and 12B-002 (PI L. Sjouwerman), and were obtained to monitor M31's supermassive black hole, M31* and the associated central region (e.g., Garcia et al., 2010; Yang et al., 2017). Observations were obtained in the A, B, and BnA configurations of the VLA. This provided 0.3″ and 1″ FWHM resolution at 6 GHz in the A and B configurations respectively, and resolved out most of the diffuse emission from M31. All data were obtained in full Stokes mode, and because they were obtained over a period of Jansky VLA commissioning, bandwidths varied between 256–4096 MHz, and the central frequency also varied. For all wide-band data ($\geq$2048 MHz bandwidth), there were 14 spectral windows with frequency settings in common centered at 6.8 GHz; these are the windows used for imaging and they yield a total bandwidth of 1792 MHz. For the narrower band data (256 MHz of bandwidth), we used both spectral windows, which were centered at 4.9 GHz. Note that the 12B-002 epochs also included wide-band data centered at 4.9 GHz, and these data were ultimately averaged (in the image plane) with the

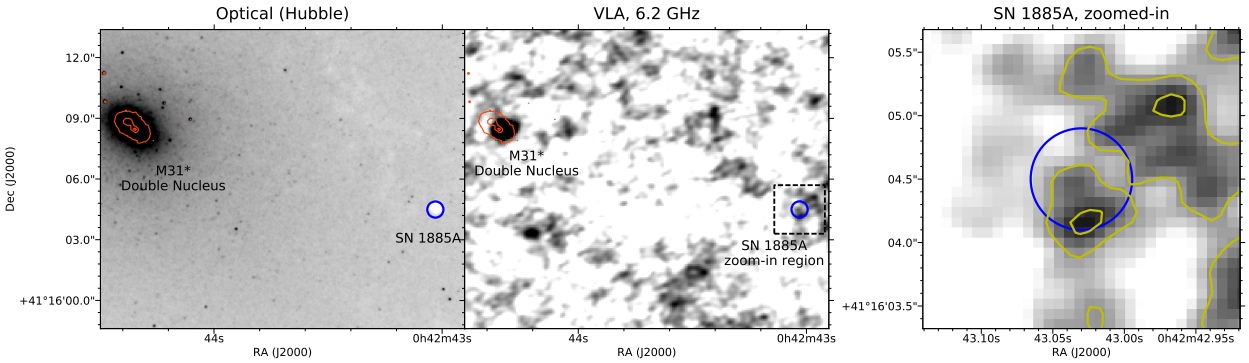

Figure 37: Three-panel image of the vicinity of SN 1885A. *Left*: HST FR388N image showing the Ca-II absorption (blue) in the SN 1885A remnant (Fesen et al., 2007). The red contours towards the top-left of the frame highlight the optical double-nucleus of M31, as imaged with *HST*. The blue circle to the right outlines the Ca-II remnant of SN 1885A and has a radius of 0.4″. *Center*: VLA 6.2 GHz radio continuum image, with the optical contours (red) and the SN 1885A absorption profile overlaid as a blue circle. The dashed-square shows the region around SN 1885A zoomed-in in the next panel. *Right*: Same VLA image, but zoomed in to emphasize the diffuse emission regions. The extent of the panel is the same as the dashed-square region from the central panel. The blue circle is also the same from the central panel, denoting the 0.4″ radius absorption profile of SN 1885A. The yellow contours trace the 6.2 GHz emission, with their lowest level at 1.82 μJy beam^{-1} (1.4 σ), and then at 3.64 μJy beam^{-1}.

Table 4: Details of the archival VLA datasets for the central arc-minute of M31.

UT Date	Project Code	Configuration	Time On Source (hr)	Frequency (GHz)	Bandwidth (MHz)
2011 May 19	11A-178	BnA	1.7	4.9	256
2011 May 28	11A-178	BnA	1.9	4.9	256
2011 Jun 5	11A-178	BnA→A	1.9	4.9	256
2011 Jul 1	11A-178	A	1.9	4.9	256
2011 Jul 27	11A-178	A	1.9	4.9	256
2011 Aug 27	11A-178	A	1.9	4.9	256
2011 Sep 2	SD487	A	5.2	4.9	256
2011 Sep 4	11A-137	A	0.7	6.8	2048
2011 Sep 6	11A-137	A	0.7	6.8	2048
2011 Sep 7	SD487	A	5.2	4.9	256
2012 Jun 1	SD487	B	0.6	6.8	2048
2012 Jun 6	SD487	B	0.6	6.8	2048
2012 Jun 12	SD487	B	0.6	6.8	2048
2012 Jul 1	SD487	B	0.6	6.8	2048
2012 Aug 14	SD487	B	0.6	6.8	2048
2012 Oct 29	SD487	A	0.6	6.8	2048
2012 Dec 22	12B-002	A	1.3	4.9/6.8	4096
2012 Dec 30	12B-002	A	0.6	6.8	4096

narrower band data.

Data were calibrated using the complex gain calibrator J0038+4137 and the flux calibrator 3C48, using standard routines in AIPS [1]. Editing for bad antennae and radio frequency interference was carried out in AIPS using `spflg` and `tvflg`. We concatenated all wide-band data together and all narrower-band data together using the task `dbcon` within AIPS. Imaging of each of the two concatenated data sets was performed using `imagr` with natural weighting (Briggs Robust value of 5, Briggs, 1995) and a minimum baseline length of 5 kilo-wavelengths. The lower frequency data (mostly narrower in bandwidth) yielded an image at 4.9 GHz with an RMS sensitivity of 2.1 μJy beam^{-1} and a FWHM resolution of $0.67'' \times 0.48''$. The wide band data produced an image at 6.8 GHz with an RMS sensitivity of 1.6 μJy beam^{-1} and a FWHM resolution of $0.64'' \times 0.60''$. To produce the deepest image possible, we smoothed both images to have a resolution of $0.68'' \times 0.61''$ (synthesized beam position angle -80°). We then co-added the narrow and wide band images, weighting by 1/(image noise)^2, yielding an image centered at 6.2 GHz with an RMS noise of 1.3 μJy beam^{-1}. As SN 1885A is offset from the image center (and the center of M31) by just $15.2''$, a negligible fraction of the $3.3'$ radius primary beam, we do not apply a primary beam correction since it would be $< 5\%$.

C. SN 1885A IN THE RADIO

To compare our radio images with archival narrow-band *HST Space Telescope* images of SN 1885A, where the SN is seen in Ca-II H and K absorption (Fesen et al. 2007; also see the left panel of Figure 37), we must first register the images to a common world coordinate system (WCS). The radio image is accurately placed on the J2000 system, as the phase calibrator has a positional accuracy $<0.002''$; therefore, uncertainties in the optical WCS dominate.

The Local Group Galaxies Survey (LGGS; Massey et al., 2006) has imaged M31 in multiple optical filters and provides a WCS based on the USNO-B1.0 catalog, which has an RMS astrometric accuracy of ∼0.2 arcsec (Monet et al., 2003). To place this on the Inter-

[1] http://www.aips.nrao.edu/index.shtml

national Celestial Reference System, we shifted the LGGS WCS by a small amount (Δ RA = -0.003s, Δ Dec = -0.13″) to come into optimal alignment with the UCAC2 and UCAC3 catalogs. The final astrometric accuracy of the LGGS image is 0.1″ RMS (P. Massey, private communication), which is sufficiently accurate for this work.

The monochromatic field of view of the FR388N ramp filter on *HST*/ACS is limited, and there are very few stars in common between the Ca-II image and the LGGS images. For this reason, we use an intermediary broad-band *HST* image—an ACS F435W image observed in 2004 (HST program 10006; PI Garcia)—to provide a wider field of view and a solid comparison with the U-band LGGS Field 5 image. Using *koords* of the KARMA software package (Gooch, 1996), we register the images (allowing for both x/y shifts and rotation) based on six stars in common and find an RMS of 0.02″. Next, we register the narrow-band Ca-II image to the newly-registered F435W image using a similar procedure; seven stars in common imply an RMS of 0.0025″. Propagating through, the accuracy of the final WCS on the Ca-II image is 0.1 arcsec. The absorption-line remnant of SN 1885A is shown in the left panel in Figure 37. It is centered at RA= $00^{\rm h}42^{\rm m}43.03^{\rm s}$, Dec = $+41°16'04.5''$. As measured from its Ca-II absorption, the remnant has a radius of 0.40″ (1.5 pc at an assumed distance of 785 kpc), implying a time-averaged expansion velocity of $12,400 \pm 1,400$ km s^{-1} (Fesen et al., 2007). The absorption profile would be just slightly resolved in our 6.2 GHz image. The central and right panels of Figure 37 show our radio maps at the position of SN 1885A, with a blue circle showing the position of the Ca-II absorption. Note that there is substantial sensitivity in our radio images on angular scales larger than the synthesized beam ($\sim$0.64″ diameter), as we co-added A and B configuration data together.

Our naturally weighted image shows diffuse clumps of radio continuum emission pervading the inner regions of M31. This diffuse emission is present at a low level at the location of SN 1885A (peak flux 4.1 μJy, or 2.6σ significance), but the emission appears to be part of the background diffuse emission, and may not be distinct to the SNR. In other words, there are many other similar patches of emission present in M31's central region which are not coincident with a SNR, so there is no evidence that the low-level excess flux is attributable to SN 1885A.

To further investigate, we also imaged M31's central region using a Briggs Robust value

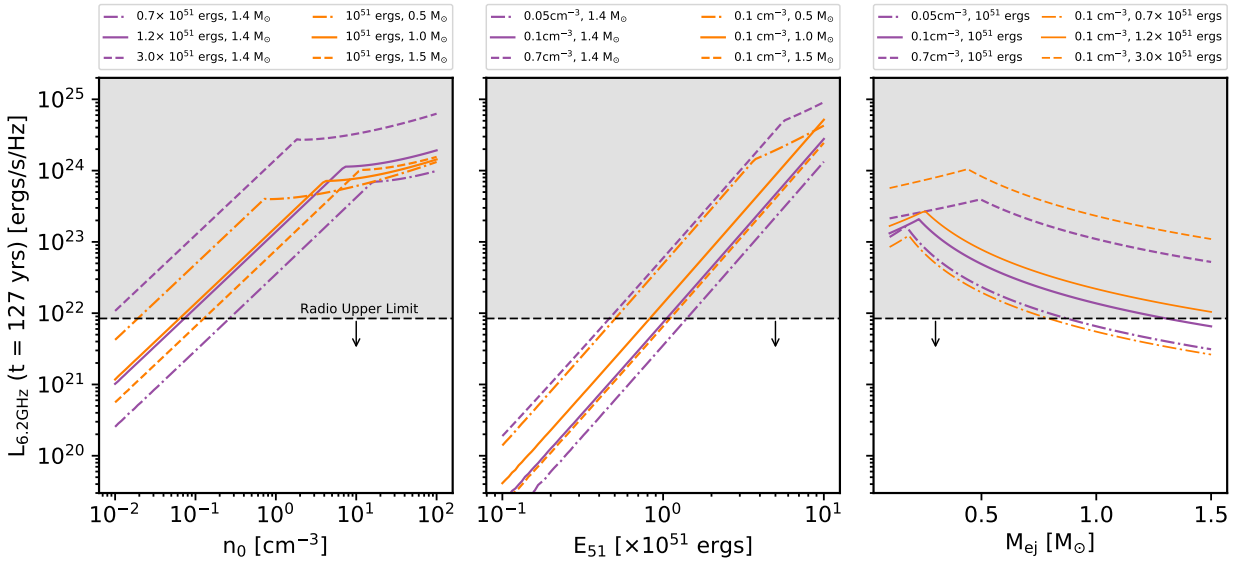

Figure 38: The 6.2 GHz radio luminosity at the age of SN 1885A (127 years) predicted by the radio light curve model (Section IV.D) as a function of the ISM density (left), kinetic energy (middle) and ejecta mass (right). The change in the slope at higher densities (left panel), higher energies (middle panel) and lower ejecta masses (right panel) is because of the onset of the Sedov-Taylor phase by this age. Each panel also shows light curves for different values of the other two parameters. The grey region is excluded by the radio upper limit (dashed) from VLA observations in Section IV.C.

of 0, which down-weights the shorter baselines and diffuse emission. This image has an RMS sensitivity of 1.9 μJy beam^{-1} and a FWHM resolution of $0.34'' \times 0.30''$. A 2.8 σ peak in flux density is still visible coincident with the southwestern rim of SN 1885A (peak of 5.4 μJy). Again, it is not clear if this flux is associated with SN 1885A or diffuse emission pervading the central regions of M31. We take this potential emission into account in calculating our upper limit on the flux of SN 1885A, adding the summed flux over a region to the 3σ uncertainty borne of image noise. Assuming that the dimensions of SN 1885A match those of the Ca-II absorption, we find a 3σ upper limit, $<$6.8 μJy. If we instead allow for the possibility that the radio emission could be located at larger radius that the Ca-II absorption (coincident with the fastest moving material), and measure the radio upper limit in a region $0.60''$ in radius (1.5 times the Ca-II SNR radius), we find a 3σ upper limit, $<$11.4 μJy. We take this conservative upper limit in our analysis throughout the rest of this paper.

As a side note, we also investigated the possible radio detection of SN 1885A mentioned by Sjouwerman & Dickel (2001), offset by 1.3 arcsec from the center of the Ca-II remnant in our wcs-corrected image described above (claimed J2000 position of RA = $00^{\rm h}42^{\rm m}43.136^{\rm s}$, Dec=$41°16'05.06''$. Sjouwerman & Dickel (2001) find that this putative source has a flux, 27 ± 10 μJy at 8.4 GHz, and is slightly extended in their images. The source however is detected only at 2.7σ significance, and we do not see any notable 6.2 GHz flux at this location in our deeper image. We therefore believe this tentative detection of SN 1885A is erroneous.

D. RADIO LIGHT CURVE MODELING

1. Summary of model

We will use the SNR radio light curve model described in Sarbadhicary et al. (2017a) to constrain the ambient density (n_0, in units of cm^{-3}), kinetic energy (E_k), and ejecta mass (M_{ej}, in units of M$_\odot$) of SN 1885A and G1.9+0.3. While we refer the reader to the paper for details of the radio light curve physics (see Appendix A in Sarbadhicary et al., 2017a), we will

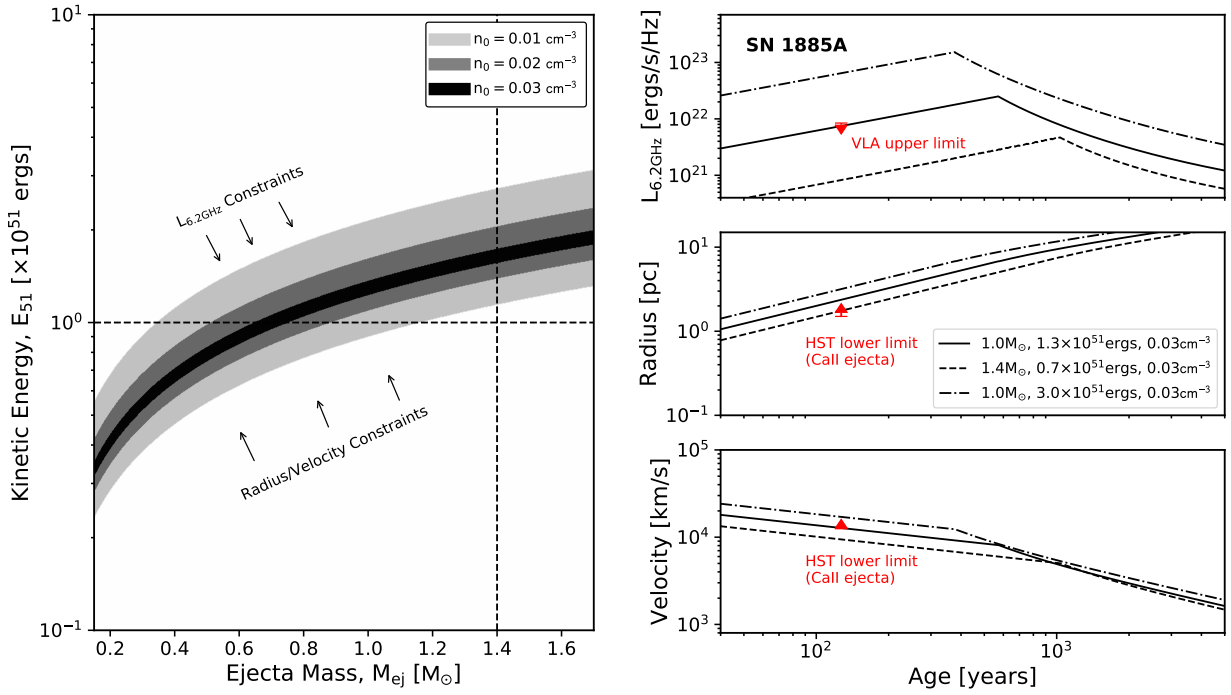

(a) (b)

Figure 39: *a)* Constraints on M_{ej}, E_{51} and n_0 for SN 1885A from our upper limit on the radio flux from VLA, and the lower limits on shock radius and velocity from the outermost Ca-II ejecta from HST images. The direction from which each observational limit constrains the parameter space is shown by arrows. Each shaded band corresponds to a particular n_0, and shows all possible values of E_{51} and M_{ej} that simultaneously satisfy the three observational limits. The bands get narrower for higher n_0 because of the opposing constraints from luminosity and radius/velocity, as shown with arrows. The crosshairs mark the fiducial explosion parameters for SNe Ia: $M_{ej} = 1.4\ M_\odot$ and $E_{51} = 1$. *b)* Light curves, radii and velocity curves of SN 1885A for different values n_0, E_{51} and M_{ej}. The solid line was chosen from darkest band in a) and is consistent with all three observational limits. The dashed and dash-dotted lines were chosen from outside the shaded parameter bands in a), and are not consistent with all the observational limits.

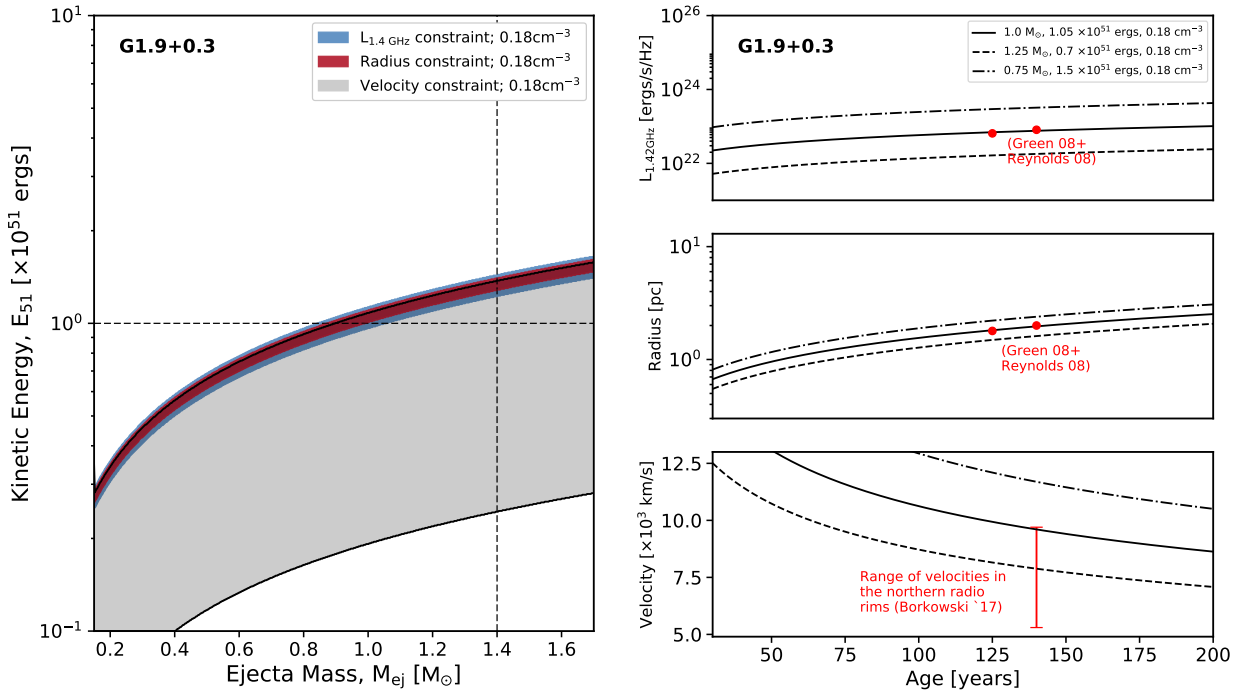

(a) (b)

Figure 40: t

Constraints on M_{ej}, E_{51} and n_0 for G1.9+0.3 from archival VLA data. a) The blue and red band corresponds to values of M_{ej} and E_{51}, for a given n_0, for which the model radio luminosities and radii, respectively, agree with observations in 1993 and 2008, as recorded in Green et al. (2008). The grey band shows all parameter values for which the model shock velocities lie within the observed range in the northern radio rim. b) Light curves, radii and velocity curves for G1.9+0.3 produced for different values n_0, E_{51}, M_{ej}. The solid curves, which satisfy all three constraints, correspond to n_0, E_{51} and M_{ej} taken from common overlapping region of radio luminosity, radius and velocity parameter space in a), while the dashed and dash-dotted lines are taken from non-overlapping regions, and therefore do not satisfy all the observations.

briefly describe its basic features here. The radio emission is assumed to be optically-thin synchrotron emission which, according to diffusive shock acceleration theory, is produced by non-thermal electrons accelerated by the forward shock (Axford et al., 1977; Krymskii, 1977; Bell, 1978; Blandford & Ostriker, 1978) as it interacts with the circum-stellar medium (Chevalier, 1982, 1998; Berezhko & Völk, 2004b). The forward shock radius (R_s) and velocity (v_s) is calculated from Truelove & McKee (1999),

$$R_s = (1.29\text{pc})\, t_{100}^{0.7} n_0^{-0.1} E_{51}^{0.35} M_{ej}^{-0.25}, \tag{IV.1a}$$

$$v_s = \left(8797\text{km s}^{-1}\right) t_{100}^{-0.3} n_0^{-0.1} E_{51}^{0.35} M_{ej}^{-0.25}, \tag{IV.1b}$$

assuming a power-law ejecta, $n = 10$. This is generally assumed for compact progenitors like WDs with a polytropic index of 3/2 (Matzner & McKee, 1999; Chomiuk et al., 2012, 2016). We note however that our results at the age of SN1885A are relatively insensitive to the value n. Here t_{100} is the SNR age in units of 100 years, and $E_{51} = E_k/10^{51}$ ergs. The ejecta dominated solution is valid until $t \lesssim (203.5\text{ yrs})\, E_{51}^{-1/2} M_{ej}^{5/6} n_0^{-1/3}$, at which point the SNR transitions to the Sedov-Taylor phase.

The synchrotron luminosity L_ν is a function of the synchrotron-emitting volume, the strength of the magnetic field and the population of accelerated electrons, all of which depend on R_s and v_s. A large magnetic field strength (few 100 μG, almost 2 orders of magnitude above the ambient field) is required for efficient acceleration of particles in SNR shocks (Völk et al., 2005; Warren et al., 2005; Morlino et al., 2010), which, in turn, helps produce more synchrotron emission per accelerated electron. In our model, the energy density in this amplified, upstream field is a fraction ϵ_b^u of the shock energy density ($\propto n_0 v_s^2$). Motivated by semi-analytic studies (Bell, 1978, 2004; Amato & Blasi, 2009) and recent first-principle kinetic simulations (Caprioli & Spitkovsky, 2014a,b), we assume $\epsilon_b^u = 1/2\,(v_s/c + 1/M_A)$, where M_A is the Alfvén Mach Number. The first and second teRMS are contributions from non-resonant and resonant instabilities induced in the upstream magnetic field by the streaming particles. The energy density in the accelerated electrons is similarly assumed to be a fraction ϵ_e of the shock energy density, and characterized by a power-law spectra with index, p. However, ϵ_e is an uncertain parameter in our model because of the incomplete understanding of electron injection in non-relativistic shocks (Park et al., 2015; Spitkovsky,

2016). Typically, $\epsilon_e \sim 10^{-4}$ in young SNRs based on their multi-wavelength spectra (Morlino & Caprioli, 2012) while $\epsilon_e \gtrsim 10^{-3}$ for a population of SNRs, where older, Sedov SNRs will dominate (Sarbadhicary et al., 2017a). Meanwhile, the spectral index is usually $p = 2.2-2.5$ for young SNRs (Caprioli, 2012). For both SN 1885A and G1.9+0.3, we assume $\epsilon_e = 10^{-4}$ and $p = 2.2$, and then discuss the effects of changing these parameters in Section IV.E.

In Figure IV.C, we show how the radio luminosity predicted by the Sarbadhicary et al. (2017a) model at the age of SN 1885A (127 years) behaves for different values of n_0, E_{51} and M_{ej}. The luminosity increases with increasing density and kinetic energy, but decreases with increasing ejecta mass. This is because when the SNR shock interacts with denser material, or has higher kinetic energy, it leads to higher energy densities in the amplified magnetic field and relativistic electrons, both of which are proportional to ρv_s^2. This leads to increasing synchrotron luminosity. For higher ejecta masses however, v_s is smaller because of smaller energy per unit ejecta mass available in the outermost moving ejecta. The energy in the magnetic fields and electrons is therefore smaller, leading to smaller radio luminosities. The upper limit in Figure IV.C already indicates that low density will be necessary to explain SN 1885A, but a more systematic analysis of the parameter space is discussed in the next sections.

2. Application to SN 1885A

The model described above allows us to explore in detail the full parameter space of n_0, E_{51} and M_{ej} relevant to SN 1885A. Specifically, we look for values of n_0, E_{51} and M_{ej} that simultaneously satisfy the following observational limits at an age of 127 years.

I. *Radio luminosity*: $L_\nu \leq 8.43 \times 10^{21}$ ergs s^{-1} Hz^{-1} at 6.2 GHz, which is the 3σ upper limit of 11.4 μJy derived in Section IV.C, taking into account the patch of diffuse emission coincident with the SN. We assume a distance = 785 $\pm$ 25 kpc to M31 (McConnachie et al., 2005).

II. *Radius*: $R_s \geq 1.52$ pc, which is the extent of outermost CaII emission in the Fesen et al. (2015) image. Since the forward shock wave cannot be behind the ejecta, we treat this as the lower limit to R_s.

III. *Velocity*: $v_s \geq 12500$ km s^{-1}, which is the outer velocity component of the CaII absorption profile (Fesen et al., 2015), and is treated as a lower limit to v_s for the same reason as above.

3. Application to SNR G1.9+0.3

The detectable emission in radio from G1.9+0.3 over the last 2 decades can provide stronger constraints on the parameter space of n_0, E_{51} and M_{ej} than SN 1885A (see Green et al., 2008; De Horta et al., 2014, and references therein). The objective is to find all values of n_0, E_{51} and M_{ej} for which the model predicts luminosities, radii and velocities that satisfy all the following observations within the uncertainties of each measurement.

I. *Radio luminosity*: A 1.4 GHz integrated flux of 0.74 ± 0.038 Jy in 1993 (Condon et al., 1998) and 0.935 ± 0.047 Jy in 2008 (Green et al., 2008) was measured for G1.9+0.3. At a distance of 8.5 kpc (Reynolds et al., 2008), these fluxes correspond to luminosities of $(6.4 \pm 0.3) \times 10^{22}$ ergs s^{-1} Hz^{-1} and $(8.1 \pm 0.4) \times 10^{22}$ ergs s^{-1} Hz^{-1} respectively.

II. *Radius*: The mean radius of G1.9+0.3 in 2008 was 2 pc, based on the X-ray profile of Reynolds et al. (2008), and therefore 1.79 pc at the time of the Condon et al. (1998) measurement, if we assume a constant expansion rate of 0.65 % per year (Green et al., 2008).

III. *Velocity*: A shock velocity range of 5300 km s^{-1} - 9700 km s^{-1} is measured in the bright northern radio rim of G1.9+0.3, reflecting the significant asymmetry in the expansion, where 5300 km s^{-1} is the median velocity in the N-NE region, and 9700 km s^{-1} is the median velocity in the NW region (Borkowski et al., 2017). Because of this wide range of observed velocities, we first constrain the parameter space allowed by the range of velocities, then see where the constraints from the luminosity and radius measurements overlap.

We also fix the following parameters in our model based on multi-wavelength observations,

I. The ages of G1.9+0.3 at the time of Reynolds et al. (2008) measurement was 140 years, and Condon et al. (1998) was 125 years.

II. $\epsilon_e = 10^{-4}$, which is consistent with the measured electron-to-proton ratio from the non-thermal radio and X-ray spectra (Ksenofontov et al., 2010; Pavlović, 2017) and upper limits on cosmic-ray acceleration efficiency from gamma-ray observations (H.E.S.S. Collaboration et al., 2014).

III. $p = 2.2$, which means the synchrotron spectral index $= (p-1)/2 = 0.6$, which is the same as measured from the integrated radio emission in Green et al. (2008).

E. RESULTS

1. SN 1885A

Figure 39(a) shows the constraints on the parameter space of SN 1885A from our analysis in Section IV.D.2. The shaded regions show values of n_0, E_{51}, M_{ej} that predict luminosities, radii and shock velocities that are consistent with the observational limits in Section IV.D.2. We see that a range of M_{ej} and E_{51} are plausible, and higher values of E_{51} are associated with higher M_{ej}. This is because higher M_{ej} leads to smaller energy per unit mass of the forward-moving ejecta, and therefore a higher kinetic energy is required to produce the same radio luminosity, shock radius and velocity. As we increase n_0, the parameter space in Figure 39(a) shrinks. This is because for higher densities, the radio luminosity increases, while the radius and velocity decreases (as explained in Section IV.D). As a result, a smaller range of values of E_{51} is allowed by the observational limits for a given value of M_{ej}. At $n_0 = 0.04$ cm^{-3}, the allowed parameter space vanishes because no value of E_{51} and M_{ej} can simultaneously satisfy the flux, radius and velocity limits. We can treat this as an upper limit on the ambient density. No such limit can be obtained for M_{ej} and E_{51} because all 3 quantities - luminosity, radius and velocity - increases with M_{ej} and E_{51}, unlike the case of n_0. As a result, we can only obtain ranges of values of M_{ej} and E_{51} that are plausible for SN 1885A, depending on the value of n_0. For $n_0 = 0.01 - 0.03$ cm^{-3} and $M_{ej} = 0.6 - 1.4$ M$_\odot$, which is a typical range of ejecta masses seen in cosmological samples of Type Ia (Scalzo et al., 2014), we find that SN 1885A had to have $E_{51} = 0.9$-1.7. Although SN 1885A is not yet producing detectable

radio emission, $E \gtrsim 10^{51}$ ergs is still required by our model to explain the highest velocity component of the Ca ejecta. In Section IV.F, we will further discuss our measured density upper limit and the M_{ej}-E_{51} parameter space in the context of SN Ia progenitor models and observations of the M31 central region.

To check the validity of the parameter space, we show the predicted radio light curves, radii and shock velocities for different values of n_0, E_{51} and M_{ej} in Figure 39(b). For example, $n_0 = 0.03$ cm^{-3}, $M_{ej} = 1.2$ M$_\odot$ and $E_{51} = 1.4$ fall in the darkest region in Figure 39(a), and predict luminosities below the radio upper limit, velocities and radii above the optical lower limits. On the other hand, any set of values outside the shaded regions either predict luminosities above the upper limit, or velocities and radii below the lower limit. Note from Figure 39(b) that the shock velocity provides a stronger lower limit to our parameter space than radius.

We also checked the robustness of our results to changes in our assumptions about electron acceleration, particularly the parameters ϵ_e and p. We recall that the upper limit on $n_0 = 0.04$ cm^{-3} was for $\epsilon_e = 10^{-4}$ and $p = 2.2$. For $\epsilon_e = 10^{-3}$ and $p = 2.2$, the upper limit reduces to $n_0 \sim 0.01$ cm^{-3}, and predicted energies are lower than Figure 39(a). This is because efficient electron acceleration makes SNRs brighter, and the model requires even lower ambient densities and energies to remain consistent with the dim radio upper limit. For $\epsilon_e = 10^{-4}$ and $p = 2.5$, we get a higher density upper limit of $n_0 = 0.07$ cm^{-3}. This is because a steeper energy spectrum produces fewer electrons at GeV-energies that contribute to the synchrotron luminosity in the GHz range. As a result, the model can still satisfy the radio upper limit with larger values of n_0. Taking these systematics into account, $n_0 = 0.07$ cm^{-3} is the highest possible value of the upper limit in our model, given the observational limits in Section IV.D.2. Deep, multi-wavelength observations in the future will help put stronger, independent constraints on the population of accelerated particles in SN 1885A.

2. G1.9+0.3

Figure 40(a) shows the M_{ej}-E_{51} parameter space of G1.9+0.3 that are consistent with the observational constraints in Figure 40(b). The parameter space constrained by velocity is

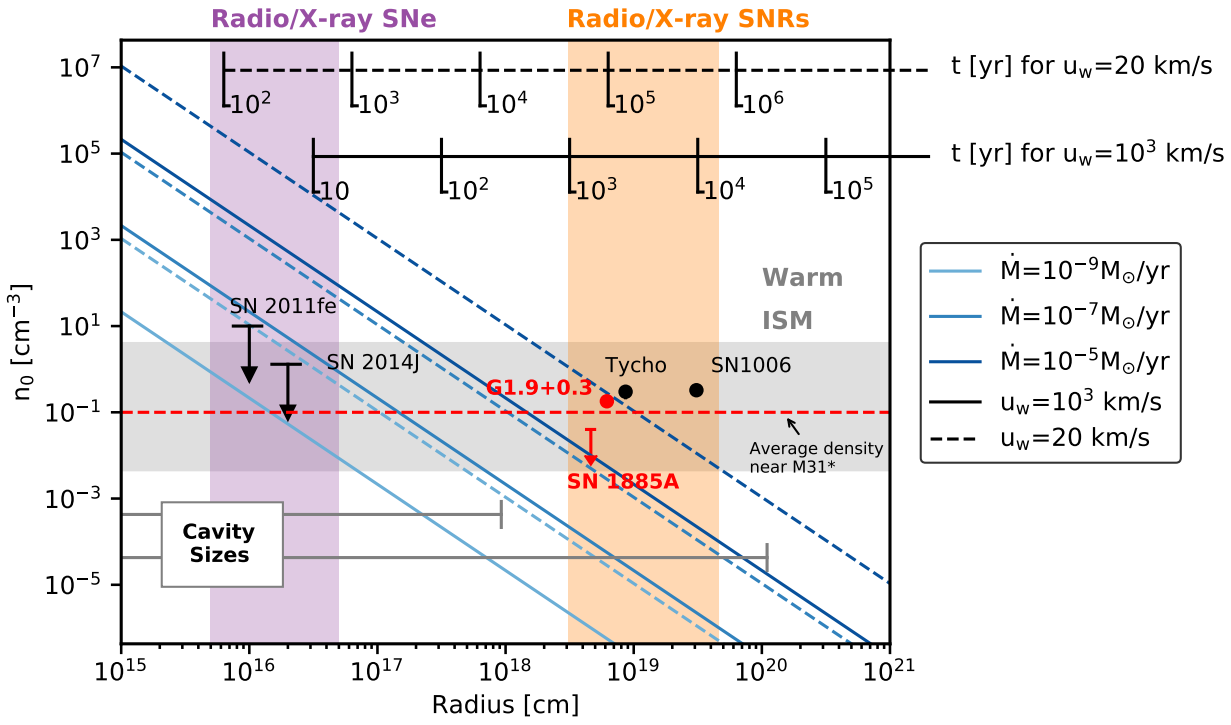

Figure 41: Circumstellar densities and radii of well-known Type Ia SNe and confirmed Type Ia SNRs studied in radio or X-rays, along with SN 1885A and G1.9+0.3 from this work (shown in red). The blue dashed and dotted lines indicate different CSM profiles of the form $n_0 = \dot{M}/4\pi\mu m_H u_w^2$ ($\dot{M}$ - mass loss rate, u_w - wind velocity, μ=1.4) created by isotropic mass loss at constant rates and constant velocities given in the legend box. The horizontal grey bars show examples of cavity sizes created by accretion-driven outflows from the progenitor due to fast and slow winds (Badenes et al., 2007). The ruler on top shows the timescales on which these CSM profiles formed in the pre-SN stage. The grey region shows the typical extent of the warm ISM phase (Ferrière, 2001). The red dashed line indicates the average ISM of the M31* circumnuclear region where SN 1885A is located

the largest because of the wide range of velocities seen in the northern radio rim. Since SNRs are brighter and smaller for higher n_0, the parameter spaces constrained by radio luminosity and radius will change in opposite directions for varying n_0, which allows a measurement of n_0 from the common parameter space of radio luminosity, radius and velocity. We find that G1.9 evolved in $n_0 \approx 0.18$ cm^{-3} and exploded with $E_{51} = 0.8$-1.4 for $M_{ej} = 0.6$-1.5 $M_\odot$, or $E_{51} = 1$-1.3 for $M_{ej} = 1$-1.4 $M_\odot$. However, lower E_{51} and M_{ej} are not ruled out by our parameter space.

As with SN 1885A, we checked the validity of parameter space by showing the predicted light curves, shock radii and velocities for different parameter values in Figure 40(b). Values of n_0, E_{51} and M_{ej} that fall in the common area of parameter space constrained by radio luminosity, radius and velocity in Figure 40(a) are consistent with our observations, whereas any value taken from outside the common area are not consistent with all three constraints.

We re-checked out results for different ages of G1.9+0.3, given the uncertainty in the kinematically-derived age measurements (Reynolds et al., 2008; Carlton et al., 2011; De Horta et al., 2014). We find that our model cannot simultaneously satisfy all the observational limits - luminosity, radius and the velocity range - for ages < 140 years. For ages > 140 years, we can satisfy the observations for $n_0 \gtrsim 0.1$ cm^{-3}. It is likely therefore that G1.9 was a slightly less energetic explosion, but evolving in a denser ambient medium compared to SN 1885A. In Section IV.F.2, we discuss these constraints further in the context of SN Ia models and previous measurements in the literature.

F. DISCUSSION

1. Progenitor scenarios of SN 1885A

a. Clues from the density upper limit Our constraints on SN 1885A in Section IV.E.1 can shed some light on plausible progenitor scenarios for the event. In the standard single-degenerate (SD) scenario, a WD accretes mass from a non-degenerate companion and explodes once it gets close enough to the Chandrasekhar limit, $M_{ch} = 1.4$ $M_\odot$ (Whelan &

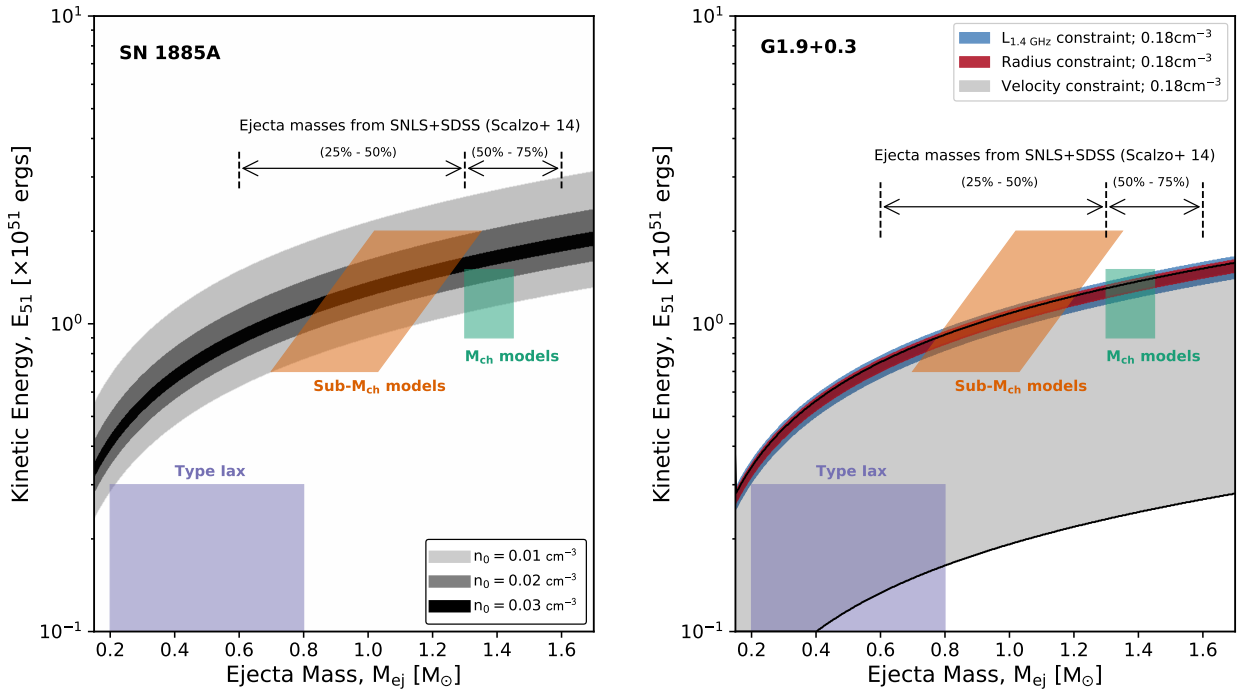

(a) (b)

Figure 42: Same as Figures 39(a) and 40(a), but overlaid with different SN Ia progenitor models. The parameter space of M_{ch} models is taken from Iwamoto et al. (1999); Badenes et al. (2003), Sub-M_{ch} models from Woosley & Kasen (2011); Shen et al. (2017) and Type Iax from Foley et al. (2013, 2016). The arrows are meant to indicate the typical range of M_{ej} for SNe Ia, and are taken from the distribution of M_{ej} measured by Scalzo et al. (2014) from a sample of 337 cosmological SN Ia from SDSS and SNLS.

Iben, 1973; Li & van den Heuvel, 1997; Tutukov & Yungelson, 1996; Han & Podsiadlowski, 2004). Because the accretion process is likely non-conservative, some kind of circum-stellar medium (CSM) is expected around SD SN Ia progenitors (see Wang & Han, 2012; Maoz et al., 2014, for reviews). If the material lost is ejected from the surface of the WD, large outflow velocities (several 1000 km s^{-1}) are expected, and the CSM should take the form of a large, low-density, energy-supported cavity. For lower outflow speeds, most of the material might remain close to the progenitor in a $\rho \propto r^{-2}$ structure (Figure 41). We refer the reader to Badenes et al. (2007) for a more detailed discussion and examples of CSM structures around Type Ia SN progenitors.

Our density upper limit of 0.04 ± 0.03 cm^{-3} suggests that SN 1885A is interacting with very little, if any, CSM material. A similar upper limit of 0.1 cm^{-3} was also suggested by the X-ray non-detection of SN 1885A (Perets et al., 2011). Such low densities at the radius of SN 1885A can be theoretically produced by a r^{-2} CSM profile for some values of mass loss rates (Figure 41). We believe this is unlikely because the average density of M31* circumnuclear region, where SN 1885A is located, is about 0.1 cm^{-3} (Dosaj et al., 2002; Garcia et al., 2005), which is similar to the value of the density upper limit of SN 1885A, although slightly on the higher side. If SN 1885A had been interacting with denser material in the past, our measured n_0 would have been higher than that of the uniform ISM surrounding the remnant. This effect would have been evident from the constraints in Figure 39(a), as the denser ISM would result in a smaller and slower remnant.

The allowed densities from our analysis could also mean that SN 1885A is evolving inside a low-density cavity. A suite of possible cavity structures around Type Ia SN progenitors were explored using hydrodynamical models by Badenes et al. (2007), which showed that such cavities typically have densities $\approx 10^{-3} - 10^{-4}$ cm^{-3} preceded by a cavity wall of density $\approx 10 - 100$ cm^{-3}. In Figure 41, we show examples of the largest and smallest cavities produced by this study. The actual size and structure of the cavities depend on the outflow luminosity, duration of progenitor mass loss and the pressure in the ISM (see Figures 3-5 and Tables 1-2 in Badenes et al. (2007) for examples of cavity structures for various progenitor parameters and mass-loss prescriptions). The non-detection of SN 1885A in our work requires such a cavity to be just larger than 4×10^{18} cm, and produced on timescales of 10^3 -

10^5 years, depending on the outflow velocity. Future observations in X-ray and radio will be necessary to detect any possible signature of shock interaction with a cavity wall. However, most SNRs with a confirmed Type Ia origin do not show definitive signatures of evolution inside a progenitor-driven low-density cavity (Badenes et al., 2007), and therefore such a scenario, while not ruled out, is statistically unlikely for SN 1885A.

On the other hand, the interpretation that SN 1885A is simply expanding inside the bulk ISM also seems favorable because the density upper limit is similar to the average density of the M31* circumnuclear region, and characteristic of the warm ISM phase (Figure 41). In fact, the M31* circumnuclear region is mostly dominated by warm-ionized and diffuse X-ray emitting hot gas, with no significant detection of denser neutral or molecular gas (Braun et al., 2009; Li et al., 2009; Li, 2011). This would mean that the environment of SN 1885A was relatively unmodified by the progenitor evolution. Such a scenario might indicate a WD-WD progenitor model, which is not as strictly associated with accretion-driven mass loss and presence of CSM, unlike the SD models (although see Shen et al., 2013; Raskin & Kasen, 2013). The delay-time distributions of such WD-WD models (Maoz & Mannucci, 2012) are also comparable to the SAD near SN 1885A (Saglia et al., 2010).

SN 1885A joins the growing sample of thermonuclear SNe that have been undetected by radio (Panagia et al., 2006; Hancock et al., 2011; Chomiuk et al., 2016) and X-ray observations (Russell & Immler, 2012), including SN2011fe (Horesh et al., 2012; Chomiuk et al., 2012; Margutti et al., 2012) and SN2014J (Pérez-Torres et al., 2014; Margutti et al., 2014). These non-detections have made SD scenarios involving a giant companion unlikely for these events, although main-sequence or subgiant stars are still possible within the observational limits (Horesh et al., 2012; Chomiuk et al., 2016). A rare subset of Type Ia SNe, called Ia-CSM, show strong Hα emission lines indicative of a hydrogen-rich CSM (Silverman et al., 2013), but such events have evaded radio detection (Chomiuk et al., 2016). This could be because the events are distant (> 60 Mpc), thereby falling below the VLA sensitivity limit, and/or because their ejecta is optically thick. Follow-up late time observations of these events in the radio and X-ray can shed more light on the environments of thermonuclear SNe.

b. Clues from kinetic energy-ejecta mass constraints The constrained M_{ej}-E_{51} parameter space for SN 1885A can be compared with values that are usually associated with Chandrasekhar (M_{ch}) and sub-Chandrasekhar (sub-M_{ch}) models for normal Type Ia SNe (Figure 42(a), model references are in the caption). In M_{ch} models, the accreting WD mass has to be near M_{ch} to ignite C in the degenerate core (Iwamoto et al., 1999; Maeda et al., 2010; Blondin et al., 2013). Sub-M_{ch} models provide an alternate route to SN Ia, characterized by $M_{ej} < M_{ch}$, through a *double-detonation*, i.e. detonation of an accreted layer of He on the surface of the primary WD, leading to a second detonation in the degenerate C/O core (Nomoto, 1982b; Woosley & Weaver, 1994; Bildsten et al., 2007; Woosley & Kasen, 2011; Shen et al., 2017). Scalzo et al. (2014) showed that $25-50\%$ of Type Ia SNe have light curves indicative of $M_{ej} < 1.4$ $M_{\odot}$.

One can see that for plausible densities within the upper limit, our constrained parameter space coincides with a larger area of the parameter space for sub-M_{ch} models than for M_{ch} models. If we assume SN 1885A was a standard 10^{51} ergs explosion, then from Figure 39(a) we get $M_{ej} \approx 0.7$ $M_{\odot}$ for $n_0 = 0.03$ cm^{-3}, and $M_{ej} \approx 0.3-1.2$ $M_{\odot}$ for $n_0 = 0.01$ cm^{-3}. An explosion with $M_{ej} = 1.4$ $M_{\odot}$ would require $n_0 < 6 \times 10^{-3}$ cm^{-3}, almost an order of magnitude below the upper limit. For lower energies, the range of allowed M_{ej} is even smaller. For example, if SN 1885A was a 7×10^{50} ergs explosion, we get $M_{ej} \approx 0.4$ $M_{\odot}$ for $n_0 = 0.03$ cm^{-3}, and $M_{ej} \approx 0.15-0.8$ $M_{\odot}$ for $n_0 = 0.01$ cm^{-3}. While these constraints cannot definitively rule out an M_{ch} explosion model for SN 1885A, a sub-M_{ch} explosion seems the more likely explanation. Evidence from studies in other wavelength also support a sub-M_{ch} origin for SN 1885A. For example, the *Chandra* X-ray upper limit cannot be explained by M_{ch} delayed-detonation models (Perets et al., 2011), and the narrow primordial V-band light curve from de Vaucouleurs & Corwin (1985) requires very low-mass ejecta, $M_{ej} \sim 0.1-0.3$ $M_{\odot}$ and energies $\sim 2.2 \times 10^{50}$ ergs (Chevalier & Plait, 1988; Perets et al., 2011). A sub-M_{ch} origin is at odds, however, with the distribution of Ca and Fe in the *HST* absorption profile of the ejecta, which favors an off-centered, M_{ch} delayed-detonation explosion. (Fesen et al., 2007, 2015).

Motivated by the fast light curve of SN 1885A, we also checked if our results are consistent with the properties of Type Iax SNe. These are a class of transients that are similar to Type

Ia, but characterized by low peak luminosities, ejecta velocities and masses (see Jha, 2017, for references and review). The low ejecta masses and kinetic energies inferred from the light curve is similar to that of known Type Iax SNe (Foley et al., 2013; McCully et al., 2014). In Figure 42(a), we show a plausible parameter space for Type Iax SNe with the purple box, derived from estimates of ejecta masses and photospheric velocities given in Foley et al. (2013); McCully et al. (2014); Foley et al. (2016) and Jha (2017). The range of E_k for SN 1885A, based on our limits on radio flux, optical radius and velocity, is still in general higher than that of Type Iax SNe. On the other hand, García-Berro et al. (2017) recently showed that 3D models of interacting C/O or O/Ne WDs that are invoked for Ca-rich transients (Perets et al., 2010; Kasliwal, 2012) can produce Ca and Fe distribution that looks similar to SN 1885A (Fesen et al., 2015). Thus, while our observational constraints do not energetically favor a Type Iax origin for SN 1885A, we cannot rule out the possibility that SN 1885A originated from some class of thermonuclear transient that is different from SNe Ia.

2. Progenitor scenarios for G1.9+0.3

Our constraints on the parameter space for G1.9+0.3, although tighter than SN 1885A, is less constraining on the common SN Ia progenitor scenarios. Our measured $n_0 = 0.18$ cm^{-3} from the radio emission of G1.9+0.3 is higher than the estimated $n_0 = 0.02$ cm^{-3} obtained by modeling the shock dynamics of G1.9+0.3 inferred from X-ray images (Reynolds et al., 2008; Carlton et al., 2011; Pavlović, 2017), but in agreement with analysis of VLA and ATCA images[2] (De Horta et al., 2014), which infers $n_0 \lesssim 0.3$ cm^{-3} using the numerical model of Berezhko & Völk (2004a). Nevertheless, these densities are still much higher than densities expected inside wind-blown cavities, and within the density range of the warm ISM phase (see Figure 41). A dense, inhomogeneous ambient medium around G1.9+0.3 may not be surprising given the large difference in expansion rates around the remnant (Borkowski et al., 2017) and the brightening radio emission. It is unclear though, if this ambient medium is associated with the progenitor, or if G1.9+0.3 is encountering an over-dense region of the

[2]Australia Telescope Compact Array, https://www.narrabri.atnf.csiro.au/

ISM. The allowed range of E_{51} inferred in Section IV.E.2 can be satisfied by both M_{ch} and sub-M_{ch} models, but not by the lower-energy range of Type Iax SNe (Figure 42(b)). These results are at least consistent with detailed analyses of the X-ray abundances and ionization properties of the ejecta of G1.9+0.3 (Borkowski et al., 2010, 2013; Yamaguchi et al., 2014) which suggested an asymmetric, delayed-detonation explosion. We also note that unlike SN 1885A, we have no constraints from the optical light curve, which would have been undetectable because of the high line-of-sight absorption towards G1.9+0.3 (Reynolds et al., 2008).

3. The SN to SNR transition

We can also make predictions about the future radio evolution of SN 1885A and G1.9+0.3 from their known ages, and constrained properties from Section IV.E. While we are not certain if SN 1885A is producing any radio emission, the upper limit is still consistent with a young ejecta-dominated SNR expanding in a very low density ambient medium and is expected to brighten over time. Assuming that SN 1885A is just below the detection limit of 11.4 μJy (Figure 43), we predict that it will brighten to a light curve maximum of about 15 μJy in 6.2 GHz images in roughly another 150 years, if it was a very low energy explosion, or $\sim 31\mu$Jy in another 570 years if it was a normal, energetic Type Ia. If SN 1885A went off in lower densities, the brightening period will be even longer.

For the similarly aged G1.9+0.3, radio brightening is already evident. In fact, at the location of SN 1885A in M31, G1.9+0.3 would have had a radio brightness = (0.93 Jy) $(0.0085 \text{ Mpc})^2/(0.785 \text{ Mpc})^2 = 109$ μJy (or ~ 45 μJy at 6.2 GHz), which would have been detectable at a level of almost 28σ. We expect G1.9+0.3 to brighten for roughly another 270 years up to a flux of about 2.2 Jy in 1.4 GHz, if we assume a normal, 1.4 $M_\odot$ explosion. The brightening period is smaller than the prediction of Pavlović (2017) mostly because we measure almost an order of magnitude higher ambient density around G1.9+0.3 as a result of keeping the M_{ej} - E_{51} parameter space flexible in Section IV.E.

Prior to SN 1885A and G1.9+0.3, the behavior of SNe in the age range of 80-300 years was not well constrained by observations. Cowsik & Sarkar (1984) showed that old radio SNe are

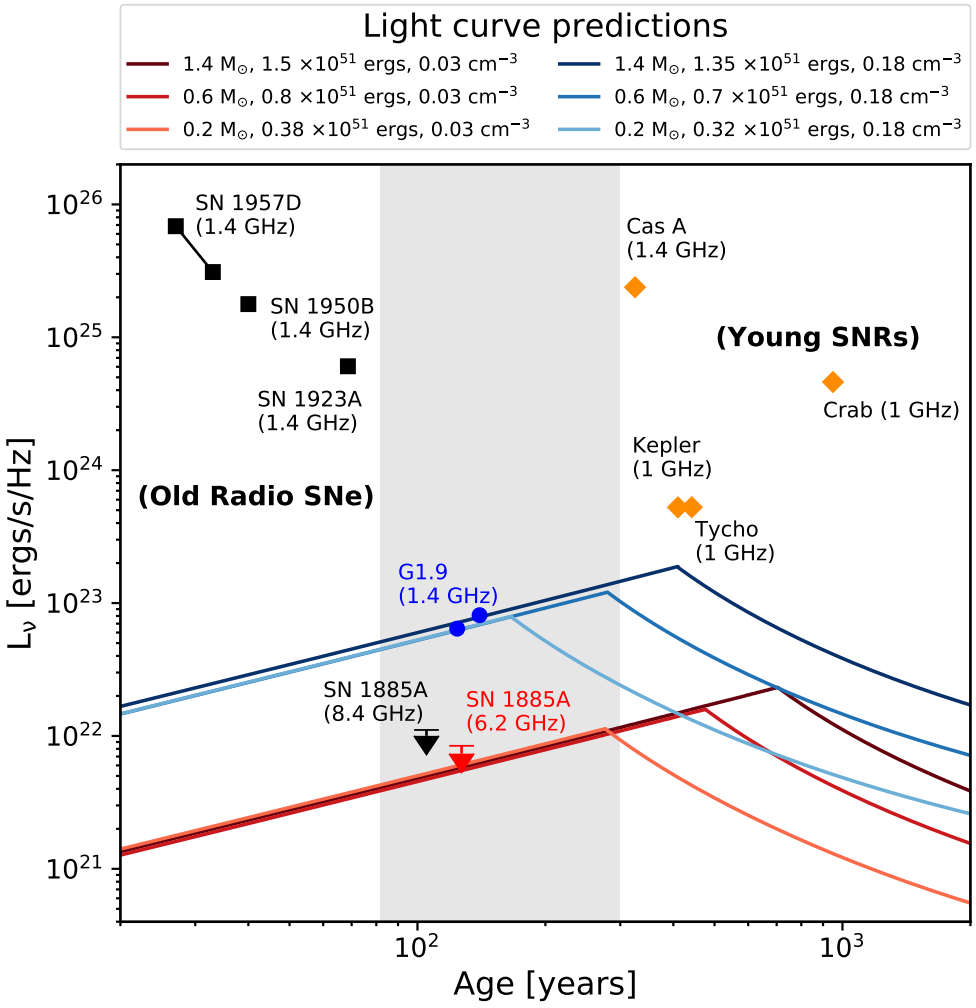

Figure 43: Light curve predictions of SN 1885A and G1.9+0.3 from values of energy, M_{ej} and ambient densities constrained from radio and optical absorption images. The blue points show the two 1.4 GHz measurements of G1.9+0.3 from Condon et al. (1998) and Green et al. (2008). The 8.4 GHz (black) and 6.2 GHz (red) upper limits on SN 1885A are from Crane et al. (1992) and this work, respectively. Also shown are some of the oldest SNe and the youngest SNRs, from both thermonuclear and core-collapse origin, with detectable radio emission. The gray shaded region is where our sample is lacking in SNe and SNRs, and objects like G1.9+0.3 and SN 1885A hold the key to constraining this period of evolution. **Object references:** SN 1957D, 1950B (Cowan et al., 1994), SN 1923A (Eck et al., 1998), Cas A, Kepler, Tycho and Crab (Fesen et al., 2006; Green, 2014b; Yamaguchi et al., 2014; Green, 2017; Trotter et al., 2017).

expected to 'turn on' radio emission during this phase as the forward shock begins to sweep up increasing amounts of ISM material. The observed brightening of G1.9+0.3 and lack of emission from SN 1885A indeed suggests that SNe can be transitioning to the SNR phase during this age-range, if enough ambient medium is present to produce emission. Future high resolution and high sensitivity radio and X-ray observations can find more SN 1885A-like objects, which will further observationally constrain the SN-SNR transition region.

G. CONCLUSIONS

We presented the deepest radio image at the site of SN 1885A by reducing and co-adding ∼29 hours of 4-8 GHz VLA data of the M31 central region between 2011-2012. The final 6.2 GHz image has an RMS noise sensitivity of 1.3 μJy, and shows regions of diffuse emission at 2.6σ near SN 1885A. This emission is still present even if the site is re-imaged by down-weighting the shorter baselines. It is inconclusive whether the emission is uniquely associated with SN 1885A because such diffuse emission patches are scattered throughout the M31 central region. We assume a conservative 3σ upper limit of 11.4 μJy on the radio flux throughout the paper, taking into account this diffuse emission, and the possibility that the forward shock extends beyond the optical absorption region of SN 1885A. In comparison, the similarly aged SNR G1.9+0.3 in our Galaxy would have had a radio flux of $\sim$ 45 μJy at 6.2 GHz at the distance of M31, which makes it almost 4 times more radio luminous than SN 1885A.

We explored the parameter space of ISM density-kinetic energy-ejecta mass of SN 1885A and G1.9+0.3 using the radio light curve model of Sarbadhicary et al. (2017a). Based on the upper limit on the radio flux from VLA, and the lower limit on the shock radius and velocity from HST, SN 1885A may have exploded in a very low density environment with an upper limit of 0.04 cm^{-3} ($\pm$0.03 cm^{-3}, if systematic uncertainties from the electron acceleration model is taken into account). For a density of 0.03 cm^{-3}, SN 1885A would have exploded with kinetic energies of $(1.3 - 1.7) \times 10^{51}$ ergs for ejecta masses in the range of $1 - 1.4$ M$_\odot$, usually associated with SN Ia. For even lower ambient densities, the range of kinetic energies allowed by observations is larger. The same light curve model was applied to the similarly

aged SNR G1.9+0.3 which already had measurements of the integrated flux, shock radii and velocities from VLA and *Chandra* observations. These observations constrained an ambient density of 0.18 cm^{-3} around G1.9+0.3, denser than the ambient medium around SN 1885A, and kinetic energies of $(1 - 1.3) \times 10^{51}$ ergs for the same range of ejecta masses.

These measurements provided some clues about the progenitors of these events. While G1.9+0.3 seems consistent with both M_{ch} and sub-M_{ch} explosion models, SN 1885A seems less likely to have originated from a M_{ch} explosion, based on the energetics, the very low ambient density, and the lack of any radio detection in the past. This conclusion is supported by the observation and analysis of *Chandra* X-ray upper limit by (Perets et al., 2011), but is at odds with the analysis of the ejecta from optical absorption, and the primordial light curve. A Type Iax origin is also energetically disfavored for both SN 1885A and G1.9+0.3. The similarity of our density constraint around SN 1885A and warm ISM-like density of the M31* circumnuclear region could mean that the SN1885A is evolving inside a relatively clean environment, which is generally not associated with single-degenerate SN Ia channels.

The measured flux and known ages of G1.9+0.3 and SN 1885A make them ideal candidates for studying the 'turn-on' phase of radio emission in SNRs. Our combined VLA and optical constraints suggest that SN 1885A will brighten for at least another 150 years (if it was a very low energy explosion) or up to 570 years, for a normal, 1.4 $M_{\odot}$ explosion. For G1.9+0.3, the brightening period is expected to continue for another $\sim$ 270 years, assuming a normal 1.4 $M_{\odot}$ explosion with energy $> 10^{51}$ ergs.

These results also underscore the importance of deep multi-wavelength observations and monitoring of SN 1885A in the future. While the observational limits in this study provided some hints about the origin and evolution of SN 1885A, an actual detection of the ejecta will resolve many of the discrepancies and confirm the actual explosion scenario. Future high resolution and high sensitivity telescopes such as MeerKAT [3], The Square Kilometer Array (SKA) [4] and the Next-Generation VLA [5] have the potential to discover many intermediate-age SNe and young ejecta-dominated SNRs in the Local Group and beyond, and provide further observational constraints on the SN-SNR transition phase. Additionally,

[3]http://www.ska.ac.za/science-engineering/meerkat/
[4]http://www.ska.ac.za/
[5]https://public.nrao.edu/futures/

the historical light curve and the current images of the ejecta of SN 1885A provides a unique consistency check between SN progenitor and SNR evolution models. In a forthcoming paper, we will analyze the latest X-ray observations of SN 1885A by running a full grid of M_{ch} and Sub-M_{ch} models, and a Markov Chain Monte Carlo analysis of the historical light curve and color evolution, and compare with our VLA results.

H. ACKNOWLEDGEMENTS

We would like to thank Rob Fesen and Mike Garcia for discussions and suggestions for our work. SKS acknowledges helpful discussions with Ryan Foley and Enrico Ramirez-Ruiz on optical light curves and transients, and Janos Botyanszki and Héctor Martínez-Rodríguez for guidance with M_{ch} and Sub-M_{ch} models. SKS, LC and CB acknowledge NSF/AST-1412980 for support of this work. The National Radio Astronomy Observatory is a facility of the National Science Foundation operated under cooperative agreement by Associated Universities, Inc. This research has made use of the NASA Astrophysics Data System (ADS) Bibliographic Services. This work made use of the IPython package (Pérez & Granger, 2007), SciPy (Jones et al., 2001–), NumPy (Van Der Walt et al., 2011), matplotlib, a Python library for publication quality graphics (Hunter, 2007), Astropy, a community-developed core Python package for Astronomy (Astropy Collaboration et al., 2013), AIPS (Greisen, 1990), and KARMA (Gooch, 1996).

V. THESIS SUMMARY

My thesis was motivated by the question: what are the different scenarios that lead to the production of Type Ia and core-collapse SNe? While we know Type Ia SNe are produced by the thermonuclear runaway inside a carbon-oxygen WD, what type of a companion does the exploding WD require? A main-sequence star, or a red-giant, a He-donor star, or perhaps another WD? Does the WD even need to reach the critical mass of M_{ch}=1.4 $M_{\odot}$ to explode, or are their sub-M_{ch} processes that dominate the production of Type Ia? For core-collapse SNe, the progenitor scenarios are better understood because of many direct detections of the progenitors of nearby SNe. However, many open questions remain: Do red-supergiants above 17-18 $M_{\odot}$ successfully explode as a SN, or do they produce a 'failed' SN - a weak transient event as the star directly collapses to a black hole? Do the stripped-envelope variety of supernovae (Type Ib/Ic/IIb) arise from singular Wolf-Rayet stars, or exclusively from binary evolution channels of massive stars? Such questions are of critical importance given the central role played by SNe in the structural and chemical evolution of the universe, as well as in measuring the fundamental parameters of ΛCDM cosmological theory.

To answer these questions, I have contributed to the development of the delay-time distribution (DTD) technique to directly measure the rates and contributions of different SN progenitor channels in the universe. The DTD is the most direct way to validate specific evolutionary models of progenitors. Most importantly, it does this not for specific SNe, but for an entire population of SNe, thereby answering the general question of how successfully can a progenitor model explain the observed class of SN.

My first project was on optimizing the DTD technique for SNR surveys and SAD maps of Local Group galaxies. The proximity of these galaxies provided more reliable SADs compared to distant galaxies, where SADs are based on integrated spectra. Such maps have

already been constructed for the MCs and M31, and therefore the Local Group DTD required progress in two major avenues: a) getting a large SNR survey with well-understood completeness, and b) a model of the evolution and visibility times of SNRs of that survey. In Sarbadhicary et al. (2017a), I built the latter: a model of a SNR population based on the latest physics of radio emission from SNRs, and detailed multi-wavelength maps of star-formation and interstellar gas in a Local Group galaxy to serve as observational anchor (in this case, M33).

The SNR model can successfully reproduce the radio luminosity function of the M33 SNRs for a SN rate of $\sim 3 \times 10^{-3}$ SN/year, a scale height of 200 pc for neutral hydrogen, and the fraction of shock energy in accelerated electrons of about 4.2×10^{-3}. The latter measurement is one of the most detailed measurements of the efficiency of electron acceleration in non-relativistic shocks, which will be useful to constrain theories of the poorly-understood electron injection in such shocks. Most importantly, the model estimated the visibility times of SNRs, showing that it scales as $N_H^{-1/3}$ (N_H being the hydrogen column density) for about 70% of the remnants, because these remnants evolve completely through the Sedov-Taylor to the radiative phase. The 30% remnants showed visibility times uncorrelated with density because their light curves were cutoff by the detection limit of the survey. The model therefore provides a way to quantify the bias due to missing SNRs - a potential source of systematic error - in our DTD calculations.

The next step in the Local Group SN DTD project is obtaining a large SNR survey with well-quantified completeness. For this purpose, I am currently assisting Prof. Laura Chomiuk and her student, Jessica Maldonado (Michigan State University) to assemble a survey of SNRs in M31 using one of the most sensitive radio interferometers in the world, the Very Large Array (VLA). We are currently testing the observations and data-reduction using the A-configuration - the highest possible resolution with the VLA - to look for small SNRs. We will use these results to apply for longer observing times with the VLA.

The flexibility of the DTD method, and the availability of SAD maps of our Local Group galaxies allowed me to test the DTD method on objects other than SNe, such as RR Lyrae and Cepheid variables. Calculating a DTD with these objects can serve as a consistency check for the DTD method, since catalogs of these objects are much more abundant and

complete compared to SNRs, and independent estimates of their ages exist from their light curves and host stellar clusters. In addition, RR Lyrae and Cepheids are the most important distance indicators in the Local Group, and has put unique constraints on the stellar populations of Local Group galaxies. Therefore it is important to know if multiple progenitor channels also exist for these objects, in order to accurately use these objects as population tracers.

For the RR Lyrae DTD from the OGLEIV survey, we found that about 40% RR Lyrae progenitors are $>$ 10 Gyrs old, consistent with current expectations from cluster measurements, but about 50% come from ages between 1-10 Gyrs, which is generally not assumed in the literature. We introduced a variety of statistical checks to verify this signal, such as inclusion of errors from the SAD maps, checking false positives with artificial DTDs, and treating star clusters as separate cells in the map. However, the RR Lyrae DTD appears robust to all these tests, and cannot be explained by models using variations in mass and metallicity only. A similar conundrum exists for horizontal branch stars in globular clusters, called the second parameter effect, although more detailed modeling with population synthesis models can uncover the physical origin of the 'young' RR Lyrae signal. For now, we advise caution against interpreting the age of stellar populations based on the presence of RR Lyrae alone. The Cepheid DTD finds progenitors mostly in the age range of 20-200 Myrs, which is more consistent with Cepheid ages measured using current stellar evolution and pulsational models. We do however, find a signal between 500-800 Myr, which does not have a counterpart in current Cepheid-age measurements. Further investigation is needed to uncover the origin of this signal.

I also pursued direct observations and modeling of radio emission from SNRs to determine possible progenitor scenarios (Sarbadhicary et al., 2017b). Radio is mostly sensitive to the bulk energy exchange between the SN shock and the circumstellar medium, whose properties depend on the mass-loss processes associated with the progenitor. Radio observations can therefore be used to trace the progenitor channels through constraints on mass-loss history of the progenitor. I applied my Sarbadhicary et al. (2017a) model to the deep VLA observations of SN1885A and G1.9+0.3, which are both $\gtrsim$ 100 years old, and the youngest thermonuclear SNe in the Local Group. In particular, SN1885A has been an enigmatic

event because of its unusually fast primordial light curve, and non-detection of its present-day ejecta, except in optical absorption against the M31 bulge. We found that SN 1885A is evolving inside a very-low density environment (~ 0.04 cm^{-3}), similar to the warm ISM and average density of the M31 bulge, indicating a possibly 'clean' circum-stellar environment. Its energetics are also consistent with a sub-M_{ch} explosion, although an M_{ch} explosion cannot be ruled out. G1.9+0.3 is evolving inside a higher density environment (~ 0.2 cm^{-3}) with similar energetics that are consistent with both M_{ch} and sub-M_{ch} explosions. Such late-time radio observations on larger SNe is a promising avenue for narrowing down the statistics of Type Ia progenitors, especially with upcoming telescopes like MeerKAT, LOFAR and SKA.

A. FUTURE OUTLOOK

The DTD method explored in this thesis is a particularly exciting tool for studying SN progenitors and stellar astrophysics in the upcoming era of big-data surveys. The potential for DTD in extragalactic surveys of SNe has already been demonstrated, although the main limitation has been the spatially-averaged, integrated spectra of the host galaxies. It is expected that stellar age measurements in extragalactic surveys will improve with ongoing Integral Field Spectroscopy (IFS) surveys like MaNGA and CaLIFA, which can hone in on the local environment of extragalactic SNe. Proposed telescopes like the upcoming James Webb Space Telescope (JWST) and Wide-Field Infrared Survey Telescope (WFIRST) are expected to provide resolved stellar-age distributions with unprecedented photometric depths and fields of view. Given the large volume of SN data expected from upcoming fast-cadence telescopes like Zwicky Transient Facility (ZTF) and Large Synoptic Survey Telescope (LSST), it will be possible to calculate well-resolved DTDs of SNe to complement our Local Group DTD, and further narrow down the enigmatic progenitor channels of SNe. DTDs for variable stars will substantially improve with the large stellar population data expected from LSST, and deeper stellar age maps from the SMASH survey. Additionally, the DTD can be applied to *any* category of stellar objects (e.g. red supergiants, Wolf-Rayet stars, X-ray binaries, novae etc) since catalogs of these objects exist or is ongoing in the Local Group. With the im-

proved understanding of systematics from our variable star DTD projects, the DTD method is poised to provide a unique perspective on the stellar evolution paradigm of various stellar species of interest.

APPENDIX

THE SUPERNOVA REMNANT RADIO LIGHT CURVE MODEL

Most of the content in this appendix was published in the Monthly Notices to the Royal Astronomical Society journal as Sarbadhicary et al. (2017a), titled *"Supernova Remnants in the Local Group - I. A model for the radio luminosity function and visibility times of supernova remnants"*. Collaborators: Carles Badenes (University of Pittsburgh), Laura Chomiuk (Michigan State University), Damiano Caprioli (University of Chicago) & Daniel Huizenga (Michigan State University).

A.1 ENERGY SPECTRUM OF ACCELERATED ELECTRONS

Classically, acceleration of ions and electrons by SNRs has been described by the theory of diffusive shock acceleration (DSA). According to DSA, injected particles gain energy by being repeatedly scattered across the shock front by strong magnetic turbulence (Axford et al., 1977; Krymskii, 1977; Bell, 1978; Blandford & Ostriker, 1978) The mechanism naturally predicts a power-law spectra for the accelerated electrons that resembles the cosmic ray spectrum observed on earth (Caprioli, 2015). The theory was subsequently modified to account for the effects of streaming particles on the shock structure, the particle spectrum and the scattering of the particles upstream (Drury, 1983; Blandford & Eichler, 1987; Jones

& Ellison, 1991; Malkov & Drury, 2001). Evidence of electron DSA in SNRs has been gleaned from the featureless, synchrotron X-ray emission in the shells of young SNRs such as SN1006 (Koyama et al., 1995), Tycho (Warren et al., 2005) and Cas A (Stage et al., 2006) as well as gamma ray emission in SNRs (e.g. Morlino & Caprioli, 2012; Ackermann et al., 2013; Slane et al., 2014) which also provided evidence of efficient hadron acceleration.

Based on predictions of DSA, we assume the non-thermal synchrotron-emitting electrons are described by a power-law,

$$N(E) = N_0 E^{-p} \tag{.1}$$

where we choose $p = 2.2$ in our model, since the cosmic ray spectrum in some SNRs shows a deviation from the classical DSA spectrum with $p = 2$ (Caprioli, 2012). The normalization N_0 can be written as,

$$N_0 = (p-2)\ \epsilon_{\rm e}\ \rho_0\ v_s^2\ E_m^{(p-2)} \tag{.2}$$

by assuming the average energy density of the electrons accelerated above a minimum energy E_m $(= m_e c^2)$ is a constant fraction $\epsilon_{\rm e}$ of the post-shock energy density $\sim \rho_0 v_s^2$ (Soderberg et al., 2005; Chevalier & Fransson, 2006), where ρ_0 is the ISM density (g/cm^{-3}) and v_s is the shock velocity. Since $N_0 \propto v_s^2$, we see that the number of available synchrotron emitting electrons at any time during the SNR lifetime strongly varies with the shock velocity.

A.2 MAGNETIC FIELD AMPLIFICATION

SNR shocks can amplify the surrounding magnetic field by over 2 orders of magnitude. This was evident in observations of thin X-ray rims around historical SNRs (Bamba et al., 2005; Warren et al., 2005; Völk et al., 2005; Parizot et al., 2006), which implied the presence of strong magnetic fields to confine synchrotron-emitting electrons near the shock vicinity. *Chandra* observations of the pre-shock region of SN1006 suggests that this amplification must be induced in the upstream (Morlino et al., 2010). The alternative scenario where damping of the magnetic field in the shock downstream produces the thin X-ray rims (Pohl et al., 2005) is inconsistent with the frequency dependence of the rim widths (Ressler et al., 2014).

Table 5: Expressions for shock radius and velocity for Type Ia and CC SNRs based on Truelove & McKee (1999). We define $t_2 = t/(100\text{ yrs})$, $t_4 = t/(10^4\text{ yrs})$, $E_{51} = E/(10^{51}\text{ergs})$ as the kinetic energy of explosion, $M_{\rm ej} = M/(1\text{M}_\odot)$ as the ejecta mass and n_0 as the ambient medium density in units of 1cm^{-3}. The onset of Sedov-Taylor phase happens at $t = t^*(423\text{ years})E_{51}^{-1/2}M_{\rm ej}^{5/6}n_0^{-1/3}$, where $t^* = 0.481$ for Type Ia, and 0.424 for CC SNRs.

Ejecta-dominated		
SN Type	Shock Radius, $R_s(t) =$	Shock velocity, $v_s(t) =$
Type Ia	(1.29 pc) $t_2^{0.7}\ E_{51}^{0.35}\ n_0^{-0.1}\ M_{\rm ej}^{-0.25}$	(8797 km/s) $t_2^{-0.3}\ E_{51}^{0.35}\ n_0^{-0.1}\ M_{\rm ej}^{-0.25}$
Core Collapse	(1.26 pc) $t_2^{0.75}\ E_{51}^{0.38}\ n_0^{-0.08}\ M_{\rm ej}^{-0.29}$	(9213 km/s) $t_2^{-0.25}\ E_{51}^{0.38}\ n_0^{-0.08}\ M_{\rm ej}^{-0.29}$
Sedov Taylor		
Type Ia/ Core Collapse	(12.5 pc) $t_4^{0.4}\ E_{51}^{0.2}\ n_0^{-0.2}$	(490 km/s) $t_4^{-0.6}\ E_{51}^{0.2}\ n_0^{-0.2}$

Field amplification results from excitation of unstable wave modes by the streaming of accelerated particles ahead of the shock. These modes may be resonant with the Larmor radius of the accelerated particles (Bell, 1978) or non-resonant with shorter wavelengths that grow faster than resonant modes (Bell, 2004). During earlier stages, i.e. free expansion and early Sedov-Taylor, when the shock velocity is high and particle acceleration is efficient, substantial field amplification is caused by non-resonant modes, whereas resonant Bell modes become important to the field amplification as the SNR becomes older and the shock weakens (Amato & Blasi, 2009; Caprioli & Spitkovsky, 2014a). We split the calculation of the amplified field into these two regimes. The energy density of the amplified upstream magnetic field, B_u can be written as a fraction, $\epsilon_{\rm b}^{\rm u}$ of the shock energy density,

$$\epsilon_{\rm b}^{\rm u} = \frac{B_u^2/8\pi}{\rho_0 v_s^2} \tag{.3}$$

We can scale $\epsilon_{\rm b}^{\rm u}$ with the Alfvén Mach number of the shock, M_A and the efficiency of particle acceleration, $\xi_{\rm cr}$, defined as the fraction of the shock energy in cosmic rays (ions + electrons).

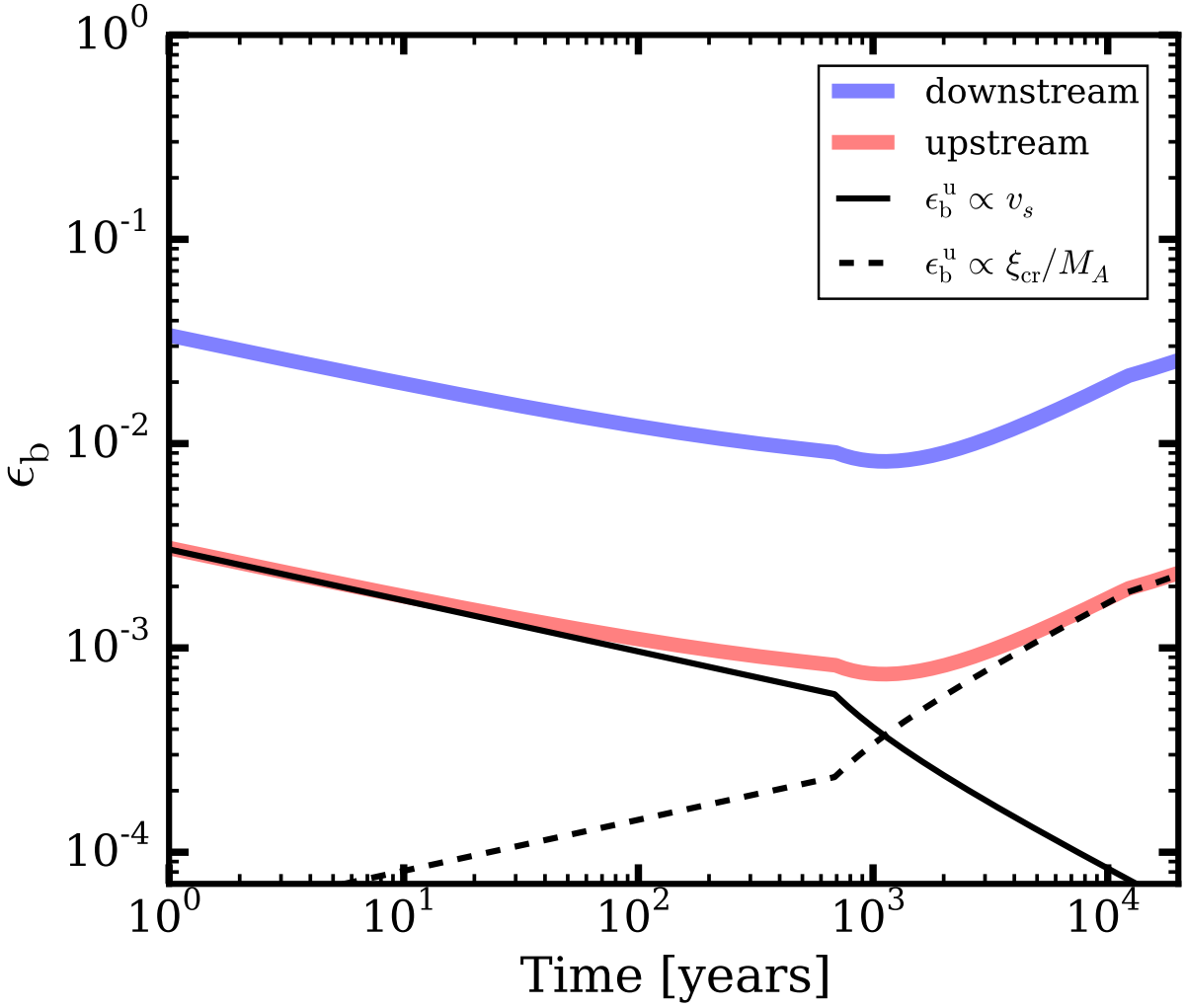

Figure 44: Time evolution of ϵ_b in the upstream (denoted as ϵ_b^u in the text) and in the downstream for an SNR with 5 $M_\odot$ ejecta and 10^{51} ergs evolving into $n_0 = 1$ cm^{-3}. The solid black line represent field amplification characterized by non-resonant wave modes, and dashed line represent amplification contributed by mostly resonant Bell modes. The red band shows the combined solution for ϵ_b^u we use in the model. The downstream value, shown with the blue band, is produced by compression of the upstream field and its values are consistent with estimates for known SNRs (Völk et al., 2005).The kink in the curves is the transition from the ejecta-dominated to the Sedov-Taylor solution (Table 5)

We define $M_A = v_s/v_A$, where v_A is the Alfvén velocity, given by $v_A = B_0/\sqrt{4\pi\rho_0}$. Following Crutcher (1999), the unshocked, background ISM magnetic field B_0 is given by,

$$B_0 = 9\mu\mathrm{G}\left(\frac{\rho_0}{1.6\times10^{-27}\ \mathrm{g\ cm^{-3}}}\right)^{0.47} \tag{.4}$$

For high M_A ($\gtrsim$ 100) where non-resonant modes dominate, Bell (2004) argued that the amplified field saturates to a value, $B^2/8\pi \sim 1/2(v_s/c)\xi_{\rm cr}\rho_0 v_s^2$, due to increasing tension in the field lines. Using Eq (.3), we can write $\epsilon_{\rm b}^{\rm u}$ as,

$$\epsilon_{\rm b}^{\rm u} = \frac{1}{2}\left(\frac{v_s}{c}\right)\xi_{\rm cr} \tag{.5}$$

For field amplification with significant contribution from resonant modes, Caprioli & Spitkovsky (2014a) showed that the amplification scales as $B^2/B_0^2 \approx \xi_{\rm cr}M_A$. Using the definition of and Eq. (.3), we can write

$$\epsilon_{\rm b}^{\rm u} = \frac{1}{2}\frac{\xi_{\rm cr}}{M_A} \tag{.6}$$

Considering the dual roles of resonant and non-resonant streaming instabilities, we assume $\epsilon_{\rm b}^{\rm u}$ for our model SNRs of the form,

$$\epsilon_{\rm b}^{\rm u} = \frac{\xi_{\rm cr}}{2}\left(\frac{v_s}{c} + \frac{1}{M_A}\right) \tag{.7}$$

We assume $\xi_{\rm cr} = 0.1$ for all SNRs, but the cosmic ray acceleration efficiency has been shown to decrease in weakened shocks (Caprioli & Spitkovsky, 2014a). Based on this result, we set $\xi_{\rm cr}/10^{-2} = 0.15M_A + 6$ for shocks with $M_A \lesssim 30$.

The downstream magnetic field, B is amplified by compression of the upstream field. Assuming B_u is isotropic, and only the transverse components are compressed, B can be written as,

$$B = \sqrt{\frac{1+2\eta^2}{3}}B_u \tag{.8}$$

where η is the compression ratio $\approx 4M^2/(M^2+2)$ given by the Rankine-Hugoniot jump conditions for a strong, non-radiative shock, where M is the magneto-sonic Mach number. Since our SNR shocks have $v_s \geq 200$ km/s, they will have $M \gtrsim 10$. throughout. As a result, $\eta \approx 4$ throughout the SNR lifetime.

The evolution of $\epsilon_{\rm b}^{\rm u}$ is shown in Figure 44, and sets the general shape of our radio light curves in the Sedov-Taylor stage. The range of values spanned by the downstream $\epsilon_{\rm b} = \epsilon_{\rm b}^{\rm u}(1+2\eta^2)/3$ is consistent with estimates in the downstream shock region of shell-type SNRs (Völk et al., 2005).

A.3 SNR DYNAMICS

We follow the work of Truelove & McKee (1999) which provides analytical expressions for the shock radius and velocity for the ejecta-dominated and Sedov-Taylor phases that closely match numerical results. In this formalism, each SNR starts as an explosion within a very small volume, depositing kinetic energy E_{51} (in units of 10^{51} ergs) and ejected mass $M_{\rm ej}$ which drives a spherically symmetric shock into a uniform ISM with number density n_0 (These quantities are selected for each SNR by the Monte-Carlo scheme described in Section II.B.1). The resulting SNR consists of a forward shock, followed by a layer of shocked ISM, and a 'contact discontinuity' that separates these outer layers from inner layers of shocked ejecta and the reverse shock. We are only interested in the forward shock since its larger volume and higher velocity generates most of the synchrotron emission (Chevalier & Fransson, 2006).

The interaction of the power law SNR ejecta ($\rho \propto v_s^{-n}$) with a uniform ambient medium gives rise to $R_s \propto t^{(n-3)/n}$ and $v_s \propto t^{-3/n}$ in the ejecta-dominated phase that smoothly connects with the self-similar Sedov-Taylor solution, $R_s \sim t^{2/5}$ and $v_s \propto t^{-3/5}$ in the TM99 model. This feature allows us to generate an analytical light curve that spans the SNR lifetime up to the radiative phase, where we assume the synchrotron emission shuts off. We select $n = 10$ for Type Ia SN, which describes a stellar envelope with polytrope = 4/3, such as a WD envelope, expelled by the SN shock (Matzner & McKee, 1999; Chomiuk et al., 2016) and $n = 12$ for core collapse (CC) SNRs (Chevalier, 1982).

Table 5 lists the scaling relations for R_s and v_s in the ejecta-dominated and Sedov-Taylor phases. Both Type Ia and CC SNR ejecta expand rapidly during the ejecta-dominated phase. However, CC SNRs expand slightly faster than Type Ia's, because the steeper density profile

of CC ejecta puts more energy per unit mass in the outer ejecta near the forward shock, allowing it to be decelerated at a slower pace by the ISM. At around 423 years, R_s and v_s varies according to the Sedov solution, which is the same for both Type Ia and CC SNRs since they have no memory of the initial ejecta mass at this stage. This causes the Sedov-Taylor light curves to be the same for both Type Ia and CC SNRs.

A.4 RADIO LUMINOSITY

We follow the circumstellar interaction model of radio synchrotron emission of Chevalier (1998) where emission at lower frequencies is assumed to be suppressed by synchrotron self-absorption. Although some SN light curves are better described by free-free emission (Panagia et al., 2006), the choice of optically thick emission process in our case is irrelevant because SNRs are already optically thin. We consider an SNR as the stage when the radio emission turns on as a result of circumstellar interaction of the ejecta, in contrast with intermediate-age radio SNe (Cowan & Branch, 1985; Stockdale et al., 2001).

In the Chevalier (1998) model, the SNR radio emission region is approximated as a projected disc in the sky with radius R and thickness s with the same emitting volume,

$$\pi R_s^2 s = \epsilon_f \left(\frac{4}{3}\pi R_s^3\right) \tag{.9}$$

where $\epsilon_f \approx 0.38$ is the emission filling factor (Chomiuk et al., 2016). The synchrotron luminosity emitted from such a configuration is given as,

$$L_\nu = 4\pi^2 R_s^2 \left(\frac{c_5}{c_6}\right) B^{-1/2} \left[1 - \exp\left\{-\left(\frac{\nu}{\nu_1}\right)^{-(p+4)/2}\right\}\right] \left(\frac{\nu}{2c_1}\right)^{5/2} \tag{.10}$$

where R_s is the SNR radius, B is the downstream magnetic field amplified by cosmic-ray induced instabilities, N_0 and γ are parameters of the electron spectrum in Eq. (.1), ν is the frequency and $c_5 = 9.68 \times 10^{-21}$, $c_6 = 8.1 \times 10^{-41}$ and $c_1 = 6.27 \times 10^{18}$ in cgs units are constants (Pacholczyk, 1970). The frequency at which the SNR ejecta transitions from optically thick to thin is,

$$\nu_1 = 2c_1 (s c_6 N_0)^{2/(p+4)} B^{(p+2)/(p+4)} \tag{.11}$$

A.5 LIKELIHOOD MODEL FOR COMPARING RADIO LUMINOSITY FUNCTION

We compare the radio LFs of the observed and model SNRs using a maximum likelihood method prescribed in Badenes et al. (2010), with similar implementations in Maoz & Rix (1993) and Badenes & Maoz (2012). Each LF is divided into several bins, and we assume the probability of finding j SNRs in the ith bin, for which the model predicts n_i SNRs is a Poisson distribution,

$$P(j|n_i) = \frac{\mathrm{e}^{-n_i} n_i^j}{j!} \tag{.12}$$

Because binning the LFs can result in loss of information, we checked the effects of increasing the number of bins and found that the constraints on our parameter space in Section II.C are almost unchanged even if the number of bins are doubled.

We assumed a Poisson likelihood since very few SNRs will occupy the bright end of the LF. We account for the fluctuation in the number of SNRs every year in the steady state by taking several snapshots of the population at different ages and obtaining an aggregate of LFs, which is compared with observations. Therefore, n_i the mean number of SNRs per luminosity bin. In order to reduce statistical errors in n_i, we generate the steady state at a higher SN rate (e.g. $\sim 20\ R$), and then scale down the LF, and therefore the statistical errors in n_i, by the same factor. The likelihood of the model is thus given by,

$$\ln\ \mathcal{L}(R, z_0, \epsilon_\mathrm{e}) = \sum_{i=1}^{N_{bins}} \ln\ P(j|n_i) \tag{.13}$$

We used this likelihood function to compute the probability distributions of the respective parameters by marginalizing over the nuisance parameters, as shown by the shaded regions and histograms in Figure 6. We sampled 10 data points per parameter to recover the marginal probabilities and then interpolated between these values to construct the probability contours. This was done because of the sizable computational time required for generating each steady state SNR population for a given vector of parameters. Because of this, the peaks of our marginalized probabilities may slightly fluctuate, but the areas of parameter space ruled out by our model remain stable.

BIBLIOGRAPHY

Abbott, B. P., Abbott, R., Abbott, T. D., et al. 2016, Astrophysical Journal Letters, 818, L22

Ackermann, M., Ajello, M., Allafort, A., et al. 2013, Science (New York, N.Y.), 339, 807

Adams, S. M., Kochanek, C. S., Gerke, J. R., & Stanek, K. Z. 2017a, Monthly Notices of the Royal Astronomical Society, 469, 1445

Adams, S. M., Kochanek, C. S., Gerke, J. R., Stanek, K. Z., & Dai, X. 2017b, Monthly Notices of the Royal Astronomical Society, 468, 4968

Alcock, C., Allsman, R. A., Alves, D. R., et al. 2000, Astrophysical Journal, 542, 281

Alonso-García, J., Mateo, M., & Worthey, G. 2004, Astronomical Journal, 127, 868

Amato, E., & Blasi, P. 2009, Monthly Notices of the Royal Astronomical Society, 392, 1591

Amato, E., & Blasi, P. 2017, ArXiv e-prints, arXiv:1704.05696

Anderson, R. I., Ekström, S., Georgy, C., Meynet, G., & Saio, H. 2017, in European Physical Journal Web of Conferences, Vol. 152, European Physical Journal Web of Conferences, 06002

Andrews, B. H., Weinberg, D. H., Schönrich, R., & Johnson, J. A. 2017, Astrophysical Journal, 835, 224

Antoniou, V., & Zezas, A. 2016, Monthly Notices of the Royal Astronomical Society, 459, 528

Astropy Collaboration, Robitaille, T. P., Tollerud, E. J., et al. 2013, Astronomy & Astrophysics, 558, A33

Asvarov, A. I. 2014, Astronomy and Astrophysics, 561, A70

Auchettl, K., Lopez, L., Badenes, C., et al. 2018, ArXiv e-prints, arXiv:1804.10210

Axford, W. I., Leer, E., & Skadron, G. 1977, International Cosmic Ray Conference, 11, 132

Baade, W., & Zwicky, F. 1934, Proceedings of the National Academy of Science, 20, 259

Badenes, C. 2010, Proceedings to the National Academy of Sciences of the United States of America, 107, 7141

Badenes, C., Borkowski, K. J., Hughes, J. P., Hwang, U., & Bravo, E. 2006, Astrophysical Journal, 645, 1373

Badenes, C., Bravo, E., Borkowski, K. J., & Domínguez, I. 2003, Astrophysical Journal, 593, 358

Badenes, C., Harris, J., Zaritsky, D., & Prieto, J. L. 2009, Astrophysical Journal, 700, 727

Badenes, C., Hughes, J. P., Bravo, E., & Langer, N. 2007, Astrophysical Journal, 662, 472

Badenes, C., Hughes, J. P., Cassam-Chenaï, G., & Bravo, E. 2008, Astrophysical Journal, 680, 1149

Badenes, C., & Maoz, D. 2012, Astrophysical Journal, 749, L11

Badenes, C., Maoz, D., & Ciardullo, R. 2015, Astrophysical Journal Letters, 804, L25

Badenes, C., Maoz, D., & Draine, B. T. 2010, Monthly Notices of the Royal Astronomical Society, 407, 1301

Baker, M., & Willman, B. 2015, Astronomical Journal, 150, 160

Bamba, A., Yamazaki, R., Yoshida, T., Terasawa, T., & Koyama, K. 2005, Astrophysical Journal, 621, 793

Bandiera, R., & Petruk, O. 2010, Astronomy and Astrophysics, 509, A34

Barniol Duran, R., Whitehead, J. F., & Giannios, D. 2016, Monthly Notices of the Royal Astronomical Society, 462, L31

Baumgardt, H., Parmentier, G., Anders, P., & Grebel, E. K. 2013, Monthly Notices of the Royal Astronomical Society, 430, 676

Begelman, M. C., & Sarazin, C. L. 1986, Astrophysical Journal Letters, 302, L59

Bell, A. R. 2004, Monthly Notices of the Royal Astronomical Society, 353, 550

Bell, . 1978, Monthly Notices of the Royal Astronomical Society, 182, 147

Berezhko, E. G., Ksenofontov, L. T., & Völk, H. J. 2009a, Astronomy and Astrophysics, 505, 169

—. 2012, Astrophysical Journal, 759, 12

Berezhko, E. G., Pühlhofer, G., & Völk, H. J. 2009b, Astronomy and Astrophysics, 505, 641

Berezhko, E. G., & Völk, H. J. 2004a, Astronomy and Astrophysics, 427, 525

—. 2004b, Astronomy and Astrophysics, 427, 525

Berezhko, E. G., & Völk, H. J. 2006, Astronomy and Astrophysics, 451, 981

Berger, E., Kulkarni, S. R., & Chevalier, R. A. 2002, Astrophysical Journal, 577, L5

Beringer, J., Arguin, J. F., Barnett, R. M., et al. 2012, Physical Review D, 86, 010001

Berkhuijsen, E. M. 1984, Astronomy and Astrophysics, 140, 431

Bersten, M. C., Folatelli, G., García, F., et al. 2018, Nature, 554, 497

Bertelli, G., Nasi, E., Girardi, L., & Marigo, P. 2009, Astronomy and Astrophysics, 508, 355

Besla, G., Kallivayalil, N., Hernquist, L., et al. 2012, Monthly Notices of the Royal Astronomical Society, 421, 2109

Betoule, M., Kessler, R., Guy, J., et al. 2014, Astronomy and Astrophysics, 568, A22

Bica, E., Bonatto, C., Dutra, C. M., & Santos, J. F. C. 2008, Monthly Notices of the Royal Astronomical Society, 389, 678

Bildsten, L., Shen, K. J., Weinberg, N. N., & Nelemans, G. 2007, Astrophysical Journal Letters, 662, L95

Blair, W. P., Winkler, P. F., & Long, K. S. 2012, The Astrophysical Journal Supplement, 203, 8

Blanco, V. M. 1992, Astronomical Journal, 104, 734

Blandford, R., & Eichler, D. 1987, Physics Reports, 154, 1

Blandford, R. D., & Ostriker, J. P. 1978, Astrophysical Journal, 221, L29

Blasi, P., Amato, E., & Caprioli, D. 2007, Monthly Notices of the Royal Astronomical Society, 375, 1471

Blondin, J. M., Wright, E. B., Borkowski, K. J., & Reynolds, S. P. 1998, Astrophysical Journal, 500, 342

Blondin, S., Dessart, L., Hillier, D. J., & Khokhlov, A. M. 2013, Monthly Notices of the Royal Astronomical Society, 429, 2127

—. 2017, Monthly Notices of the Royal Astronomical Society, 470, 157

Bono, G., Caputo, F., Cassisi, S., Castellani, V., & Marconi, M. 1997a, Astrophysical Journal, 479, 279

Bono, G., Caputo, F., Cassisi, S., Incerpi, R., & Marconi, M. 1997b, Astrophysical Journal, 483, 811

Bono, G., Caputo, F., & Castellani, V. 2006, Memorie della Societa Astronomica Italiana, 77, 207

Bono, G., Dall'Ora, M., Caputo, F., et al. 2011, in RR Lyrae Stars, Metal-Poor Stars, and the Galaxy, ed. A. McWilliam, Vol. 5, 1

Bono, G., Marconi, M., Cassisi, S., et al. 2005, Astrophysical Journal, 621, 966

Bono, G., Braga, V. F., Pietrinferni, A., et al. 2016, Memorie della Societa Astronomica Italiana, 87, 358

Borkowski, K. J., Gwynne, P., Reynolds, S. P., et al. 2017, Astrophysical Journal Letters, 837, L7

Borkowski, K. J., Reynolds, S. P., Green, D. A., et al. 2010, Astrophysical Journal Letters, 724, L161

Borkowski, K. J., Reynolds, S. P., Hwang, U., et al. 2013, Astrophysical Journal Letters, 771, L9

Boubert, D., Fraser, M., Evans, N. W., Green, D. A., & Izzard, R. G. 2017, Astronomy and Astrophysics, 606, A14

Branch, D., Fisher, A., & Nugent, P. 1993, Astronomical Journal, 106, 2383

Braun, R. 2012, Astrophysical Journal, 749, 87

Braun, R., Thilker, D. A., Walterbos, R. A. M., & Corbelli, E. 2009, Astrophysical Journal, 695, 937

Bressan, A., Marigo, P., Girardi, L., et al. 2012, Monthly Notices of the Royal Astronomical Society, 427, 127

Briggs, D. 1995, High Fidelity Deconvolution of Moderately Resolved Sources (D. Briggs)

Buonanno, R., Corsi, C. E., Castellani, M., et al. 1999, Astronomical Journal, 118, 1671

Burrows, A. 2013, Reviews of Modern Physics, 85, 245

Cacciari, C., & Clementini, G. 2003, in Lecture Notes in Physics, Berlin Springer Verlag, Vol. 635, Stellar Candles for the Extragalactic Distance Scale, ed. D. Alloin & W. Gieren, 105–122

Caprioli, D. 2012, Journal of Cosmology and Astroparticle Physics, 7, 038

—. 2015, ArXiv e-prints, arXiv:1510.07042

Caprioli, D., & Spitkovsky, A. 2014a, Astrophysical Journal, 783, 91

—. 2014b, Astrophysical Journal, 794, 46

Carlton, A. K., Borkowski, K. J., Reynolds, S. P., et al. 2011, Astrophysical Journal Letters, 737, L22

Case, G. L., & Bhattacharya, D. 1998, Astrophysical Journal, 504, 761

Catelan, M. 2000, Astrophysical Journal, 531, 826

—. 2009, Astrophysics and Space Science, 320, 261

Catelan, M., Bellazzini, M., Landsman, W. B., et al. 2001, Astronomical Journal, 122, 3171

Catelan, M., & de Freitas Pacheco, J. A. 1995, Astronomy and Astrophysics, 297, 345

Chakraborti, S., Childs, F., & Soderberg, A. 2016, Astrophysical Journal, 819, 37

Chandrasekhar, S. 1931, Astrophysical Journal, 74, 81

Chen, H.-W. 2017, in Astrophysics and Space Science Library, Vol. 430, Gas Accretion onto Galaxies, ed. A. Fox & R. Davé, 167

Chevalier, R. A. 1982, Astrophysical Journal, 259, 302

—. 1998, Astrophysical Journal, 499, 810

Chevalier, R. A., & Fransson, C. 2006, Astrophysical Journal, 651, 381

Chevalier, R. A., Fransson, C., & Nymark, T. K. 2006, Astrophysical Journal, 641, 1029

Chevalier, R. A., & Plait, P. C. 1988, Astrophysical Journal Letters, 331, L109

Chini, R., Hoffmeister, V. H., Nasseri, A., Stahl, O., & Zinnecker, H. 2012, Monthly Notices of the Royal Astronomical Society, 424, 1925

Choi, J., Dotter, A., Conroy, C., et al. 2016, Astrophysical Journal, 823, 102

Chomiuk, L., & Povich, M. S. 2011, Astronomical Journal, 142, 197

Chomiuk, L., & Wilcots, E. M. 2009, Astrophysical Journal, 703, 370

Chomiuk, L., Soderberg, A. M., Moe, M., et al. 2012, Astrophysical Journal, 750, 164

Chomiuk, L., Soderberg, A. M., Chevalier, R. A., et al. 2016, Astrophysical Journal, 821, 119

Cioffi, D. F., McKee, C. F., & Bertschinger, E. 1988, Astrophysical Journal, 334, 252

Clement, C. M., Muzzin, A., Dufton, Q., et al. 2001, Astronomical Journal, 122, 2587

Clementini, G. 2010, in Variable Stars, the Galactic halo and Galaxy Formation, ed. C. Sterken, N. Samus, & L. Szabados

Clementini, G., Ripepi, V., Molinaro, R., et al. 2018, ArXiv e-prints, arXiv:1805.02079

Condon, J. J., Cotton, W. D., Greisen, E. W., et al. 1998, Astronomical Journal, 115, 1693

Conroy, C. 2013, Annual Reviews of Astronomy and Astrophysics, 51, 393

Cordier, D., Goupil, M. J., & Lebreton, Y. 2003, Astronomy and Astrophysics, 409, 491

Corsi, A., Gal-Yam, A., Kulkarni, S. R., et al. 2016, Astrophysical Journal, 830, 42

Cowan, J. J., & Branch, D. 1985, Astrophysical Journal, 293, 400

Cowan, J. J., Roberts, D. A., & Branch, D. 1994, Astrophysical Journal, 434, 128

Cowsik, R., & Sarkar, S. 1984, Monthly Notices of the Royal Astronomical Society, 207, 745

Cox, A. N. 1980, Annual Reviews of Astronomy and Astrophysics, 18, 15

Cox, J. P. 1963, Astrophysical Journal, 138, 487

Crane, P. C., Dickel, J. R., & Cowan, J. J. 1992, Astrophysical Journal Letters, 390, L9

Crowther, P. A. 2007, Annual Reviews of Astronomy and Astrophysics, 45, 177

Crutcher, R. M. 1999, Astrophysical Journal, 520, 706

Dalcanton, J. J., Williams, B. F., Lang, D., et al. 2012, The Astrophysical Journal Supplement, 200, 18

Dalcanton, J. J., Fouesneau, M., Hogg, D. W., et al. 2015, Astrophysical Journal, 814, 3

Dale, D. A., Cohen, S. A., Johnson, L. C., et al. 2009, Astrophysical Journal, 703, 517

Davies, B., & Beasor, E. R. 2018, Monthly Notices of the Royal Astronomical Society, 474, 2116

De Horta, A. Y., Filipovic, M. D., Crawford, E. J., et al. 2014, Serbian Astronomical Journal, 189, 41

de Vaucouleurs, G., & Corwin, Jr., H. G. 1985, Astrophysical Journal, 295, 287

Dékány, I., Minniti, D., Majaess, D., et al. 2015, Astrophysical Journal Letters, 812, L29

Dickey, J. M., & Lockman, F. J. 1990, Annual Reviews of Astronomy and Astrophysics, 28, 215

Dopita, M. A. 1979, The Astrophysical Journal Supplement, 40, 455

Dopita, M. A., Binette, L., & Tuohy, I. R. 1984, Astrophysical Journal, 282, 142

Dosaj, A., Garcia, M., Forman, W., et al. 2002, in Astronomical Society of the Pacific Conference Series, Vol. 262, The High Energy Universe at Sharp Focus: Chandra Science, ed. E. M. Schlegel & S. D. Vrtilek, 147

Dotter, A. 2008, Astrophysical Journal Letters, 687, L21

—. 2013, Memorie della Societa Astronomica Italiana, 84, 97

Draine, B. T. 2011, Physics of the Interstellar and Intergalactic Medium

Drake, A. J., Graham, M. J., Djorgovski, S. G., et al. 2014, The Astrophysical Journal Supplement, 213, 9

Drout, M. R., Soderberg, A. M., Gal-Yam, A., et al. 2011, Astrophysical Journal, 741, 97

Drout, M. R., Soderberg, A. M., Mazzali, P. A., et al. 2013, Astrophysical Journal, 774, 58

Drout, M. R., Chornock, R., Soderberg, A. M., et al. 2014, Astrophysical Journal, 794, 23

Drury, L. O. 1983, Reports on Progress in Physics, 46, 973

Duric, N., Viallefond, F., Goss, W. M., & van der Hulst, J. M. 1993, AAPs, 99, 217

Dwarkadas, V. V. 2014, Monthly Notices of the Royal Astronomical Society, 440, 1917

Eck, C. R., Cowan, J. J., & Branch, D. 2002, Astrophysical Journal, 573, 306

Eck, C. R., Roberts, D. A., Cowan, J. J., & Branch, D. 1998, Astrophysical Journal, 508, 664

Eddington, A. S. 1926, The Observatory, 49, 88

Edwards, Z. I., Pagnotta, A., & Schaefer, B. E. 2012, Astrophysical Journal, 747, L19

Eldridge, J. J., Stanway, E. R., Xiao, L., et al. 2017, ArXiv e-prints, arXiv:1710.02154

Elmegreen, B. G., & Scalo, J. 2004, Annual Reviews of Astronomy and Astrophysics, 42, 211

Espey, B. R., & Crowley, C. 2008, in Astronomical Society of the Pacific Conference Series, Vol. 401, RS Ophiuchi (2006) and the Recurrent Nova Phenomenon, ed. A. Evans, M. F. Bode, T. J. O'Brien, & M. J. Darnley, 166

Evans, N. E., Bond, H. E., Schaefer, G. H., et al. 2013, Astronomical Journal, 146, 93

Farmer, R., Fields, C. E., & Timmes, F. X. 2015, Astrophysical Journal, 807, 184

Faucher-Giguère, C.-A., Quataert, E., & Hopkins, P. F. 2013, Monthly Notices of the Royal Astronomical Society, 433, 1970

Faulkner, J., & Iben, Jr., I. 1966, Astrophysical Journal, 144, 995

Ferrière, K. M. 2001, Reviews of Modern Physics, 73, 1031

Fesen, R., Hoeflich, P., & Hamilton, A. 2016, in Supernova Remnants: An Odyssey in Space after Stellar Death, 115

Fesen, R. A., Gerardy, C. L., McLin, K. M., & Hamilton, A. J. S. 1999, Astrophysical Journal, 514, 195

Fesen, R. A., Höflich, P. A., & Hamilton, A. J. S. 2015, Astrophysical Journal, 804, 140

Fesen, R. A., Höflich, P. A., Hamilton, A. J. S., et al. 2007, Astrophysical Journal, 658, 396

Fesen, R. A., & Milisavljevic, D. 2016, Astrophysical Journal, 818, 17

Fesen, R. A., Saken, J. M., & Hamilton, A. J. S. 1989, Astrophysical Journal Letters, 341, L55

Fesen, R. A., Hammell, M. C., Morse, J., et al. 2006, Astrophysical Journal, 645, 283

Filippenko, A. V. 1989, Publications of the Astronomical Society of the Pacific, 101, 588

—. 1997, Annual Reviews of Astronomy and Astrophysics, 35, 309

Filippenko, A. V., & Sargent, W. L. W. 1986, Astronomical Journal, 91, 691

Filippenko, A. V., Richmond, M. W., Branch, D., et al. 1992, Astronomical Journal, 104, 1543

Fink, M., Röpke, F. K., Hillebrandt, W., et al. 2010, Astronomy and Astrophysics, 514, A53

Foglizzo, T. 2017, Explosion Physics of Core-Collapse Supernovae, ed. A. W. Alsabti & P. Murdin, 1053

Foley, R. J., Jha, S. W., Pan, Y.-C., et al. 2016, Monthly Notices of the Royal Astronomical Society, 461, 433

Foley, R. J., Challis, P. J., Chornock, R., et al. 2013, Astrophysical Journal, 767, 57

Fransson, C., & Chevalier, R. A. 1989, Astrophysical Journal, 343, 323

Freedman, W. L., & Madore, B. F. 2010, Annual Reviews of Astronomy and Astrophysics, 48, 673

Frieman, J. A., Turner, M. S., & Huterer, D. 2008, Annual Reviews of Astronomy and Astrophysics, 46, 385

Fusi Pecci, F., & Bellazzini, M. 1997, in The Third Conference on Faint Blue Stars, ed. A. G. D. Philip, J. Liebert, R. Saffer, & D. S. Hayes, 255

Gal-Yam, A., & Maoz, D. 2004, Monthly Notices of the Royal Astronomical Society, 347, 942

Galbany, L., Anderson, J. P., Sánchez, S. F., et al. 2018, Astrophysical Journal, 855, 107

Gallart, C., Zoccali, M., & Aparicio, A. 2005, Annual Reviews of Astronomy and Astrophysics, 43, 387

Garcia, M. R., Williams, B. F., Yuan, F., et al. 2005, Astrophysical Journal, 632, 1042

Garcia, M. R., Hextall, R., Baganoff, F. K., et al. 2010, Astrophysical Journal, 710, 755

García-Berro, E., Badenes, C., Aznar-Siguán, G., & Lorén-Aguilar, P. 2017, Monthly Notices of the Royal Astronomical Society, 468, 4815

Garofali, K., Williams, B. F., Hillis, T., et al. 2018, Monthly Notices of the Royal Astronomical Society, 479, 3526

Garofali, K., Williams, B. F., Plucinsky, P. P., et al. 2017, Monthly Notices of the Royal Astronomical Society, 472, 308

Gaskell, C. M., Cappellaro, E., Dinerstein, H. L., et al. 1986, Astrophysical Journal Letters, 306, L77

Geha, M., Brown, T. M., Tumlinson, J., et al. 2013, Astrophysical Journal, 771, 29

Gent, F. A., Shukurov, A., Fletcher, A., Sarson, G. R., & Mantere, M. J. 2013, Monthly Notices of the Royal Astronomical Society, 432, 1396

Gerke, J. R., Kochanek, C. S., & Stanek, K. Z. 2015, Monthly Notices of the Royal Astronomical Society, 450, 3289

Gil de Paz, A., Boissier, S., Madore, B. F., et al. 2007, The Astrophysical Journal Supplement, 173, 185

Girichidis, P., Naab, T., Walch, S., et al. 2016, Astrophysical Journal, 816, L19

Gooch, R. 1996, in ASP Conf. Ser., Vol. 101, Astronomical Data Analysis Software and Systems V, ed. G. H. Jacoby & J. Barnes, 80

Gordon, S. M., Duric, N., Kirshner, R. P., Goss, W. M., & Viallefond, F. 1999, The Astrophysical Journal Supplement, 120, 247

Gordon, S. M., Kirshner, R. P., Long, K. S., et al. 1998, The Astrophysical Journal Supplement, 117, 89

Graur, O., Bianco, F. B., Huang, S., et al. 2017a, Astrophysical Journal, 837, 120

Graur, O., Bianco, F. B., Modjaz, M., et al. 2017b, Astrophysical Journal, 837, 121

Graur, O., Rodney, S. A., Maoz, D., et al. 2014, Astrophysical Journal, 783, 28

Green, D. A. 2014a, Bulletin of the Astronomical Society of India, 42, 47

—. 2014b, Bulletin of the Astronomical Society of India, 42, 47

—. 2017, A Catalogue of Galactic Supernova Remnants (2017 June version), Cavendish Laboratory, Cambridge, United Kingdom

Green, D. A., Reynolds, S. P., Borkowski, K. J., et al. 2008, Monthly Notices of the Royal Astronomical Society, 387, L54

Grefenstette, B. W., Harrison, F. A., Boggs, S. E., et al. 2014, Nature, 506, 339

Grefenstette, B. W., Fryer, C. L., Harrison, F. A., et al. 2017, Astrophysical Journal, 834, 19

Greisen, E. W. 1990, in Acquisition, Processing and Archiving of Astronomical Images, ed. G. Longo & G. Sedmak, 125–142

Griest, K. 1991, Astrophysical Journal, 366, 412

Hachisu, I., Kato, M., & Nomoto, K. 1996, Astrophysical Journal Letters, 470, L97

—. 1999, Astrophysical Journal, 522, 487

Hamilton, A. J. S., & Fesen, R. A. 2000, Astrophysical Journal, 542, 779

Hammer, F., Yang, Y. B., Wang, J. L., et al. 2018, Monthly Notices of the Royal Astronomical Society, 475, 2754

Han, Z., & Podsiadlowski, P. 2004, Monthly Notices of the Royal Astronomical Society, 350, 1301

Hancock, P. J., Gaensler, B. M., & Murphy, T. 2011, Astrophysical Journal Letters, 735, L35

Hao, C.-N., Kennicutt, R. C., Johnson, B. D., et al. 2011, Astrophysical Journal, 741, 124

Harris, J., & Zaritsky, D. 2004, Astronomical Journal, 127, 1531

—. 2009, Astronomical Journal, 138, 1243

Heckman, T. M., & Thompson, T. A. 2017, ArXiv e-prints, arXiv:1701.09062

Heiles, C. 1987, Astrophysical Journal, 315, 555

H.E.S.S. Collaboration, Abramowski, A., Aharonian, F., et al. 2014, Monthly Notices of the Royal Astronomical Society, 441, 790

Hill, A. S., Ryan Joung, M., Mac Low, M.-M., et al. 2012, Astrophysical Journal, 750, 104

Hillebrandt, W., Kromer, M., Röpke, F. K., & Ruiter, A. J. 2013, Frontiers of Physics, 8, 116

Hillebrandt, W., & Niemeyer, J. C. 2000, Annual Reviews of Astronomy and Astrophysics, 38, 191

Hirata, K., Kajita, T., Koshiba, M., et al. 1987, Physical Review Letters, 58, 1490

Holland-Ashford, T., Lopez, L. A., Auchettl, K., Temim, T., & Ramirez-Ruiz, E. 2017, Astrophysical Journal, 844, 84

Holtzman, J. A., Gallagher, III, J. S., Cole, A. A., et al. 1999, Astronomical Journal, 118, 2262

Hopkins, P. F., Quataert, E., & Murray, N. 2012, Monthly Notices of the Royal Astronomical Society, 421, 3488

Horesh, A., Kulkarni, S. R., Fox, D. B., et al. 2012, Astrophysical Journal, 746, 21

Horiuchi, S., Beacom, J. F., Kochanek, C. S., et al. 2011, Astrophysical Journal, 738, 154

Horiuchi, S., Nakamura, K., Takiwaki, T., Kotake, K., & Tanaka, M. 2014, Monthly Notices of the Royal Astronomical Society, 445, L99

Howell, D. A. 2011, Nature communications, 2, 350

Hunter, J. D. 2007, Computing In Science & Engineering, 9, 90

Iben, Jr., I. 1974, Annual Reviews of Astronomy and Astrophysics, 12, 215

Iben, Jr., I., & Tutukov, A. V. 1984, The Astrophysical Journal Supplement, 54, 335

Iwamoto, K., Brachwitz, F., Nomoto, K., et al. 1999, The Astrophysical Journal Supplement, 125, 439

Jacyszyn-Dobrzeniecka, A. M., Skowron, D. M., Mróz, P., et al. 2016, Acta Astronomica, 66, 149

Janka, H.-T. 2017, Neutrino-Driven Explosions, ed. A. W. Alsabti & P. Murdin, 1095

Jennings, Z. G., Williams, B. F., Murphy, J. W., et al. 2014, Astrophysical Journal, 795, 170

Jennings, Z. G., Williams, B. F., Murphy, J. W., et al. 2014, Astrophysical Journal, 795, 170

Jerkstrand, A., Smartt, S. J., Sollerman, J., et al. 2015, Monthly Notices of the Royal Astronomical Society, 448, 2482

Jha, S. W. 2017, ArXiv e-prints, arXiv:1707.01110

Johnson, L. C., Seth, A. C., Dalcanton, J. J., et al. 2017, Astrophysical Journal, 839, 78

Jones, E., Oliphant, T., Peterson, P., et al. 2001–, SciPy: Open source scientific tools for Python, , , [Online; accessed ¡today¿]

Jones, F. C., & Ellison, D. C. 1991, Space Science Reviews, 58, 259

Joung, M. K. R., & Mac Low, M. 2006, Astrophysical Journal, 653, 1266

Jurcsik, J., & Kovacs, G. 1996, Astronomy and Astrophysics, 312, 111

Jurić, M., Ivezić, Ž., Brooks, A., et al. 2008, Astrophysical Journal, 673, 864

Karczmarek, P., Wiktorowicz, G., Iłkiewicz, K., et al. 2017, Monthly Notices of the Royal Astronomical Society, 466, 2842

Kasliwal, M. M. 2012, 29, 482488

Kasliwal, M. M., Kulkarni, S. R., Gal-Yam, A., et al. 2012, Astrophysical Journal, 755, 161

Katsuda, S., Morii, M., Janka, H.-T., et al. 2018, Astrophysical Journal, 856, 18

Keller, S. C. 2008, Astrophysical Journal, 677, 483

Kelly, P. L., Fox, O. D., Filippenko, A. V., et al. 2014, Astrophysical Journal, 790, 3

Kennicutt, R. C., & Evans, N. J. 2012, Annual Reviews of Astronomy and Astrophysics, 50, 531

Kennicutt, Jr., R. C. 1998, Astrophysical Journal, 498, 541

Kennicutt, Jr., R. C., Lee, J. C., Funes, S. J., J. G., Sakai, S., & Akiyama, S. 2008, The Astrophysical Journal Supplement, 178, 247

Kerzendorf, W. E., Schmidt, B. P., Asplund, M., et al. 2009, Astrophysical Journal, 701, 1665

Kerzendorf, W. E., Schmidt, B. P., Laird, J. B., Podsiadlowski, P., & Bessell, M. S. 2012, Astrophysical Journal, 759, 7

Kerzendorf, W. E., Strampelli, G., Shen, K. J., et al. 2018, Monthly Notices of the Royal Astronomical Society, 479, 192

Khokhlov, A. M. 1991, Astronomy and Astrophysics, 245, 114

Kim, C.-G., & Ostriker, E. C. 2015, Astrophysical Journal, 802, 99

Kim, C.-G., & Ostriker, E. C. 2015, Astrophysical Journal, 815, 67

Kinman, T. D., & Brown, W. R. 2010, Astronomical Journal, 139, 2014

Kippenhahn, R., & Weigert, A. 1990, Stellar Structure and Evolution, 192

Kochanek, C. S. 2014, Astrophysical Journal, 785, 28

Kochanek, C. S., Beacom, J. F., Kistler, M. D., et al. 2008, Astrophysical Journal, 684, 1336

Kochanek, C. S., Khan, R., & Dai, X. 2012, Astrophysical Journal, 759, 20

Koyama, K., Petre, R., Gotthelf, E. V., et al. 1995, Nature, 378, 255

Kozłowski, S., Udalski, A., Wyrzykowski, Ł., et al. 2013, Acta Astronomica, 63, 1

Kraft, R. P. 1977, in IAU Colloq. 42: The Interaction of Variable Stars with their Environment, ed. R. Kippenhahn, J. Rahe, & W. Strohmeier, 521

Kraft, R. P., & Schmidt, M. 1963, Astrophysical Journal, 137, 249

Kromer, M., Sim, S. A., Fink, M., et al. 2010, Astrophysical Journal, 719, 1067

Krymskii, G. F. 1977, Akademiia Nauk SSSR Doklady, 234, 1306

Ksenofontov, L. T., Völk, H. J., & Berezhko, E. G. 2010, Astrophysical Journal, 714, 1187

Kunder, A., Chaboyer, B., & Layden, A. 2010, Astronomical Journal, 139, 415

Kushnir, D., Katz, B., Dong, S., Livne, E., & Fernández, R. 2013, Astrophysical Journal Letters, 778, L37

Layden, A. C., Ritter, L. A., Welch, D. L., & Webb, T. M. A. 1999, Astronomical Journal, 117, 1313

Lazzarini, M., Hornschemeier, A. E., Williams, B. F., et al. 2018, Astrophysical Journal, 862, 28

Leaman, J., Li, W., Chornock, R., & Filippenko, A. V. 2011, Monthly Notices of the Royal Astronomical Society, 412, 1419

Leavitt, H. S. 1908, Annals of Harvard College Observatory, 60, 87

Lee, J. H., & Lee, M. G. 2014, Astrophysical Journal, 786, 130

Lee, J. H., & Lee, M. G. 2014, Astrophysical Journal, 793, 134

Leroy, A. K., Walter, F., Brinks, E., et al. 2008, Astronomical Journal, 136, 2782

Lewis, A. R., Dolphin, A. E., Dalcanton, J. J., et al. 2015, Astrophysical Journal, 805, 183

Lewis, A. R., Simones, J. E., Johnson, B. D., et al. 2017, Astrophysical Journal, 834, 70

Li, M., Ostriker, J. P., Cen, R., Bryan, G. L., & Naab, T. 2015, Astrophysical Journal, 814, 4

Li, W., Leaman, J., Chornock, R., et al. 2011, Monthly Notices of the Royal Astronomical Society, 412, 1441

Li, W., Bloom, J. S., Podsiadlowski, P., et al. 2011, Nature, 480, 348

Li, X.-D., & van den Heuvel, E. P. J. 1997, Astronomy and Astrophysics, 322, L9

Li, Z. 2011, in Astronomical Society of the Pacific Conference Series, Vol. 439, The Galactic Center: a Window to the Nuclear Environment of Disk Galaxies, ed. M. R. Morris, Q. D. Wang, & F. Yuan, 468

Li, Z., & Chevalier, R. A. 1999, Astrophysical Journal, 526, 716

Li, Z., Wang, Q. D., & Wakker, B. P. 2009, Monthly Notices of the Royal Astronomical Society, 397, 148

Lien, A., Chakraborty, N., Fields, B. D., & Kemball, A. 2011, Astrophysical Journal, 740, 23

Livio, M., & Mazzali, P. 2018, Physics Reports, 736, 1

Long, K. S., Blair, W. P., Winkler, P. F., et al. 2010, The Astrophysical Journal Supplement, 187, 495

Longmore, A. J., Dixon, R., Skillen, I., Jameson, R. F., & Fernley, J. A. 1990, Monthly Notices of the Royal Astronomical Society, 247, 684

Longmore, A. J., Fernley, J. A., & Jameson, R. F. 1986, Monthly Notices of the Royal Astronomical Society, 220, 279

Lopez, L. A., & Fesen, R. A. 2018, Space Science Reviews, 214, 44

Lopez, L. A., Ramirez-Ruiz, E., Badenes, C., et al. 2009, Astrophysical Journal, 706, L106

Lopez, L. A., Ramirez-Ruiz, E., Huppenkothen, D., Badenes, C., & Pooley, D. A. 2011, Astrophysical Journal, 732, 114

Lorén-Aguilar, P., Isern, J., & García-Berro, E. 2009, Astronomy and Astrophysics, 500, 1193

Lyman, J. D., Bersier, D., James, P. A., et al. 2016, Monthly Notices of the Royal Astronomical Society, 457, 328

Mac Low, M.-M., & McCray, R. 1988, Astrophysical Journal, 324, 776

Mackey, A. D., Huxor, A., Ferguson, A. M. N., et al. 2006, Astrophysical Journal Letters, 653, L105

Maeda, K., Röpke, F. K., Fink, M., et al. 2010, Astrophysical Journal, 712, 624

Maeder, A. 2009, Physics, Formation and Evolution of Rotating Stars, doi:10.1007/978-3-540-76949-1

Maggi, P., Haberl, F., Kavanagh, P. J., et al. 2016, Astronomy and Astrophysics, 585, A162

Majaess, D. J., Turner, D. G., & Lane, D. J. 2009, Monthly Notices of the Royal Astronomical Society, 398, 263

Malkov, M. A., & Drury, L. O. 2001, Reports on Progress in Physics, 64, 429

Maoz, D., & Badenes, C. 2010, Monthly Notices of the Royal Astronomical Society, 407, 1314

Maoz, D., & Badenes, C. 2010, Monthly Notices of the Royal Astronomical Society, 407, 1314

Maoz, D., Hallakoun, N., & Badenes, C. 2018, Monthly Notices of the Royal Astronomical Society, 476, 2584

Maoz, D., & Mannucci, F. 2012, Publications of the Astronomical Society of Australia, 29, 447

Maoz, D., Mannucci, F., & Brandt, T. D. 2012, Monthly Notices of the Royal Astronomical Society, 426, 3282

Maoz, D., Mannucci, F., Li, W., et al. 2011, Monthly Notices of the Royal Astronomical Society, 412, 1508

Maoz, D., Mannucci, F., & Nelemans, G. 2014, Annual Reviews of Astronomy and Astrophysics, 52, 107

Maoz, D., & Rix, H.-W. 1993, Astrophysical Journal, 416, 425

Maoz, D., & Sharon, K. 2010, Astrophysical Journal, 722, 1879

Marconi, M. 2009, in American Institute of Physics Conference Series, Vol. 1170, American Institute of Physics Conference Series, ed. J. A. Guzik & P. A. Bradley, 223–234

Marconi, M., Coppola, G., Bono, G., et al. 2015, Astrophysical Journal, 808, 50

Margutti, R., Parrent, J., Kamble, A., et al. 2014, Astrophysical Journal, 790, 52

Margutti, R., Soderberg, A. M., Chomiuk, L., et al. 2012, Astrophysical Journal, 751, 134

Margutti, R., Kamble, A., Milisavljevic, D., et al. 2017, Astrophysical Journal, 835, 140

Martin, J., Rea, N., Torres, D. F., & Papitto, A. 2014, Monthly Notices of the Royal Astronomical Society, 444, 2910

Martínez-Rodríguez, H., Piro, A. L., Schwab, J., & Badenes, C. 2016, Astrophysical Journal, 825, 57

Martínez-Rodríguez, H., Badenes, C., Yamaguchi, H., et al. 2017a, Astrophysical Journal, 843, 35

—. 2017b, Astrophysical Journal, 843, 35

Martizzi, D., Faucher-Giguere, C.-A., & Quataert, E. 2015, Monthly Notices of the Royal Astronomical Society, 450, 504

Massey, P., Olsen, K. A. G., Hodge, P. W., et al. 2006, Astronomical Journal, 131, 2478

Massey, P., Olsen, K. A. G., Hodge, P. W., et al. 2006, Astronomical Journal, 131, 2478

Mateu, C., Vivas, A. K., Downes, J. J., et al. 2012, Monthly Notices of the Royal Astronomical Society, 427, 3374

Mathewson, D. S., & Clarke, J. N. 1973, Astrophysical Journal, 180, 725

Matteucci, F., Spitoni, E., Recchi, S., & Valiante, R. 2009, Astronomy and Astrophysics, 501, 531

Matthews, L. D., Marengo, M., Evans, N. R., & Bono, G. 2012, Astrophysical Journal, 744, 53

Matzner, C. D., & McKee, C. F. 1999, Astrophysical Journal, 510, 379

Maund, J. R., Smartt, S. J., Kudritzki, R. P., Podsiadlowski, P., & Gilmore, G. F. 2004, Nature, 427, 129

Maund, J. R., Spyromilio, J., Höflich, P. A., et al. 2013, Monthly Notices of the Royal Astronomical Society, 433, L20

Mazzali, P. A., Chugai, N., Turatto, M., et al. 1997, Monthly Notices of the Royal Astronomical Society, 284, 151

McConnachie, A. W., Irwin, M. J., Ferguson, A. M. N., et al. 2005, Monthly Notices of the Royal Astronomical Society, 356, 979

McCray, R., & Fransson, C. 2016, Annual Reviews of Astronomy and Astrophysics, 54, 19

McCully, C., Jha, S. W., Foley, R. J., et al. 2014, Astrophysical Journal, 786, 134

McKee, C. F., & Cowie, L. L. 1975, Astrophysical Journal, 195, 715

McKee, C. F., & Ostriker, J. P. 1977, Astrophysical Journal, 218, 148

Meng, X. C., Chen, W. C., Yang, W. M., & Li, Z. M. 2010, Astronomy and Astrophysics, 525, A129

Milisavljevic, D., & Fesen, R. A. 2017, ArXiv e-prints, arXiv:1701.00891

Miller, G. E., & Scalo, J. M. 1979, The Astrophysical Journal Supplement, 41, 513

Minniti, D., Contreras Ramos, R., Zoccali, M., et al. 2016, Astrophysical Journal Letters, 830, L14

Moe, M., & Di Stefano, R. 2017, The Astrophysical Journal Supplement, 230, 15

Moehler, S., Landsman, W. B., & Dorman, B. 2000, Astronomy and Astrophysics, 361, 937

Moll, R., Raskin, C., Kasen, D., & Woosley, S. E. 2014, Astrophysical Journal, 785, 105

Monet, D. G., Levine, S. E., Canzian, B., et al. 2003, Astronomical Journal, 125, 984

Monteagudo, L., Gallart, C., Monelli, M., Bernard, E. J., & Stetson, P. B. 2018, Monthly Notices of the Royal Astronomical Society, 473, L16

Morlino, G., Amato, E., Blasi, P., & Caprioli, D. 2010, Monthly Notices of the Royal Astronomical Society, 405, L21

Morlino, G., Bandiera, R., Blasi, P., & Amato, E. 2012, Astrophysical Journal, 760, 137

Morlino, G., & Caprioli, D. 2012, Astronomy and Astrophysics, 538, A81

Morrissey, P., Conrow, T., Barlow, T. A., et al. 2007, The Astrophysical Journal Supplement, 173, 682

Müller, B. 2016, Publications of the Astronomical Society of Australia, 33, e048

Naab, T., & Ostriker, J. P. 2017, Annual Reviews of Astronomy and Astrophysics, 55, 59

Neilson, H. R. 2014, Astronomy and Astrophysics, 563, A48

Neilson, H. R., & Lester, J. B. 2008, Astrophysical Journal, 684, 569

—. 2009, Astrophysical Journal, 690, 1829

Neilson, H. R., Schneider, F. R. N., Izzard, R. G., Evans, N. R., & Langer, N. 2015, Astronomy and Astrophysics, 574, A2

Nelemans, G., Toonen, S., & Bours, M. 2013, in IAU Symposium, Vol. 281, Binary Paths to Type Ia Supernovae Explosions, ed. R. Di Stefano, M. Orio, & M. Moe, 225–231

Nemec, J. M., Cohen, J. G., Ripepi, V., et al. 2013, Astrophysical Journal, 773, 181

Nomoto, K. 1980, Space Science Reviews, 27, 563

—. 1982a, Astrophysical Journal, 253, 798

—. 1982b, Astrophysical Journal, 257, 780

Nomoto, K., & Iben, Jr., I. 1985, Astrophysical Journal, 297, 531

Nomoto, K., Kobayashi, C., & Tominaga, N. 2013, Annual Reviews of Astronomy and Astrophysics, 51, 457

Nugent, P. E., Sullivan, M., Cenko, S. B., et al. 2011, Nature, 480, 344

O'Connor, E., & Ott, C. D. 2011, Astrophysical Journal, 730, 70

Offner, S. S. R., Clark, P. C., Hennebelle, P., et al. 2014, Protostars and Planets VI, 53

Olsen, K. A. G. 1999, Astronomical Journal, 117, 2244

Olszewski, E. W., Suntzeff, N. B., & Mateo, M. 1996, Annual Reviews of Astronomy and Astrophysics, 34, 511

Origlia, L., Rood, R. T., Fabbri, S., et al. 2007, Astrophysical Journal, 667, L85

Owocki, S. 2014, ArXiv e-prints, arXiv:1409.2084

Pacholczyk, A. G. 1970, Radio astrophysics. Nonthermal processes in galactic and extragalactic sources

Paczynski, B. 1986, Astrophysical Journal, 304, 1

Pagnotta, A., & Schaefer, B. E. 2015, Astrophysical Journal, 799, 101

Panagia, N., Van Dyk, S. D., Weiler, K. W., et al. 2006, Astrophysical Journal, 646, 369

Parizot, E., Marcowith, A., Ballet, J., & Gallant, Y. A. 2006, Astronomy and Astrophysics, 453, 387

Park, J., Caprioli, D., & Spitkovsky, A. 2015, Physical Review Letters, 114, 085003

Park, S., Badenes, C., Mori, K., et al. 2013, Astrophysical Journal Letters, 767, L10

Patnaude, D., & Badenes, C. 2017, ArXiv e-prints, arXiv:1702.03228

Patnaude, D. J., Lee, S.-H., Slane, P. O., et al. 2015, Astrophysical Journal, 803, 101

—. 2017, Astrophysical Journal, 849, 109

Pavlović, M. Z. 2017, Monthly Notices of the Royal Astronomical Society, 468, 1616

Paxton, B., Bildsten, L., Dotter, A., et al. 2011, The Astrophysical Journal Supplement, 192, 3

Pejcha, O., & Thompson, T. A. 2015, Astrophysical Journal, 801, 90

Perets, H. B., Badenes, C., Arcavi, I., Simon, J. D., & Gal-yam, A. 2011, Astrophysical Journal, 730, 89

Perets, H. B., Gal-Yam, A., Mazzali, P. A., et al. 2010, Nature, 465, 322

Pérez, F., & Granger, B. E. 2007, Computing in Science and Engineering, 9, 21. http://ipython.org

Pérez-Torres, M. A., Lundqvist, P., Beswick, R. J., et al. 2014, Astrophysical Journal, 792, 38

Perlmutter, S., Aldering, G., Goldhaber, G., et al. 1999, Astrophysical Journal, 517, 565

Peters, C. L., Lopez, L. A., Ramirez-Ruiz, E., Stassun, K. G., & Figueroa-Feliciano, E. 2013, Astrophysical Journal, 771, L38

Peterson, R. C. 1982, Astrophysical Journal, 258, 499

Phillips, M. M. 1993, Astrophysical Journal Letters, 413, L105

Piersimoni, A. M., Bono, G., & Ripepi, V. 2002, Astronomical Journal, 124, 1528

Pietrzyński, G., Thompson, I. B., Gieren, W., et al. 2010, Nature, 468, 542

Piro, A. L., & Bildsten, L. 2008, Astrophysical Journal, 673, 1009

Podsiadlowski, P., Joss, P. C., & Hsu, J. J. L. 1992, Astrophysical Journal, 391, 246

Podsiadlowski, P., Mazzali, P. A., Nomoto, K., Lazzati, D., & Cappellaro, E. 2004, Astrophysical Journal, 607, L17

Pohl, M., Yan, H., & Lazarian, A. 2005, Astrophysical Journal, 626, L101

Ponder, K. A., Wood-Vasey, W. M., & Zentner, A. R. 2016, Astrophysical Journal, 825, 35

Porter, A. L., Leising, M. D., Williams, G. G., et al. 2016, Astrophysical Journal, 828, 24

Preston, G. W. 1959, Astrophysical Journal, 130, 507

—. 1964, Annual Reviews of Astronomy and Astrophysics, 2, 23

Prichard, L. J., Guhathakurta, P., Hamren, K. M., et al. 2017, Monthly Notices of the Royal Astronomical Society, 465, 4180

Pritzl, B. J., Smith, H. A., Catelan, M., & Sweigart, A. V. 2001, Astronomical Journal, 122, 2600

—. 2002, Astronomical Journal, 124, 949

Rampadarath, H., Morgan, J. S., Soria, R., et al. 2015, Monthly Notices of the Royal Astronomical Society, 452, 32

Raskin, C., & Kasen, D. 2013, Astrophysical Journal, 772, 1

Reimers, D. 1975, Memoires of the Societe Royale des Sciences de Liege, 8, 369

Reina-Campos, M., & Kruijssen, J. M. D. 2017, Monthly Notices of the Royal Astronomical Society, 469, 1282

Ressler, S. M., Katsuda, S., Reynolds, S. P., et al. 2014, Astrophysical Journal, 790, 85

Rest, A., Suntzeff, N. B., Olsen, K., et al. 2005, Nature, 438, 1132

Reynolds, S. P., Borkowski, K. J., Green, D. A., et al. 2008, Astrophysical Journal Letters, 680, L41

Reynoso, E. M., Hughes, J. P., & Moffett, D. A. 2013, Astronomical Journal, 145, 104

Riess, A. G., Filippenko, A. V., Challis, P., et al. 1998, Astronomical Journal, 116, 1009

Riess, A. G., Macri, L. M., Hoffmann, S. L., et al. 2016, Astrophysical Journal, 826, 56

Riess, A. G., Casertano, S., Yuan, W., et al. 2018, Astrophysical Journal, 855, 136

Rigault, M., Copin, Y., Aldering, G., et al. 2013, Astronomy and Astrophysics, 560, A66

Ripepi, V., Clementini, G., Di Criscienzo, M., et al. 2007, Astrophysical Journal Letters, 667, L61

Russell, B. R., & Immler, S. 2012, Astrophysical Journal Letters, 748, L29

Saglia, R. P., Fabricius, M., Bender, R., et al. 2010, Astronomy and Astrophysics, 509, A61

Salaris, M., & Cassisi, S. 2005, Evolution of Stars and Stellar Populations, 400

Salaris, M., Cassisi, S., & Pietrinferni, A. 2016, Astronomy and Astrophysics, 590, A64

Salaris, M., Held, E. V., Ortolani, S., Gullieuszik, M., & Momany, Y. 2007, Astronomy and Astrophysics, 476, 243

Salpeter, E. E. 1955, Astrophysical Journal, 121, 161

Sana, H., de Mink, S. E., de Koter, A., et al. 2012, Science, 337, 444

Sandage, A. 2004, Astronomical Journal, 128, 858

Sandage, A., & Tammann, G. A. 2006, Annual Reviews of Astronomy and Astrophysics, 44, 93

Sandage, A., & Wallerstein, G. 1960, Astrophysical Journal, 131, 598

Sandage, A., & Wildey, R. 1967, Astrophysical Journal, 150, 469

Sarajedini, A. 2009, in IAU Symposium, Vol. 258, The Ages of Stars, ed. E. E. Mamajek, D. R. Soderblom, & R. F. G. Wyse, 221–232

Sarajedini, A. 2011, in RR Lyrae Stars, Metal-Poor Stars, and the Galaxy, ed. A. McWilliam, Vol. 5, 181

Sarajedini, A., Yang, S.-C., Monachesi, A., Lauer, T. R., & Trager, S. C. 2012, Monthly Notices of the Royal Astronomical Society, 425, 1459

Sarbadhicary, S. K., Badenes, C., Chomiuk, L., Caprioli, D., & Huizenga, D. 2017a, Monthly Notices of the Royal Astronomical Society, 464, 2326

Sarbadhicary, S. K., Chomiuk, L., Badenes, C., et al. 2017b, ArXiv e-prints, arXiv:1709.05346

Scalzo, R. A., Ruiter, A. J., & Sim, S. A. 2014, Monthly Notices of the Royal Astronomical Society, 445, 2535

Schaefer, B. E., & Pagnotta, A. 2012, Nature, 481, 164

Schröder, K.-P., & Cuntz, M. 2005, Astrophysical Journal Letters, 630, L73

Sedov, L. I. 1959, Similarity and Dimensional Methods in Mechanics

Seitenzahl, I. R., Cescutti, G., Röpke, F. K., Ruiter, A. J., & Pakmor, R. 2013, Astronomy and Astrophysics, 559, L5

Shen, K. J., Bildsten, L., Kasen, D., & Quataert, E. 2012, Astrophysical Journal, 748, 35

Shen, K. J., Guillochon, J., & Foley, R. J. 2013, Astrophysical Journal Letters, 770, L35

Shen, K. J., Kasen, D., Miles, B. J., & Townsley, D. M. 2017, ArXiv e-prints, arXiv:1706.01898

—. 2018, Astrophysical Journal, 854, 52

Silva Aguirre, V., Catelan, M., Weiss, A., & Valcarce, A. A. R. 2008, Astronomy and Astrophysics, 489, 1201

Silverman, J. M., Nugent, P. E., Gal-Yam, A., et al. 2013, The Astrophysical Journal Supplement, 207, 3

Sim, S. A., Röpke, F. K., Hillebrandt, W., et al. 2010, Astrophysical Journal Letters, 714, L52

Sjouwerman, L. O., & Dickel, J. R. 2001, in AIP Conf. Ser., Vol. 565, Young Supernova Remnants, ed. S. S. Holt & U. Hwang, 433

Skowron, D. M., Soszyński, I., Udalski, A., et al. 2016, Acta Astronomica, 66, 269

Skowron, J., Ryu, Y.-H., Hwang, K.-H., et al. 2018, Acta Astronomica, 68, 43

Slane, P., Lee, S.-H., Ellison, D. C., et al. 2014, Astrophysical Journal, 783, 33

Smartt, S. J. 2015, Publications of the Astronomical Society of Australia, 32, e016

Smartt, S. J., Eldridge, J. J., Crockett, R. M., & Maund, J. R. 2009, Monthly Notices of the Royal Astronomical Society, 395, 1409

Smecker-Hane, T. A., Cole, A. A., Gallagher, III, J. S., & Stetson, P. B. 2002, Astrophysical Journal, 566, 239

Smith, H. A. 2004, RR Lyrae Stars, 166

Smith, N. 2014, Annual Reviews of Astronomy and Astrophysics, 52, 487

Smith, N., Li, W., Filippenko, A. V., & Chornock, R. 2011, Monthly Notices of the Royal Astronomical Society, 412, 1522

Soderberg, A. M., Kulkarni, S. R., Berger, E., et al. 2005, Astrophysical Journal, 621, 908

Soderberg, A. M., Nakar, E., Berger, E., & Kulkarni, S. R. 2006, Astrophysical Journal, 638, 930

Soderblom, D. R. 2010, Annual Reviews of Astronomy and Astrophysics, 48, 581

Soszyński, I., Udalski, A., Szymański, M. K., et al. 2014a, Acta Astronomica, 64, 177

—. 2014b, Acta Astronomica, 64, 177

—. 2015a, Acta Astronomica, 65, 297

—. 2015b, Acta Astronomica, 65, 233

—. 2016a, Acta Astronomica, 66, 131

Soszyński, I., Pawlak, M., Pietrukowicz, P., et al. 2016b, Acta Astronomica, 66, 405

Soszyński, I., Udalski, A., Szymański, M. K., et al. 2016c, Acta Astronomica, 66, 131

—. 2017a, Acta Astronomica, 67, 103

—. 2017b, Acta Astronomica, 67, 297

Spitkovsky, A. 2016, in Supernova Remnants: An Odyssey in Space after Stellar Death, 96

Stage, M. D., Allen, G. E., Houck, J. C., & Davis, J. E. 2006, Nature Physics, 2, 614

Stockdale, C. J., Goss, W. M., Cowan, J. J., & Sramek, R. A. 2001, Astrophysical Journal, 559, L139

Stockdale, C. J., Kelley, M. T., Weiler, K. W., et al. 2007, in American Institute of Physics Conference Series, Vol. 937, Supernova 1987A: 20 Years After: Supernovae and Gamma-Ray Bursters, ed. S. Immler, K. Weiler, & R. McCray, 264–268

Stockdale, C. J., Maddox, L. A., Cowan, J. J., et al. 2006, Astronomical Journal, 131, 889

Stockdale, C. J., Rupen, M. P., Cowan, J. J., Chu, Y.-H., & Jones, S. S. 2001, Astronomical Journal, 122, 283

Sturch, C. 1966, Astrophysical Journal, 143, 774

Sukhbold, T., & Woosley, S. E. 2014, Astrophysical Journal, 783, 10

Taam, R. E. 1980, Astrophysical Journal, 242, 749

Taam, R. E., Kraft, R. P., & Suntzeff, N. 1976, Astrophysical Journal, 207, 201

Taddia, F., Sollerman, J., Leloudas, G., et al. 2015, Astronomy and Astrophysics, 574, A60

Tammann, G. A., Loeffler, W., & Schroeder, A. 1994, The Astrophysical Journal Supplement, 92, 487

Taubenberger, S. 2017, ArXiv e-prints, arXiv:1703.00528

Taylor, G. 1950, Proceedings of the Royal Society of London Series A, 201, 159

Thompson, T. A., Quataert, E., & Murray, N. 2009, Monthly Notices of the Royal Astronomical Society, 397, 1410

Thrall, H. 2008, in Astronomical Society of the Pacific Conference Series, Vol. 390, Pathways Through an Eclectic Universe, ed. J. H. Knapen, T. J. Mahoney, & A. Vazdekis, 200

Tojeiro, R., Wilkins, S., Heavens, A. F., Panter, B., & Jimenez, R. 2009, The Astrophysical Journal Supplement, 185, 1

Totani, T., Morokuma, T., Oda, T., Doi, M., & Yasuda, N. 2008, Publications of the Astronomical Society of Japan, 60, 1327

Trotter, A. S., Reichart, D. E., Egger, R. E., et al. 2017, Monthly Notices of the Royal Astronomical Society, 469, 1299

Truelove, J. K., & McKee, C. F. 1999, The Astrophysical Journal Supplement, 120, 299

Turatto, M., Benetti, S., Cappellaro, E., et al. 1996, Monthly Notices of the Royal Astronomical Society, 283, 1

Tutukov, A., & Yungelson, L. 1996, Monthly Notices of the Royal Astronomical Society, 280, 1035

Udalski, A., Szymanski, M., Kaluzny, J., Kubiak, M., & Mateo, M. 1992, Acta Astronomica, 42, 253

Udalski, A., Szymański, M. K., & Szymański, G. 2015, Acta Astronomica, 65, 1

Udalski, A., Pont, F., Naef, D., et al. 2008, Astronomy and Astrophysics, 482, 299

van den Bergh, S. 1967, Astronomical Journal, 72, 70

—. 1995, Astrophysical Journal Letters, 451, L65

van den Heuvel, E. P. J., Bhattacharya, D., Nomoto, K., & Rappaport, S. A. 1992, Astronomy and Astrophysics, 262, 97

Van Der Walt, S., Colbert, S. C., & Varoquaux, G. 2011, Computing in Science & Engineering, 13, 22

Van Dyk, S. D. 2017, Philosophical Transactions of the Royal Society of London Series A, 375, 20160277

Van Dyk, S. D., Zheng, W., Brink, T. G., et al. 2018, ArXiv e-prints, arXiv:1803.01050

Vandenberg, D. A., Bolte, M., & Stetson, P. B. 1996, Annual Reviews of Astronomy and Astrophysics, 34, 461

Vink, J. 2012, The Astronomy and Astrophysics Review, 20, 49

Völk, H. J., Berezhko, E. G., & Ksenofontov, L. T. 2005, Astronomy and Astrophysics, 433, 229

Völk, H. J., Berezhko, E. G., & Ksenofontov, L. T. 2005, Astronomy and Astrophysics, 433, 229

Walch, S., Girichidis, P., Naab, T., et al. 2015, Monthly Notices of the Royal Astronomical Society, 454, 246

Wang, B., & Han, Z. 2012, New Astronomy Reviews, 56, 122

Warren, J. S., Hughes, J. P., Badenes, C., et al. 2005, Astrophysical Journal, 634, 376

Weidner, C., Kroupa, P., Pflamm-Altenburg, J., & Vazdekis, A. 2013, Monthly Notices of the Royal Astronomical Society, 436, 3309

Weiler, K. W., Panagia, N., Montes, M. J., & Sramek, R. A. 2002, Annual Reviews of Astronomy and Astrophysics, 40, 387

Weisz, D. R., Dolphin, A. E., Skillman, E. D., et al. 2013, Monthly Notices of the Royal Astronomical Society, 431, 364

—. 2014, Astrophysical Journal, 789, 147

Wellons, S., Soderberg, A. M., & Chevalier, R. A. 2012, Astrophysical Journal, 752, 17

Whelan, J., & Iben, Jr., I. 1973, Astrophysical Journal, 186, 1007

White, R. L., & Long, K. S. 1991, Astrophysical Journal, 373, 543

Williams, B. F., Naik, S., Garcia, M. R., & Callanan, P. J. 2006, Astrophysical Journal, 643, 356

Williams, B. F., Dolphin, A. E., Dalcanton, J. J., et al. 2017, Astrophysical Journal, 846, 145

Winkler, P. F., Gupta, G., & Long, K. S. 2003, Astrophysical Journal, 585, 324

Wongwathanarat, A., Janka, H.-T., Müller, E., Pllumbi, E., & Wanajo, S. 2017, Astrophysical Journal, 842, 13

Wood-Vasey, W. M., Miknaitis, G., Stubbs, C. W., et al. 2007, Astrophysical Journal, 666, 694

Woods, T. E., Ghavamian, P., Badenes, C., & Gilfanov, M. 2017, Nature Astronomy, 1, 800

—. 2018, ArXiv e-prints, arXiv:1807.03798

Woosley, S. E. 2016, Astrophysical Journal Letters, 824, L10

Woosley, S. E., & Kasen, D. 2011, Astrophysical Journal, 734, 38

Woosley, S. E., Langer, N., & Weaver, T. A. 1995, Astrophysical Journal, 448, 315

Woosley, S. E., & Weaver, T. A. 1994, Astrophysical Journal, 423, 371

Wuyts, S., Förster Schreiber, N. M., Lutz, D., et al. 2011, Astrophysical Journal, 738, 106

Wyrzykowski, L., Skowron, J., Kozłowski, S., et al. 2011a, Monthly Notices of the Royal Astronomical Society, 416, 2949

Wyrzykowski, Ł., Kozłowski, S., Skowron, J., et al. 2011b, Monthly Notices of the Royal Astronomical Society, 413, 493

Yamaguchi, H., Badenes, C., Petre, R., et al. 2014, Astrophysical Journal Letters, 785, L27

Yamaguchi, H., Badenes, C., Foster, A. R., et al. 2015, Astrophysical Journal, 801, L31

Yang, R.-z., Sun, X.-n., & Aharonian, F. 2016, ArXiv e-prints, arXiv:1612.02262

Yang, Y., Li, Z., Sjouwerman, L. O., Yuan, F., & Shen, Z.-Q. 2017, Astrophysical Journal, 845, 140

Yaron, O., Prialnik, D., Shara, M. M., & Kovetz, A. 2005, Astrophysical Journal, 623, 398

Yasuda, N., & Fukugita, M. 2010, Astronomical Journal, 139, 39

Yoachim, P., & Dalcanton, J. J. 2006, Astronomical Journal, 131, 226

Yoon, S.-C. 2017, Monthly Notices of the Royal Astronomical Society, 470, 3970

Zapartas, E., de Mink, S. E., Izzard, R. G., et al. 2017, Astronomy & Astrophysics, 601, A29

Zaritsky, D. 1999, Astronomical Journal, 118, 2824

Zaritsky, D., Harris, J., Thompson, I. B., & Grebel, E. K. 2004, Astronomical Journal, 128, 1606